Table of Contents

List of Figures

List of Tables

Nomenclature

Abbreviations

3D – Three Dimensional

CE – Contractile Element

CPM – Continuous Passive Motion

dof – degrees of freedom

EDF – Error Dependency Function

EKF – Extended Kalman Filter

GUI – Graphical User Interface

LMS – Least Mean Square

MEM – Matrix Element Matching

MIMO – Multi-Input Multi-Output

PE – Parallel-elastic Element

RLS – Recursive Least Square

ROM – Range Of Motion

SE – Series-elastic Element

SISO – Single-Input Single-Output

Definition of Terms

Ankle/Talocrural joint – The articulation between the Tibia, Fibula and Talus

Subtalar joint – The articulation between the Talus and Calcaneus

Sagittal plane – the anatomical plane separating the body into left and right portions

Frontal plane – the anatomical plane separating the body into front and back portions

Transverse plane – the anatomical plane separating the body into top and bottom portions

Lateral – used to describe the side of a body part which is away from the sagittal plane of the human body

Medial – used to describe the side of a body part which is facing towards the sagittal plane of the human body

Shank – the portion of the lower limb between the knee and the ankle

Plantarflexion – rotation of the foot on the sagittal plane so that the toes are brought away from the shank

Dorsiflexion – rotation of the foot on the sagittal plane so that the toes are brought closer towards the shank

Inversion – Rotation of the foot so that the lateral side of the foot is moved closer to the sagittal plane of the human body

Eversion – Rotation of the foot so that the medial side of the foot is moved away from the sagittal plane of the human body

Abduction/External Rotation – Rotation of the foot on the transverse plane so that the big toe is moved away from the sagittal plane of the human body

Adduction/Internal Rotation – Rotation of the foot on the transverse plane so that the big toe is moved closer towards the sagittal plane of the human body

Euler Angles – A sequence of angles used to define orientation of an object through consecutive rotations about the specified axes. For examples, XYZ Euler angles give the X rotation about the x-axis, followed by a Y rotation about the resulting y-axis and then the Z rotation about the resulting z-axis

Joint space – generalised coordinates used to describe the motion or force quantities along the actuators of a robot

Task space – generalised coordinates used to describe the motion or force quantities in the operational space of a robot.

Singular Value Decomposition (SVD) – A matrix factorisation which represents a rectangular matrix as the product of a unitary matrix, a rectangular diagonal matrix with non negative real numbers along its diagonal, and another unitary matrix.

Singular Values – The values along the leading diagonal of the rectangular diagonal matrix resulting from the singular value decomposition of a matrix.

Condition Number – The ratio between the maximum and minimum singular values of a matrix

Rank deficient – A matrix is considered to be rank deficient if it has zero as a singular value.

Null vector – A null vector of a matrix is a column vector of unit length whereby the matrix multiplication of this matrix and the null vector will result in a zero vector

Null space – A column-wise collection of the null vectors of a matrix

Manipulator Jacobian – A matrix describing the linear mapping between the joint space velocity and task space velocity

Robot singularity – A point in the robot workspace whereby the Manipulator Jacobian becomes rank deficient.

Chapter 1 Introduction

Robots can be considered as reprogrammable devices which can be used to complete certain tasks in an autonomous manner. While robots have long been used for automation of industrial processes, there is a growing trend where robotic devices are used to provide services for end users. An area where robots are believed to have a significant impact is healthcare. Accessibility to healthcare services is a vital component to improve the quality of life. However, the trend of aging populations will certainly increase demand on healthcare and create more strain on the already limited resources available [1, 2]. For this reason, much research had been dedicated to medical and healthcare robots [3]. As ankle sprain is a very common form of musculoskeletal injuries and requires a comprehensive rehabilitation program to avoid recurrent injuries [4], application of robots in ankle rehabilitation will be greatly beneficial in providing additional resources to facilitate the physical therapy of patients suffering from ankle injuries. The overall aim of this research is therefore to develop a robot to facilitate physical therapy of the human ankle. This chapter provides background information on issues relating to this research, starting with the motivations behind the development of rehabilitation robots for physical therapy and successful examples of such systems. An overview of strategies used to control the physical interaction of robots with their environment is also provided. This is followed by a description of the general procedures involved in ankle rehabilitation. The motivations and objectives for this research, as well as the structure of this thesis are also detailed at the end of this chapter.

1.1 Rehabilitation Robots

Robots were used for rehabilitation purposes since the 1960s [5]. Application of robots in rehabilitation was initially more focused on replacing lost functions in individuals with physical disabilities through the use of devices such as robotic orthoses, robotic workstations, feeding devices and robotic wheelchairs [1]. Over the last two decades however, there has been an increasing amount of research into the use of robots in physical therapy [2, 3, 6-9]. This Section will discuss the main motivations behind this trend, notable robotic systems used for the rehabilitation of upper and lower limbs, as well as the some of the important features of these rehabilitation robots. In the context of this research, rehabilitation robots used for physical therapy purposes are considered as devices which utilises active feedback control to provide guidance, assistance or resistance to patients during their rehabilitation exercises.

1.1.1 Motivation for Rehabilitation Robots

One of the main motivations behind the adoption of robots in physical therapy is the potential improvement in productivity [7, 10]. Physical therapy normally requires manual manipulation of the patient's affected limb, and these manipulations can be rather repetitive and labour intensive [8, 11]. Consequently, such rehabilitation exercises can easily lead to the onset of fatigue in the therapist, thus limiting the duration and intensity of the therapy session. Since robots are well suited for repetitive tasks and can be designed to have adequate force capabilities, their use in the execution of these exercises will be able to reduce the physical workload of therapists, and can potentially allow the therapists to simultaneously oversee the treatment of multiple patients in a supervisory role [7, 8]. Additionally, by removing the physically demanding component of a therapist's workload, application of robots in rehabilitation also has the potential of reducing the likelihood of repetitive stress injuries amongst physical therapists.

The use of robots in physical therapy also offers further advantages due to their high repeatability and ability to collect vast amount of quantitative data when equipped with appropriate sensors. Since therapists mainly operates based on their "feel", their evaluation of the patient's condition can be rather subjective. By using robotic devices, diagnosis and prognosis can be made more objectively with the help of quantitative data, and comparisons between different cases can also be made more easily [8, 12]. The high repeatability of the robotic devices also allows therapy to be applied more consistently and will help to identify the effectiveness of the treatment. As a result, in addition to the delivery of physical therapy, robots can also contribute to rehabilitation research.

Research has advocated that active participation of the patient in physical therapy is important in enhancing its effectiveness [2, 13, 14]. This means that the patient will have to be motivated to carry out the required rehabilitation exercises. Robotic systems can provide a rich graphical user interface which can be designed to capture the attention of the patient. Many existing rehabilitation robots for the upper limb have administered robotic therapy in the form of "video games"[2, 9, 15, 16], where the required trajectory or end point of motion is displayed on a monitor and the patient is required to follow the target. This has made the rehabilitation exercises more goal-oriented and makes the exercises more engaging, thus giving the patients added motivation to complete the required exercises.

Several successful rehabilitation robots have undergone clinical trials and are currently being used in hospitals and clinics for neuromotor rehabilitation. Results from these clinical trials are predominantly positive, suggesting that the use of intensive robotic therapy on stroke patients has the effect of reducing the level of impairment and improving the mobility of the affected limb [3, 6, 17].

1.1.2 Examples of Rehabilitation Robots

Existing robots designed for physical therapy are commonly involved with neuromotor training of patients suffering from neurological disorders [3, 17]. Robots used in this capacity are generally required to manipulate the patient's affected limb by guiding it along certain motion trajectories. For the rehabilitation of upper limbs, the MIT-MANUS is one of the more successful devices which had been clinically tested [2, 6, 7, 18]. The basic module of this robot is capable of guiding the patient's arm in two degrees of freedom motion on the horizontal plane, thus targeting motion in the shoulder and elbow joints. Additional modules were also developed to allow motion along the vertical direction, as well as motion of the wrist. The robotic manipulator used in this system was designed to have a low inertia and high back-drivability, making it inherently compliant and safe to operate. The rehabilitation exercises are carried out with the aid of a graphical user interface which provides visual feedback to the patient to indicate the location of their hand. The robot is controlled using a reference force field which gives the relationship between the desired patient-robot interaction force and the position of the patient's hand. Additionally, this force field is also designed to evolve with the performance of the patient in previous runs of the exercises in order to set the difficulty at a level that is challenging but yet manageable.

In terms of lower limb rehabilitation, the Lokomat® is a commercially available treadmill based gait rehabilitation system [19]. This robotic system operates by suspending the patient over the treadmill to provide body weight support. A robotic orthosis is worn by the patient to guide the patient's lower limb through the gait cycle. Various control strategies had been devised to allow variation of the actual lower limb trajectory from the predefined reference trajectory to permit a certain degree of gait customisation for different patients [11, 13, 20, 21]. Additionally, it employs an assistance as required philosophy whereby the robotic orthosis will only provide assistive force if the patient fails to carry out the required gait pattern. Another rehabilitation robot used for gait training is the adaptive foot orthosis. This robot has a smaller scale compared to the Lokomat and takes the form of a wearable device driven by a series elastic actuator (an electric linear actuator placed in series with an elastic element). This orthosis has the ability to modify the stiffness at the ankle joint through different phase of the gait cycle. Additionally, it can also adapt its damping parameters to minimise the occurrence of drop foot gait [22].

Even though neuromotor task training is by far the biggest application area in therapeutic robots, devices were also developed for rehabilitation of musculoskeletal injuries. These robots share many similar requirements as those used for neuromotor rehabilitation. In fact, apart from the capability for passive and assisted motion of the affected limb, such robots also need to be able to provide resistive and proprioceptive training. A more detailed discussion on robots designed for ankle rehabilitation is presented in Chapter 2 of this thesis.

1.1.3 Common Features of Rehabilitation Robots

It can be seen that the examples of rehabilitation robots presented above share several common traits. The obvious feature found in all these robots is the emphasis on the user's safety. As the patient is tightly coupled to the rehabilitation robot during its operation, it is vital that the patient-robot interaction forces or torques be maintained at safe levels to prevent any injuries. This therefore requires the robotic devices to have some degree of compliance or in other words, be backdriveable. Inherent backdriveability can be realised by using a low actuator transmission ratio or by decoupling the actuator mass from its end point through use of elastic elements. These are respectively achieved by the MIT-MANUS and the adaptive foot orthosis described in the previous section. Alternatively, force feedback control can also be used to reduce the apparent actuator mass and improve the backdriveability of actuators [23, 24].

Physical characteristics such as size, shape, mass, joint kinematics, motion range and joint dynamics can vary considerably between individuals. Additionally, the level and severity of injuries are also likely to be different across different patients. Robots designed for rehabilitation must therefore be adjustable or adaptable so that they can cater for a larger population with different rehabilitative needs. Extrinsic characteristics such as size and shape are related to the ergonomics of the device and can generally be accommodated through incorporation of an adjustment mechanism or by replacing certain components in the device. On the other hand, variations in mass, joint kinematics and joint stiffness, will alter the mechanical properties of the robot's operating environment, and can dictate whether safe operation of the rehabilitation robot is possible. For example, closed loop system stability is influenced by joint dynamics, while joint kinematics determines directions of admissible motion. If these characteristics are not taken into consideration in the robot controller, the robot may become unstable or it may apply excessive forces in non-compliant directions, thus presenting a dangerous scenario for the patient. As a result, it is crucial that rehabilitation robots have the capability to operate safely in a range of environments. This can be achieved through use of robust or adaptive control strategies. Adaptive control strategies are also important in allowing the robot to cater for patients with different capabilities in performing the rehabilitation program due to the specific extent of their injuries.

Another common feature among rehabilitation robots is the need to control the physical interaction between the patient and the robot. This means that both the motion of the robot and the contact forces applied to the patient must be regulated. Motion regulation is generally required when guiding the patient's limb along paths which are representative of reaching tasks for the upper limb or trajectories which corresponds to normal gait pattern for the lower limb. The requirement to control forces and torques on the other hand can arise from concerns of the patient's safety or from the need to apply resistive effort for strength training exercises.

1.2 Interaction Control

Traditionally, many robotic devices are position controlled and various mature control techniques had been developed for the design of position controllers. However, when robots are deployed in applications that require significant physical interaction with the external environment, pure position control is no longer adequate [25]. This is because the design of the position controller is normally done by considering the dynamics of the robot alone and treats externally applied forces/torques as disturbances. However, when the robot comes into contact with an external environment, the assumed robot model may no longer be valid and the robot will therefore deviate from its intended behaviour. Furthermore, as large controller gains are normally used in position controllers to minimize position tracking errors, interaction with a stiff environment will result in large position errors which can in turn lead to force build up at the contact interface. This is of course unacceptable for robots which interact closely with humans as it is likely to cause injuries to the user. Clearly, a control strategy which takes more than just position into consideration is needed for the control of rehabilitation robots. Interaction control is an approach which aims to regulate both the forces and motion of a robot which is in contact with an external environment. Two groups of interaction control schemes are commonly used. They are hybrid force-position control and impedance control [26, 27].

Hybrid force-position control [28] is a control strategy which splits the task space into two complementary subspaces using a selection matrix. A position control strategy is then applied in one of the subspace and force control in the other. Normally, directions where constraint-free motion is permissible are position controlled while force control is applied in the constrained directions. This will allow accurate realisation of the desired force and motion when the kinematic constraints in the environment are known with little or no uncertainty. While such constraints may be well known in an industrial setting, there can be considerable variations in the joint kinematics of different individuals. This would mean that hybrid force-position control may still result in large interaction forces due to imprecise definition of the free motion directions. Furthermore, if the robot were to move from a constraint-free state to a constrained state, a switch in the control law is required since all directions need be position controlled prior to contact and the hybrid position-force control should only be active after contact had been made.

Impedance control is another type of interaction control scheme which aims to maintain a prescribed relationship between force and motion of the robot. This relationship is termed the mechanical impedance and is defined as the dynamic ratio of the error in applied forces to the velocity error of the robot end effector. It is also often expressed as a second order system as shown in (1.1) [29].

$$F - F_d = M(\ddot{x}_d - \ddot{x}) + B(\dot{x}_d - \dot{x}) + K(x_d - x) \tag{1.1}$$

$$Z(s) = \frac{F_e(s)}{\dot{X}_e(s)} = \frac{Ms^2 + Bs + K}{s} \tag{1.2}$$

Where M is the inertia parameter, B is the damping parameter and K is the stiffness parameter. This relationship is also commonly expressed in its Laplace transformed form given by (1.2). Perfect realisation of the impedance controller will therefore allow the robot end effector to behave in such a way that it is equivalent to the desired mass-spring-damper system. It can be seen from (1.1) that impedance control is a more unified motion control approach. This is because the robot will behave as a position controlled system in the absence of any external and desired forces (no interaction). Consequently, unlike the hybrid position-force controller, no switching of control law is required for impedance control [26].

Selection of the target manipulator impedance is an important issue in impedance control since it establishes the physical behaviour of the controlled manipulator. For a single-input-single-output system, it can be seen that an infinite impedance will result in pure position control while a zero impedance will lead to pure force control. From this observation, impedance control can be designed to give a similar performance as hybrid position-force control by selecting larger impedance values in directions of free motion and smaller impedance values in constrained directions. While the selection of target impedances can be achieved through experimental trial and error, more systematic approaches can also be taken. Researchers have suggested that the choice of impedance parameters should be based on optimisation of certain objective functions. For instance, the target impedance can be chosen to be proportional to the environmental admittance (the inverse of impedance) to minimise a weighted sum of position error and actuator force [29].

It is evident from the above discussion that impedance control is a more robust interaction control scheme compared to hybrid force-position control. It is therefore not surprising that a large proportion of rehabilitation devices have employed some form of impedance control to deal with the variability found among patients[2, 30-33]. However, the more robust nature of impedance control does not mean that knowledge of the operating environmental is no longer important. Information of the environmental dynamic characteristics can be used to alter robot behaviour in such a manner that the robot performance can be enhanced. The ability to adapt the impedance controller according to changes in environmental conditions is therefore a desired feature in rehabilitation robots.

Several adaptive impedance controllers were developed to allow adaptation to variability in the robot dynamics [34-36]. This is due to the fact that a computed torque control approach is often used in position based impedance controllers to allow the desired impedance to be realised with higher accuracy. Since this control approach relies on accurate compensation of the robot dynamics, uncertainties in the robot dynamic parameters will degrade the controller performance. This issue is particularly important for fast moving robots where the robot dynamic terms are large due to high accelerations and velocities. Serial robots are also more severely affected as they generally have larger link inertias. However, if the manipulator is designed in such a way that the robot inertia is low, robot performance may not be severely affected by the lack of such dynamic compensation terms. In fact, impedance control can be successfully implemented using merely proportional derivative position control in some applications [24]. With this in mind, computational resources can potentially be allocated for adaptation of environmental parameters instead of robot parameters if the robot dynamic terms are relatively small in magnitude (in comparison with the interaction forces/moments) and when the application involves motion of lower velocity and acceleration.

1.3 Ankle Rehabilitation

The human ankle is one of the most complex structures in the human musculoskeletal system and plays an important role in maintaining body balance during ambulation [37]. A pictorial view of the various bones and ligaments found at the foot and ankle are shown in Figure 1.1. In general use, the term "ankle" is used to describe the structure which encompasses both the ankle and subtalar joints, where the ankle (or talocrural) joint is the articulation between three bones of the lower limb, namely tibia, fibula and talus. The subtalar joint on the other hand, is formed by the interface between the talus and calcaneus and is located beneath the ankle joint.

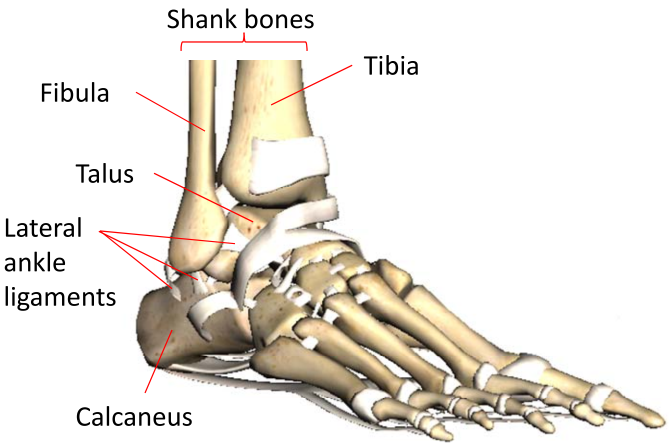

Figure 1.1: Bones and ligaments at the human foot and ankle.

Due to its location, the human ankle is frequently subjected to large loads which can reach up to several times the body weight. The exposure to such large loads also means a higher likelihood of injuries. In fact, the ankle is the most common site of sprain injuries in the human body, with over 23,000 cases per day in the United States [4]. In New Zealand, approximately 82,000 new claims related to ankle injuries were made to the Accident Compensation Corporation (ACC) in the year 2000/2001, costing an estimated 19 million NZD and making ankle related claims the fourth biggest cost for ACC [38].

Ankle sprains are injuries which involve the over-stretching or tearing of ligaments around the ankle and are often sustained during sporting or physical activities. Ankle sprains can be classified into several grades, ranging from mild overstretching to complete disruption of ankle ligaments. Depending on the severity of the sprain, the time required for recovery can range from 12 days to more than 6 weeks [39]. Researchers have reported that a significant number (>40%) of severe ankle sprains can develop into chronic ankle instability [39], which makes the ankle more susceptible to further injuries in the future. Chronic ankle instability is thought to be caused by a combination of mechanical and functional instability at the ankle. Mechanical instability is used to refer to changes of the ankle anatomy which makes it more prone to future sprain injuries, while functional instability refers to changes which give rise to insufficiencies in the ankle neuromuscular system, such as impaired proprioception, muscle weakness and reduced neuromuscular control [4].

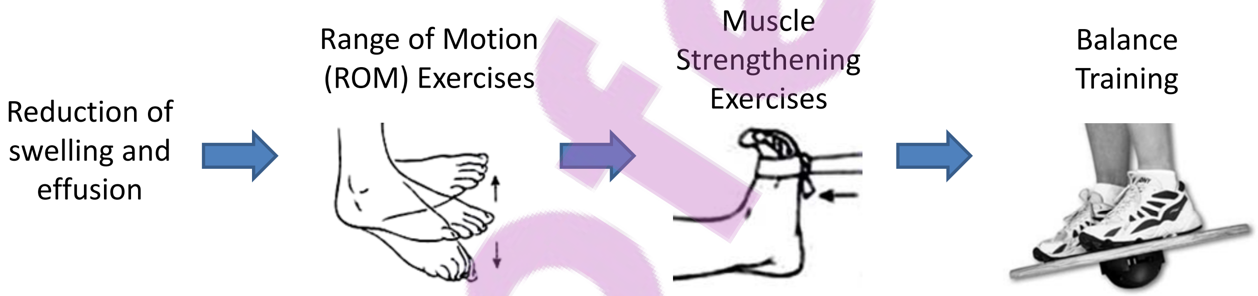

Figure 1.2: The typical ankle rehabilitation program for ankle sprains

The general rehabilitation program for ankle sprains is carried out in stages as shown in Figure 1.2. The initial stage of treatment right after injury is considered the acute phase of rehabilitation and is focused on reducing effusion and swelling at the affected to promote healing of the injured tissues. A reduction in effusion can be achieved with elevation, application of ice and compression. The affected ankle is also often immobilised. However, as prolonged immobilisation of the ankle can lead to reduced Range of Motion (ROM) and muscular atrophy, the next phase of ankle rehabilitation typically involve ROM and muscle strengthening exercises. With reduced effusion, the rehabilitation enters into the subacute phase where active and passive ROM exercises are normally carried out within the pain-free range of the patient to improve the range of motion and reduce muscular atrophy. Research has also suggested that this has the ability to stimulate healing of torn ligaments [39].

The rehabilitative phase is achieved once pain free weight bearing gait is possible. During this phase, ROM exercises are continued together with the commencement of muscle stretching and resistive exercises [39]. The resistance level of these strengthening exercises should be increased as the patient progresses with recovery. Muscle stretching is important to assist the recovery of joint ROM while resistance training is used to improve the strength of muscles surrounding the ankle to prevent future injuries [40]. Finally, proprioceptive and balancing exercises should be carried out towards the end of the rehabilitation program (functional phase) to enhance the patients' sense of joint position, thus giving them better foot and ankle coordination and improving their ability to respond to sudden perturbations at the ankle [39].

As can be seen from the previous discussion, muscular strength and good proprioception are vital in preventing functional instability in the ankle. Emphasis must therefore be placed in these areas and an extensive rehabilitation program is needed to minimise the likelihood of recurrent injuries. The repetitive and tedious nature of such exercises therefore makes robotic devices an attractive alternative to manual manipulation. However, the great variability observed between different patients due to either their level of injury or their ankle characteristics such as joint limits and stiffness also means that any robotic device employed in this area must be adaptive to allow it to cater for the requirements of specific patients.

1.4 Research Objectives and Motivation

The ultimate goal of this research is to develop a platform based ankle rehabilitation robot which can be effectively used to facilitate physical therapy of the human ankle. The main feature desired from this system is the capability to adapt to users with varying ankle physical characteristics including range of motion, joint stiffness and muscle strength.

1.4.1 Development of an Ankle Rehabilitation Robot

Due to the high incidence and potentially lengthy rehabilitation period of ankle injuries, there is significant demand for the treatment of such injuries. As physical therapy is vital in the promotion of recovery and prevention of future injuries, effort is required to ensure the availability of this service. Introduction of robots in ankle rehabilitation will allow delegation of tedious rehabilitation tasks to the robot, and allow therapists to extend care to more patients. As discussed previously, robots can also be used as evaluation tools to determine the progress and capability of the patient. This means that robots can potentially be used to determine whether a patient has achieved a suitable level of muscle strength and proprioceptive capability required to prevent future injuries.

A survey of existing ankle rehabilitation robots shows that the end effectors of existing platform based systems are typically constrained about a centre of rotation which does not coincide with the actual ankle joint[10, 31, 32, 41, 42]. A result of this is that the user's shank will not be stationary during operation of these robots if the natural ankle-foot motion is to be maintained. Consequently, orientation and interaction moments of the robotic platform are unlikely to be equivalent to the actual displacement and moments found between the foot and the shank. This therefore makes these existing devices less suitable for evaluation purposes due to the greater uncertainties in the motion/force information.

A main objective of this research is therefore to develop a suitable robotic device that can carry out ankle rehabilitation exercises. Particular focus will be placed on ROM exercises and resistive exercises for muscle strengthening. To allow potential use of the robot as an evaluation tool, the device must also be able to reliably measure the orientation and moments of the ankle-foot structure, and it is proposed that this be achieved through appropriate design of the robot kinematics to minimise movements of the user’s shank during robot operation.

1.4.2 Construction of a Computational Ankle Model

Knowledge of the mechanical environment within which the robot operates can contribute to improved performance and safety of the robot. It is therefore important that the human ankle be modelled, both in terms of its kinematics and dynamics. The ankle mechanical characteristics are ultimately governed or “parameterised” by the ankle anatomy and biomechanics. While the exact geometry and locations of the anatomical structures are different between individuals, the overall ankle anatomy remains largely similar. The overall biomechanics of the ankle of different people must therefore fit a particular pattern despite quantitative variations in the observed ankle mechanical properties. In order to better appreciate this pattern, understanding of the ankle biomechanics is required. This need has given rise to another objective of this research, which involves the construction of a computational model of the human ankle by considering its kinematics, bone geometry and ligament/tendon properties. While such computational models are not uncommon in the literature, they are typically designed to serve as tools to analyse foot pathology and to study foot biomechanics, but not as tools to facilitate the development of robot controllers [43-48].

In this research, the developed model will be used in controller simulation to test the feasibility of the proposed control scheme or control parameters prior to their actual implementation. Additionally, the resulting model can also form a basis upon which a gain scheduled control scheme can be devised. Furthermore, the model can be equally applied in the evaluation of different control schemes or rehabilitation trajectories by providing information on the forces and moments applied to the ankle anatomical structures such as bones, ligaments and tendons. The model required in this work must therefore be sufficiently complex to allow extraction of the desired force and moment quantities, but yet computationally tractable to permit simulations in longer time durations.

1.4.3 Development of an Adaptive Interaction Control Scheme

In order to maintain the safety of the patient, suitable control strategy must be developed to ensure that the robot is compliant or backdriveable so that the robot can yield its position when an external load is applied by the patient. At the same time, the robot must still be able to influence the patient’s ankle motion in a manner so that it can achieve the required rehabilitation goals. This makes interaction control an essential component of the ankle rehabilitation robot. Owing to its generality and relative robustness to kinematic uncertainty, impedance control has been the more popular choice of interaction control scheme in rehabilitation robots. It can also be seen throughout this chapter that the ability to adapt to individual patient’s joint characteristic and capabilities can result in safer operation and potentially improved therapeutic outcome. This makes adaptability an important prerequisite for a successful rehabilitation robot. Consequently, the final and most important objective in this research is the development of an adaptive impedance controller. This controller should be capable of changing its controller parameters according to variations in the foot orientation and ankle characteristics. Additionally, it should also be able to adapt the assistance provided to the user to encourage their active participation [2, 14, 49].

In order to ensure safe operation, the stiffness of the robot should ideally be varied according to the compliance of the ankle-foot structure so that excessive forces/moments will not be applied in foot configurations which are close to the joint limits. In addition to the modification of robot stiffness or damping, adaptive behaviour can also be introduced through modification of the reference force trajectories as in [50]. However, due to the coupling of ankle rotations, movement of the foot in the rotational space is most likely constrained. Special attention must therefore be placed in this research to establish adaptation schemes which can accommodate constrained motions in the rotational space.

1.5 Thesis Outline

This thesis details the work carried out in this research to meet the above objectives. A literature review on the state of the art of the design and control of ankle rehabilitation robots, kinematic and computational biomechanical models for the human ankle and interaction control strategies is presented in Chapter 2. Chapter 3 then details the development of a new redundantly actuated parallel robot for ankle rehabilitation, whereby the workspace and singularity analyses of the mechanism is presented, together with a description of the robot hardware and user interface.

Since knowledge of the ankle kinematics and biomechanics of the human ankle can greatly facilitate controller development, works relating to the identification and modelling of this information are presented in Chapters 4, 5 and 6. More specifically, the ankle kinematic model used in this research and its online parameter identification are discussed in Chapter 4. Different online identification techniques are compared in Chapter 4 and a modified recursive least squares algorithm is also presented to carry out the parameter identification of a biaxial ankle model with variable joint axis orientations. Chapter 5 then presents the formulation of the rigid body based computational biomechanical model developed in this research, while Chapter 6 discusses validation of the above ankle model through the use of simulation and experimental data. This is accompanied by a sensitivity analysis of the developed model. Lastly, the potential application of the model in the optimisation of rehabilitation trajectories is also demonstrated.

The final few chapters of this thesis are dedicated to discussions on the control schemes developed for the ankle rehabilitation robot. The development of a multi-input-multi-output actuator force controller is presented in Chapter 7, where the kinematic constraints and inertia of the parallel mechanism are taken into account in the controller to achieve partial decoupling between the actuator forces. The stability and robustness of the proposed control scheme are investigated using a simplified manipulator model and experimental results are presented to show the advantage of the proposed approach over one which controls the actuator forces in an independent manner. Chapter 8 then discusses the detailed dynamic modelling of the parallel mechanism and integrates this model with the actuator and ankle dynamics to form a complete system model. The control schemes used to realise basic impedance control and to resolve the actuation redundancy are also presented, while issues encountered during implementation of these control schemes are also addressed. Chapter 8 then ends with simulation and experimental results of the proposed impedance control scheme.

After the establishment of the basic robot control scheme, the adaptive interaction control schemes developed in this research are discussed in Chapters 9 and 10. Two adaptive modules of the interaction controller are described, beginning with one which adjusts the robot impedance parameters by making use of the ankle stiffness characteristics obtained from the computational ankle model, as well as the ankle and subtalar joint displacements estimated from the online kinematic parameter identification algorithm (Chapter 9). The second of these modules is presented in Chapter 10 as an assistance adaptation scheme which generates a feed forward assistive force according to the performance of the user. This scheme is based on an existing adaptation rule developed in [50] but modifications were made in this research to improve the performance of the original scheme during active or constrained motions. Again, simulation and experimental results are also included in these chapters to show the efficacy of the proposed approaches.

Finally, Chapter 11 of this thesis is used to present the outcomes, conclusions and contributions of this research, together with relevant future works which can be done to further advance the developed system. This research had produced publications in an international journal, peer reviewed international conferences and an invited book chapter [51-55]. Certain sections of this thesis are therefore based on these published works.

1.6 Chapter Summary

This chapter has highlighted the main motivations and objectives of this research through an overview of rehabilitation robots, interaction control and rehabilitation of ankle sprains. The main incentives for the use of robotic devices in physical therapy can be summarised as: their ability to reduce physical workload of therapists; the possibility to log relevant data for more objective diagnosis and prognosis; and their potential in making rehabilitation exercises more engaging experience via interactive user interfaces. A study on several successful rehabilitation robots have highlighted that backdriveability, interaction control and adaptability are important elements in rehabilitation robots.

The high incidence rate of ankle injuries and the extensive rehabilitation process required to reduce recurrent injuries have made it a suitable candidate for the application of robotic therapy. While robotic devices had been developed for ankle rehabilitation, further improvements of these existing devices are required to enhance their adaptability and functionality. One of the main objectives of this research therefore involves the development of a new ankle rehabilitation robot to provide an improvement on some of the existing solutions. As controller development can be facilitated with greater understanding of the operating environment, the second objective of this research is to construct a computational ankle model to describe the human ankle biomechanics. Lastly, the final objective of this research is to develop an adaptive interaction control scheme for the ankle rehabilitation robot so that it can improve the robot’s safety and performance by considering the changes in its operating environment.

Chapter 2 Literature Review

This chapter presents an up-to-date review of important works which pertain to this research. This review is divided into three main parts, each relating to an objective of this research. It begins with a survey of existing ankle rehabilitation devices designed for use in gait assistance and treatment of ankle sprains. An overview of the kinematic and computational biomechanical models of the human ankle is also provided. This is followed by a review of the state-of-the-art of interaction control strategies, with primary focus on its application in rehabilitation robots. Finally, the reviewed materials are assimilated in a discussion that highlights issues in ankle rehabilitation robots that require further development, and are hence the subject of investigation for this research.

2.1 Existing Ankle Rehabilitation Devices

Robotic devices had been developed for the rehabilitation of the human ankle. Although the main rehabilitation problem considered in this research is that of sprained ankle rehabilitation, devices used for gait rehabilitation for neurological disorders are also considered in this discussion for completeness. Ankle rehabilitation devices can be classified into two categories in terms of the mobility of the device during operation. These are wearable robots and robotic platforms with stationary bases. Wearable ankle rehabilitation robots typically take the form of a robotic orthosis or exoskeleton (Figure 2.1) and are used to correct the user's gait pattern. Robotic platforms (Figure 2.2) on the other hand, manipulate the user's foot using their end effectors and are generally developed to facilitate the treatment of ankle sprains.

Figures removed due to third party copyright issues.
Images can be accessed through:
Figure 2.1a: Fig. 8 of [12]
Figure 2.1b: Fig. 2 of [56]
Figure 2.1c: Fig. 1 of [57]

Figure 2.1: Examples of wearable ankle rehabilitation robots. (a) The anklebot developed in [12]; (b) The robotic gait trainer developed in [56]; (c) The pneumatically powered ankle foot orthosis developed in [57]. (Images reproduced from [12], [56] and [57]).

```
Figures removed due to third party copyright issues.
Images can be accessed through:
Figure 2.2a: Fig. 1 of [10]
Figure 2.2b: Fig. 4a of [41]
Figure 2.2c: Original figure not available at [58] at
time of writing. Similar figure can be obtained from
Fig. 2a of [9]
```

Figure 2.2: Examples of platform based ankle rehabilitation robots. (a) The ankle exerciser developed in [10]; (b) The reconfigurable ankle rehabilitation robot developed in [41]; (c) The Rutgers Ankle rehabilitation interface developed in [9]. (Images reproduced from [10], [41], and [58]).

2.1.1 Wearable Ankle Rehabilitation Robots

One of the main problems encountered in the gait of patients suffering from neurological disorders is the inability to control the ankle and foot position during ambulation, thus resulting in abnormal gait pattern. This is normally observed in the form of "foot drop", a term used to describe the situation when the patient fails to rotate the foot upwards during walking, thus causing the foot to slap onto the ground and the toes to drag on the floor. This phenomenon is due to the loss of control for ankle dorsiflexor muscles. Ankle foot orthosis (AFO) is a commonly used remedy for foot drop. These orthosis in its simplest form are braces moulded to fit the patients' foot which can prevent involuntary foot drop through the use of elastic elements.

To enable their use in gait rehabilitation, robotic devices developed for preventing foot drop must be wearable. It must also be controlled to limit the downward rotation of the foot during certain phase of gait. It is therefore not surprising that many robots used in this capacity take the form of actuated orthoses or exoskeletons. While some of these devices provide actuated motion in only one degree of freedom (dof) to influence foot plantarflexion and dorsiflexion [22, 57, 59-61], others also include the possibility of controlled or passive inversion and eversion movements [12, 30, 62, 63]. The internal-external rotation of the foot however, is rarely controlled as it is assumed to be a negligible component of gait.

The actuators used in wearable ankle robots developed in the literature are typically of lower inertia to allow higher mobility due to the wearable nature of the device. The actuators are also chosen to be inherently backdriveable to ensure the safety of the user. An example of such actuators is the series elastic actuators used in [22, 61]. This family of actuators is constructed by placing an electric motor in series with a compliant elastic element. The compliant element therefore isolates the motor inertia from the actuator end point inertia and the force applied by the actuator can be regulated by controlling the deformation of the compliant element. These actuators are normally used with stiffness control and are in general utilised to influence the mechanical behaviour of the ankle joint rather than to provide large assistive moments.

Pneumatic muscle is another type of actuator commonly used in wearable ankle robots due to its high power to weight ratio and inherent compliance. It is typically used in systems with higher moment capacity, thus allowing these devices to provide a greater level of assistance during the user’s gait. The disadvantage however is the requirement of a source of compressed air and the nonlinear dynamics of the actuators. Both position control [56] and proportional myoelectric control [57, 59, 60] strategies had been applied on systems using pneumatic muscles. Position control is generally used to drive the length of the muscles to values which correspond to the desired foot configuration/orientation while proportional myoelectric control activates the pneumatic muscles according to the myoelectric signals measured from the user/patient’s leg muscles.

In addition to the above actuators, conventional electric drives had also been utilised in some designs [12, 30, 63, 64]. These actuators are typically used with a low transmission ratio to reduce the effective inertia of the device and to reduce the amplification of friction within the actuators. Control of such systems is therefore also rather straight forward through the use of simple impedance control schemes which do not require any force feedback. As displacement and torque of such electric drives can be readily measured and controlled, some of the rehabilitation robots developed with conventional electrical actuators also double as evaluation tools to gather information on the human ankle. Examples of this can be found in [12, 30], where the proposed ankle robot had been used to estimate the stiffness of the human ankle. Similarly, the robot developed in [64] was also used to estimate the ankle kinematic and impedance parameters.

Some notable features can also be identified in the wearable ankle robots considered in this review. The first is the incorporation of some element of intelligence into these devices. For example, adaptability was introduced in [22] to improve the performance of the AFO by adjusting the AFO stiffness to reduce the occurrences of drop foot gait, while the previous gait velocity is used in [61] to generate references for subsequent gait cycles. Additionally, knowledge of the general gait pattern had also been incorporated in higher level control schemes which coordinate the switching of AFO behaviour according to the current phase of gait.

Another important feature worth noting can be found in the mechanical designs of [12, 30, 56, 63] (Figure 2.1a and Figure 2.1b), where the AFOs were designed to be under-actuated when not attached to the user/patient. The advantage of this is that it will not be necessary to align the AFO’s kinematic constraints to those of the human ankle, thus allowing the device to cater for a wider range of users and reducing setup time. Furthermore, with an appropriate design, the device will be able to provide control or support in the important degrees of freedom while at the same time acting passively in the remaining directions. This therefore helps to maintain natural movement of the ankle-foot structure and ensures that no unnecessary constraints are imposed on the user's ankle-foot complex.

2.1.2 Platform Based Ankle Rehabilitation Robots

A range of platform based devices had also been developed by researchers for the purpose of sprained ankle rehabilitation [9, 31, 32, 41, 42, 65]. They are therefore designed to carry out various ankle rehabilitation exercises such as motion therapy and muscle strength training. Motion therapy can be divided into passive, active-assist and active exercises, each requiring a different level of participation from the patient, ranging from no active effort in the passive exercises to full user driven motion in active exercises. Strength training on the other hand requires the robot to apply a resistive load to impede the user's movement to improve muscle strength.

One of the key differences between these platform based devices and the wearable devices discussed previously is that the platform based devices have a fixed base and thus cannot be used during gait training. Given the rather limited range of motion at the ankle-foot complex, parallel mechanisms are typically used for multiple dof systems to reduce the size of the robot. With the exception of the Stewart platform based device proposed in [9] which is capable of six dof motion, most researchers have opted for designs which offer two or three dof in rotational motion, where robot movements in the yaw direction (internal-external rotation) are typically constrained on two dof devices. Most of the lower dof devices also include a central strut in the robot's kinematic structure to provide the kinematic constraint required to restrict the movement of the end effector so that it is purely rotational [10, 31, 32, 41, 42, 66] (Figure 2.2a and Figure 2.2b).

Different actuators had been used in platform based ankle rehabilitation robots. The Stewart platform based device in [9] and the reconfigurable ankle rehabilitation platform in [31, 41] have utilised pneumatic cylinders to provide actuation, while electric motors were used in devices developed in [42, 67, 68]. A custom designed electric actuator was proposed in [10, 32] to improve actuator backdriveability, whereby a cable-driven pulley system is used to convert the rotational motion of a DC motor to linear motion of the actuator rod.

A variety of control schemes had been implemented on these platform based ankle rehabilitation robots. One approach involves the use of either pure force or pure position control for the execution of different exercises [9]. For instance, position control of the platform is typically used for passive range of motion ankle exercises where the user's foot is guided by the robot along the prescribed rehabilitation trajectory, or for isometric exercises where the orientation of the robot is kept constant while the user exerts a particular moment on the robot. Force control on the hand is used to maintain a desired level of interaction torque between the user and the robot during resistive or assistive exercises. Impedance/admittance control strategies had also been implemented, usually through a position based approach whereby the robot's reference trajectory is modified based on the desired robot impedance and the measured interaction forces/moments [10, 31, 32, 41]. Such control schemes are also generally used with a computed torque/inverse dynamics based position controller to allow accurate tracking of the desired reference trajectories. While the basic interaction control schemes had been implemented on existing platform based ankle rehabilitation robots, little emphasis had been placed on the realisation of adaptive control in such devices to allow adjustment of the robot behaviour due to variation in the user's joint characteristics and capability.

2.2 Ankle Kinematics and Computational Ankle Models

One of the objectives of this research is to develop a computational ankle model to facilitate development of the robot controller. In order to establish a suitable model, a good understanding on the ankle kinematics and existing computational ankle models are required. This section therefore provides an overview of existing studies in these areas.

2.2.1 Kinematics of the Human Ankle

Kinematics of the ankle-foot complex had been extensively studied in the literature. The simplest representation of ankle foot motion is that of a hinge joint perpendicular to the sagittal plane. This description considers the entire foot as a rigid body that can rotate about the shank in the plantarflexion and dorsiflexion directions. This is however a gross oversimplification of the ankle-foot motion as movements in other degrees of freedom are ignored. Additionally, early studies had found from examination of the talus bone surface geometry that the axis of rotation of the talus will vary with its orientation [69, 70]. The actual kinematics of the foot is therefore very complex as it is governed by the articulating surfaces between the different foot bones, as well as constraints imposed by ligaments, tendons and soft tissues. This was highlighted in various studies which investigated the movement patterns of foot bones in terms of six degree of freedom motion in either in vitro or in vivo scenarios [71-74]. The general findings of these works were that the axes of rotations of the ankle and subtalar joints do vary rather considerably between different foot orientations and different individuals/specimens. Additionally, translational motions of the joint centres were also recorded, although it was found that these movements are typically within the range of one to two centimetres.

Information of ankle kinematics is essential in applications such as gait analysis, diagnosis of normal ankle-foot function and design of implants for total ankle replacement. However, the complex motion observed at the ankle makes it difficult to describe the complete ankle kinematics concisely with a mathematical model. Models of varying levels of complexity had been established for different applications [37]. As discussed above, the simplest model used is that of a single hinge joint model (Figure 2.3a). Furthermore, ankle foot motion had been described as purely rotational using an effective spherical joint (Figure 2.3b) [75], while the biaxial model which considers the foot motion to be equivalent to rotations about two hinge/revolute joints in series was also widely adopted in literature (Figure 2.3c) [43, 44, 76-80]. Additionally, recent studies had modelled the ankle-foot kinematics using four-bar linkages and spatial parallel mechanisms [74, 81].

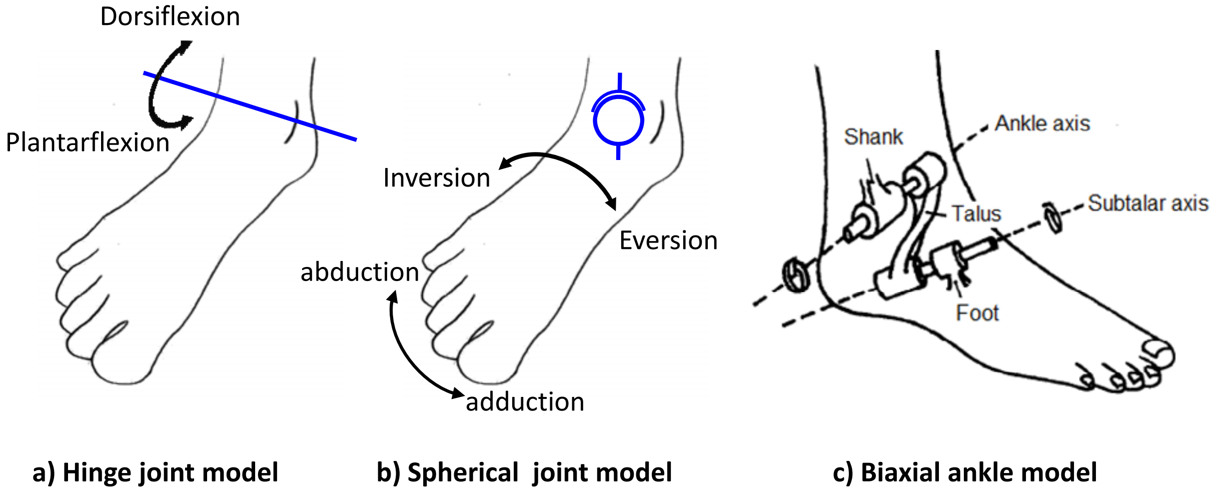

Figure 2.3: Kinematic models used to describe ankle motion. (Adapted from[76])

The problem with the single hinge joint model is that it does not consider any foot motion out of the sagittal plane. On the other hand, the shortcoming of using a spherical joint model is that the reaction moments at the ankle cannot be described since a spherical joint can only transmit forces but not moments [79]. The biaxial model can be considered a better description of the ankle-foot kinematics compared to the spherical joint model as it is based more closely on the actual ankle-foot anatomy by using the revolute joints to approximate the motion between the shank and talus and between the talus and calcaneus. However, as discussed previously, analyses of the ankle-foot motion in full six degrees of freedom have revealed that the orientation and location of these revolute joints are dependent on the foot configuration. As a result, the biaxial model is still an incomplete description of the ankle-foot kinematics. The use of parallel kinematic structures to describe foot motions had shown some encouraging results. However, while the four bar linkage model fits the observed data quite well, it only does so in two degrees of freedom. By including bone articulation into a three dimensional kinematic model, the approach involving the use of spatial parallel mechanism has the potential to give a more anatomically accurate account of the motion experienced by the foot bones. Nevertheless, this method can be computationally intensive if more realistic bone surface geometries were to be used to enhance accuracy.

Since large inter-subject variability is observed in ankle kinematics, a user specific description of ankle kinematics should be used to adapt the robot behaviour to suit the current user. Most of the studies in literature that considers subject specific ankle kinematics in full six degrees of freedom have utilised either motion tracking systems or medical imaging techniques [72, 73, 79, 82, 83]. As these methods typically require offline processing, they are not suited for use in real time systems. A simpler kinematic model with reduced degrees of freedom which is amenable to online parameter identification is therefore more appropriate for this research. Additionally, since this representation of the ankle kinematics will also be incorporated in the dynamic model of the ankle foot structure, the use of a straightforward model will reduce the computational complexity of the system, thus making its simulation more tractable. For the above reasons, the biaxial ankle model appears to be the more sensible model choice and its parameter estimation will be further discussed.

Parameter identification for a biaxial kinematic model was investigated by van den Bogert in an in vivo manner using visual markers placed on the subject's foot [79]. The biaxial model considered has 12 parameters and these are determined through minimisation of the discrepancies between marker positions obtained from the assumed model and from measurements using the Levenberg-Marquardt algorithm. The resulting ankle and subtalar joint orientations using this method were found to be similar to corresponding values obtained from in vitro anatomical studies of the ankle. Good fit of the model in terms of the marker positions was also reported, with relatively small rigid body errors. Lewis et al. had also investigated the parameter identification of the biaxial ankle model on both a biaxial mechanical linkage and on cadaveric foot specimens [82]. The optimisation algorithm used is largely similar to that described by van den Bogert except that the ankle and subtalar joint displacements were estimated through optimisation using the Gauss-Newton algorithm. It was reported that the parameter identification of the biaxial mechanical linkages shows results that are largely consistent with the actual kinematic parameters of the structure. Considerable discrepancies however were observed between the ankle and subtalar joint orientations computed from the optimisation algorithm and the average helical axes obtained from successive measurements of the foot bone orientations. This had therefore led them to conclude that the biaxial ankle model with fixed revolute joints can only give a limited representation of the actual ankle-foot kinematics, and that an alternative model, perhaps one with configuration dependent joint axes orientations, be explored. It should be noted that both the previous works discussed above on the identification of biaxial ankle kinematic model parameters were completed using offline optimisation techniques.

2.2.2 Computational Ankle Models

Studies in the biomechanical characteristics of the ankle go beyond that of understanding the kinematic behaviour of the ankle. It seeks also to identify how the human ankle will react under certain loading conditions, as well as the loading distribution among different anatomical structures of the ankle-foot complex such as foot bones, ligaments, tendons and other soft tissues.

The moment-displacement relationship of the ankle had been extensively investigated. While many of the studies concentrated on the moment-displacement relationship along the flexion direction [84-87], there are also reported works on the inversion-eversion [88] and adduction-abduction directions [89]. Regardless of the directions being considered, such relationships were generally found to be rather nonlinear, with low ankle stiffness near the neutral position of the foot but much higher stiffness as the foot is moved towards its joint limits.

Due to the complex anatomy of the ankle-foot structure, the understanding of its end point stiffness or compliance characteristics alone may not be adequate to allow true appreciation of the loading on different anatomical elements of the ankle and foot. To overcome this problem, computational ankle models can be used to simulate the desired loading conditions and obtain forces or stresses being applied on anatomical elements of interest. Other advantages of such models are that it can be used to evaluate sensitivity of the ankle-foot complex towards changes in certain biomechanical properties, and its lower demand on physical resources compared to cadaveric studies [90]. Due to it many advantages, researchers have utilised such computational models, sometimes in combination with experimental studies, for diagnosis purposes, to study injury mechanisms and to evaluate effectiveness of surgical interventions [43-45, 47, 48, 91, 92]. As with the case of ankle kinematic models, complexities of these computational ankle models vary greatly with their application. They range from two dimensional rigid body models to detailed three dimensional finite element models, and can be implemented on commercially available software packages or through purpose-built programs. A discussion on the methodologies used in the development of some of these models for the ankle-foot structure is given below.

One of the core components of a computational ankle model is a description of the ankle-foot kinematics as it determines how the foot bones will move relative to one another, thus ultimately influencing the length of ligaments and muscle-tendon units, as well as deformation of other soft tissues. While the use of a three dimensional contact constraints [45, 47, 48, 93] can lead to more realistic results, it can be computationally intensive and therefore limit the speed of simulations. In this aspect, the biaxial ankle kinematic model described previously appears to be able to provide a good balance between simplicity and the ability to provide a reasonably description of the ankle-foot motion.

Another important modelling decision is found in the treatment of bones and soft tissues. Some models treat the bones as rigid bodies and ignore effects caused by deformation of soft tissues [43-45, 78], while others applied finite element analysis on the bones and soft tissue in order to obtain the stress distribution across the articulating bone surfaces [47, 48, 91]. Clearly, use of finite element analysis will improve the accuracy of the model at the expense of increased computational complexity.

Effects of ligaments on the ankle foot biomechanics had also been considered in some models. Typically, they are treated as tension only elastic elements which lengths are dependent on the configurations of foot bones [45, 47, 48, 93]. Some models however include the influence of ligaments on passive joint stiffness as a lumped effect, and describe it through application of nonlinear resistive moment-displacement functions at the ankle and subtalar joints [43, 44]. Properties of muscles and tendons are also commonly included in computational models which require consideration of active muscular contractions [43, 44, 78], and these models typically employ a Hill based muscle model and are often used for gait analysis. Models which involve explicit modelling of the ligaments and muscle-tendon units generally require the acquisition of bone geometry and ligament/tendon attachment locations by means of medical imaging, and this can add to the complexity of the model. However, as forces and strains along the ligaments/tendons can be extracted from such models, the added complexity can be justified for applications requiring greater insights into the loading on these anatomical elements.

2.3 Interaction Control in Rehabilitation Robots

Since rehabilitation robots operate in close contact with the user, the robot-user physical interaction must be appropriately controlled to ensure that the user’s safety is not compromised. Additionally, the level of forces applied and motion of the limb or joint under rehabilitation should also be regulated in such a way so that the desired goal of rehabilitation can be achieved. For example, rehabilitation exercises involving strength training requires that resistance be applied to the user’s motion to stimulate strengthening of muscles around the affected joints. Clearly, interaction control involves the simultaneous consideration of both force and position and conventional position control or force control on their own will not be able to satisfy the requirements of rehabilitation robots. Having said that however, it should be noted that most of the current interaction controller still utilises a motion or force control scheme as an inner control loop, and a corresponding force or motion outer loop is applied to complete the interaction controller. The action of the outer loop is generally determined by a higher level controller which is used to alter the desired robot-user interaction behaviour according to factors such as the nature of the rehabilitation exercise and the capability of the user. This high level interaction controller is where the more intelligent functionalities of the robot are implemented to focus on achieving better therapeutic outcome. This section will provide a review on motion/force control strategies used in the inner control loop. Additionally, higher level control strategies used to improve rehabilitation functions are also discussed.

2.3.1 Motion/ Force Control Strategies

The main goal of interaction control is to establish a certain relationship between force and motion, and this relationship is typically expressed as either a mechanical impedance or admittance.

To realise these relationships, both force and motion of the robot have to be obtained from sensors and acted upon accordingly through application of suitable control laws. However, the most tightly controlled loop in a rehabilitation robot typically deals with only one of the two interaction variables, and these control loops are considered as low level controllers in this review. These lower level control loops of the interaction controllers are generally implemented using conventional position (or force) control to ensure that the desired motion (or force) is applied to the robot. An outer loop is then applied to alter this desired motion (or force) depending on the measured force (or motion) so that the overall behaviour of the robot resembles that of a mechanical system exhibiting the desired impedance or admittance.

Inner loop position/velocity control

In additional to the commonly used Proportional-Integral-Derivative (PID) controller, another popular strategy used in the implementation of a position controlled inner loop is the computed torque control [94]. This method is an established method for position tracking of robotic manipulators and operates by linearising the robot dynamics through application of feedback terms which aim to cancel the nonlinear terms in the robot dynamic equations. An additional proportional derivative (PD) term acting on the position error is also applied to facilitate tracking of the reference position. The computed torque control scheme therefore requires a good knowledge of the robot dynamics as well as the ability to measure actuator velocities. In applications where the robot velocity is low, the velocity dependent terms can be neglected and gravity compensation alone can be used to reduce the computational complexity of this approach [15].

Variants of the computed torque control laws had been used in interaction control of rehabilitation robots [10, 49, 95, 96]. In robots with inner position control loops, the observed interaction forces are used to compute reference accelerations according to the desired impedance relationship. These reference accelerations are then fed to the inner motion control loop to realise the prescribed interaction behaviour.

Inner loop force/torque control

Inner force or torque control loops can also be used to provide the required interaction behaviour. In this alternative approach, the motion of the robot is used to generate the force/torque reference. Similar to the case of motion control, the simplest force controller can be obtained through the use of PID type controllers. More advanced control strategies such as disturbance observers [97, 98] had also been used to reject disturbances stemming from frictional forces and unmodelled dynamics. It should be noted that computed torque control used in robot motion control also ultimately requires some form of actuator level force/torque control. This is because it operates on the assumption that the desired torque is accurately delivered by the actuators.

Naturally, actuator force control can be carried out with the feedback of actuator forces. The main challenge associated with the implementation of control laws requiring force feedback however is system stability. Since compliant force sensors are typically required to measure the actuator force, it contributes to additional position feedback [99]. As a result, large sensor stiffness will lead to a large effective position feedback gain, thus creating severely underdamped systems which could become unstable when higher order umodelled dynamics are taken into account. Force sensors that are too soft on the other hand will result in inaccurate position measurements due to additional unmonitored force sensor deformations.

Researchers have proposed that the passivity of the controlled system must be preserved if stability were to be maintained during interaction with arbitrary passive environments [100, 101]. This imposes an upper limit on the force feedback gain that can be used depending on how the actuator mass is distributed when the actuator's first resonance is considered in the actuator model. Since the main contribution of increasing the force feedback gain had been shown in [23] to be a reduction in the apparent actuator inertia, the above limitation also restricts the extent to which this inertia can be reduced. Recent work however had proposed the use of environmental information to relax the passivity criterion to permit performance improvements of the actuator [102, 103]. The authors of [102, 103] have imposed bounds on the expected human arm impedance and utilised it to numerically compute force feedback gains that satisfy the robust stability criterion based on the small gain theorem.

An alternative strategy in the regulation of actuator force involves the use of a force sensorless control scheme. Instead of measuring the actuator force/torque through force/torque sensors, this method uses a disturbance observer based approach [104] to estimate the reaction torque/force from current and motion variables. This was shown in [105] to reduce the oscillations found in the resulting force response. Such a control strategy however requires the measurement of actuator velocity and a good knowledge of model parameters such as actuator inertia, damping and friction. Torque control was also achieve in [106] through the use of a position disturbance observer in the control of a rotary series elastic actuator, which consisted of a highly geared motor coupled in series with a torsional spring. In this approach, torque control is realised by accurately controlling the deformation within the torsional spring.

While a considerable amount of research had been made in force/torque control, manipulator force control is still mainly achieved by independent control of individual actuators, where the torque or force of each actuator is regulated in its own feedback loop. It is therefore worthwhile to investigate whether force control performance can be improved when the robot actuators are treated collectively as a multi-input multi-output system.

2.3.2 Interaction Controllers for Rehabilitation Robots

Basic interaction controllers

One of the most basic form of interaction controllers can be found in simple impedance control [24], which essentially applies the torque command in an open loop manner without any force feedback. This torque command however is determined based on the desired impedance relationship and the discrepancies between the desired and actual robot motion. Due to the lack of force feedback, this interaction control approach has poorer disturbance rejection but does not suffer from the stability issues discussed previously. It is therefore suitable for use with devices with low inherent inertia and low friction. Force feedback control can also be used in impedance control schemes to allow reduction of the apparent robot inertia and improve the force tracking ability of the robot. However, the force feedback gain and hence the performance improvement are again limited due to stability constraints.

Natural admittance control [107] can be used to regulate the end point admittance of a robotic manipulator. It does so by using both force and velocity feedback in the same control loop. It was proposed that the mechanical admittance used in this approach be selected in such a way that the apparent end point mass of the controlled system is identical to that of the actual physical system to maintain passivity. Stiffness and damping characteristics however can be chosen as desired. Additionally, the velocity feedback gain is chosen to be large so that effects of disturbance forces such as friction can be reduced.

Higher level interaction control

In addition to the basic interaction control strategies described above, higher level interaction control schemes had also been investigated in rehabilitation robots, with many such schemes focusing on improving the safety and incorporating adaptability in the rehabilitation robots. These higher level controllers are also generally designed with a particular type of rehabilitation exercise in mind.

Safety and adaptability in rehabilitation robots are somewhat related. For instance, different patients will have different joint or limb kinematics. It is therefore unreasonable to have the robot strictly enforce one set of rehabilitation trajectories for all patients as it may result in application of large forces and thus lead to discomfort/injuries. In fact, impedance control in itself can be viewed as having a built-in adaptive mechanism as it permits positional deviation from a virtual reference when external forces are encountered. Some higher level interaction controllers extend on this and provide greater freedom to the user to dictate the actual path taken in rehabilitation. However, the extent of this freedom must also be bounded to ensure that the required exercises are still being carried out.

In order to achieve adaptability of this nature, some controllers for lower limb rehabilitation define a particular region or tunnel around the reference trajectory within which the interaction forces between the robot and user is minimised [11, 13]. This is typically achieved through feed forward compensation of the robot inertial and gravitational forces. It is also possible to reduce the time dependency nature of the reference trajectory by identifying the reference point using a nearest neighbour approach [11]. Various strategies for the adaptation of rehabilitation trajectory had also been considered in [21] for a position controlled gait rehabilitation robot. Some of these strategies were aimed at reducing the active patient torques through modification of the reference gait trajectory while another utilises impedance control to allow deviation from the reference trajectory. The recorded deviation due to impedance control is then incorporated into the reference trajectory of the next gait cycle.

An alternative approach taken in [49] to provide adaptability in upper limb rehabilitation is to avoid the prescription of reference trajectories in the Cartesian space, and instead define the virtual trajectory in terms of Euclidean distance to the desired end point. In other words assistance is given to the user through impedance control when the distance between the current position and the end position exceeds that desired for the particular time instant. In [2], a moving potential field is used to define the level of forces applied to move the user’s limb to the current reference position. This potential field however is selected in such a way that it will not impede the user’s movement should the current arm position be closer to the target destination compared to the current reference. This means that the controller is designed so that it would not penalise users when they are performing better than required.

One other way to improve safety is to use a smaller manipulator impedance to allow larger deviations from the reference trajectory. An obvious shortcoming associated with this approach is that certain positions in the limb or joint range of motion will not be reached as insufficient forces are available for guidance. A method to overcome this problem is to apply a reference force on top of the force command generated from impedance control. This will provide adequate forces to move the affected limb or joint while also allowing for greater flexibility in terms of the limb or joint position. In [50], this reference force is generated from a series of radial basis functions which weights are adaptively tuned to compensate the inertial and gravitational forces of the robot and user.

Another aspect of adaptability can be described as the ability of the robot to cater for the physical capability of the patients. Various researchers have proposed that robots used in neuromotor training should encourage the patient to actively participate in the rehabilitation exercises by providing assistance or intervention only when it is needed [2, 17, 20, 50]. It was also observed that given the opportunity, the user will decrease their effort and rely on the robot’s assistance to complete the rehabilitation exercises [14]. Robots used in rehabilitation must therefore also be able to adjust the task difficulty or level of assistance it provides to the user according to some performance indicator. A common approach is to reduce the level of assistance over time. This can be done by reducing the assistive forces by decreasing the impedance or feed forward force parameters as in [49, 50]. Clearly, a mechanism must also be put in place to halt the decay in assistance should the performance of the patient deteriorate, and this is typically accomplished via the addition of a term which increases the reference force or impedance parameter based on variables derived from motion error. A fuzzy inference system has also be used in [95] to vary the robot behaviour between that of a minimal interaction force controlled and impedance controlled robot depending on the position tracking errors. This means that when the user is moving as required, the robot will merely actuate to support its own gravitational and inertial forces. However, as the user fails to follow the required motion trajectories, the robot will provide assistance according to the prescribed impedance relationship.

In [2], difficulty of the rehabilitation exercises is adjusted based on performance measures which combines the active power produced by the user and the motion of the user to deduce the user's ability in movement generation as well as the accuracy of the produced motion. It was proposed that the time period of each repetition of the rehabilitation exercise and the stiffness of the robot be regulated based on these performance measures to make the exercises more challenging when the user is performing better than expected and slightly easier when the user is not performing as required.

2.4 Discussion

It can be seen from the above review that ankle rehabilitation robots had already been proposed in the literature, with wearable devices mainly aimed at gait rehabilitation and platform based devices focusing more on treatment of ankle sprains. However, it should be noted that the Stewart platform based ankle rehabilitation robot had also been applied in the area of stroke rehabilitation [16], thus indicating that it is worthwhile to develop an ankle rehabilitation robot which can be potentially extended to cater for treatment of both ankle sprains and neurological disorders.

One major shortcoming in existing platform based ankle rehabilitation devices with two to three dofs is that the rotation of the robot end effector is typically constrained about a point on the robot rather than allowing the user's lower limb to govern the end effector motion as in the designs proposed in [12, 30, 56, 63]. The consequence of this is that the motion of the user's foot will not be limited to movements between the shank and the foot during operation of the robot. Under such conditions, measurements of the robot end effector orientation may no longer be the true ankle joint displacements, thus limiting the repeatability of the actual ankle foot motion while also compromising the ability of the robot to act as a reliable evaluation/measurement tool. This issue is therefore addressed during the mechanical design of the ankle rehabilitation device developed in this research.

Additionally, even though existing platform based ankle rehabilitation devices are already capable of basic interaction control and can perform various rehabilitation exercises, not much emphasis was placed on the adaptability of these devices. As the kinematics and impedance characteristics of the ankle can vary considerably between individuals, the controller for rehabilitation robots should ideally be able to detect these variations and adjust for it accordingly. An example of this is the reduction of robot impedance in regions of large stiffness to prevent exertion of excessive forces. It is therefore the intention of this research to incorporate adaptability into an ankle rehabilitation robot through online parameter estimation. A suitable interaction control scheme can then be developed to capitalise on the additional information available to improve the safety of the device. Furthermore, the assistance adaptation schemes available in robots designed for motor training were also considered in this research so that the developed device will not only be able to accommodate variations in the users' joint characteristics, but also adapt its behaviour to ensure that the level of assistance provided is based on the user's capability to carry out the required exercises. While the aim of this research is to create a system which is primarily targeted at rehabilitation of sprained ankles, development of an assistance adaptation scheme will also facilitate future extension of the developed system to cover neuromotor rehabilitation.

It is worth noting that many of the assistance adaptation schemes varies the assistive effort either directly or indirectly based on observation on the position tracking errors [14, 49, 50], and the adaptation rules are typically formulated in ways which does not place much consideration on the possibility of constrained motion in the robot's task space. This is perhaps due to the predominant application of these algorithms in upper limb rehabilitation where the subject's arm can normally move within the workspace of interest in a constraint-free manner. This is however unlikely to be the case for ankle-foot movements due to the existence of coupled rotations which imposes constraints in the three dimensional rotational space. Assistance adaptation rules which are more suitable for constrained motion are therefore investigated in this work.

It can be seen from the above discussion on ankle models that numerous computational ankle models had been developed to study foot pathology and biomechanics. However, to the best of the author's knowledge, none of these models were applied in the controller development of ankle rehabilitation devices. In addition to its use in controller simulation and in providing information on the configuration dependent ankle characteristics such as ankle stiffness which can be used for parameter adaptation and stability analysis of the interaction controller, a suitable computational ankle model can also be used to approximate the forces along different ligaments or muscle-tendon units as well as reaction forces and moments encountered at the ankle and subtalar joints. It can therefore also serve as a tool to evaluate the performance of a controller or the effectiveness of a particular rehabilitation program. It can be seen that a computational ankle model which provide all the functionalities above will greatly facilitate the overall goal of this research in the development of an adaptive ankle rehabilitation robot. Such a model is therefore developed in this research to facilitate both the design and implementation of the adaptive control scheme.

Lastly, given the considerable variation in the ankle kinematics and the need to incorporate adaptability into the developed system, user specific ankle kinematic parameters should ideally be available to facilitate adjustment of the controller parameters. It can be seen that while identification of the biaxial ankle kinematic model had been explored in the literature, such identification was carried out in an offline manner. However, due to the real time requirements of this application, an online parameter identification algorithm is required. Consequently, the development of such an algorithm is also addressed in this research. Due to the importance of computational tractability, it is proposed that a biaxial ankle model be used to describe the ankle kinematics in the identification algorithm. However, as it is commonly found in literature that orientations of the ankle and subtalar joint axes change with foot configuration, the conventional biaxial ankle model with constant axes orientations is also extended in this research to allow variation of these parameters with foot displacement so that a better fit between the model and measured foot orientations can be obtained.

2.5 Chapter Summary

This Chapter presented a review of existing works which are relevant to this research. The different types of ankle rehabilitation devices developed in the literature were considered, with particular focus on their mechanical design, actuation methods and control schemes. Subsequently, studies relating to ankle kinematics and computational modelling of the ankle were also examined. The state of the art of interaction control strategies suitable for rehabilitation robots was then reviewed. Finally, the reviewed materials were analysed to highlight the issues to be addressed. These issues include the development of a platform based ankle rehabilitation robot which can offer more controlled foot-shank motion, the development of an adaptive interaction control scheme for the resulting ankle rehabilitation robot, the construction of a computational ankle model to facilitate controller design and investigation into the online identification of ankle kinematics.

Chapter 3 Development of the Ankle Rehabilitation Robot

Various robotic devices had been developed for ankle rehabilitation but most of the platform based ankle rehabilitation systems have a common problem whereby the measured end effector orientation may not be representative of the actual foot-shank displacement due to pivoting of the end effector about a point which does not coincide with the ankle centre of rotation. This research therefore seeks to propose a new robot which addresses this particular issue. One of the major design requirements for an ankle rehabilitation robot is that it must possess an adequate workspace which is free from singularities. Additionally, it must also satisfy certain force/torque requirements imposed by the types of rehabilitation exercises being implemented. Further to these basic specifications, the robot must also be safe to operate and adequately instrumented to allow the implementation of an appropriate control scheme. This chapter begins with an overview of the design requirements of an ankle rehabilitation robot. A suitable kinematic structure of the robot is then proposed. Workspace, singularity and force analyses of mechanisms having this structure are then presented. Subsequently, additional design considerations of the ankle rehabilitation robots are also discussed. This is followed by a description of the robot hardware and user interface.

3.1 **Design Requirements**

In order to carry out different ankle rehabilitation exercises, the robot to be developed must have a workspace that is similar to or in excess of the typical range of motion encountered at the human ankle. The ankle-foot motion is primarily rotational, and is often described by rotations on three mutually perpendicular anatomical planes. These rotations are illustrated in Figure 3.1. The plane which distinguishes the left and right sides of the body is termed the sagittal plane. The frontal plane as its name suggests, divides the body into front and back halves. Finally, the transverse plane divides the body into top and bottom portions. Rotational motion of the foot on the sagittal plane is termed plantarflexion when the toes are pushed further away from the head and dorsiflexion in the opposing direction. Inversion is used to describe the rotation of the foot on the frontal plane where the inner or medial side of the foot is raised upwards, with eversion being its complementary motion. Lastly, internal rotation or adduction is used to describe rotational motion on the transverse plane which moves the toes towards the centre of the body while movement in the contrary direction is termed external rotation or abduction. The typical motion limits along these different directions as determined in an in vitro study by Siegler et al. [108] are shown in Table 3.1.

For the purpose of this thesis, the quantification of different rotations of the foot is made through the use of Euler angles. The XYZ Euler angle convention had been adopted whereby the orientation of the foot is described by a rotation about an x-axis, followed by a rotation about the resulting y-axis and then finally a rotation about the resulting z-axis. The angular displacements about these axes are referred to as the X, Y and Z Euler angles respectively. The arrangement of the axes (see Figure 3.1a) were selected in such a way that in the absence of rotations about other axes, the plantar/dorsiflexion movement is described by the X Euler angle; the inversion/eversion movement is described by the Y Euler angle, and the abduction/adduction movement is described using the Z Euler angle.

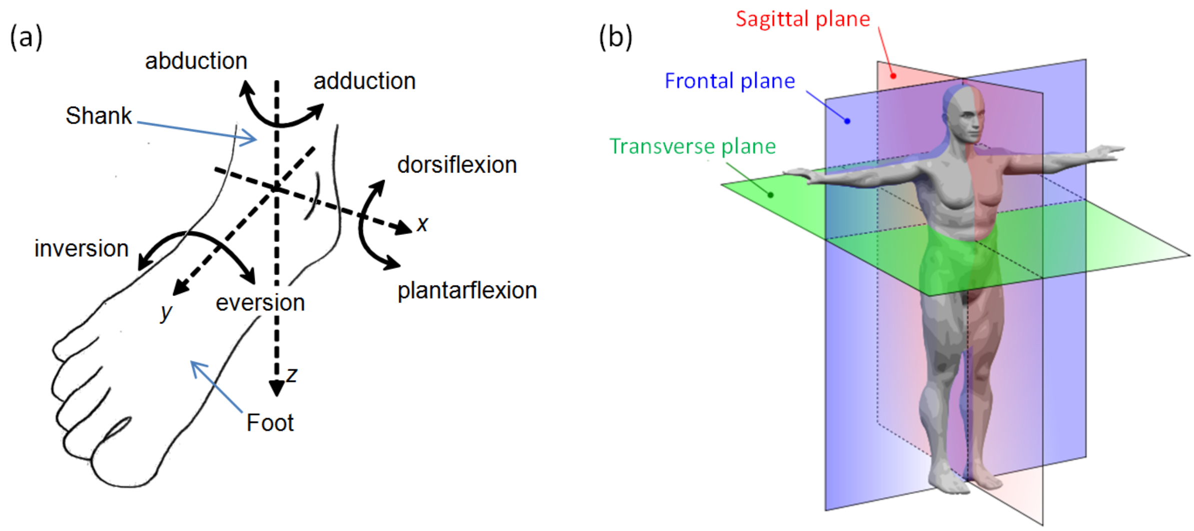

Figure 3.1: (a) Rotational motions of the human ankle. (b) anatomical planes of the human body (adapted from [109])

Table 3.1: Typical range of motion at the human ankle

Type of motion	Maximum allowable motion		
	Range	Mean	Standard deviation
Dorsiflexion	20.3° to 29.8°	24.68°	3.25°
Plantarflexion	37.6° to 45.75°	40.92°	4.32°
Inversion	14.5° to 22°	16.29°	3.88°
Eversion	10° to 17°	15.87°	4.45°
Internal rotation	22° to 36°	29.83°	7.56°
External rotation	15.4° to 25.9°	22.03°	5.99°

Data reproduced from [108]

It can be seen that the extent of motion available in different directions are quite different and that the overall ankle range of motion is rather small. It should be noted that since the robot should be able to cater for both the left and right legs, the different motion limits in the inversion-eversion and internal-external rotation directions will be inverted in the robot coordinate frame when a foot from the different side of the body is placed on the robot. The limits of the required robot rotational workspace on the frontal and transverse planes are therefore symmetric.

Another quantity that has a significant influence on the design of the ankle rehabilitation robot is the level of moment that the ankle-foot structure is expected to experience during rehabilitation. In terms of maximum moment required at the plantar/dorsi-flexion motion, results from an in vivo study in [84] have found that a maximum range of 71.7Nm is required to move the foot of the subject passively from maximum plantarflexion to maximum dorsiflexion. The same study also evaluated the torques produced by maximum voluntary contraction of the subjects and the corresponding values for dorsiflexion and plantarflexion are 54.4Nm and 126.0Nm respectively. Similar results in terms of passive ankle moments were also observed in an in vitro study by Paranteau et al which gives a maximum dorsiflexion moment as -44Nm and a maximum plantarflexion moment of about 37Nm [88]. Maximum joint torque in the inversion-eversion directions is also available from [88], where values of 33Nm in inversion and 44Nm in eversion were reported. Unfortunately, maximum torque for internal/external rotation is not available from the above studies. The robot used in this research was therefore designed by assuming that the maximum internal/external rotation moments are similar in magnitude to the inversion/eversion moments. In summary, the moment requirements of the ankle rehabilitation robot are set at 100Nm for moments about the X Euler angle axis, and 40Nm for the remaining two Euler angles axes.

In terms of functionality, ankle rehabilitation robots will have to be able to accommodate different types of rehabilitation exercises. As can be seen from the review of existing ankle rehabilitation robots in Chapter 2, these include passive, active-assist and active range of motion (ROM) exercises, as well as muscle strengthening routines. Passive ROM exercises will involve the robot guiding the user’s foot through its permissible range of motion when the user’s foot remains relaxed. Active-assist ROM exercises on the other hand require the robot to “cooperate” with the user to perform the required foot motion, providing assistance on an as-needed basis, while active ROM exercises hands full control of the foot motion to the user, with the robot providing minimal interaction forces/moments. As for realisation of muscle strength training exercises, the robot should be able provide a constant level of resistance to the foot or vary the resistance according to the extent of displacement (i.e. act as an elastic element).

3.2 Determination of a Suitable Robot Kinematic Structure

Parallel mechanisms have a kinematic structure whereby the end effector is connected to a fixed base through multiple actuated links. Due to this arrangement, parallel robots have several advantages over their serial counterparts. One of these advantages is higher positioning accuracy since errors in the actuated joints no longer accumulate as in the case of serial robots. Furthermore, since the end effector is supported by multiple actuators, the load capacity of the mechanism can also be increased. As actuators of a parallel robot is located at its base rather than on its moving links, the total load moved by the manipulator is also reduced. As a result, parallel mechanisms can be used to achieve higher bandwidth in motion (e.g. Delta robot).

Due to its many advantages and the relatively large loads experienced at the ankle and foot, parallel mechanisms are excellent candidates for ankle rehabilitation devices. In fact, the human lower leg and foot can itself be viewed as a parallel mechanism with the foot being the end effector and the muscles spanning across the ankle being the actuating links. From the above discussion, it can be seen that there is sufficient motivation for the use of a parallel robot in this research. The major shortcomings of parallel mechanisms however, come in the form of a reduced workspace and increased kinematic singularities [110, 111]. Fortunately, as the range of motion of the human ankle is rather limited, the smaller workspace of parallel manipulators may still be adequate provided that suitable kinematic parameters are selected for the mechanism. Singularities on the other hand pose a much greater concern and must be considered in the design of the manipulator. This research had therefore placed special attention on the workspace and singularity analyses during development of the ankle rehabilitation platform.

Existing ankle rehabilitation devices can be broadly classified as platform based or exoskeleton based and many have a parallel kinematic structure. The platform based devices are mainly used in the rehabilitation of sprained ankle and the typical setup requires only the foot of the user to be secured onto the robot end effector. Exoskeleton based devices on the other hand allows the user to don the robot and is generally used for gait rehabilitation. In this case, the base and end effector robot are attached to different limb segments across the ankle.

In many platform based devices, the robot end effector is often constrained about a centre of rotation which is usually not coincident with the actual ankle centre. As a result of this, the shank of the user is unlikely to remain stationary during the operation of the device and the rotational motion at the end effector in such platforms will not necessarily be identical to the relative rotations between the shank and the foot. This means that the use of such devices in measurements of ankle characteristics such as range of motion and ankle stiffness may yield erroneous or inconsistent results. Additionally, these designs also exert poorer control over the foot configuration and ankle moment since the ankle joint is not completely isolated from the remaining joints on the lower limb. For more advanced control strategies which adapt the robot behaviour with respect to the foot configuration, the above shortcoming can also lead to incorrect selection of controller gains. The above problem is avoided in some of the exoskeleton based designs, where the human lower limb is utilised as part of the robot kinematic constraints and the shank is secured in place during operation. The downside to this however is that the robot kinematics is not fully known since the robot is under-actuated prior to it being fitted onto the user. Consequently, the control of such robots can be more challenging than the fully constrained platform based manipulators. Given its ability to provide more accurate estimates of ankle-foot configuration, this research has taken the latter approach and incorporated it into the design of a platform based ankle rehabilitation robot.

The mobility or number of degrees of freedom available in a spatial mechanism is given by the Grubler's mobility formula shown in (3.1) [111], where M is the mobility of the mechanism, n is the number of rigid links present in the mechanism (including the fixed base), g is the total number of active and passive joints and f_i is the degree of freedom for the i^{th} joint.

$$M = 6(n - g - 1) + \sum_{i=1}^{i=g} f_i \tag{3.1}$$

In the proposed setup, the foot of the user is attached to the end effector and the shank is attached to the base of the mechanism. In the absence of any actuating links, the only kinematic constraint between the base and the end effector will be the human ankle joint. In this scenario, n_0 = 2 and g_0 = 1. Consequently, the mobility of this mechanism, M_0, is identical to that of the natural ankle joint. Clearly, actuated links must be included in the mechanism to allow control of the rehabilitation device, however, it should be noted that the mobility after the addition of actuated links must be identical to M_0 if the natural motion of the foot is to be preserved.

Since the actuated link must be connected to both the base and end effector for the formation of a parallel mechanism, the number of rigid body segments introduced by each actuated link must be one less than the number of joints added to the system (i.e. $\Delta n = \Delta g - 1$). According to (3.1), it can be seen that the mobility of the mechanism will decrease upon the addition of actuated links if the total degrees of freedom of the joints on each actuated link is less than six. Based on this observation, the kinematic structure of the actuated links was chosen to be U$\underline{\text{P}}$S to maintain the mechanism mobility at that of the human ankle. In the above notation, U is used to represent a universal joint, P for a prismatic joint and S for a spherical joint. The line beneath P is used to indicate that the prismatic joint is being actuated. The joints in a U$\underline{\text{P}}$S link structure therefore has six degrees of freedom in total, just enough to prevent any reduction in the mobility of the mechanism. Using this link structure, the number of actuated links also dictates the number of actuated degrees of freedom in the system.

3.3 Workspace, Singularity and Force Analyses

Due to the incorporation of the human ankle as part of the parallel mechanism, its kinematic description must be established prior to any analyses on the workspace, singularities and moment capabilities of the ankle rehabilitation robot. Although foot motion is often depicted through rotations about two oblique revolute joints in series [76, 80, 112], its actual movement pattern appears to be more complicated with coupled translations and rotations. Studies had found that the orientations of the revolute joints in the biaxial model can vary significantly between individuals. Furthermore, it had also been found that such axes orientations also vary with the configuration of the foot. Based on these findings, the generality of results obtained from using a specific biaxial ankle model in the workspace and singularity analysis would be compromised. A natural choice of a kinematic model to replace the biaxial model is a spherical joint as it can cater for all possible rotational motion. However, this approach still fails to address the effects of translational motion. As the movement of the ankle can be considered primarily rotational with limited translational movement of its instantaneous axis of rotation [73], analyses which consider the ankle as a spherical joint can still be used to give an indication of the available workspace and singular regions.

A more conservative estimate of the workspace and singular regions can be obtained by analysing the link lengths and manipulator Jacobians at different orientations for a variety of ankle joint centre locations. From such analyses, the intersection of all the workspaces computed in this manner will represent the minimum workspace while the union of all singular regions obtained will give the singular regions in the worst case scenario. However, to reduce computational complexity, all preliminary analyses will be done by assuming a single ankle centre of rotation and the conservative estimates will only be computed for the mechanism used in the final design.

3.3.1 Analysis for 3 Link Parallel Mechanism

As discussed previously, the addition of one U$\underline{\text{P}}$S link to the kinematic structure will add one actuated degree of freedom to the system. As the ankle joint is treated as a spherical joint, there are three rotational degrees of freedom in the overall parallel mechanism. As a result, three actuated links are necessary to provide full motion control capability for this assumed mechanism. The kinematic structure of the three link parallel robot considered in this design is shown in Figure 3.2, together with an illustration of the variables used to parameterise the attachment points of the actuated links. It should be noted that due to the axes convention used, the kinematic structure shown in Figure 3.2 is actually vertically inverted when compared to how the mechanism would operate in real life, where the foot of the user will be secured on the end effector while the shank is attached to the base platform. It is also worth noting that a symmetric distribution of actuated link attachment points about the y-z plane should be preferred due to the symmetry of the required workspace about the Y and Z Euler angles.

In Figure 3.2, the attachment points of the actuated links on the base are denoted by B_i while their attachments on the end effector are represented by P_i. Based on the U$\underline{\text{P}}$S link structure, point B_i is coincident with the centre of the universal joint while point P_i is coincident with the centre of the spherical joint or equivalent on the i^{th} actuated link. Point O had also been defined on the base platform where it acts as the origin of the robot global coordinate frame. The points B_i and O are constrained to lie on the same plane and their relative positions are parameterised in polar coordinates. The projections of points P_i on the end effector can similarly be represented in polar coordinates. In addition to that, the distance between P_i and the end effector plane is also set to be constant for all i, and is denoted by Δ. Finally, the point A is defined as the centre of the spherical joint used to represent the human ankle.

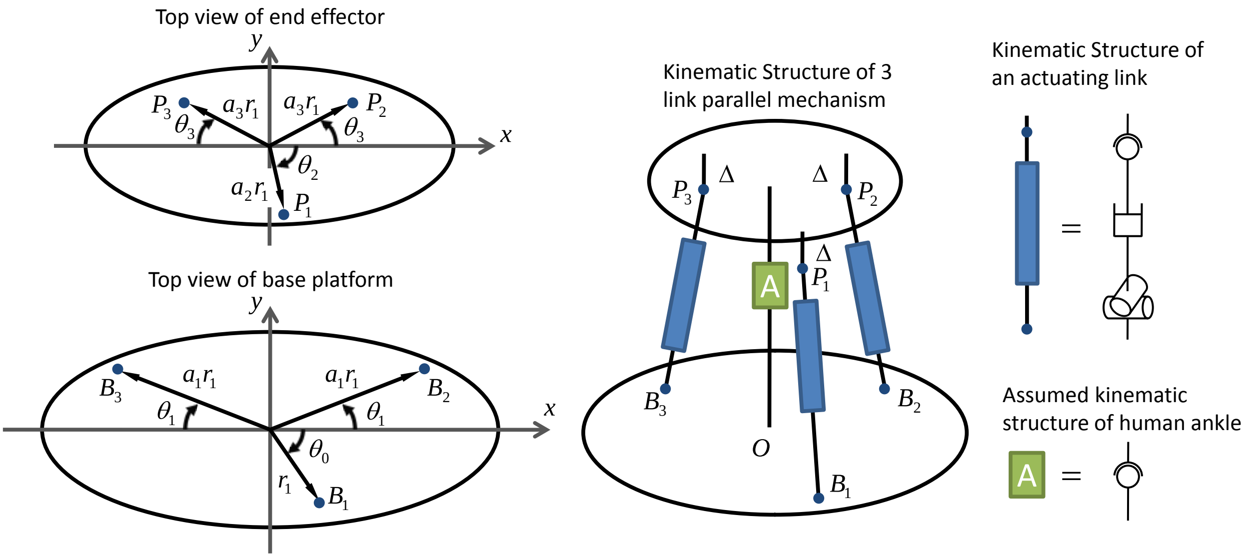

Figure 3.2: Kinematic structure of the three link parallel mechanism

Using the proposed kinematic structure, the end effector can be seen to pivot about the actual ankle centre and not an external point. Consequently, when the shank is fixed on the base platform and the foot placed on the robot end effector, the robot would have completely isolated the ankle joint. Motion and moments of the end effector taken about the ankle centre will therefore respectively provide accurate indications of the relative orientation and moments between the user's foot and shank.

Inverse kinematics

The inverse kinematics of a parallel mechanism is the mapping that relates a particular end effector orientation to its corresponding joint displacements in terms of lengths of the actuated links. Such a relationship can be easily established using the kinematic parameters described above. By using the subscript 0 to represent quantities relating to the zero orientation, a pose where the end effector orientation is identical with that of the robot global frame, the link vector ($L_i \in \mathbb{R}^3$) of the i^{th} actuated link can be written as (3.2), while its length is given by (3.3).

$$L_i = \overrightarrow{OA} + R\left(\overrightarrow{AP_{i,0}}\right) - \overrightarrow{OB} \tag{3.2}$$

$$l_i = \sqrt{{L_i}^T L_i} \tag{3.3}$$

Computation of reachable workspace

Results obtained from the inverse kinematics are highly relevant for the determination of the workspace available in the parallel mechanism. Assuming that the passive joints have been selected so that the limiting factor on the robot workspace is solely that of the length of the actuated prismatic joint, an end effector orientation can only pass as a point in the robot workspace if all the actuated link lengths fall within an allowable range. This range is typically controlled by the retracted and extended lengths of the linear actuator used in the link. For the purpose of initial analysis, it is assumed that the permissible ranges for the actuator lengths are centred about their respective values at the zero orientation. More precisely, the inequality denoting the constraint on actuated link lengths can be given as (3.4), where Δl_{max} is the maximum stroke length of the linear actuator and $l_{i,0}$ is the length of the i^{th} actuated link at the zero orientation.

$$l_{i,0} - 0.5\Delta l_{max} \leq l_i \leq l_{i,0} + 0.5\Delta l_{max} \tag{3.4}$$

Computation of singularity measure

The manipulator Jacobian is a matrix which describes the relationship between joint space and task space velocities of a robot. For parallel mechanisms where a unique set of joint space coordinates can be assigned to a given task space configuration, the manipulator Jacobian $J \in \mathbb{R}^{n_l \times 3}$ is the gradient matrix which relates the task space velocity $\dot{\Theta}$ to the joint space velocity $\dot{l} \in \mathbb{R}^{n_l}$ as shown in (3.5). Note that n_l is the total number of actuated links. It is also worth noting that the transpose of the manipulator Jacobian is used to relate the joint space forces $F \in \mathbb{R}^{n_l}$ to task space forces $\tau \in \mathbb{R}^3$, as shown in (3.6). Analysis of the manipulator Jacobian can therefore provide information on the kinematics and kinetics of a robot at a particular configuration. The manipulator Jacobian for the proposed parallel kinematic structure can be obtained from differentiation of the inverse kinematics relationship shown in (3.2). Specifically, the i^{th} row of the manipulator Jacobian is given by (3.7).

$$\dot{l} = J\dot{\Theta} \tag{3.5}$$

$$\tau = J^T F \tag{3.6}$$

$$J_i = \frac{1}{l_i} {L_i}^T \left[\frac{\partial R}{\partial \theta_x} P_{i,0} \quad \frac{\partial R}{\partial \theta_y} P_{i,0} \quad \frac{\partial R}{\partial \theta_z} P_{i,0} \right] \tag{3.7}$$

An important role of the manipulator Jacobian is in the identification of singular configurations of the robot. Singular configurations are poses of the robot whereby the manipulator Jacobian is rank deficient. This means that singular configurations are generally related to an infinite condition number or zero matrix determinant (if the manipulator Jacobian is a square matrix). Rank deficiency in the manipulator Jacobian will lead to the loss of controllability of the robot, where the realisation of task space forces along certain directions will not be possible regardless of the joint space forces being applied. Alternatively, singular configurations can be viewed as poses where the manipulator gains additional degree(s) of freedom in motion since the presence of a null space in the manipulator Jacobian will allow certain task space velocities to exist even though all actuators are locked (i.e. joint space velocities is uniformly zero). Clearly, singular configurations are generally undesirable and must be eliminated from the workspace of the manipulator though selection of appropriate robot kinematic parameter. Even though singularities may only occur at certain points in the robot task space, it is also generally more difficult to control the robot at configurations around these singular points. As a result, a good design should aim to improve the manipulability of the robot by reducing the condition numbers of manipulator Jacobian across all points in the task space.

Force Analysis

As the transpose of the manipulator Jacobian also acts as a linear mapping between joint space and task space forces, it can be used to identify the actuator forces required to produce a particular task space moment. This normally involves the inversion of the manipulator Jacobian (or application of the psueudo-inverse if the manipulator is redundantly actuated). Clearly, the force requirements would change with the task space coordinates of the manipulator. The maximum desired moments were therefore applied at various end effector configurations and the largest of the resultant joint space forces was treated as the actuator force specification. The configurations considered include the neutral position, a supinated (plantarflexed, inverted and adducted) foot configuration, a pronated (dorsiflexed, everted and abducted) foot configuration, and at configurations where a rotation close to the joint motion limit is made about one of the coordinate axes while the displacements along the remaining two are kept at zero (i.e. pure dorsiflexion/plantarflexion, pure inversion/eversion and pure abduction/adduction).

In the force analysis, the vectors along which moments are applied were different for different foot configurations considered. The main motivation for this arrangement is to reduce the number of computations required in the analysis by only applying forces in directions where they are expected at a particular configuration. Since the foot will have a tendency to move towards the neutral position, passive motion of the foot will be initiated by the robot applying a force in the direction where it is moving. The opposite however is true for active exercises where the robot is providing a resistive force. In either case, the direction of moment application should be similar to the direction of the position vector taken from the zero orientation to the foot configuration being considered (e.g. force analysis for a plantarflexed foot orientation should involve application of moments in the plantarflexion-dorsiflexion direction). The exception for this is of course the neutral position, where a much larger range of moments (in terms of direction) can be applied to move or resist the motion of the foot. The above rationale had been taken into account to select the combination of maximum moments to be applied at different foot configurations during the force analysis (refer to Appendix A for details).

Analysis results and discussion

Apart from the workspace, singularity and force requirements, the resultant design must also meet certain spatial constraints to ensure that it can be used in practice. Since the robot developed in this research is used for ankle rehabilitation, the kinematic parameters of the robot must be selected in such a way that it can accommodate the placement of the foot on the end effector. With this in mind, several sets of kinematic parameters for the proposed three link parallel mechanism had been selected and analysed. The details of these kinematic parameters are provided in Table 3.2. The actuator force requirement, robot workspace and condition numbers of the manipulator Jacobians were computed for each of these designs and the results of these are summarised in Table 3.3.

Table 3.2: Kinematic parameters of designs considered in the three link manipulator analysis.

Design ID	r_1	a_1	a_2	a_3	θ_0	θ_1	θ_2	θ_3	Δ	$\overrightarrow{OA}$
A	0.2 m	0.9	0.4	0.45	-90°	45°	-90°	30°	0.05 m	$\begin{bmatrix}0\\0\\0.36\end{bmatrix}$ m
B	0.11m		0.7	0.75	-90°			30°		
C	0.2m		0.3	0.35	-90°			30°		
D	0.2m		0.5	0.55	-90°			30°		
E	0.2m		0.4	0.45	-60°			30°		
F	0.2m		0.4	0.45	-90°			45°		

Table 3.3: Design analysis results for different three link designs.

Design	F_{max} (N)	Workspace	Manipulability
A	3119.1	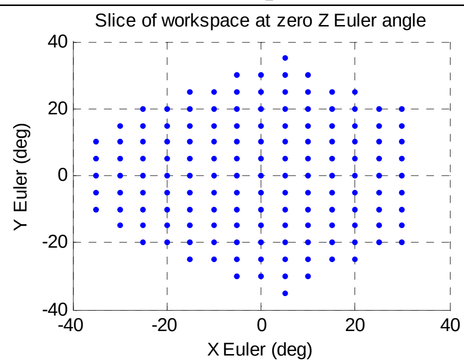	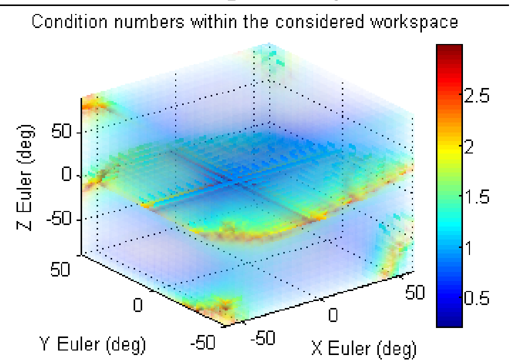

<table>
<tr><th>Design</th><th>F_{max} (N)</th><th>Workspace</th><th>Manipulability</th></tr>
<tr><td>B</td><td>6327.4</td><td>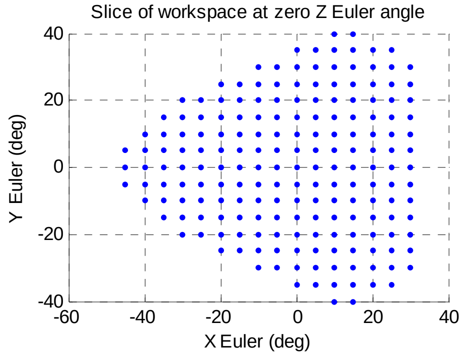</td><td>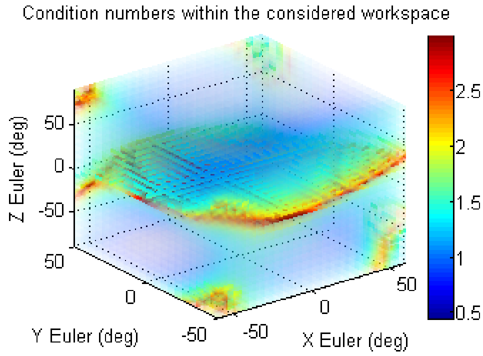</td></tr>
<tr><td>C</td><td>4651</td><td></td><td>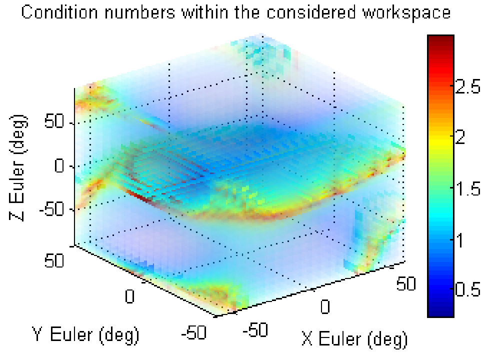</td></tr>
<tr><td>D</td><td>4609.8</td><td>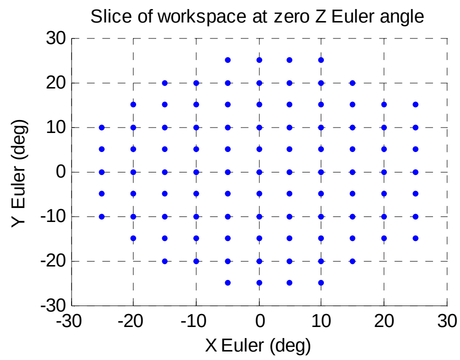</td><td>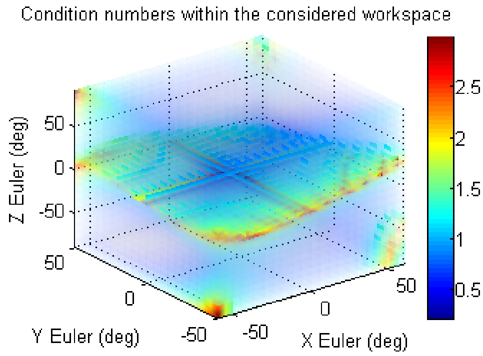</td></tr>
<tr><td>E</td><td>3438.5</td><td>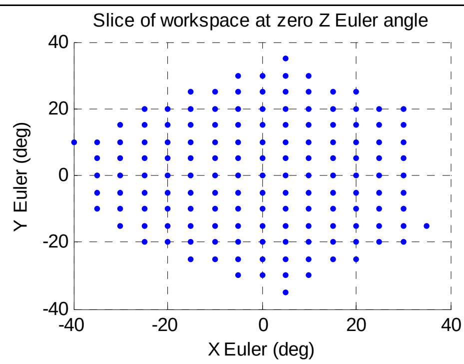</td><td>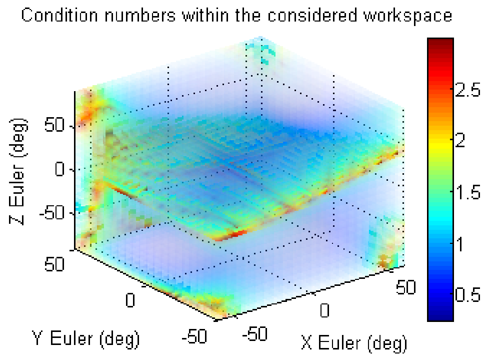</td></tr>
<tr><td>F</td><td>2781.8</td><td>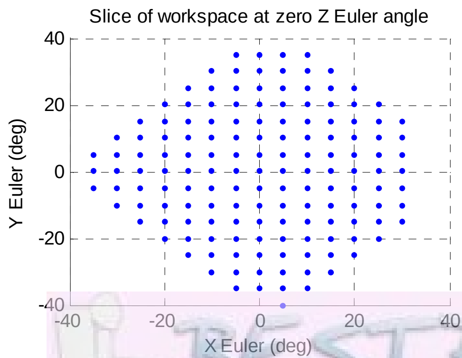</td><td>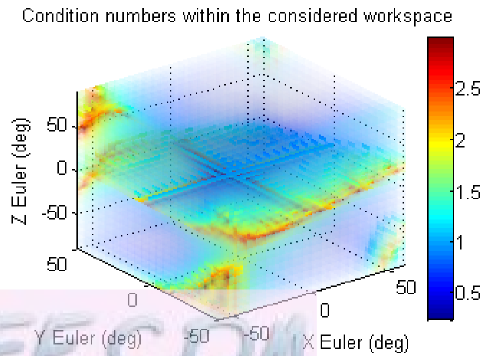</td></tr>
</table>

It can be seen from these results that the manipulator workspace is rather dependent on the separation of the attachment points on the end effector, where a decrease in separation will result in an increase in workspace volume. This is not surprising since shorter paths are traversed at points closer to the centre of rotation and the workspace is mainly limited by the available stroke length of the actuators. A look at the force requirements however suggests that smaller separation of attachment points can potentially lead to greater force requirements at certain end effector configurations. This is again expected since the moment arm of the actuator forces decreases when the attachment points are placed closer to the centre of rotation. The above observations show that both workspace and force requirements are conflicting design criteria and a compromise must be met between the two. In terms of the robot manipulability, it can be seen that a greater difference between the separation distances of attachment points on the base and end effectors can potentially lead to reduced condition numbers in the manipulator Jacobians. Another important observation is that a region of robot configurations with ill conditioned manipulator Jacobians, or in other words, low manipulability, appears to persist within the workspace for all the parameter sets considered.

For illustrative purposes, the results for one of these mechanisms (which kinematic parameters are given in Table 3.4) are shown in Figure 3.3 to Figure 3.5. Figure 3.3 shows a slice of the robot workspace when the rotation about the Z Euler axis is zero. An inspection of this plot shows that this robot configuration can produce about 32° and 36° of maximum plantarflexion and dorsiflexion respectively. Additionally, the maximum inversion-eversion motion is around 36°. A three dimensional view of workspace volume is also shown in Figure 3.4, and it can be seen that the largest range of motion of the robot is by far in the yaw direction, with maximum rotations of over 90°. The workspace regions with low manipulability are also indicated by the red point clouds in Figure 3.4, where they appear to form a region/surface which separates the workspace in two. A better visualisation of the task space configurations with low manipulability is given in the volumetric plot shown in Figure 3.5. In this plot, the condition numbers of the manipulator Jacobians at different orientations are represented in a colour spectrum and plotted on the three dimensional axes. In addition to the colour coding, the transparency of the points are also affected by the condition numbers, where configurations with lower condition number is assigned a higher transparency. Using this arrangement, regions with low manipulability becomes more easily identifiable. It should also be noted that to allow better visualisation, the colour coding was done in the base 10 logarithmic scale and the condition numbers were saturated at 1000.

Table 3.4: Kinematic parameters for the three link parallel mechanism

Parameter	r_1	a_1	a_2	a_3	θ_0	θ_1	θ_2	θ_3	Δ	$\overrightarrow{OA}$
Value	0.2 m	0.9	0.4	0.45	-90°	45°	-90°	30°	0.05 m	[0 0 0.36] m

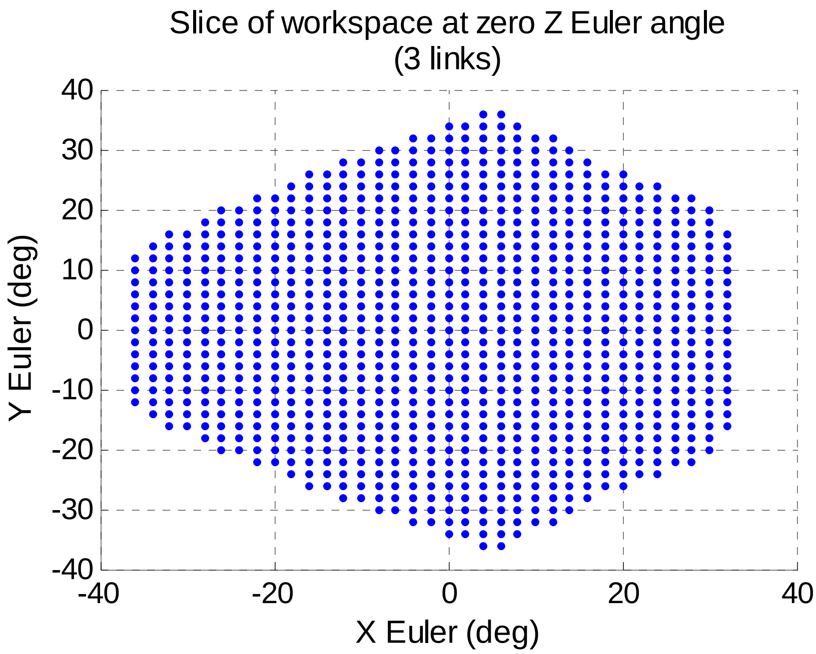

Figure 3.3: A slice of the robot workspace at zero Z Euler angle for the three link parallel mechanism.

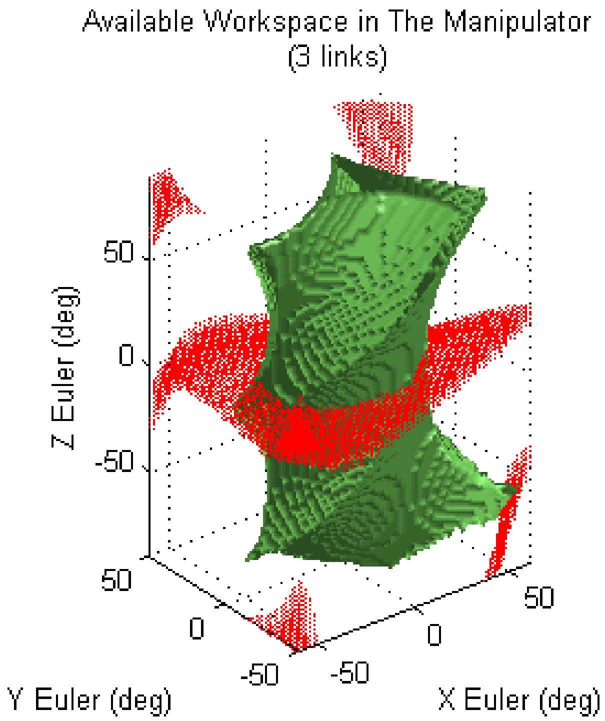

Figure 3.4: Superposition of the workspace volume on regions of the task space with low manipulability (configurations where condition number >50) for the three link parallel mechanism.

It can be confirmed from Figure 3.5 that there is indeed a surface with low manipulability in the middle of the task space considered in this analysis. This surface effectively splits the workspace of the robot into two segments and prevents controlled motion from one segment to the other. This is clearly unacceptable as a full range of foot motion is desired. A remedy for this problem is the inclusion of an additional actuated link which is suitably placed so that an additional direction for moment application is made available. Consequently, it will be less likely for the manipulator

Jacobian to become rank deficient. This can also help reduce the condition number of the manipulator Jacobians and reduce the force required from each individual actuator. It should be noted however that the resulting robot will then become redundantly actuated if the human ankle is considered to be only capable of rotational motion in three degrees of freedom.

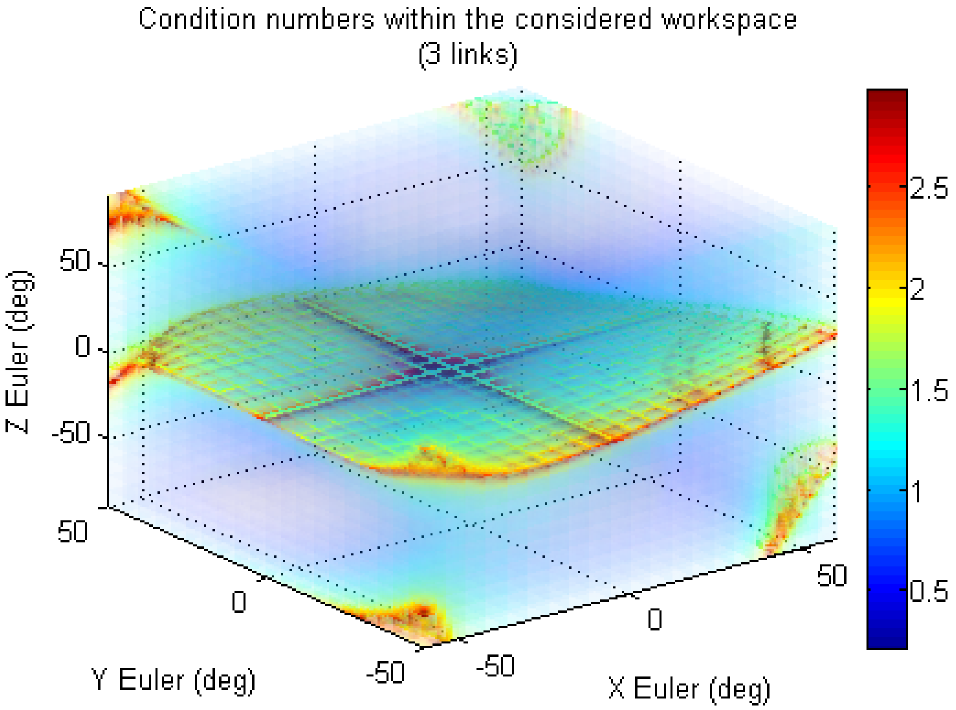

Figure 3.5: Plot indicating the distribution of manipulator Jacobian condition numbers throughout the manipulator task space for the three link parallel mechanism. The colour spectrum is assigned to the base 10 logarithms of the condition numbers.

3.3.2 Analysis for 4 Link Parallel Mechanism

The attachment points of the four link mechanism on the end effector and the base platform considered in this research shares the same parameterisation as the three link version. The kinematic structure of the mechanism can therefore be represented by Figure 3.6.

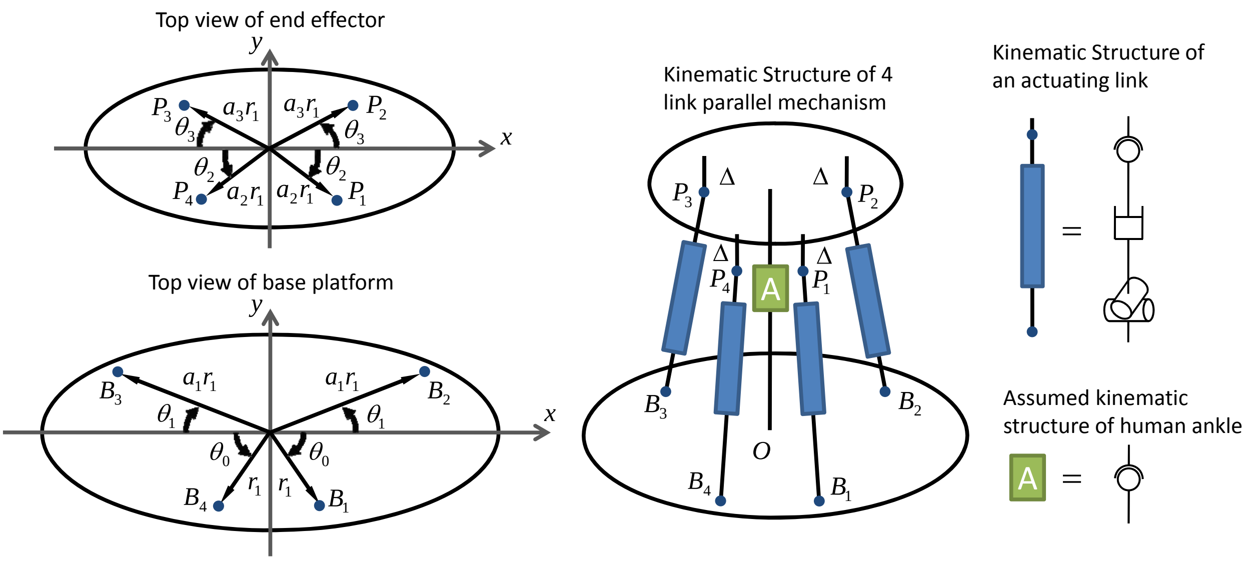

Figure 3.6: Kinematic structure of the three link parallel mechanism

Analysis results and discussion

The same workspace, singular region and actuator force analyses as above were carried out on a four link mechanism with kinematic parameters given in Table 3.5 and the results are shown in Figure 3.7 to Figure 3.9. It can be seen from these results that the manipulability of the task space have significantly improved due to the presence of an extra actuated link, where both Figure 3.8 and Figure 3.9 shows that the regions with the highest condition numbers are actually located outside the workspace of the robot. The new kinematic parameters of this parallel mechanism also appear to be capable of producing a larger robot workspace in the flexion directions, with maximum plantarflexion of about 52° and maximum dorsiflexion of about 48°. The motion limits about the Y-Euler axis however was found to decrease slightly to 34°, but still satisfies the required range of motion. Lastly, the range of Z Euler rotations in the workspace is also more than adequate to accommodate the natural ankle movements. An inspection of the actuator force requirements also shows that with four actuators, the maximum actuator force exerted to achieve the prescribed task space moment is now reduced to about 1700N from over 3000N in the three link mechanism.

Table 3.5: Kinematic parameters for the four link parallel mechanism

Parameter	r_1	a_1	a_2	a_3	θ_0	θ_1	θ_2	θ_3	Δ	$\overrightarrow{OA}$
Value	0.2 m	0.9	0.4	0.45	-45°	45°	-30°	30°	0.05 m	[0 0 0.36] m

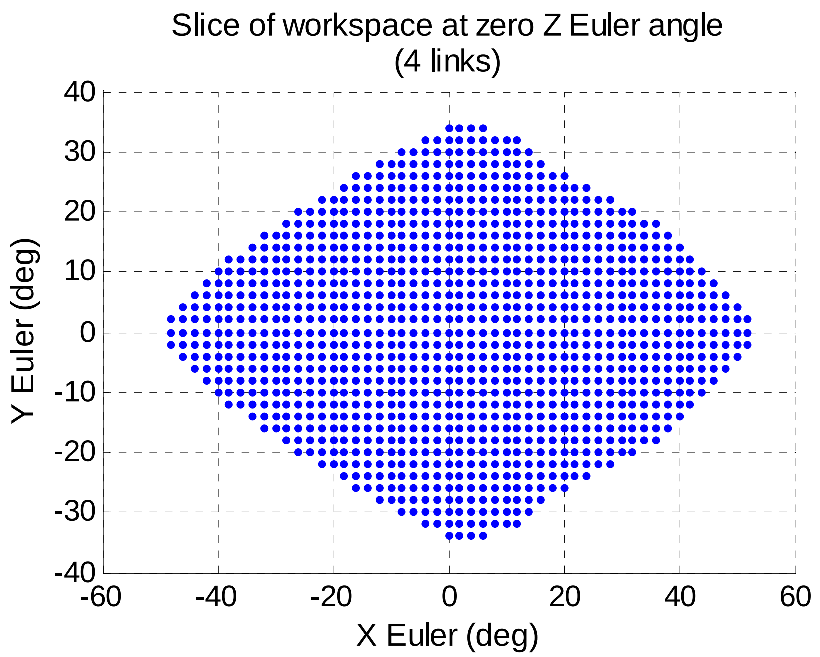

Figure 3.7: A slice of the robot workspace at zero Z Euler angle for the four link parallel mechanism.

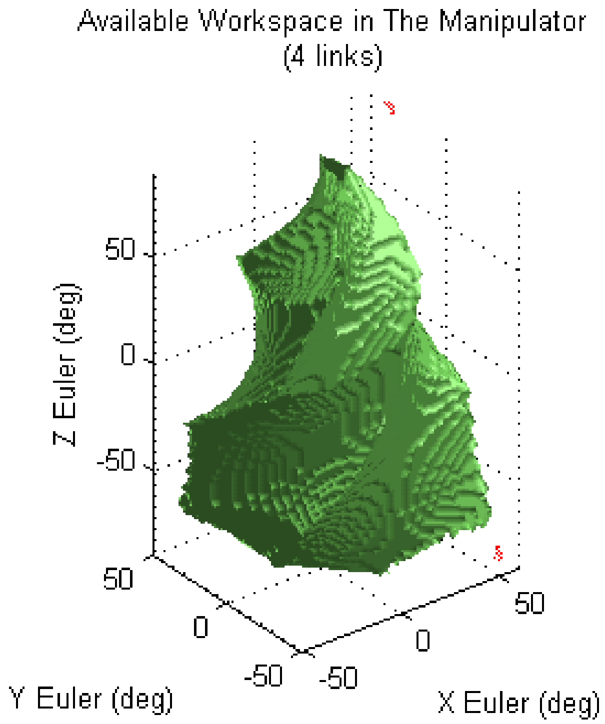

Figure 3.8: Superposition of the workspace volume on regions of the task space with low manipulability (configurations where condition number >50) for the four link parallel mechanism.

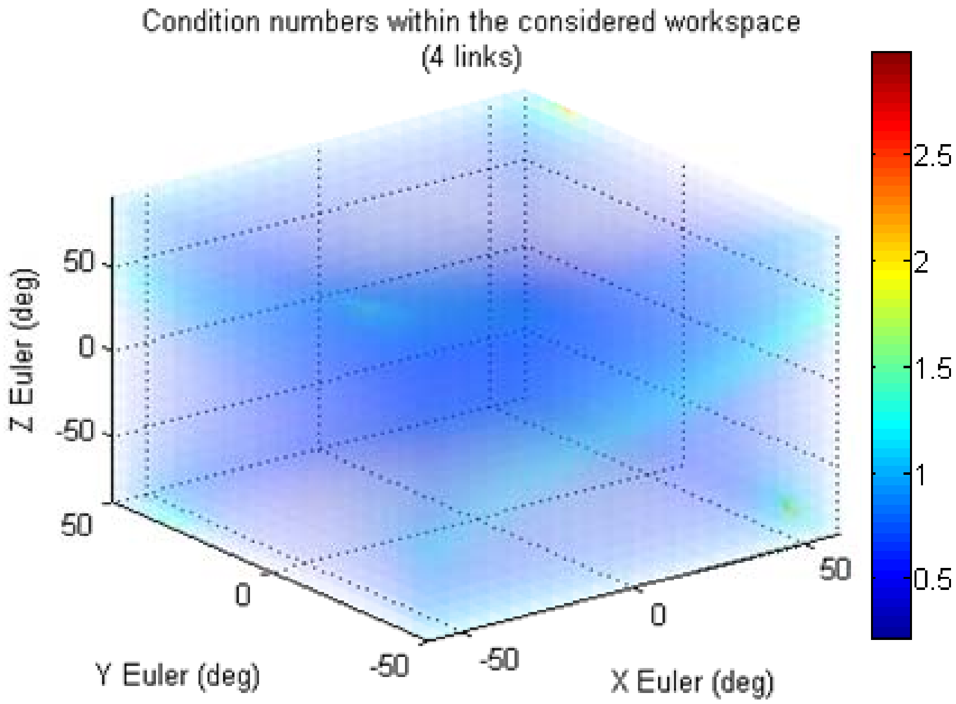

Figure 3.9: Plot indicating the distribution of manipulator Jacobian condition numbers throughout the manipulator task space for the four link parallel mechanism. The colour spectrum is assigned to the base 10 logarithms of the condition numbers.

3.3.3 Evaluation of 4 Link Design with Additional Constraints

Since the four link mechanism appears to outperform the three link design in almost all aspects, it had been adopted in the final design of the ankle rehabilitation robot. However, it should be noted that the analyses carried out above was only completed for a single ankle centre of rotation. As discussed previously, the complex kinematics of the ankle means that this centre is likely to vary during operation of the robot. Furthermore, the previous analyses also assumed that there were no violations of passive joint limits. The actual workspace of the robot may therefore be smaller than the results shown above. Further investigation is therefore required to evaluate the true capability of the final design.

Consideration of passive joint limits

The universal joint displacements were computed for different end effector configurations to study the influence of passive joint limits on the robot workspace, and it was found that these angular displacements largely remained between ±32° throughout the entire robot workspace. This is within the permissible motion range of the universal joints used in this work (±35°) and therefore will not affect the previously determined robot workspace. The configuration of the spherical joints were also analysed and it was found that when viewed in the local end effector coordinates, the unit vector representing the line of action of the actuated link can deviate as much as 87° from its initial orientation. This is beyond the range of motion of typical spherical joints and therefore poses a challenge in the realisation of the actual mechanism. To overcome this problem, the spherical joint in the proposed mechanism is replaced with a set of three mutually intersecting revolute joints. Such a joint complex is shown in Figure 3.10. It can be seen that the proposed joint complex will function as a spherical joint as long as axes *a* and *c* do not become parallel. This non-parallel condition therefore forms part of the passive joint constraint which must be considered in obtaining the final robot workspace. Additionally, another constraint in the passive joint displacement can be obtained by imposing a non-interference condition between block A and block C. By taking into account both constraints and the geometry of the components, the permissible angle between axis *a* and axis *c* was estimated to be from 50° to 180°, as illustrated in Figure 3.10.

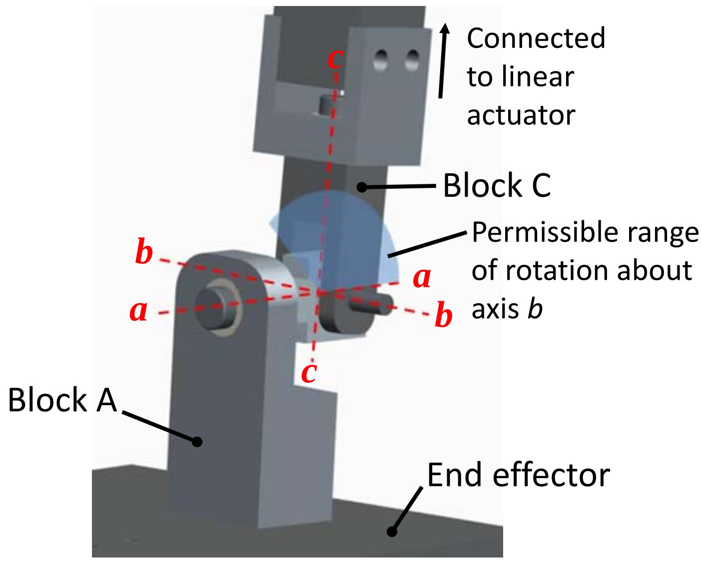

Figure 3.10: Illustration of the joint limit on the effective spherical joint.

Variation of assumed ankle centre

In addition to the application of passive joint limits, the workspace and condition numbers for the final design were also computed for different locations of the spherical joint (i.e. $\overrightarrow{OA}$) to simulate the translation of the actual ankle centre of rotation. In the final design analysis, $\overrightarrow{OA}$ was varied within a 30mm cube centred about its nominal location. Positions of the end effector attachment points, $P_{i,0}$ were however, held constant with respect to the global robot frame. The choice of the 30mm cube was based on sources in the literature which estimates the range of ankle translation to be between 10-20mm [73]. It should be noted that the workspace produced from this analysis will also have some safety margin against small deviations in the foot placement location on the robot end effector. The upper and lower bounds of the actuator lengths used in this analysis also differed slightly with those of the original analysis where actuator length limits are dependent on the actuator lengths at the neutral foot configuration. In the final design, the construction of the actuated links was made to be uniform across all links and they therefore share the same motion limits. Analysis of the reachable workspace had shown that this design decision had the effect of improving the maximum motion allowable in the plantarflexion direction at the expense of smaller dorsiflexion movements. Since the original dorsiflexion motion limit is well in excess of the natural dorsiflexion motion limit, this design change is not expected to significantly compromise the ability of the proposed robot in meeting the workspace requirements.

Analysis results and discussion

The results obtained from the above analysis are shown in Figure 3.11 to Figure 3.13. It can be seen from these plots that the robot workspace and task space manipulability have both reduced with the introduction of passive joint limits and variations in the spherical joint centre. However, results suggests that the estimated range of motion can still be considered adequate, with a maximum plantarflexion of 44°, maximum dorsiflexion of 36° and maximum inversion-eversion of 26°. The available abduction and adduction motion again remains large at about 70°. It can also be seen from Figure 3.12 and Figure 3.13 that although the regions with condition numbers over the designated threshold had grown in size, these regions are still located outside the robot workspace. As a result, the manipulability of the robot within its workspace is not severely deteriorated with the variation of the spherical joint centre.

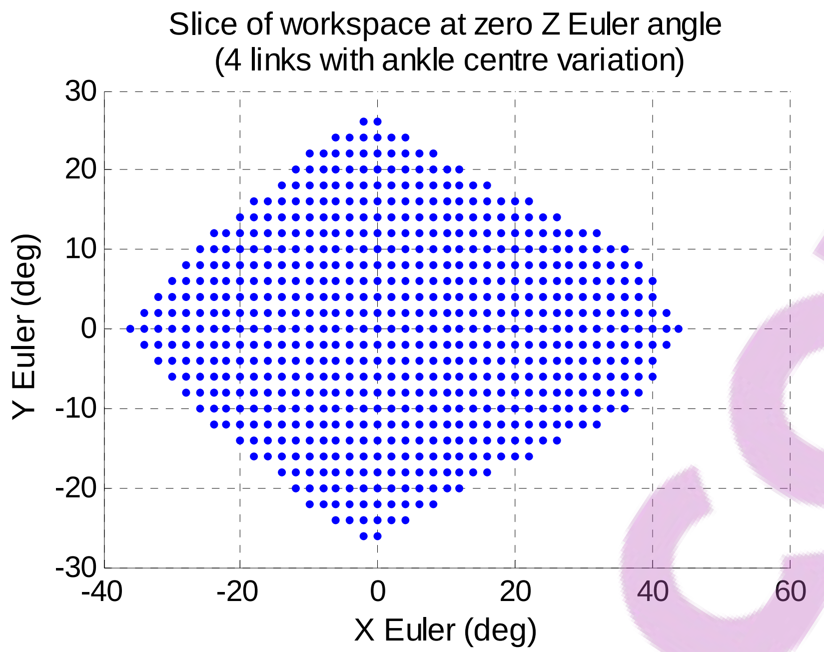

Figure 3.11: The common robot workspace at zero Z Euler angle. The information shown is that for the four link parallel mechanisms obtained by varying $\overrightarrow{OA}$ within a 30mm cube centred about its nominal value.

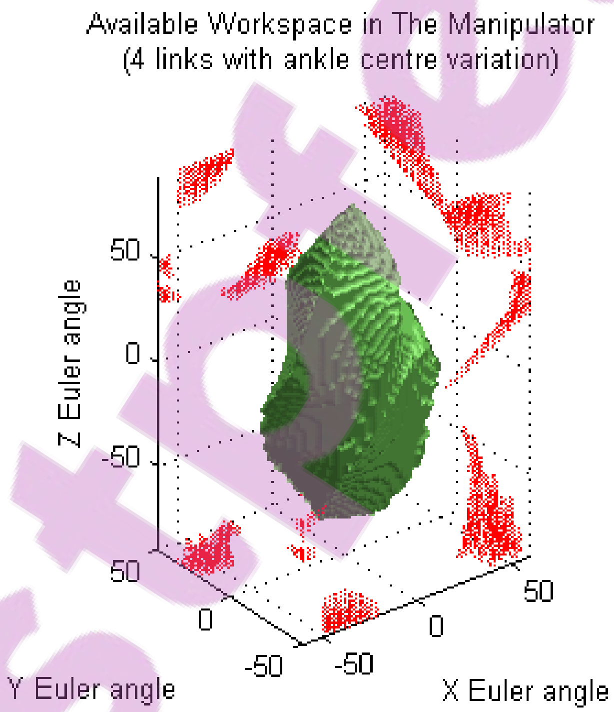

Figure 3.12: Superposition of the common workspace volume on regions of the task space with low manipulability (configurations where largest condition number >50). The information shown is that for four link parallel mechanisms obtained by varying $\overrightarrow{OA}$ within a 30mm cube centred about its nominal value. Note that the common workspace shown is the intersection of all the reachable workspaces computed by varying $\overrightarrow{OA}$, while the low manipulability region shown is the union of all the low manipulability regions obtained by varying $\overrightarrow{OA}$.

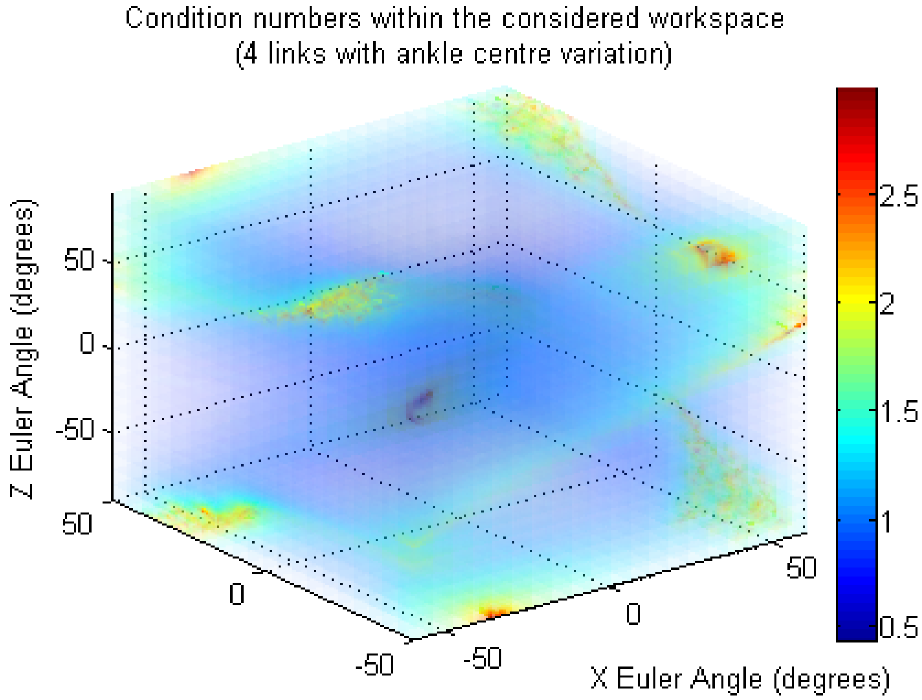

Figure 3.13: Plot indicating the distribution of the largest manipulator Jacobian condition numbers throughout the manipulator task space. The colour spectrum is assigned to the base 10 logarithms of the condition numbers and the information shown is that for four link parallel mechanisms obtained by varying $\overrightarrow{OA}$ within a 30mm cube centred about its nominal value. Note that the condition numbers used to generate the plot are the largest among the results obtained from varying $\overrightarrow{OA}$.

The moment capacity of the final design can also be evaluated by considering the maximum forces available from the actuators. This can be done by considering the maximum moments that can be applied at all end effector orientations which belong to the common workspace and taking the smallest of these values. Note that this moment analysis was carried out on each of the X, Y and Z directions by using a maximum actuator force output of 2000N. The moment capacity and the maximum achievable end effector orientations of the final design are summarised in Table 3.6. It can be seen that the movements and moments achievable by the four linked parallel mechanism are similar to what is required for the X and Y directions, and in excess of what is needed in the Z direction, thus indicating the capability of the proposed structure to perform the required rehabilitation exercises.

Table 3.6: Motion limits and moment capacity of the 4 link parallel mechanism (with consideration of ankle centre variation)

Direction	Maximum motion	Moment capacity
Plantarflexion (positive X)	44°	151Nm
Dorsiflexion (negative X)	36°	151Nm
Inversion (positive Y)	26°	38Nm
Eversion (negative Y)	26°	38Nm
External rotation/Abduction (positive Z)	72°	68Nm
Internal rotation/Adduction (negative Z)	72°	68Nm

3.4 System Description

A prototype of the ankle rehabilitation robot had been constructed using the kinematic parameters investigated above. Brushed DC motor driven linear actuators (Ultra Motion Bug Linear Actuator 5-B.125-DC92_24-4-P-RC4/4) had been used as the actuated prismatic joint in the prototype. The linear actuator was chosen based on the stroke length and force requirements of the mechanism, with an actuator stroke length of 0.1m, force capacity of over 2000N and a top speed of 0.066m/s. In terms of sensors, linear potentiometers were built into the actuators to provide measurement of the actuator lengths. Additionally, a two axis inclinometer (Signal Quest SQ-SI2X-360DA) was also attached to the end effector platform to allow the measurement of its pitch and roll angles. Lastly, four tension compression load cells (Omega Engineering LC201-300) were also installed at the interface between the linear actuator and the effective spherical joints to monitor the forces along the actuated links. The ankle rehabilitation robot developed in this research is shown in Figure 3.14, both in the form of a three dimensional model and in the form of a photograph depicting how the robot interacts with the user. In terms of controller hardware, an embedded controller (National Instruments NI-PXI 8106) had been used together with a DAQ card (National Instruments NI-PXI-6229) to carry out the signal processing and execute the real time control functions of the prototype. The embedded controller was also connected to a PC to receive user commands and display the sensor measurements through a user interface developed using the LabView programming environment. A block diagram of the overall system is given in Figure 3.15.

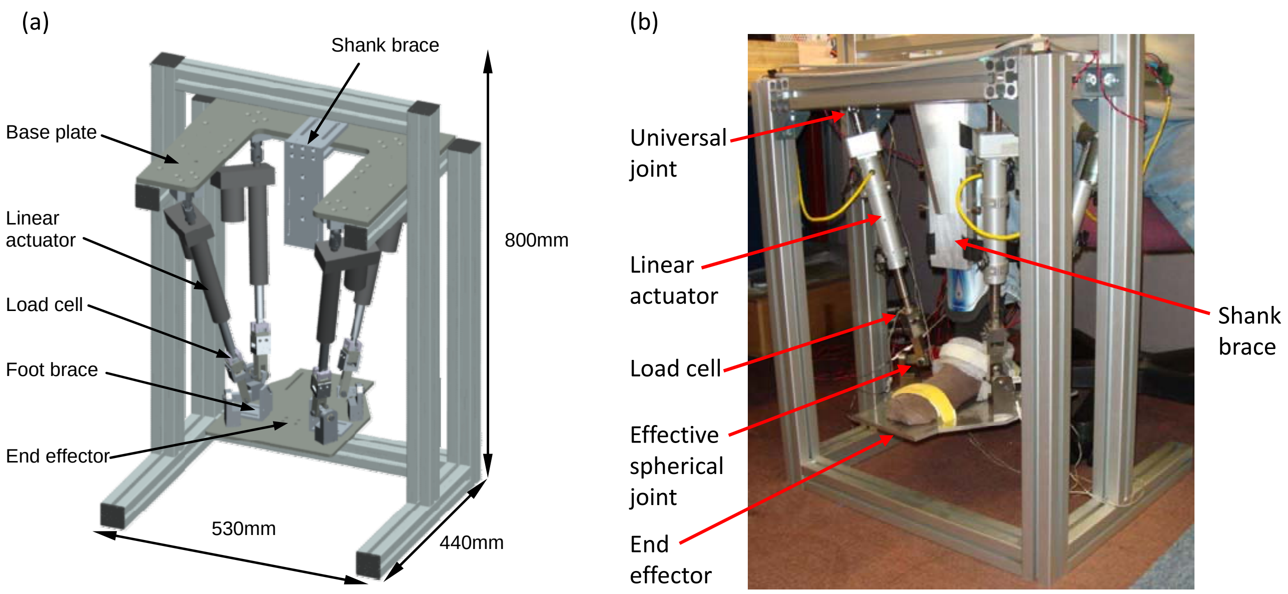

Figure 3.14: The 3D CAD model of the developed ankle rehabilitation robot (a) and a photograph showing the robot with the user's lower limb attached (b).

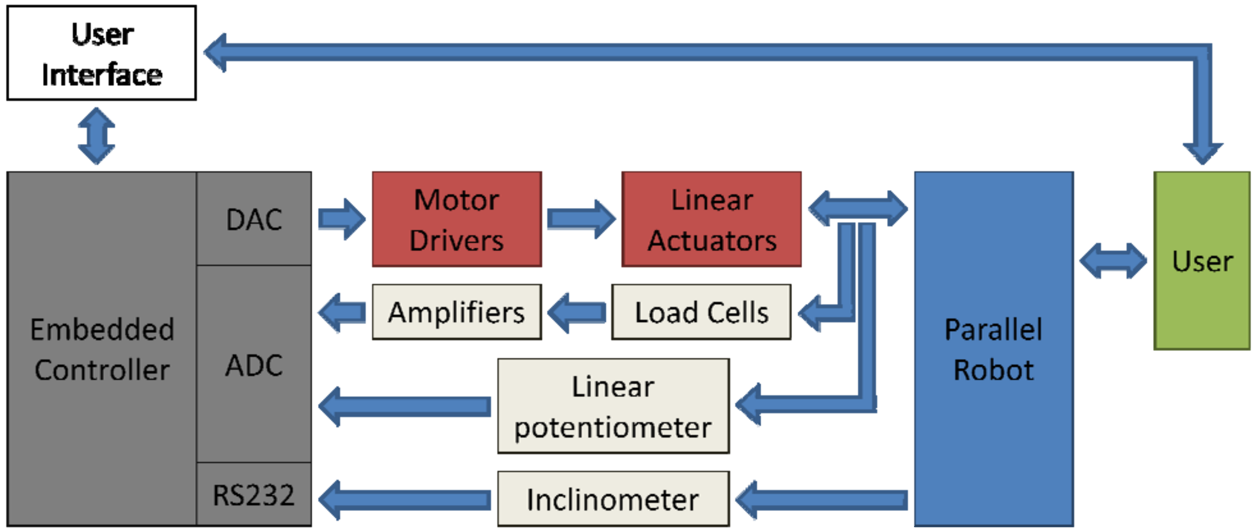

Figure 3.15: A block diagram showing various hardware and software components of the ankle rehabilitation robot developed in this research.

The graphical user interface (GUI) developed for the end user is also shown in Figure 3.16. This GUI was designed to provide visual feedback regarding the foot orientation and the level of moments applied in different directions of rotation. Orientation of the actual foot is presented as the solid red block while the desired foot orientation is shown as the semi-transparent blue block. In addition to the three dimensional visualisation of the instantaneous foot orientation provided in the top left plot, a time history of the desired and measured Euler angles relating to the foot orientation is also displayed in the top right graph of the user interface. The estimated instantaneous robot-user interaction moments on the other hand are presented in the bottom left area of the GUI. This is also accompanied by a time history of the interaction moments on the bottom right graph. A separate interface is also available for the use of the therapist/technician, where it can be used to define the rehabilitation trajectory and to modify the robot control parameters to permit different types of rehabilitation exercises.

As discussed previously, the movement of the end effector will ultimately rely on the kinematic constraints of the user's ankle. As such, the effective centre of rotation of the platform is unlikely a fixed point in space. Furthermore, it is also not known precisely. However, from the perspective of the controller, the kinematics of the platform must be defined as a rotation about a known point. As a result, an assumed spherical joint centre is used. This point is the point A used in the kinematic analyses carried out in previous sections and is considered to remain constant relative to the end effector coordinate frame. Clearly, if the actual motion of the end effector is not a perfect rotation about this assumed spherical joint centre, this point will be seen to experience translation in the global robot coordinate frame (i.e. $\overrightarrow{OA}$ is not constant). The end effector orientation estimated from kinematics based on the originally assumed $\overrightarrow{OA}$ is therefore inaccurate. In fact, the forward kinematics may even fail to converge due to contradictions between the assumed and actual robot configuration. A solution to this problem proposed in this work is to incorporate sensors on the end effector to directly measure its orientation. The two axis inclinometer used in this research was therefore installed to serve this purpose. While it only provides information on two of the three rotational degrees of freedom, these measurements can be used in conjunction with the four actuator link lengths to estimate the remaining yaw angle of the end effector, as well as an the correct location of $\overrightarrow{OA}$.

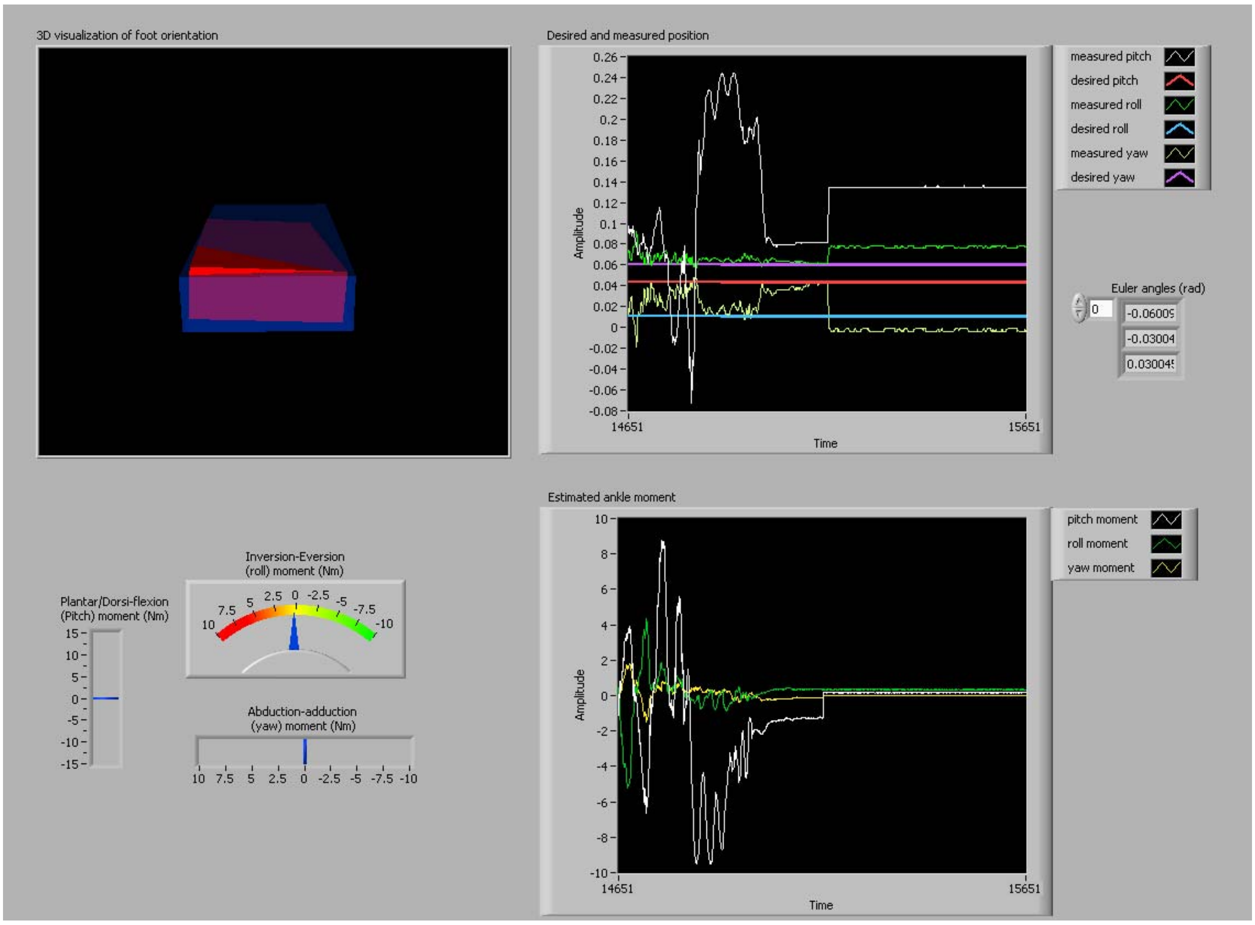

Figure 3.16: End user GUI for the developed ankle rehabilitation robot.

Although most of the existing platform based ankle rehabilitation devices utilise a six degree of freedom force torque sensor to measure the interaction torque between the foot and the robot, a different approach had been taken in this research by measuring the forces along the actuators using load cells placed along the linear actuators. The main reason for this design decision is to reduce the distance between the base of the platform and the effective centre of rotation of the user's foot, thus allowing a larger workspace for the same actuator stroke length. Additionally, it also allows monitoring of individual actuator forces to allow actuator level force feedback control. The shortcoming associated with this approach is that the actual robot-foot interaction wrench can only be estimated by considering the measured actuator forces, robot kinematic parameters and the robot inertia properties since the sensing elements are not located at the actual robot-foot interface. This is however considered to be acceptable as the inertial forces of the platform are expected to be relatively small compared with the interaction forces and moments between the robot and the user.

3.5 Chapter Summary

This chapter presented the design of the ankle rehabilitation robot used in this research. This design differs from existing platform based devices in the sense that the user’s ankle is treated as part of the robot kinematic constraint and that the shank of the user is fixed during operation of the robot. Since the resulting design isolates the ankle joint during its operation, it can be used to provide more accurate indications of the displacements and moments at the ankle joint. Consequently, it is a more suitable measurement/evaluation tool compared with some of the existing platform based ankle rehabilitation devices.

The workspace and force requirements of the robot were established by considering the ankle characteristics and this information had been taken into account in the design process. By considering the human ankle as part of the robot’s kinematic constraint, an appropriate parallel kinematic structure had been selected for this new platform based ankle rehabilitation robot to ensure that the robot can guide the user’s foot along its natural path of motion. Workspace and singularity analyses had also been carried out on three and four linked versions of the proposed parallel mechanism. It was found that the solution with four actuating links can outperform the solution with three links in terms of the elimination of singularity in the workspace of interest and a lower actuator force requirement. Additionally workspace and singularity analyses were also performed to validate the suitability of the final four link design by factoring in the mechanical constraints imposed by the passive joints and the uncertainties in the ankle kinematics. Finally, a description of the system hardware and GUI were also presented, together with a discussion on the rationale used in sensor selection.

Chapter 4 Online Identification of a Biaxial Ankle Model

Knowledge of ankle kinematics is a fundamental requirement when constructing a dynamic model of the human ankle since the kinematic constraints at the ankle-foot complex can be used to select suitable generalised coordinates to describe ankle-foot motion. Since these generalised coordinates can be used as reference variables to estimate the configuration dependent mechanical properties of the ankle-foot structure, they are invaluable in advanced control schemes which aim to adapt or vary robot impedance according to the operating environment. Implementation of such a control scheme will require a good grasp of the subject specific ankle kinematic behaviour, and this information should ideally be obtained during operation of the robot to maximise the adaptability of the robotic device. Identification of the kinematic parameters of the biaxial ankle model had been discussed previously in [79, 82]. However, the identification routines presented in these papers were carried out in an offline manner and thus not suitable for use in an adaptive control scheme. A recursive algorithm was therefore developed in this research for the online identification of ankle kinematic parameters. This algorithm is detailed in this chapter, starting with a general description of ankle motion and the selection of a suitable ankle kinematic model. This is followed by the mathematical formulation of the chosen biaxial ankle kinematic model and a discussion of the steps taken to adapt existing recursive algorithms to this application. Subsequently, extensions to the conventional biaxial ankle model is also proposed and preliminary test results obtained from applying the recursive estimation algorithms on both the conventional and extended biaxial ankle models are presented. Finally, based on observations from preliminary testing, a modified recursive least squares algorithm was proposed and tested on experimental data.

4.1 Background

In general language, the term ankle is used to refer to the joint between the lower leg and the foot. Literature in anatomy however uses the ankle joint to denote the articulation between the tibia, fibula and talus. This articulation is also termed the talocrural joint. Another joint that is present at the hind foot is the subtalar joint, which is used to represent the articulation between the talus and calcaneus. For the purpose of this research, the human ankle is taken to be consisted of both the ankle and subtalar joints. Figure 4.1 shows the different foot and lower leg bones discussed previously on the right leg/foot. One of the main functions of the ankle is to transmit torques and forces between the lower leg and the ground during ambulation. Muscles and ligaments around the ankle joint also work to maintain the balance of an individual during stance and gait. The motion at the ankle is primarily rotational and the terms used to describe these motions are also shown in Figure 4.1.

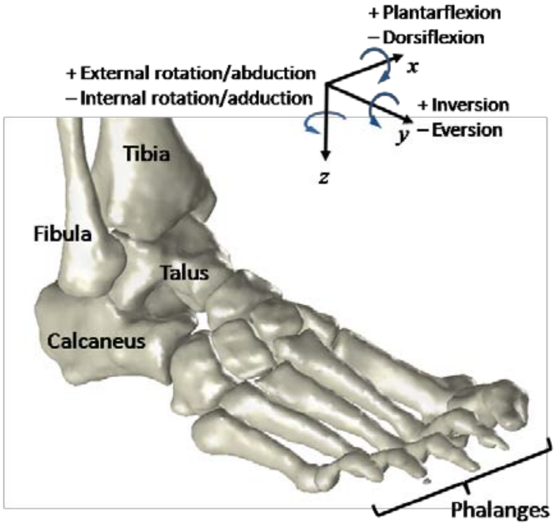

Figure 4.1: The lower leg and foot bones and the terminology used to describe various foot rotations.

Even though the general ankle motion can be treated as mainly rotational, it can be seen from [71-74, 81] that detailed studies into the matter had revealed that movements at the ankle joint are in fact more complex with coupled translation and rotations. Several mathematical models had also been proposed to capture the ankle-foot kinematic behaviour, and these models vary considerably in terms of complexities from a simple hinge joint to spatial parallel mechanisms which take into consideration bone surface articulation and influences of ligaments [74, 76, 80, 81, 112]. This research aims to develop an online identification algorithm to extract the kinematic parameters of the human ankle during operation of the proposed ankle rehabilitation robot. In order to do so, the underlying kinematic model used in the online identification algorithm must be relatively simple to ensure that the resulting identification routine computationally tractable. At the same time, the model should also have adequate complexity in order to provide a reasonable description of the coupling which exists between different rotational motions that can occur at the ankle-foot complex. Due to its relative simplicity and popular use in the literature [43, 44, 64, 79, 82], the biaxial ankle model was identified to be the ankle kinematic model which is most suitable for this research.

To the best of the author's knowledge, existing algorithms for the estimation of biaxial ankle kinematic parameters had all carried out the identification process in an offline manner using batch processing of motion capture data. The biaxial ankle model based online identification algorithm proposed in this research is presented in this chapter. An extension of the biaxial ankle model which varies the joint axes orientations according to foot configuration had also been considered in this work and is also discussed in this chapter.

4.2 Mathematical Description of the Biaxial Ankle Model

The kinematics of a biaxial ankle model with fixed relative orientations can be easily described using homogeneous transformation matrices. The resulting representation may not be the minimal parameterisation but it can more intuitively depict the location and orientation of different coordinate frames used in the model. The homogeneous transformation matrix is commonly used to describe rigid body position and orientation. It uses the orientation and translation of frame B relative to frame A to transform a point expressed in frame B coordinates to its equivalent representation in frame A. This operation is described in (4.1), where $T_{AB} \in \mathbb{R}^{4\times4}$ (4.2) is the homogeneous transformation matrix, $R_{AB} \in \mathbb{R}^{3\times3}$ is the orthonormal matrix that describes the orientation of frame B with respect to frame A and $t_{AB} \in \mathbb{R}^{3}$ is the translation from origin of frame A to frame B (expressed in frame A). $x_A \in \mathbb{R}^{3}$ is the location of the point relative to the origin of frame A, expressed in frame A coordinates. Similarly, $x_B \in \mathbb{R}^{3}$ is the location of the point relative to the origin of frame B, expressed in frame B coordinates. A diagram depicting these is shown in Figure 4.2. It is also useful to note that the inverse of a homogeneous transformation matrix can be represented by (4.3).

$$\begin{bmatrix} x_A \\ 1 \end{bmatrix} = T_{AB} \begin{bmatrix} x_B \\ 1 \end{bmatrix} \tag{4.1}$$

$$T_{AB} = \begin{bmatrix} R_{AB} & t_{AB} \\ 0_{1\times3} & 1 \end{bmatrix} \tag{4.2}$$

$$T_{AB}{}^{-1} = T_{BA} = \begin{bmatrix} R_{AB}{}^{T} & -R_{AB}{}^{T} t_{AB} \\ 0_{1\times3} & 1 \end{bmatrix} \tag{4.3}$$

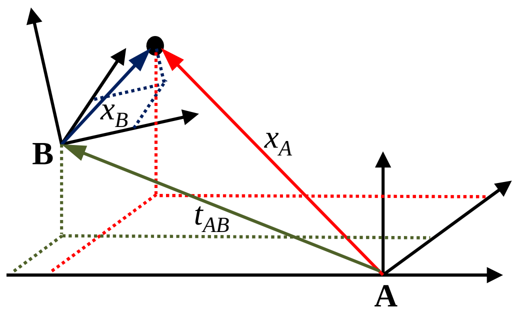

Figure 4.2: Graphical representation of variables used in (4.1**)** – (4.3).

Using the homogeneous transformation matrices, the ankle, subtalar and foot coordinate frames can be defined with respect to a fixed global frame. These frames are shown in Figure 4.3. For the purpose of this research, all foot bones from the calcaneus to the phalanges were considered as one single rigid body and its orientation and translation was represented by the foot coordinate frame. The subtalar frame was taken to be located on the talus, where its position is fixed and its orientation can change via rotation about the subtalar joint (red axis in the subtalar frame).

Similarly, the ankle frame was considered to be fixed on the tibia in terms of location and free to rotate about the ankle joint axis (red axis of the ankle frame). Since the axes of revolution are denoted as the x-axes of the coordinate frames, the orientation of the ankle frame with respect to the global coordinates can be represented by consecutively applying rotations about the y and z axes of the global frame, while the subtalar frame can be obtained by applying y and z rotations about the ankle frame. Each of these frames also uses three translations to reposition its origin at designated points in the global frame. A total of five parameters were therefore required to define each of the ankle and subtalar frames at the foot's neutral position. For convenience, the orientation of the foot coordinate frame was taken to be identical to that of the global frame and three parameters were used to determine the origin of the foot frame.

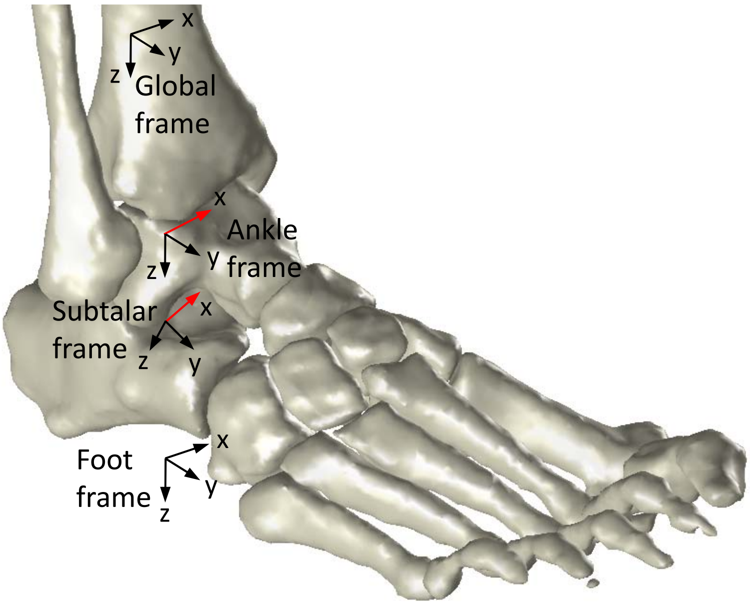

Figure 4.3: The superposition of indicative ankle, subtalar, foot and global coordinate frames on a three dimensional surface model of the foot-ankle structure. Red axes represent the axes about which rotations occur.

The homogeneous transformation matrices representing the ankle, subtalar and foot coordinate frames at the neutral foot position are given by (4.4) – (4.6), where R_z and R_y are respectively the rotational transformation matrices about the z and y axes, and subscripts a, s and f are used to represent quantities related to the ankle, subtalar and foot coordinate frames. It should also be noted that subscript i is used to indicate a variable's correspondence to the neutral foot position.

$$T_{0a,i} = \begin{bmatrix} R_{0a,i} & t_{0a} \\ 0_{1\times3} & 1 \end{bmatrix} = \begin{bmatrix} R_{z,a}R_{y,a} & t_{0a} \\ 0_{1\times3} & 1 \end{bmatrix} \tag{4.4}$$

$$T_{0s,i} = T_{0a,i}T_{as,i} = T_{0a,i}\begin{bmatrix} R_{as,i} & t_{as,i} \\ 0_{1\times3} & 1 \end{bmatrix} = T_{0a,i}\begin{bmatrix} R_{z,s}R_{y,s} & t_{as,i} \\ 0_{1\times3} & 1 \end{bmatrix} \tag{4.5}$$

$$T_{0f,i} = \begin{bmatrix} R_{0f,i} & t_{0a} \\ 0_{1\times3} & 1 \end{bmatrix} = \begin{bmatrix} I_3 & t_{0f,i} \\ 0_{1\times3} & 1 \end{bmatrix} \quad (4.6)$$

Since x-axis rotations are permissible at the ankle and subtalar joints, the final homogeneous transformation matrix associated with the foot frame can be obtained by including the angular displacements at the ankle and subtalar joints as shown in (4.7), where R_x is used to represent the transformation matrix for an x-axis rotation. It can be seen that the foot coordinate frame at the neutral position is recovered when both the ankle and subtalar displacements are zero.

$$T_{0f} = T_{0a,i} \begin{bmatrix} R_{x,a} & 0_{3\times1} \\ 0_{1\times3} & 1 \end{bmatrix} T_{0a,i}{}^{-1} T_{0s,i} \begin{bmatrix} R_{x,s} & 0_{3\times1} \\ 0_{1\times3} & 1 \end{bmatrix} T_{0s,i}{}^{-1} T_{0f,i} \quad (4.7)$$

It is worth noting that the model formulated above will generally have 16 parameters. This is because six parameters will be required to define $T_{0f,i}$ if the orientation of the neutral foot frame is left arbitrary. As the models proposed by van den Bogert and Lewis [79, 82] only use 12 parameters, the model presented above is not a minimal realisation of the biaxial model. Two of the four additional parameters can be viewed as the angular offsets needed at each revolute joint to zero the ankle and subtalar joint displacements at the neutral foot orientation. The presence of the remaining two parameters is related to the fact that the origins for the ankle and subtalar frame can be placed anywhere along the corresponding revolute axis (as illustrated in Figure 4.4). This means an additional degree of freedom is used for the location each of these origins. While the 16 parameter model allows arbitrary combinations of origins along these two axes, the location of these origins is constrained in the 12 parameter model to lie on points where the distance between lines representing the two axes is at its minimum. For the purpose of simulation, the added number of parameters will not make any difference to the resulting foot motion as these models describe identical kinematic constraints.

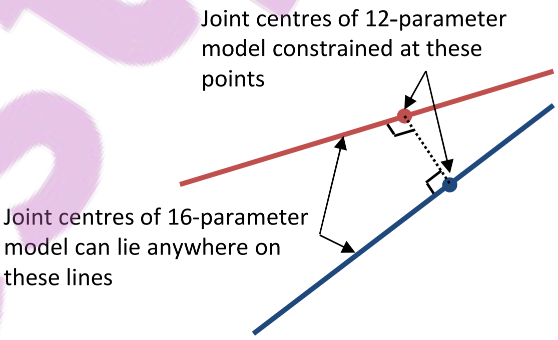

Figure 4.4: Diagram showing additional degrees of freedom available in the 16-parameter kinematic model when compared with the 12 parameter model.

4.3 Identification of the Reduced Biaxial Model

Where parameter identification is concerned, additional parameters will introduce redundancy in the system to be identified and this may lead to problems in estimation results. Models with no redundancy are therefore preferred in the formulation of system identification problems. However, while algorithms used in [79, 82] are designed to identify both orientation and location of the ankle and subtalar revolute joints, the emphasis of the identification algorithm in this research is mainly on the orientations of the ankle and subtalar joint axes, which are required for controller parameter adaptation strategies, the translations of the foot rigid bodies are therefore not considered in the proposed parameter identification scheme and the redundant parameters used to describe the joint centres in the kinematic formulation presented above were not of any interest in this work. It is also important in this application that the neutral foot position corresponds with zero ankle and subtalar joint displacements, and it can be seen that this condition is inherently satisfied in the kinematic model defined above, hence justifying the inclusion of the two additional axes orientation parameters in the proposed estimation problem.

The foot orientation as obtained from the kinematic model, $\hat{R}_{0f}$ is represented by the rotational transformation matrix in (4.7) and it takes the form of (4.8) when the initial orientation of the foot is taken to be identical to that of the global reference frame.

$$\hat{R}_{0f} = R_{0a,i} R_{x,a} R_{as,i} R_{x,s} {R_{as,i}}^T {R_{0a,i}}^T \tag{4.8}$$

As previously discussed, $R_{0a,i}$ and $R_{0s,i}$ can each be defined using two rotations. A biaxial kinematic model with fixed revolute joints therefore has four parameters governing its final orientation. Since these are the only parameters of interest for this work, the identification problem used in this application can be made simpler than those described in [79, 82], thus making it more feasible for online implementation.

Formally, the kinematic model considered in this study is represented by (4.9). It can be seen that this model outputs the model foot orientations in terms of Euler angles $\widehat{\Theta}$, and uses the model parameters, ρ and joint displacements, θ_{as} as inputs. Here, $\rho = [\theta_{z,a}\ \theta_{y,a}\ \theta_{z,s}\ \theta_{y,s}]^T$, where $\theta_{z,a}$ is the *z*-rotation angle for the ankle axis, $\theta_{y,a}$ is the *y*-rotation angle for the ankle axis, $\theta_{z,s}$ is the *z*-rotation angle for the subtalar axis, and $\theta_{y,s}$ is the *y*-rotation angle for the subtalar axis. These parameters will be collectively referred to as the axis tilt angles hereafter.

$$\widehat{\Theta} = f(\rho, \theta_{as}) = g(\rho, \Theta) \tag{4.9}$$

Since the ankle and subtalar joint angles cannot be readily measured, they have to be estimated from the Euler angles used to describe the observed foot orientation, Θ. By keeping this in mind, it can be seen that $\widehat{\Theta}$ is in fact a function of ρ and Θ. The parameter identification problem in this study is therefore one which seeks to minimise the differences between Euler angles estimated from the kinematic model and those obtained via measurement of the foot orientation. The desired model parameters are therefore the solution to (4.10), where k is the observation number and N the total number of observations.

$$\arg\min_{\rho\in\mathbb{R}^4} \sum_{k=1}^{k=N} [\Theta_k - g(\rho,\Theta_k)]^T[\Theta_k - g(\rho,\Theta_k)] \tag{4.10}$$

4.3.1 Solution of Ankle and Subtalar Joint Displacements

It can be seen from (4.9) that matching ankle and subtalar joint displacements must be computed from the observed foot orientation which is typically be expressed in the form of three Euler angles. However, it should be noted that given a set of axis tilt angles, the foot orientations realisable by the kinematic model are constrained on a “surface” in the three dimensional space of Euler angles. This is because the model foot orientation (4.8) is only dependent on the angular displacements of the ankle and subtalar revolute joints through $R_{x,a}$ and $R_{x,s}$. As a result, not all measured Euler angles will correspond exactly to a set of ankle and subtalar displacements. The ankle and subtalar joint displacements used must therefore provide a model foot orientation with minimal deviation from the measured orientation, and this had been treated as an optimisation problem in the literature [82]. In this work, two methods were derived to compute the ankle and subtalar joint displacements given a particular set of axis tilt angles and foot orientation. The first of these two methods is based on element matching of the matrices used to describe the measured and computed foot orientations. The second approach on the other hand seeks to minimise the magnitude of rotational angle required to transform between these two orientations according to the axis-angle convention. A comparison of these two approaches is presented here in this sub section.

Matrix element matching

An alternative approach involving comparisons of matrix elements was also considered in this research. This method will be referred to as the matrix element matching (MEM) approach hereafter. By reorganising (4.8) into (4.11) and partially expanding this expression, (4.12) can be obtained. Here, B_{ij} is used to refer to the element at the i^{th} row and j^{th} column in the B matrix, θ_a is the ankle displacement and θ_s is the subtalar displacement. The values of θ_a can therefore be obtained by solving the simultaneous equations given by A_{21} and A_{31} (the subscripts are again used to extract the matrix element according to its row and column). Similarly, θ_s can be solved using equations found at A_{12} and A_{13}.

$$\begin{gathered} {R_{0a,i}}^T \hat{R}_{0f} R_{0s,i} = R_{x,a} {R_{0a,i}}^T R_{0s,i} R_{x,s} \\ A = R_{x,a} B R_{x,s} \end{gathered} \tag{4.11}$$

$$A = \begin{bmatrix} B_{11} & B_{12}\cos\theta_s - B_{13}\sin\theta_s & B_{13}\cos\theta_s - B_{12}\sin\theta_s \\ B_{21}\cos\theta_a - B_{31}\sin\theta_a & \multicolumn{2}{c}{\multirow{2}{*}{A'}} \\ B_{31}\cos\theta_a + B_{21}\sin\theta_a & & \end{bmatrix} \tag{4.12}$$

Axis-angle convention based optimisation

It should be noted that the actual foot orientation R_{0f} is used in place of $\hat{R}_{0f}$ in the parameter identification algorithm. As a result, the equality in (4.12) may no longer hold for all the elements in the matrix. While the ankle and subtalar joints can be expressed explicitly in terms of the measured foot orientation and model parameters, the solution obtained by the MEM approach may not be the best solution since it only considers four of the nine elements in the orientation matrix. To verify the applicability of the results obtained through the solution of (4.12), an optimisation approach was also investigated. This optimisation approach uses the axis-angle convention to describe rigid body rotations. This convention describes three dimensional rotations using an equivalent revolution about a single axis. Using this convention, a rotational matrix can be represented as (4.13), where v_1 is the unit column vector representing the axis of revolution, ϕ is the angle of revolution about this axis while v_2 and v_3 are unit column vectors which form an orthonormal matrix together with v_1. Expanding (4.13) will allow the orientation matrix to be simplified to (4.14), which is solely dependent on v_1 and ϕ. Here $[v_1 \times]$ is the anti-symmetric matrix that describes the cross product operation involving v_1 (i.e. $[v_1 \times]b = v_1 \times b$).

$$R = [v_1\ v_2\ v_3]\begin{bmatrix} 1 & 0 & 0 \\ 0 & \cos\phi & -\sin\phi \\ 0 & \sin\phi & \cos\phi \end{bmatrix}\begin{bmatrix} {v_1}^T \\ {v_2}^T \\ {v_3}^T \end{bmatrix} \tag{4.13}$$

$$R = (\cos\phi)I_3 + (1-\cos\phi)v_1{v_1}^T + (\sin\phi)[v_1 \times] \tag{4.14}$$

Using this convention, the similarity between two orientations can be judged by a single parameter, the angular displacement ϕ. As a result, this angle can be used as the quantity to be minimised when computing the optimal ankle and subtalar joint displacements. Conveniently, due to the anti-symmetric property of $[v_1 \times]$ where $[v_1 \times] = -[v_1 \times]^T$, the cosine of ϕ can be easily computed through (4.15), and since $\cos\phi = 1$ when $\phi = 0$, the objective function, C to be minimised by varying θ_a and θ_s can be defined as (4.16).

$$\cos\phi = \frac{1}{2}\left[\mathrm{trace}\left(\frac{R+R^T}{2}\right) - 1\right] = \frac{1}{2}[\mathrm{trace}(R) - 1] \tag{4.15}$$

$$C = (1-\cos\phi)^2 = \frac{1}{4}\left[3 - \mathrm{trace}\left(\hat{R}_{0f}{\hat{R}_{0f}}^{\ T}\right)\right]^2 \tag{4.16}$$

Comparison of MEM and optimisation based approaches

The resulting ankle and subtalar displacements obtained from both the methods discussed above were compared by testing for orientations defined by a range of XYZ Euler angles at intervals of five degrees. The test parameters and results are summarised in Table 4.1 below. It can be seen from these results that joint displacements produced from both approaches are effectively identical in the range of XYZ Euler angles and the axis tilt angles tested. The MEM approach was therefore selected for use in this research as it is more computationally efficient and more suitable for use in an online identification algorithm. The justification for the reduced computational complexity is the fact that ankle and subtalar joint displacements can be computed directly in the MEM approach without the need of an optimisation routine. Additionally, the MEM approach also makes it possible to express the parameter gradient of the model foot orientation analytically, thus simplifying the implementation of gradient based parameter estimation algorithms.

Table 4.1: Summary of test parameters and results for a test to compare ankle and subtalar displacements computed using the MEM and optimisation approaches.

Description	Value	Unit
z-rotation of ankle axis, $\theta_{z,a}$	0.1	radians
y-rotation of ankle axis, $\theta_{y,a}$	0	radians
z-rotation of subtalar axis, $\theta_{z,s}$	1.2	radians
y-rotation of subtalar axis, $\theta_{y,s}$	0.6	radians
Range of X Euler angles tested	[-30 45]	degrees
Range of Y Euler angles tested	[-25 25]	degrees
Range of Z Euler angles tested	[-30 30]	degrees
Maximum absolute difference in estimated ankle joint displacement, $\left\|\tilde{\theta}_a\right\|_{max}$	5.2736e-16	radians
Maximum absolute difference in estimated subtalar joint displacement, $\left\|\tilde{\theta}_s\right\|_{max}$	3.3307e-16	radians

4.3.2 Gradient Computation of the Kinematic Model

The parameter identification of the ankle kinematic model is basically an optimisation problem, and the ability to compute the parameter gradient of the model will facilitate this process by permitting the use of line search optimisation routines. Despite the model being nonlinear in parameter, knowledge of its parameter gradient will still make the system amenable to application of online parameter identification algorithms such as the Kalman Filter, the Recursive Least Squares and the Least Mean Squares. This section will therefore describe the procedures required to compute this parameter gradient.

It can be seen from (4.9) that the output of the model is given in terms of Euler angles while the foot orientation as given by (4.8) is presented in the form of a rotational matrix. An appropriate Euler angle convention must therefore be used to describe this orientation matrix. In this chapter, the ZXY Euler angles are used since this is the convention in which the measured pitch(X) and roll(Y) measurements are supplied by the inclinometer used in the prototype ankle rehabilitation robot. As the yaw component is not readily available from the inclinometer, it is computed by considering the forward kinematics of the robot. For completeness, the relationship between a rotational matrix and its corresponding ZXY Euler angles is given in (4.17), where R_x is the matrix describing rotation about the *x*-axis by θ_x, C_x is short for $\cos\theta_x$ and S_x is short for $\sin\theta_x$. This notation extends to the *y* and *z* axes, where they are respectively indicated by the *y* and *z* subscripts. By representing the ZXY Euler angles in a column vector, it can be expressed as (4.18) when the foot orientation is known.

$$R_{0f} = R_z R_x R_y = \begin{bmatrix} C_z C_y - S_z S_x S_y & -S_z C_x & C_z S_y + S_z S_x C_y \\ S_z C_y + C_z S_x S_y & C_z C_x & S_z S_y - C_z S_x C_y \\ -C_x S_y & S_x & C_x C_y \end{bmatrix} \tag{4.17}$$

$$\Theta = \begin{bmatrix} \theta_x \\ \theta_y \\ \theta_z \end{bmatrix} = \begin{bmatrix} \sin^{-1} R_{0f32} & \tan^{-1}\left(\frac{-R_{0f31}}{R_{0f33}}\right) & \tan^{-1}\left(\frac{-R_{0f12}}{R_{0f22}}\right) \end{bmatrix}^T \tag{4.18}$$

It is also clear from previous discussion that ankle and subtalar joint displacements are a function of ρ and Θ (4.19). As a result, the parameter gradient of the ZXY Euler angles in the ankle kinematic model can be obtained by considering (4.20).

$$\theta_{as} = h(\rho, \Theta) \tag{4.19}$$

$$\frac{\partial \widehat{\Theta}}{\partial \rho} = \frac{\partial f(\rho, \theta_{as})}{\partial \rho} + \frac{\partial f(\rho, \theta_{as})}{\partial \theta_{as}} \frac{\partial \theta_{as}}{\partial \rho} \tag{4.20}$$

4.4 Online Identification Algorithms

The main objective of this work on ankle kinematic parameter estimation is to extract information of the orientations of the ankle and subtalar joint axes while the ankle rehabilitation robot is in operation. An online parameter identification algorithm is therefore crucial for the realisation of this goal. This section will discuss the application of different online parameter identification algorithms to the kinematic parameter estimation problem in this research.

4.4.1 Extended Kalman Filter/ Recursive Least Squares

The Extended Kalman Filter (EKF) is an algorithm for state estimation of nonlinear dynamic systems. It predicts system states by considering the measured system outputs, a state space model of the system dynamics and covariance matrices related to the uncertainties found in the measurements and system model. Kalman filters can also be used to simultaneously estimate both states and parameters of a system [113]. This can generally be achieved by augmentation of the parameters of interest to the system state vector. In this particular application, the emphasis is on obtaining an estimate of the system's kinematic parameters. The dynamic model of the ankle and foot motion is therefore not considered. As a result, the filter state vector consists purely of the parameters required to define the axes orientations. The underlying model for the EKF is therefore given by (4.21). Where subscript k denotes the iteration number, w is the process noise with covariance matrix Q and v the measurement noise with covariance matrix R.

$$\begin{aligned} \rho_k &= \rho_{k-1} + w_k \\ \widehat{\Theta}_k &= f\left(\rho, \theta_{as,k}\right) + v_k \end{aligned} \tag{4.21}$$

The algorithm involved in the EKF has the same form as that of a conventional Kalman filter except for the use of linearised state transition and observation matrices. It should be noted however that while the Kalman filter is an optimal state estimator, the EKF is not optimal due to the linearisation of the output function. In this problem, the state transition matrix is simply an identity matrix while the observation matrix is given by the gradient matrix computed from (4.20). The process and measurement noise covariance matrices will control the extent to which the filter will modify the model parameters to fit the measured data. The algorithm of the EKF for this application is given in Table 4.2.

Table 4.2: The EKF algorithm

Prediction step:	$\hat{\rho}_{k\mid k-1} = \hat{\rho}_{k-1\mid k-1}$ $P_{k\mid k-1} = P_{k-1\mid k-1} + Q_k$
Update step:	$\widetilde{\Theta}_k = \Theta_k - g\left(\hat{\rho}_{k\mid k-1}, \Theta_k\right)$ $\hat{\rho}_{k\mid k} = \hat{\rho}_{k\mid k-1} + P_{k\mid k-1} {H_k}^T \left(H_k P_{k\mid k-1} {H_k}^T + R_k\right)^{-1} \widetilde{\Theta}_k$ $P_{k\mid k} = \left[I - P_{k\mid k-1} {H_k}^T \left(H_k P_{k\mid k-1} {H_k}^T + R_k\right)^{-1} H_k\right] P_{k\mid k-1}$ Where $H_k = \frac{\partial \widehat{\Theta}}{\partial \rho}$ and I is an identity matrix.

The recursive least squares (RLS) algorithm is another common approach for online identification of linear models and is related to the Kalman filter. The recursive least squares adaptive filter works by "memorising" previous measurements in the form of a cross correlation matrix and the current estimated parameters. The correlation matrix is then used together with the estimation error of the current iteration to further adjust the model parameters. Even though the recursive least squares algorithm will not produce the optimal estimates for nonlinear systems, its simplicity has warranted an investigation into its effectiveness for this application. Since the RLS algorithm works with linear systems, the linearised ankle kinematic model as shown in (4.22) has to be used. It can be seen that the model is linearised about the set of parameters denoted by ρ_{lin} and the measured ZXY Euler angles given by Θ. H is the gradient of the nonlinear model about its linearisation point and is used to relate changes in Euler angles to changes to the model parameters, with $\Delta\Theta = \widehat{\Theta} - \widehat{\Theta}_{lin}$, $\Delta\hat{\rho} = \hat{\rho} - \rho_{lin}$ and $\widehat{\Theta}_{lin} = g(\rho_{lin}, \Theta)$.

$$\widehat{\Theta} \approx g(\rho_{lin}, \Theta) + \left.\frac{\partial\widehat{\Theta}}{\partial\rho}\right|_{\rho_{lin},\Theta} (\hat{\rho} - \rho_{lin}) \Rightarrow \Delta\Theta \approx H\Delta\rho \tag{4.22}$$

Using this linear model, the RLS algorithm is given by (4.23), where $\Delta\hat{\rho}$ is the deviation in model parameter needed to reduce estimation error, $\hat{\rho}$ is the estimated parameter, P is the inverse cross-correlation matrix, λ is a geometric forgetting factor where a value of 1 will lead to all historical data being considered, k is the iteration number, and I is an identity matrix.

$$\begin{aligned}
\Delta\hat{\rho}_k &= \Delta\hat{\rho}_{k-1} + P_{k-1}{H_k}^T\left(\lambda I + H_k P_{k-1}{H_k}^T\right)^{-1}\left(\Theta_k - g\left(\rho_{lin,k}, \Theta_k\right) - H_k\Delta\hat{\rho}_{k-1}\right) \\
P_k &= \tfrac{1}{\lambda}\left[P_{k-1} - P_{k-1}{H_k}^T\left(\lambda I + H_k P_{k-1}{H_k}^T\right)^{-1} H_k P_{k-1}\right] \\
\rho_k &= \rho_{lin,k} + \Delta\hat{\rho}_k
\end{aligned} \tag{4.23}$$

A comparison of the RLS and EKF algorithm reveals that they are equivalent if:

1) The process noise covariance, Q in the EKF is zero and the measurement noise covariance, R is an identity matrix.

2) The geometric forgetting factor in the RLS algorithm is unity.

3) The parameters about which the model is linearised are the same as their estimates obtained from the previous iteration ($\rho_{lin,k} = \hat{\rho}_{k-1}$)

4) Estimate of the parameter deviation vector brought forward from the previous iteration is always zero ($\Delta\hat{\rho}_{k-1} = \mathbf{0}$).

Condition 1 above implies that the RLS algorithm is essentially an EKF which assumes that the model is perfect while allowing large uncertainties in the measurements. A look at conditions 3 and 4 also suggests that recurrent update of ρ_{lin} and persistent reset of $\Delta\hat{\rho}$ will align the behaviour of the RLS algorithm with that of the EKF. Since the estimated gradient will become less accurate as the parameters deviate further from ρ_{lin}, this frequent update should be able to improve on the accuracy of the RLS algorithm. Based on the above observation, the RLS algorithm will be treated as a special case of the EKF.

4.4.2 Least Mean Square

In addition to the EKF, the parameters of the kinematic model can also be estimated through the use of the least mean square algorithm. This algorithm uses the idea of steepest descent for parameter identification and therefore also requires information on the parameter gradient of the kinematic model. However, it does not explicitly store the previous measurements in memory as with the case of EKF or RLS and is therefore more efficient in terms of memory usage. It is also less complex as computation of the inverse cross correlation matrix is not required.

The overall concept of this iterative method is to modify the model parameters so that a step would be made in the direction which will reduce the estimation error according to the information available in the current iteration. If the parameter gradient is readily available, this can be accomplished by changing the parameter estimates in the manner shown in (4.24), where η is a vector that is dependent on the estimation error.

$$\Delta\hat{\rho}_k = \Delta\hat{\rho}_{k-1} + H_k{}^T\eta \tag{4.24}$$

In order to obtain a suitable expression for η, one can first consider the case where the model is linear-in-parameter. The convergence of the above algorithm can be determined by examining the behaviour of the function (4.25), where V_k is a positive function and ρ^* is the true parameter vector of the system.

$$V_k = (\hat{\rho}_k - \rho^*)^T(\hat{\rho}_k - \rho^*) \tag{4.25}$$

Substitution of the linearised version (where Δ is removed) of (4.24) into (4.25) will then result in (4.26). It can also be seen that the parameters will converge to the optimal parameters if (4.27) holds. The minimisation of ΔV_k with respect to η then produces the optimal expression for η shown in (4.28). Since $d = H_k\rho^*$ holds for a linear system (with d being the noise free system output), η can finally be represented as (4.29).

$$\begin{aligned} V_k &= \left(\hat{\rho}_{k-1} + H_k{}^T\eta - \rho^*\right)^T\left(\hat{\rho}_{k-1} + H_k{}^T\eta - \rho^*\right) \\ &= V_{k-1} + \eta^T H_k H_k{}^T\eta + 2\eta^T H_k(\hat{\rho}_{k-1} - \rho^*) \end{aligned} \tag{4.26}$$

$$\begin{aligned} &\Delta V_k = V_k - V_{k-1} < 0 \\ &\Rightarrow \eta^T H_k H_k{}^T\eta + 2\eta^T H_k(\hat{\rho}_{k-1} - \rho^*) < 0 \end{aligned} \tag{4.27}$$

$$\begin{aligned} &\frac{d}{d\eta}\left[\eta^T H_k H_k{}^T\eta + 2\eta^T H_k(\hat{\rho}_{k-1} - \rho^*)\right] = 0 \\ &\quad\Rightarrow \eta = -\left(H_k H_k{}^T\right)^{-1} H_k(\hat{\rho}_{k-1} - \rho^*) \end{aligned} \tag{4.28}$$

$$\eta = \left(H_k H_k{}^T\right)^{-1}(d - H_k \hat{\rho}_{k-1}) \tag{4.29}$$

Incorporation of η as given in (4.29) into the parameter update algorithm will then lead to (4.30). If the nominal parameters were to be constantly updated as with the case of the RLS algorithm described above (i.e. $\Delta\hat{\rho}_{k-1}$ is perpetually reset to 0), the resulting parameter estimate at iteration k is given by (4.31), which is basically the normalised least mean squares filter. A closer look at (4.31) will suggest that this update rule is somewhat similar to the update rule used in the Gauss-Newton method. Since the ankle kinematic model is a nonlinear in parameter system, the optimality and convergence properties of the correction step shown in (4.31) are no longer guaranteed and the use of the $\left(H_k H_k{}^T\right)^{-1}$term may lead to divergence of the estimated parameters, particularly when the parameter gradient is badly conditioned or when it has a large maximum singular value. The parameter update in (4.31) is therefore reformulated as (4.32) to include a term similar to that used in the Levenberg-Marquardt algorithm [114], where the parameter ε can be used to control magnitude and direction of the step size. The use of a large ε will lead to smaller parameter updates along the direction of steepest descent for the estimation error while a small value of ε will effectively revert the algorithm back to (4.31).

$$\Delta\hat{\rho}_k = \Delta\hat{\rho}_{k-1} + H_k{}^T\left(H_k H_k{}^T\right)^{-1}(\Delta\Theta - H_k \Delta\hat{\rho}_{k-1}) \tag{4.30}$$

$$\hat{\rho}_k = \hat{\rho}_{k-1} + H_k{}^T\left(H_k H_k{}^T\right)^{-1}[\Theta_k - g(\hat{\rho}_{k-1}, \Theta_k)] \tag{4.31}$$

$$\hat{\rho}_k = \hat{\rho}_{k-1} + H_k{}^T\left(\varepsilon I + H_k H_k{}^T\right)^{-1}[\Theta_k - g(\hat{\rho}_{k-1}, \Theta_k)] \tag{4.32}$$

4.5 Kinematic Model with Configuration Dependent Axes Orientations

Lewis et al. [82] had found that the biaxial ankle model with constant revolute joint orientations can only give a crude approximation to the actual foot motion. They have also suggested that a more advanced kinematic model which allows variation of the revolute joint orientations according to joint displacements can potentially be used to provide a better description of ankle-foot motion. This section therefore explores the feasibility of such an extension to the ankle kinematic model.

4.5.1 Variation of Axis Tilt Angles with Ankle and Subtalar Joint Displacements

A simple extension of the constant axis model is to allow the axis tilt angles to vary linearly with the ankle and subtalar joint displacements. A linear relationship had been chosen as it does not introduce significant computational complexity. Additionally, while the actual dependency may not be perfectly linear, the choice of a model with linear dependency is should still be applicable as a local approximation of more complex nonlinear relationships. The new parameters involved in this modified kinematic model can therefore be represented as (4.33), where parameters of the original biaxial ankle model with constant axis tilt angles can be expressed as (4.34), with $\otimes$ as the operator for the Kronecker product. It is straight forward that the original biaxial model is a subset of this extended model where all α and β terms have the value of zero. As this configuration dependent model utilises a different parameter vector, the gradient matrix required in the estimation algorithms is also different from that given in (4.20). However, due to the similarity in the models, the required gradient matrix (4.35) can be easily obtained by reusing (4.20) and considering (4.34).

$$\rho' = [\alpha_{z,a} \quad \beta_{z,a} \quad \gamma_{z,a} \quad \alpha_{y,a} \quad \beta_{y,a} \quad \gamma_{y,a} \quad \alpha_{z,s} \quad \beta_{z,s} \quad \gamma_{z,s} \quad \alpha_{y,s} \quad \beta_{y,s} \quad \gamma_{y,s}]^T \tag{4.33}$$

$$\rho = \{I_4 \otimes [\theta_a \quad \theta_s \quad 1]\}\rho' \tag{4.34}$$

$$\frac{\partial\widehat{\Theta}}{\partial\rho'} = \frac{\partial\widehat{\Theta}}{\partial\rho}\frac{\partial\rho}{\partial\rho'} = \frac{\partial\widehat{\Theta}}{\partial\rho}\{I_4 \otimes [\theta_a \quad \theta_s \quad 1]\} \tag{4.35}$$

The major problem associated with this new parameterization is that the ankle and subtalar joint displacements can no longer be easily expressed as an explicit function of the measured ZXY Euler angles and the model parameters. Due to the increased complexity of the relationship between the model parameters, joint displacements and measured Euler angles, a numerical algorithm had been employed to resolve the joint displacements that will minimise the discrepancies between the elements of the matrix being considered in the MEM approach. Naturally, the solution of the parameter gradient of the ankle and subtalar displacements is also made more complicated. The formulation of the kinematic model with (4.33) is therefore not ideal for the purpose of online parameter identification.

4.5.2 Variation of Axis Tilt Angles with Measured Euler Angles

An alternative approach that can be used is to allow the ankle and subtalar axes orientations to vary according to the Euler angles. Since only two degrees of freedom is available in the kinematic model, it follows that only two of the three Euler angles are required to establish the configuration dependency. For simplicity, a linear variation can also be used. However, it should be noted that due to the nonlinear relationship between the joint displacements and Euler angles, the linear dependencies of axis tilt angles on the joint displacements will not be retained if these tilt angles are described as a linear function of the Euler angles. Since there is no conclusive evidence in the literature which suggests a linear relationship between the axis tilt angles and the joint displacements, variation from this original assumption should be tolerable. A matter of greater importance however is the existence of a one to one mapping between the Euler angle pair and the joint displacement. For this reason, different convention and combinations of the Euler angles should be examined to select suitable angle pairs that can be used as substitutes for the ankle and subtalar joint displacements.

As an illustrative example, Figure 4.5 shows the relationship between the joint displacements and the X and Y component of the XYZ Euler angles when the axis tilt angles are configuration independent and have the same values as those given by Inman [80]. The relationships shown here were obtained by first computing the XYZ Euler angles corresponding to the foot orientation at various ankle and subtalar joint displacements, and then reorganising the resulting data so that the ankle and subtalar joints are plotted against the X and Y Euler angles. A visual inspection of these relationships suggests that linear planes may be able to provide an adequate approximation to these surfaces. Clearly, these surfaces would vary when the model parameter changes. The selection of the Euler angle pair must therefore be based on consideration of a larger variety of model parameters. This had led to the computation of the relationships shown in Figure 4.5 across model parameters which were varied randomly about those given by Inman [80]. The result of such an analysis is presented in Figure 4.6, where 500 randomly selected sets of model parameters (all within ±0.5 rad of the nominal parameters) were used to establish the joint displacement-foot orientation relationships. In this analysis, the mappings between different pairs of Euler angles (in both the XYZ and ZXY conventions) to the ankle and subtalar joints were obtained and fitted with a linear plane. The coefficients of determination (R^2 values) of these linear planes were then computed and plotted in the box plots shown in Figure 4.6.

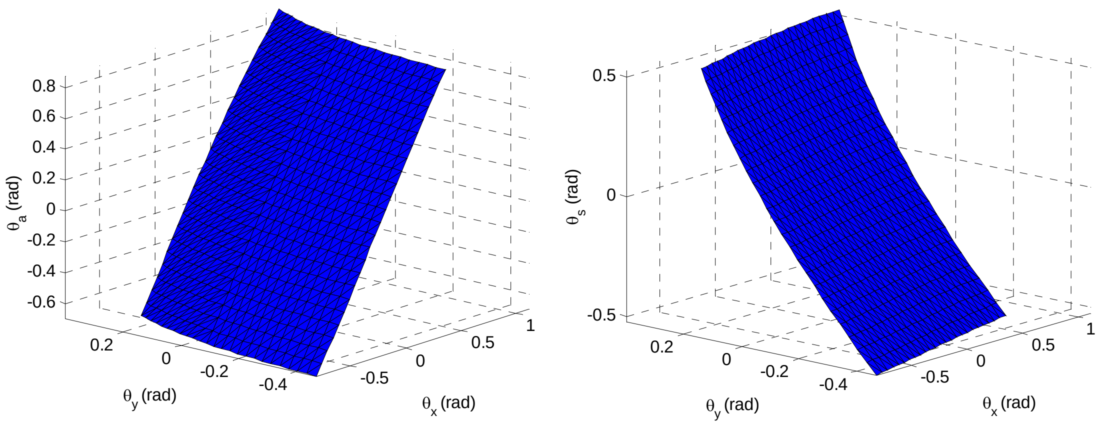

Figure 4.5: The relationships between the X and Y components of the XYZ Euler angles and the ankle and subtalar joint displacements when the axis tilt angles of the ankle kinematic model are identical to those presented in literature.

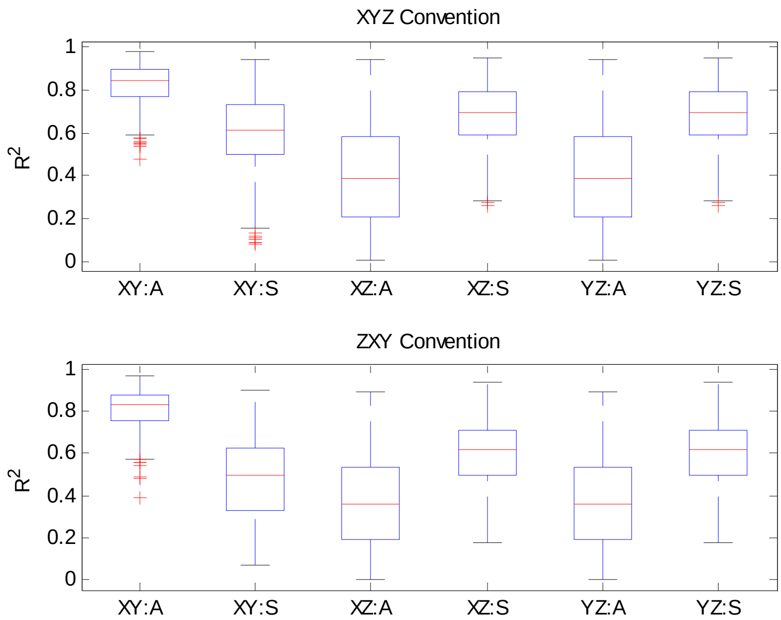

Figure 4.6: Box plots for R^2 values found by fitting a linear model through the Euler angle-joint displacement relationships over 500 randomly generated model parameters. The top plot shows the R^2 values for relationships obtained using various pair-wise combinations of the XYZ Euler angles while the bottom plot shows the same obtained using different pair-wise combinations of the ZXY Euler angles. Note that the notation of P:Q is used to identify results relating to the angle pairing P and displacement output Q, with A and S denoting the ankle and subtalar joint displacements respectively.

As it is difficult to establish whether the joint displacements are proper functions of the Euler angle pairs, the goodness of fit of the linear planes as given by the R^2 values were used as a measure of suitability for the different Euler angle pairs. This is because while a large R^2 value does not guarantee a one to one mapping between the Euler angles and the joint displacements, it does give an indication that this relationship can be well approximated by a linear model. Base on these results, the pairing of the X and Y component of the XYZ Euler angles was determined to be the best candidate to represent the ankle joint displacement. The subtalar joint displacements on the other hand seem to be better represented by the X and Z components of the XYZ Euler angles. To reduce the number of parameters involved in the extended kinematic model, the X and Y components of the XYZ Euler angles were used to represent the configuration dependency in the model, since it provides the best R^2 values for the ankle displacement and a reasonable R^2 value for the subtalar displacement.

Another issue is that the XYZ Euler angles used in this approach should be those computed from the corresponding model foot orientation, which brings back the initial dilemma of a non-explicit solution for the joint displacements. However, by accepting an approximate solution for this parameter identification problem, the measured XYZ Euler angles which are readily available from sensor measurements and forward kinematics of the robot can be used as an estimate instead to limit the increase in complexity of the estimation algorithm. The parameters of the extended kinematic model used in the final online estimation algorithm can therefore be rewritten as (4.36). Where

(4.37) is the relationship which links these parameters back to the axis tilt angles in the original ankle kinematic model. Also, $\theta_{x,XYZ}$ and $\theta_{y,XYZ}$ are respectively used to represent the X and Y components of the XYZ Euler angles relating to the measured foot orientation. The gradient matrix for the model proposed in this section can be found in a similar manner as that used in Section 4.5.1, and is shown in (4.38).

$$\rho'' = [\alpha'_{z,a} \quad \beta'_{z,a} \quad \gamma'_{z,a} \quad \alpha'_{y,a} \quad \beta'_{y,a} \quad \gamma'_{y,a} \quad \alpha'_{z,s} \quad \beta'_{z,s} \quad \gamma'_{z,s} \quad \alpha'_{y,s} \quad \beta'_{y,s} \quad \gamma'_{y,s}]^T \tag{4.36}$$

$$\rho = \{I_4 \otimes [\theta_{x,XYZ} \quad \theta_{y,XYZ} \quad 1]\}\rho'' \tag{4.37}$$

$$\frac{\partial\widehat{\Theta}}{\partial\rho'} = \frac{\partial\widehat{\Theta}}{\partial\rho}\frac{\partial\rho}{\partial\rho''} = \frac{\partial\widehat{\Theta}}{\partial\rho}\{I_4 \otimes [\theta_{x,XYZ} \quad \theta_{y,XYZ} \quad 1]\} \tag{4.38}$$

4.6 Preliminary Results

4.6.1 Simulations Involving Constant Axis Tilt Angles

This section presents several simulation results using the previously discussed online parameter identification algorithms. System identification based on data generated from the kinematic model with constant revolute joint orientation was first considered to investigate the effectiveness of the algorithms in handling nonlinear systems and to identify suitable tuning parameters for the identification algorithms. Both the EKF and LMS algorithms were tested and the algorithm parameters as well as results are summarised in Table 4.3. The EKF algorithm was tested with three different combinations of Q and R matrices while the LMS algorithm was tested with different values of ε. A random noise of ±1° is added to the measured ZXY Euler angles computed from the kinematic model. The ZXY Euler angles were generated periodically by computing the model foot orientation which corresponds to the ankle and subtalar joint displacements given by:

$$\theta_a = \frac{2\pi}{9}\sin\left(\frac{2\pi}{10}t\right) \qquad \theta_s = \frac{\pi}{6}\sin\left(\frac{2\pi}{11}t\right)$$

A smooth time dependent relationship was selected so that the simulation can better represent the case where the algorithms are acting on data obtained from actual motion trajectories. The difference in periods for the sine functions were used to allow greater coverage in the θ_a-θ_s plane. The evolution of model parameters for different trials of the EKF algorithm with constant tilt angles is shown in Figure 4.7 while that for the LMS algorithm is shown in Figure 4.8.

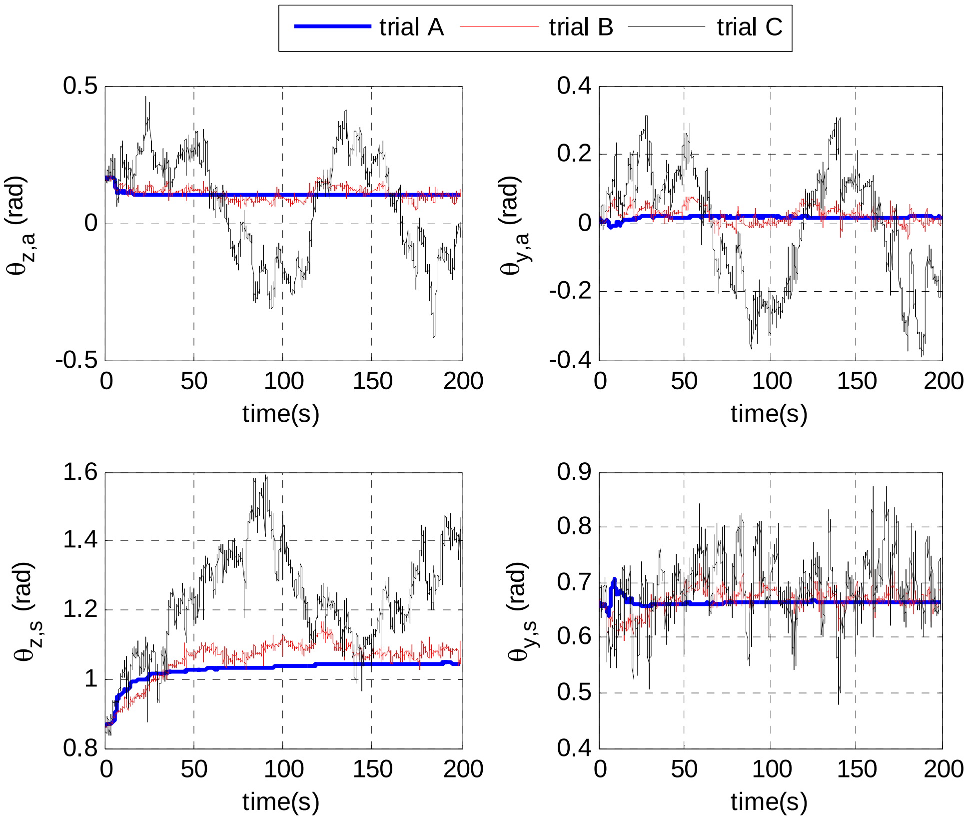

Figure 4.7: A time history of estimated parameters for EKF algorithms with different process and measurement noise covariance matrices. The blue, red and black lines represent parameters obtained from trials A, B and C respectively.

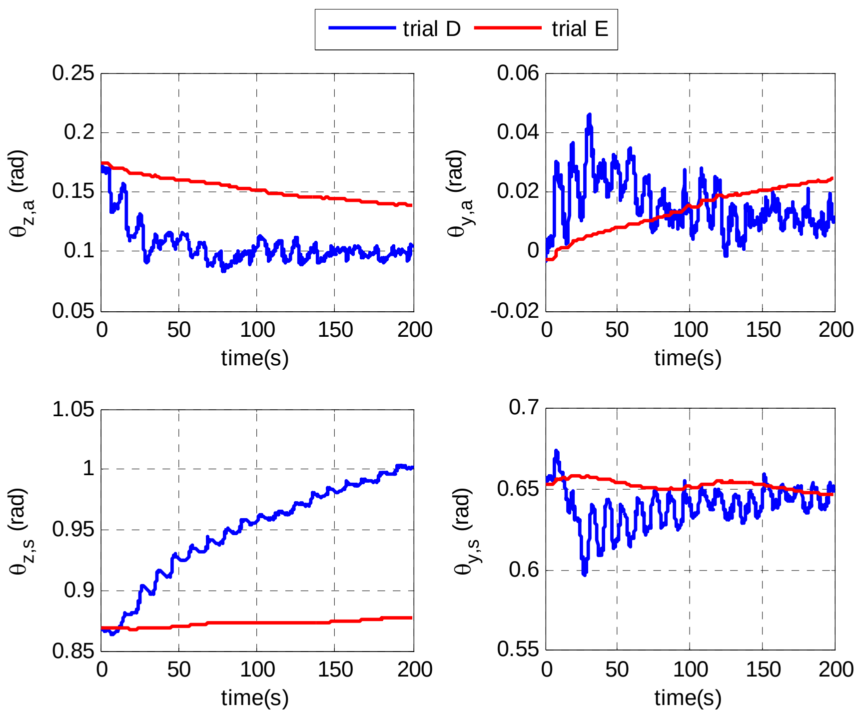

Figure 4.8: A time history of estimated parameters for the LMS algorithm with different ε values. The blue and red lines represent trials D and E respectively.

Table 4.3: Results summary of different kinematic parameter estimation algorithms on a kinematic model with constant axes tilt angles.

	(A)EKF: $Q = 0_{4\times4}, R = I_3$	(B)EKF: $Q = 0.1I_4, R = I_3$	(C)EKF: $Q = 0.1I_4, R = 0.1I_3$	(D)LMS: $\varepsilon = 10$	(E)LMS: $\varepsilon = 1000$
$\lvert\tilde{\theta}_{x,ZXY}\rvert_{max}$	0.0352	0.0358	0.0493	0.0374	0.0566
$\lvert\tilde{\theta}_{y,ZXY}\rvert_{max}$	0.0356	0.0401	0.0606	0.0488	0.0793
$\lvert\tilde{\theta}_{z,ZXY}\rvert_{max}$	0.0355	0.0411	0.1123	0.0462	0.0599
$\hat{\theta}_{z,a}$	0.1031	0.0991	-0.0285	0.1037	0.1384
$\hat{\theta}_{y,a}$	0.0169	0.0099	-0.1681	0.0115	0.0243
$\hat{\theta}_{z,s}$	1.0454	1.0657	1.3352	1.0021	0.8772
$\hat{\theta}_{y,s}$	0.6647	0.6765	0.7249	0.6497	0.6472

Actual model parameters: $\theta_{z,a}$= 0.1047, $\theta_{y,a}$= 0.0185, $\theta_{z,s}$= 1.0519, $\theta_{y,s}$ = 0.6658. All units in radians

Discussion

From these results, it can be seen that the EKF algorithm in trial A (which is equivalent to the RLS algorithm with no forgetting factor) had provided the best performance as it gives small errors in terms of the difference between measured and observed ZXY Euler angles, while also allowing the estimated model parameters to converge quickly to values close to the true parameters. An inspection of other variants of the EKF shows that the estimated parameters in trial B had drifted around their actual values, while much larger parameter variations were observed for trial C. For the LMS algorithm, it was observed that the trial with ε =10 performed relatively well, but with some small oscillations in the estimated parameters. On the other hand, the trial with a large ε was found to cause significantly slower convergence as shown in Figure 4.8.

4.6.2 Simulations Involving Configuration Dependent Axis Tilt Angles

The underlying model used in the EKF and LMS algorithms in trials A to E shown above assumes that the axis tilt angles are independent on the foot configuration. However, researchers have found that this is hardly the case for real ankle-foot structures [69, 71-73, 82]. In order to evaluate the performance of these constant tilt angle algorithms on a more realistic scenario, the ankle kinematic model used to generate the ZXY Euler angle measurements was modified in such a manner that the axis tilt angles are linearly dependent on the ankle and subtalar joint displacements. With this modification, the axis tilt angles are described using (4.34), with arbitrarily chosen linear coefficients to create dependency on ankle and subtalar displacements. The constant offsets used in the model however are the same as the constant axis tilt angles given in Table 4.3above. More specifically, the parameters of (4.34), used to generate the simulation data are summarised in Table 4.4.

Table 4.4: Parameters for the ankle kinematic model with configuration dependent axis tilt angles used in simulation.

$\alpha_{z,a}$	$\beta_{z,a}$	$\gamma_{z,a}$	$\alpha_{y,a}$	$\beta_{y,a}$	$\gamma_{y,a}$	$\alpha_{z,s}$	$\beta_{z,s}$	$\gamma_{z,s}$	$\alpha_{y,s}$	$\beta_{y,s}$	$\gamma_{y,s}$
0.3	0.1	0.1047	-0.25	0.15	0.0185	0.3	-0.15	1.0519	0.15	-0.25	0.6658

Table 4.5: Results summary of different kinematic parameter estimation algorithms on a kinematic model with axis tilt angles which varies linearly with joint displacements.

	(F)EKF: $Q = 0_{4\times4}, R = I_3$	(G)LMS: $\varepsilon = 10$	(H)EKF: $Q = 0_{12\times12}, R = I_3$ $\rho = \{I_4 \otimes [\theta_a \;\; \theta_s \;\; 1]\}\rho'$	(I)EKF: $Q = 0_{12\times12}, R = I_3$ $\rho = \{I_4 \otimes [\theta_{x,XYZ} \;\; \theta_{y,XYZ} \;\; 1]\}\rho''$
$\lvert\tilde{\theta}_{x,ZXY}\rvert_{max}$	0.1051	0.1143	0.0366	0.0364
$\lvert\tilde{\theta}_{y,ZXY}\rvert_{max}$	0.1411	0.0909	0.0375	0.0368
$\lvert\tilde{\theta}_{z,ZXY}\rvert_{max}$	0.2579	0.2009	0.0377	0.0395
$\hat{\theta}_{z,a}$	-0.0364	-0.5114	$0.3401\theta_a + 0.1736\theta_s + 0.08$	$0.2558\theta_{x,XYZ} + 0.1675\theta_{y,XYZ} + 0.0175$
$\hat{\theta}_{y,a}$	0.0684	-0.4372	$-0.2018\theta_a + 0.1195\theta_s - 0.00735$	$-0.2742\theta_{x,XYZ} + 0.1525\theta_{y,XYZ} - 0.0543$
$\hat{\theta}_{z,s}$	2.3667	1.9592	$0.2916\theta_a - 0.1848\theta_s + 1.1665$	$0.0147\theta_{x,XYZ} - 0.2048\theta_{y,XYZ} + 1.3426$
$\hat{\theta}_{y,s}$	0.5801	0.5861	$0.2123\theta_a - 0.2441\theta_s + 0.6750$	$0.2530\theta_{x,XYZ} - 0.3182\theta_{y,XYZ} + 0.7008$

Actual Parameters: $\theta_{z,a} = 0.3\theta_a + 0.1\theta_s + 0.1047$; $\theta_{y,a} = -0.25\theta_a + 0.15\theta_s + 0.0185$; $\theta_{z,s} = 0.3\theta_a - 0.15\theta_s + 1.1694$; $\theta_{y,s} = 0.15\theta_a - 0.25\theta_s + 0.6749$. All units in radians.

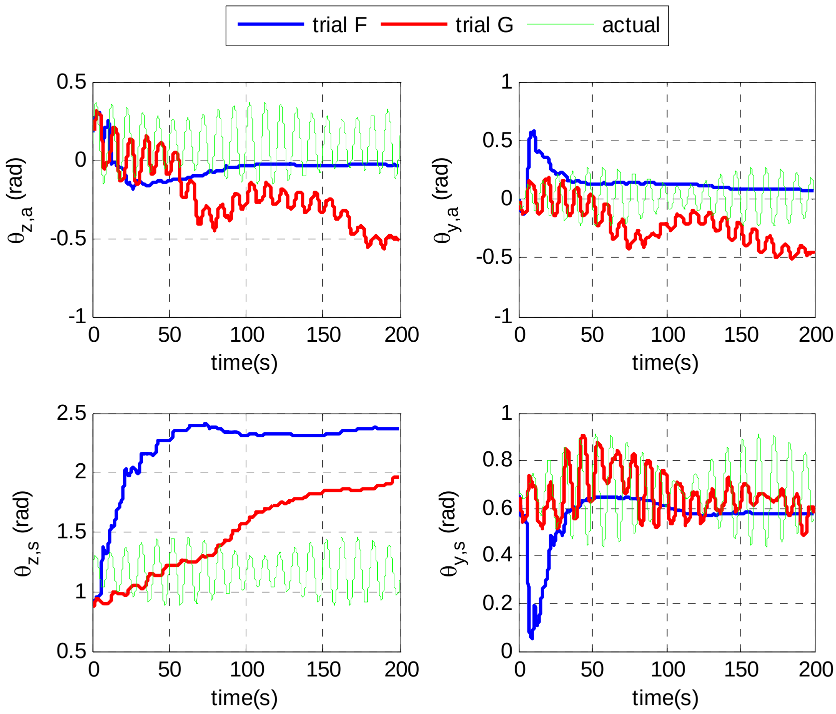

Figure 4.9: The time history of the axis tilt angle estimates obtained from case F (blue) and G (red) during the identification process. The actual axes tilt angles used in data generation is given by the green line.

The results obtained from the use of the EKF and LMS algorithms described above to estimate the parameters of this modified ankle kinematic model are shown in Table 4.5 and Figure 4.9. Two further trials were also carried out using different extensions to the kinematic model as discussed previously. The results of these are shown in Table 4.5 and Figure 4.10. The extended model used for case H has the same structure as the one used to generate the data, with the tilt angles depending linearly on the ankle and subtalar joint displacements. On the other hand, the configuration dependency of case I is expressed as a linear relation between the tilt angles and the X and Y components of the XYZ Euler angles associated with the foot orientation.

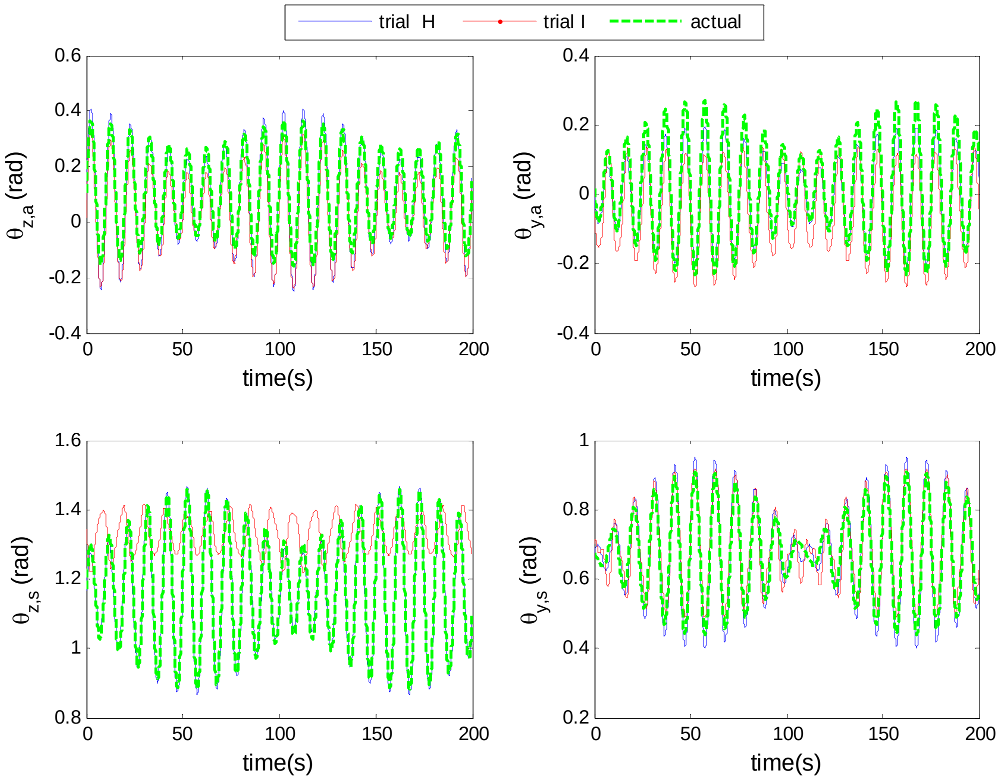

Figure 4.10: The estimated axis tilt angles using the final parameters obtain from case H (blue) and case I (red). The actual axis tilt angles used for data generation is given by the green line.

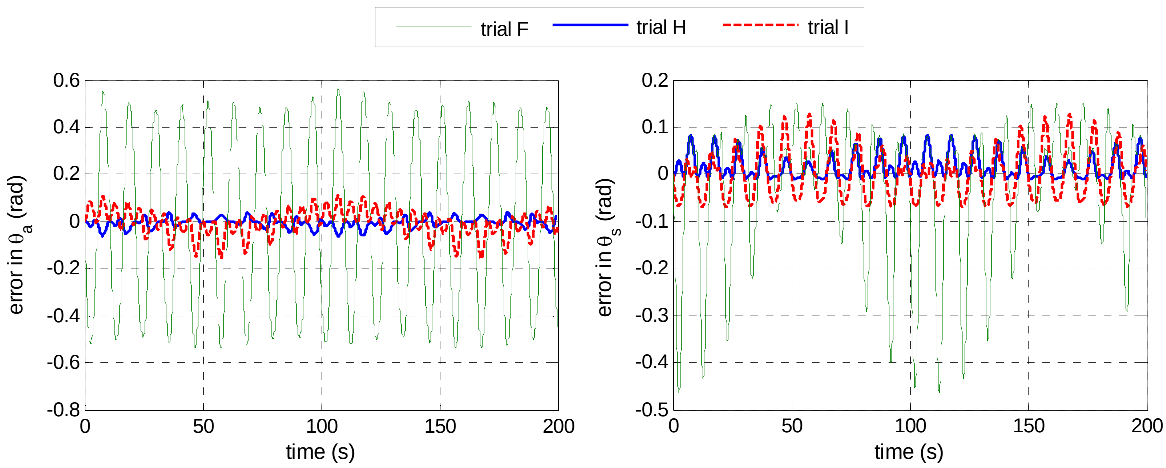

Figure 4.11: The errors in estimation of the ankle and subtalar joint angles using parameters obtained from the identification trials. Data relating to cases F, H and I are respectively given by the green, blue and red lines.

Discussion

Examination of the results from cases F and G shows that while the errors in ZXY Euler angles are not overly large, the axis tilt angles estimated from the LMS algorithm (red lines) had deviated rather significantly from the actual values. The performance for the EKF based algorithm (blue lines) is better, but still resulted in an incorrect estimate for the $\theta_{z,s}$ parameter. This indicates that the EKF and LMS algorithms based on the assumption of constant axis tilt angles are not very suitable for use when the axis tilt angles are in fact configuration dependent. When results from cases H and I are considered, it can be seen that errors in ZXY Euler angles are rather similar in both cases. However, examination of the estimated parameters had clearly shown that case H performed much better in estimating the actual axis tilt angles. This is not surprising as the algorithm used in case H is identical in structure to that used to generate the data.

It should be noted that one of the main use of this identification algorithm is to allow estimation of the ankle and subtalar joint displacements, which can then be used for gain scheduling control of the developed ankle rehabilitation robot. The ankle and subtalar joint displacements computed from the final parameters for cases F, H and I are therefore presented in Figure 4.11 to evaluate their suitability for the approximation of ankle and subtalar joint displacements. As expected, the estimation error for case H is quite small. Case I on the other hand had produced larger but still acceptable estimation errors (approximately 0.1 rad) for the ankle and subtalar displacements. The joint displacement estimation errors for case F however were significantly higher than both cases H and I. From these results, it can be seen that incorporation of axis tilt angle variations in the kinematic model can help improve the accuracy of the estimation algorithm.

It is clear from the above study that the algorithm used in case H is superior to that of case I in this scenario. Nevertheless, the algorithm used in case I is still considered to be more suitable for real time implementation. The main reason for this is that the computation time required for the algorithm used in case H is much longer than that for case I. A time of 44.9 seconds was required for simulation of case H in MATLAB (on a computer with an Intel® T9600 processor). However, it only took 5.2 seconds to simulate case I. The large difference in computation time can be attributed to the iterative algorithm required to solve for the ankle and subtalar displacements in case H. An additional argument which can somewhat support the adoption of the algorithm used in case I is that the study presented above is in fact biased towards case H since the model used for data generation is identical to the model structure used in the algorithm of case H. This may not be the case when the identification is carried out on an actual ankle and the performance of both these algorithms may actually be comparable in such a scenario.

4.6.3 Experimental Results

Since the algorithm used in case I is essentially a RLS algorithm without any exponential forgetting, a RLS algorithm based on an ankle model identical to that of case I was implemented and tested on the ankle rehabilitation robot. Experimental trials carried out on the robot were carried out on a single subject (adult male, 1.75m height) with ethics approval granted by The University of Auckland Human Participants Ethics Committee (Ref. 2009/480). The data collected for this test were obtained by first allowing the subject to move his foot through an arbitrary trajectory (free foot motion). Subsequently, the subject was instructed to maintain his foot in a relaxed state while the robot was used to guide the foot along a motion trajectory which predominantly involves flexion movement of the ankle and foot. A summary of the results of the parameter identification routine are shown in Table 4.6, Figure 4.12 and Figure 4.13.

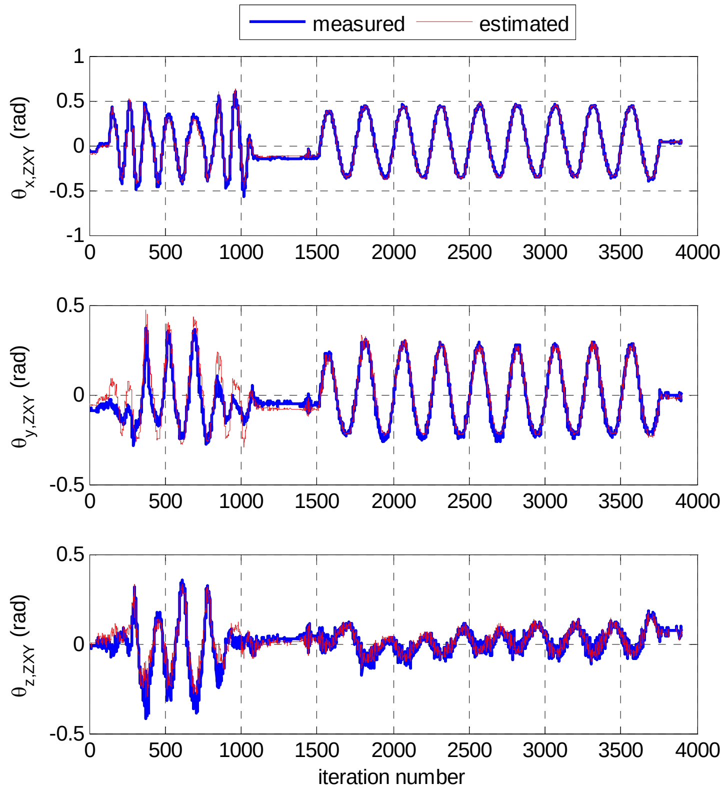

Figure 4.12: The measured and estimated ZXY Euler angles of the robot/foot orientation using the RLS algorithm. Blue lines represent the measured quantities while red lines represent the estimated values.

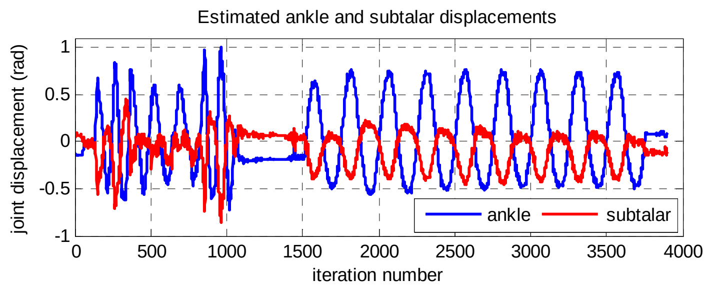

Figure 4.13: The estimated ankle (blue) and subtalar (red) joint displacements using the RLS algorithm.

Table 4.6: Results summary for the use of the conventional RLS algorithm in fitting the proposed ankle kinematic model to the experimental data.

	RLS: $\rho = \{I_4 \otimes [\theta_{x,XYZ} \quad \theta_{y,XYZ} \quad 1]\}\rho''$
$\lvert\tilde{\theta}_{x,ZXY}\rvert_{max}$	0.1248
$\lvert\tilde{\theta}_{y,ZXY}\rvert_{max}$	0.1769
$\lvert\tilde{\theta}_{z,ZXY}\rvert_{max}$	0.1475
$\hat{\theta}_{z,a}$	$0.23680\theta_{x,XYZ}$ + $0.1217\theta_{y,XYZ}$+ 0.7505
$\hat{\theta}_{y,a}$	$0.22030\theta_{x,XYZ}$ - $0.2913\theta_{y,XYZ}$ + 0.3978
$\hat{\theta}_{z,s}$	$-0.10750\theta_{x,XYZ}$ - $0.1100\theta_{y,XYZ}$ + 0.4192
$\hat{\theta}_{y,s}$	$0.00620\theta_{x,XYZ}$ + $0.2105\theta_{y,XYZ}$ + 0.6277

All units in radians

Discussion

It is clear from Table 4.6 that the estimation errors in terms of ZXY Euler angles are much larger in the experiments compared to those obtained from simulation. This can be expected since there are more error sources in the experimental setup. For instance, errors can be present in the inclinometer used to measure the pitch and roll of the robot end effector platform. Also, as the Z Euler angles are computed from the kinematic parameters of the robot and the actuator stroke lengths, they can be influenced by errors in these quantities. Lastly, unmeasured relative motion between the foot and the robot is also likely to be present since the foot is not rigidly attached on the end effector platform.

It is also apparent from the results that constant offset components of the estimated axis tilt angles are significantly different from the average values described in the literature. The effect of this is that the estimated ankle and subtalar joint displacements (as shown in Figure 4.13) had become rather large (especially for the data segment corresponding to free motion of the foot) and hence less likely to represent the true extent of displacements along the ankle and subtalar joints.

One additional limitation of the application of the conventional RLS algorithm on the ankle kinematic models with configuration dependent joint axis tilt angles is that the estimated parameters are influenced by the initial guesses used in the algorithms. It should be noted however that while the parameter estimates varied, the foot orientation estimation errors are still relatively consistent regardless of the initial conditions used. The above problem is believed to be the result of the use of a small inverse cross correlation matrix P_0 during initialisation of the estimation algorithm. The aim of this restriction was to prevent large deviations of parameter estimates from their initial/nominal values, and it was imposed after simulation runs revealed that discontinuous ankle and subtalar joint displacements estimates were obtained for small changes in measured foot orientations. Further investigation into the above phenomenon suggested that it is likely caused by utilisation of the matrix element matching approach in estimating the ankle and subtalar joint displacements when large differences exist between the achievable model orientation (determined by the assumed axis tilt angles) and the actual foot orientation. There is therefore a need to start the algorithms with a good estimate of the actual ankle and subtalar joint axis tilt angles and limit deviation from these tilt angles at all times during execution of the algorithms if the computationally efficient matrix element matching approach were to be used in the online estimation algorithms.

4.7 RLS Algorithm with Penalty on Deviation from Nominal Parameters

Preliminary results for parameter identification of the extended kinematic model using actual experimental data had suggested that the ZXY Euler angles obtained from the model foot orientation are a reasonable fit for the measured values. However, large differences between the estimated and nominal model parameters were observed. Additionally, the estimated parameters were also found to be dependent on the initial guesses used in the algorithms.

As the nominal parameters were obtained from analysis of the anatomical structure of the foot bones, it is expected that the estimated parameters will not differ too greatly from these values. To limit the deviation between estimated and nominal parameters, a modified RLS algorithm had been proposed in this work so that the objective/cost function being minimised includes a quadratic term which penalises the departure of parameters from their nominal values. This modified objective function is shown in (4.39), where N is the current iteration number of the algorithm, ρ''_{nom} is the nominal parameter vector and K is a symmetric position definite matrix which determines how severely parameter deviations will be penalised.

$$J = \sum_{k=1}^{k=N} \left[\left(\Theta_k - \widehat{\Theta}_k\right)^T \left(\Theta_k - \widehat{\Theta}_k\right) \right] + N(\rho''_N - \rho''_{nom})^T K (\rho''_N - \rho''_{nom}) \tag{4.39}$$

It is however more convenient to rewrite (4.39) as (4.40) by taking into account the linearisation of the kinematic model. Where $\Delta\Theta = \Theta - \widehat{\Theta}_{lin}$ and G is the gradient of $\widehat{\Theta}$ with respect to ρ'' that is taken about the linearisation parameters ρ''_{lin} . This relationship is expressed as (4.41), with $\Delta\widehat{\Theta} = \widehat{\Theta} - \widehat{\Theta}_{lin}$, $\Delta\rho = \rho'' - \rho''_{lin}$ and $\widehat{\Theta}_{lin} = g(\rho''_{lin}, \Theta)$.

$$J' = \sum_{k=1}^{k=N} [(\Delta\Theta_k - G_k \Delta\rho'')^T (\Delta\Theta_k - G_k \Delta\rho'')] + N(\rho''_N - \rho''_{nom})^T K (\rho''_N - \rho''_{nom}) \tag{4.40}$$

$$\widehat{\Theta} \approx g(\rho''_{lin}, \Theta) + \left. \frac{\partial \widehat{\Theta}}{\partial \rho''} \right|_{\rho''_{lin}, \Theta} (\rho'' - \rho''_{lin}) \Rightarrow \Delta\widehat{\Theta} \approx G \Delta\rho'' \tag{4.41}$$

The optimisation of J' with respect to $\Delta\rho''$ then leads to (4.42). It can be seen that this result is almost identical to that obtained from the conventional least squares problem, except for the addition of the second parameter related term (Note that $\Delta\rho''_{nom} = \rho''_{nom} - \rho''_{lin}$).

$$0 = \sum_{k=1}^{k=N} \left(-{G_k}^T \Delta\Theta_k + {G_k}^T G_k \Delta\rho''\right) + NK(\Delta\rho'' - \Delta\rho''_{nom}) \tag{4.42}$$

By augmenting gradients and measurements collected from all previous iterations, the optimal change in the model parameter is given by (4.43), where $G_{aug,k} = [{G_1}^T \ \ {G_2}^T \ \cdots \ {G_k}^T]^T$ and $\Delta\Theta_{aug,k} = [\Delta{\Theta_1}^T \ \ \Delta{\Theta_2}^T \ \cdots \ \Delta{\Theta_k}^T]^T$. It should be noted however that optimality of this solution is lost when the model is nonlinear.

$$\Delta\rho'' = \left({G_{aug,N}}^T G_{aug,N} + NK\right)^{-1}\left({G_{aug,N}}^T \Delta\Theta_{aug,N} + NK\Delta\rho''_{nom}\right) \tag{4.43}$$

A recursive algorithm for computing the solution to (4.43) at iteration k can be obtained by consideration of (4.44) and through the use of iterative update for the inverse cross correlation matrix P_k , where $P_k = \left({G_{aug,N}}^T G_{aug,N}\right)^{-1}$. The latter iterative update is identical to that used in the RLS algorithm and is shown in (4.45).

$$\left({P_k}^{-1} + kK\right)^{-1} = P_k - P_k(P_k + k^{-1}K^{-1})^{-1}P_k \tag{4.44}$$

$$P_k = \left[P_{k-1} - P_{k-1}{G_k}^T\left(I + G_k P_{k-1}{G_k}^T\right)^{-1} G_k P_{k-1}\right] \tag{4.45}$$

While the RLS algorithm stores information of previous estimation errors in the previous parameter estimate, this is difficult to accomplish with the additional penalty term. As a result, such information is stored as a separate variable μ and updated at the end of each pass of the algorithm. The modified RLS algorithm is summarised as follows:

$$\begin{aligned}
P_k &= \left[P_{k-1} - P_{k-1}{G_k}^T\left(I + G_k P_{k-1}{G_k}^T\right)^{-1} G_k P_{k-1}\right] \\
\left({P_k}^{-1} + kK\right)^{-1} &= P_k - P_k(P_k + k^{-1}K^{-1})^{-1}P_k \\
\Delta\Theta_k &= \Theta_k - g(\rho''_{lin}, \Theta_k) \\
\Delta\rho''_k &= \left({P_k}^{-1} + kK\right)^{-1}\left(\mu_{k-1} + {G_k}^T \Delta\Theta_k + K\Delta\rho''_{nom}\right) \\
\mu_k &= \mu_{k-1} + {G_k}^T \Delta\Theta_k + K\Delta\rho''_{nom} \\
\hat{\rho}''_k &= \rho''_{lin,k} + \Delta\rho''_k
\end{aligned}$$

As discussed previously, the linearisation parameter ρ''_{lin} can be updated after each pass of the RLS algorithm. In the original RLS algorithm, this is accompanied by a reset of $\Delta\rho$ variable for the next iteration, and since this variable stores information relating to previously observed errors, this data is effectively cleared. To achieve a similar effect on the above algorithm, the variable μ_{k-1} can simply be treated as zero at all times. The resulting algorithm can then be represented as:

$$\rho''_{lin,k} = \hat{\rho}''_{k-1}$$
$$P_k = \left[P_{k-1} - P_{k-1}G_k{}^T\left(I + G_kP_{k-1}G_k{}^T\right)^{-1}G_kP_{k-1}\right]$$
$$\left(P_k{}^{-1} + kK\right)^{-1} = P_k - P_k(P_k + k^{-1}K^{-1})^{-1}P_k$$
$$\Delta\Theta_k = \Theta_k - g(\rho''_{lin}, \Theta_k)$$
$$\Delta\rho''_k = \left(P_k{}^{-1} + kK\right)^{-1}\left(G_k{}^T\Delta\Theta_k + K\Delta\rho''_{nom}\right)$$
$$\hat{\rho}''_k = \rho''_{lin,k} + \Delta\rho''_k$$

4.7.1 Experimental Results

The modified RLS algorithm proposed above was also applied to the same data collected from the experimental trial discussed in the previous section. The weight matrix K had been selected so that deviation of the constant parameters from the nominal values are penalised more severely since these values should ideally be similar to the average values stated in the literature. Since little information is available on the values that should be taken by the linear coefficients, they are allowed to vary more from their nominal values (note that 0 is used as the initial guesses for these coefficients). Additionally, the modified RLS algorithm was also applied to the conventional biaxial ankle model and tested on the same experimental data. The results of these trials are summarised in Table 4.7, Figure 4.15 and Figure 4.14. Note that plots for the conventional biaxial ankle model were not shown for brevity as they appear largely similar to those shown in Figure 4.14 and Figure 4.15, except for slightly larger errors in the Z Euler angles (as indicated by the error measures shown in Table 4.7).

Table 4.7: Results summary for the use of the modified RLS algorithm in fitting the proposed ankle kinematic model to the experimental data.

	Modified RLS: $\rho = \{I_4 \otimes [\theta_{x,XYZ} \;\; \theta_{y,XYZ} \;\; 1]\}\rho$"	Modified RLS: $\rho = [\theta_{z,a} \;\; \theta_{y,a} \;\; \theta_{z,s} \;\; \theta_{y,s}]^T$
J	14.7568	16.2444
J_1	12.5997	15.2336
$\lvert\tilde{\theta}_{x,ZXY}\rvert_{max}$	0.0891	0.0825
$\lvert\tilde{\theta}_{y,ZXY}\rvert_{max}$	0.1434	0.1421
$\lvert\tilde{\theta}_{z,ZXY}\rvert_{max}$	0.1874	0.2315
$\hat{\theta}_{z,a}$	0.1123$\theta_{x,XYZ}$ + 0.2505$\theta_{y,XYZ}$ + 0.3161	0.3301
$\hat{\theta}_{y,a}$	0.4261$\theta_{x,XYZ}$ - 0.5265$\theta_{y,XYZ}$ - 0.0381	0.0309
$\hat{\theta}_{z,s}$	-0.1337$\theta_{x,XYZ}$ - 0.0526$\theta_{y,XYZ}$ + 1.0095	1.0230
$\hat{\theta}_{y,s}$	-0.1422$\theta_{x,XYZ}$ + 0.1120$\theta_{y,XYZ}$ + 0.7120	0.6713

J_1 is the first term in (4.39) and all angles are expressed in radians
$K = 0.0005 \times$ diag([1,1,10,1,1,,10,1,1,10,1,1,10]) for extended biaxial model, $K = 0.005I_4$ for conventional biaxial model.

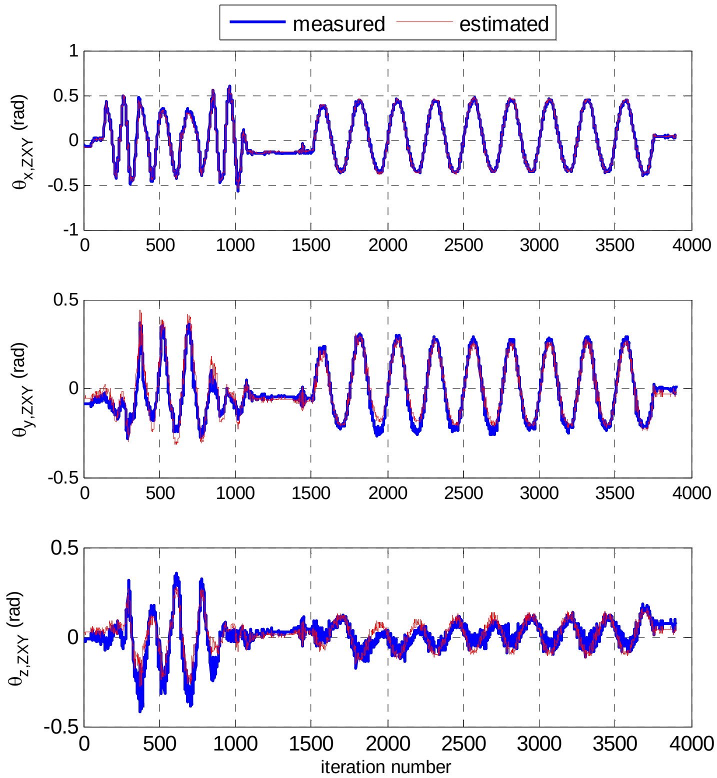

Figure 4.14: The measured and estimated ZXY Euler angles of the robot/foot orientation using the modified RLS algorithm. Blue lines represent the measured quantities while red lines represent the estimated values.

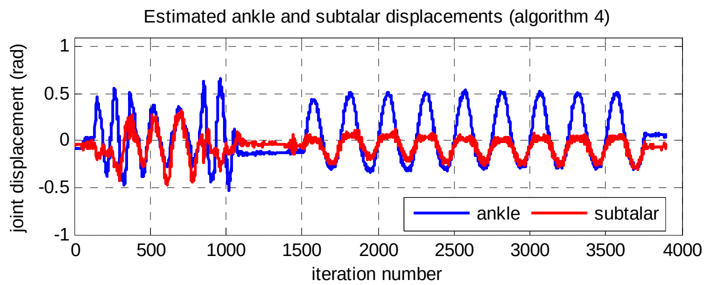

Figure 4.15: The estimated ankle (blue) and subtalar (red) joint displacements using the modified RLS algorithm.

Discussion

From these results, it can be seen that the penalty term on parameter deviation had helped reduce the deviation from the nominal parameters. It is also worth noting that this is accomplished without significant increase in the estimation errors. Since the resulting axis tilt angles in this trial take on more reasonable values, the ankle and subtalar displacements were also found to be more realistic.

In terms of consistency of the parameter estimates, it was found that use of the modified RLS algorithm had enabled the use of a much larger inverse cross correlation matrix P_0 for algorithm initialisation since the deviation of parameters is now actively restricted by the penalty term in the objective function. With a larger P_0 matrix, near identical parameter estimates were produced, even with moderate variations (0.2 rad) in the initial parameter guesses. This therefore confirms that the inconsistency in estimated parameters observed in application of the conventional RLS algorithm is indeed a result of the use of a small P_0, and that the modified algorithm is more robust to choice of initial guesses.

It is worth noting that the modified RLS algorithm worked equally well with the conventional biaxial ankle model, and produced parameter estimates which are similar in values compared to the constant offset components of the biaxial model with linearly varying axis tilt angles. While the maximum errors in the estimation of the X and Y Euler angles are marginally smaller for the algorithm based on the conventional biaxial ankle model, the error in the Z Euler angle appear to be considerably bigger, hence suggesting that more accuracy can be gained by allowing variation in the axis tilt angles. This is further supported by the fact that the error dependent term of the objective function shown in (4.39) is about 20% larger for the conventional biaxial model.

4.8 Chapter Summary

Motion of the ankle-foot structure had been modelled in this research as a series of rotations about two revolute joints (the ankle and subtalar joints). The main reason for the adoption of such a model is to obtain a relatively simple representation of ankle kinematics which can be used in the online parameter estimation of the kinematic model and also in the biomechanical modelling of the ankle-foot structure. Various online parameter identification algorithms were tested with a simplified ankle kinematic model. This model uses only the axis tilt angles as its parameters and outputs the foot orientation when given a set of ankle and subtalar joint displacements. Two methods were tested for the computation of these joint displacements and it was found that the more computationally efficient matrix element matching method produced comparable results with the optimisation based method when the foot orientations are within the range of interest and when the axis tilt angles are similar to those reported in literature. Simulation results had suggested that the RLS algorithm performs better when compared with the general EKF and LMS approaches. It had also shown that use of a constant axis tilt angle model in the estimation algorithm is inadequate when these angles are in fact changing with foot orientation.

To address the above issue, the kinematic model had been extended to allow linear variation of the tilt angles with respect to variables related to the foot orientation. Two such models were considered, one which is dependent on the ankle and subtalar joint displacements and another which is dependent on the XY components of the XYZ Euler angles. While the former extended model performed better in simulation, it is much more “expensive” to compute and since the alternative model produced acceptable estimates of the parameters and joint displacements, it was used in further testing involving data obtained from the ankle rehabilitation robot.

Application of the extended model based RLS algorithm in the kinematic model parameter estimation had resulted in axis tilt angles which are far from their nominal values. As this is not desirable, a modified RLS algorithm was proposed to penalise excessive deviation from the nominal parameters. The use of this modified RLS algorithm was found to produce parameter estimates which are more realistic with negligible compromise in the ability to fit the model outputs to the measured outputs. It was also determined that the proposed modified algorithm is equally applicable to both the conventional and extended biaxial ankle models.

Chapter 5 Computational Model of the Human Ankle

Due to significant physical interaction between the ankle rehabilitation robot and the foot of the user, it is important to obtain a better understanding of the mechanical characteristics of the human ankle and take it into consideration during design of the robot interaction controller. This chapter presents a computational ankle model developed to facilitate controller development of the ankle rehabilitation robot. To reduce its computational load, the rigid body model developed in this work is based on the biaxial ankle kinematic structure described in Chapter 4 and provides a description of the ankle mechanical characteristics through considerations of forces applied along anatomical elements around the ankle joint, which include ligaments and muscle-tendon units. The dynamics of the ankle-foot structure and its surrounding ligaments and muscle-tendon units were formulated into a state space model to facilitate simulation of the robot.

5.1 Determination of Model Complexity

Information regarding the mechanical properties of the human ankle is important for the development and evaluation of interaction control strategies for the ankle rehabilitation robot. In addition to describing the end point mechanical behaviour of the human ankle, a model with sufficient detail can also be used to estimate the forces applied to different tissues around the ankle and the reaction moments and forces exerted on the joints. This information is particularly applicable for ankle rehabilitation as injuries are typically a result of over-stretching and excessive tensioning of fibrous tissues such as ligaments and tendons. The availability of these forces can therefore facilitate the evaluation of different rehabilitation strategies. With the above in mind, the ankle model required in this research is one which can be used in controller simulations and development while also capable of providing estimates of the forces and moments acting on various ankle anatomical elements.

From the review on existing computational biomechanical ankle-foot models given in Chapter 2, it can be seen that a range of computational ankle models with varying levels of complexities had been developed by researchers to advance the understanding of foot biomechanics and to study foot related pathologies. Models belonging to the lower end of the complexity spectrum mainly involve treatment of the foot and lower limb as rigid bodies while more advanced models typically utilise finite element analysis to study stresses and strains within the soft tissues [46-48], as well as three dimensional contacts to describe the ankle kinematic behaviour [45]. While finite element models can give more accurate and realistic results, they are also more computationally intensive. The same holds for the use of three dimensional contacts to describe the kinematics between foot bones. Since this research aims to incorporate the ankle-foot dynamics into an overall robot-controller model, the use of such advanced methods will result in a system which may not be suitable for dynamic simulation over longer timescales. A three dimensional rigid body based model with relatively simple kinematic constraints is therefore considered to be a more appropriate choice for this application. Of the models discussed in Chapter 2, the model proposed by Wright et al. [43, 44] and the lower limb model available in OpenSim [78] appear to be the most fitting for this application due to their lower complexity and hence lighter computational demand. However, it should be noted that since knowledge of the forces along the ankle ligaments is important for this work and that the above models does not offer such information, a computational model had been developed specifically for this research.

5.2 Modelling of Force Elements

5.2.1 Modelling of Ligaments

The ligaments considered in the model are fibrous tissues which connect bones to bones. Ligaments are viscoelastic and can be found at various joints in the body. The main role of ligaments is to keep the articulating bones in place during motion. A ligament can be modelled as a piece of elastic string which can only apply a resistive force while in tension. The instantaneous force-length relationship of ligaments can be represented by a piecewise function shown in (5.1) [115], where F_{lig} is the tension force along the ligament and ε is the strain of the ligament. Additionally, A and B are respectively parameters used to control the magnitude and shape the exponential relationship.

$$F_{lig}(\varepsilon) = \begin{cases} 0 & \varepsilon < 0 \\ A(e^{B\varepsilon} - 1) & \varepsilon \geq 0 \end{cases} \tag{5.1}$$

The ligament force relationship shown above can produce unrealistically high tensions when the strain becomes too large. Typically, the ligaments will be damaged before they reach large forces. The use of this exponential relationship in simulation can result in an excessive increase of force for a minute increase in strain. To avoid the rapid increase of ligament forces in simulation, the exponential growth of this force is arrested when a certain force threshold is reached and replaced with a linear relationship. In this work, this threshold is set at 500N, a value which is close to the largest of the ligament failure loads reported in [115]. The actual ligament force-length relationship used in the developed model is therefore given by (5.2), where F_{thres} is the ligament force threshold (500N in this case) and ε_{crit} (5.3) is the strain required to produce F_{thres}.

$$F_{lig}(\varepsilon) = \begin{cases} 0 & \varepsilon < 0 \\ A(e^{B\varepsilon} - 1) & 0 \leq \varepsilon < \varepsilon_{crit} \\ F_{thres} + B(F_{thres} + A)(\varepsilon - \varepsilon_{crit}) & \varepsilon \geq \varepsilon_{crit} \end{cases} \tag{5.2}$$

$$\varepsilon_{crit} = \frac{1}{B}\ln\left(\frac{F_{thres}}{A} + 1\right) \tag{5.3}$$

It was also reported in literature that ligaments exhibits viscoelastic behaviour where it undergoes force relaxation after application of an initial strain. This behaviour can be modelled using a single spring in parallel to an array of serial spring-damper units. This arrangement is shown in Figure 5.1. In the case of a linear system, the sum of all the spring stiffness would yield the instantaneous stiffness while the single spring in parallel, k_3 determines the force found at steady state. The dampers therefore govern the transition between the initial and steady state forces over time.

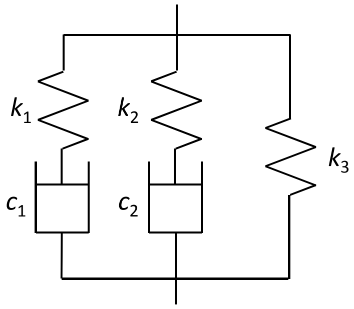

Figure 5.1: Spring damper system to model viscoelasticity of ligaments.

The work by Funk et al. has modelled the viscoelasticity of ankle ligaments using three serial spring-damper units in parallel with another spring[115]. In their formulation, three states were required to describe the ligament model. However, since many ligaments are present around the ankle and subtalar joints, the use of four state variables for each of these ligaments will lead to a large state space model. As a result, only one serial spring-damper unit is incorporated in the ligament model in this work to reduce model complexity. Using this viscoelastic model structure, the forces along the force element can be decomposed into two components, a steady state force along the single spring and a transient force along the serial spring damper unit. The total force is then merely the sum of these two forces. The relationships between these forces are shown diagrammatically in Figure 5.2. In the diagram, f_{tot} is the total force along the force element, δ_1 is the elongation along the single spring element and δ_2 is the elongation of the spring element in the serial spring-damper unit. The forces along these spring elements are respectively given by the nonlinear functions $f_1(\delta_1)$ and $f_2(\delta_2)$. The damper element is assumed to be linear with a damping coefficient of c_2 while the elongation of the damper unit is represented by δ_{2b}.

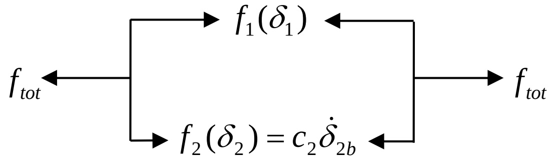

Figure 5.2: Forces found in the ligament model.

Using the above formulation, the relationships shown in (5.4) and (5.5) can be established. The state space model which describes the viscoelastic ligament force is therefore given by (5.6). It should be noted that f_1 and f_2 used in the model are simply a linearly scaled version of (5.2). Specifically, these functions can be represented as (5.7) – (5.8), with l_0 being the relaxed length of the ligament. λ_1 and λ_2 on the other hand are scaling factors which sum to unity, where a value of 0.75 has been used as the λ_1 parameter for all ligaments considered in this model.

$$f_{tot} = f_1(\delta_1) + f_2(\delta_2) = f_1(\delta_1) + c_2\dot{\delta}_{2b} \tag{5.4}$$

$$\delta_1 = \delta_2 + \delta_{2b} \tag{5.5}$$

$$\dot{\delta}_2 = \dot{\delta}_1 - \frac{1}{c_2} f_2(\delta_2) \tag{5.6}$$

$$f_1(\delta_1) = \lambda_1 F_{lig}\left(\frac{\delta_1}{l_0}\right) \tag{5.7}$$

$$f_2(\delta_2) = \lambda_2 F_{lig}\left(\frac{\delta_2}{l_0}\right) \tag{5.8}$$

5.2.2 Modelling of Muscle-Tendon Units

Skeletal muscles are tissues which contract to generate force and thus motion, while tendons are fibrous tissues which connect skeletal muscles to bones to transfer the muscle forces. As with the case of ligaments, tendons can be modelled as tension only elastic strings. However, the dynamics of the muscle is more complex, as it is an active element. The Hill based muscle model has been widely used in the literature [43, 44, 116, 117] to model muscle behaviour and was also adopted in this work. The structure of the Hill based model used to describe the muscle-tendon unit is shown in Figure 5.3. The muscle-tendon unit considered in this model consists of two components (tendon and the muscle), with the tendon component modelled as a nonlinear spring K_{SE}. The muscle component on the other hand is considered to be made up of the contractile element CE which governs the muscle's active force characteristics and the parallel element PE which determines the passive muscle behaviour. The parallel element is in turn represented as a nonlinear spring K_{PE} in series with a linear damper C_{PE}. The linear damper has been included to incorporate damping in the passive muscle behaviour and to ensure that a feasible solution is obtained in the state space model during simulation. It should also be noted that θ is the pennation angle of the muscle, which describes the angle between the direction of muscle fibres and the direction of force application along the muscle-tendon unit.

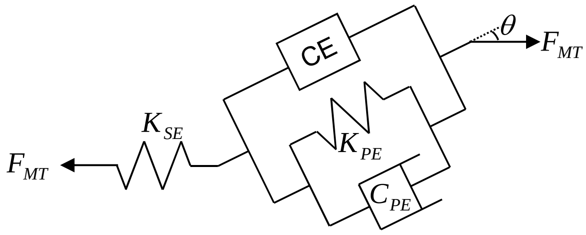

Figure 5.3: Model structure of the muscle-tendon unit.

The mathematical description of the force along the contractile element of the Hill muscle model is typically represented as (5.9). The variable A is used to denote the extent of muscle activation and can take on values between zero and unity, while the variable F_{max} is the maximum active force that can be exerted by the muscle. These variables are used to scale the product of normalised tension-length relationship, $f_{ce}(l_{ce})$ and the force-velocity relationship, $f_v(\dot{l}_{ce})$, where l_{ce} is the length of the contractile element.

$$F_{CE} = AF_{max}f_v(\dot{l}_{ce})f_{ce}(l_{ce}) \tag{5.9}$$

Additionally, the normalised tendon and parallel element force-length relationships can also be respectively represented by the functions $f_t(l_t)$ and $f_{pe}(l_{ce})$, where l_t is the tendon length. In this work, all the force-length relationships were taken to be the same as those used by default in the OpenSim software package. These functions are shown in Figure 5.4a–c and are defined through cubic spline interpolation of several known data points. In these functions, the length of the muscle/contractile element is normalised against the optimal muscle fibre length (length at which maximum active force can be produced). Although the force-length relationships used may not be exactly identical to those of the specific patient/user, the general shapes of these relationships are in line with what is typically reported in the literature [116, 118]. Consequently, they should be able to provide at least a qualitative description of the actual muscle behaviour. As the scope of this work is not to provide a patient specific ankle model, the use of these relationships can be considered acceptable. Of course, large discrepancies between the actual and model force-length relationships can still lead to significant differences in the predicted muscle forces and hence ankle motion and this is a limitation of this approach.

The force-velocity relationship of the contractile element on the other hand, is given in the form of a piecewise function shown in (5.10) [116, 117], where a_f is a parameter which is dependent on the composition of slow and fast muscle fibres in the muscle and v_{max} is the maximum contraction speed of the muscle being considered. Also, α and β are parameters used to define the force-velocity relationship when the muscle stretch velocity is positive. These parameters were chosen so that a smooth transition is possible between the two piecewise segments. They have also been selected to provide a desired limiting value for $f_v(\dot{l}_{ce})$ as the muscle velocity approaches infinity. This relationship is shown in Figure 5.4d in terms of the normalised contractile element velocity, $\dot{l}_{ce}{v_{max}}^{-1}$.

$$f_v(\dot{l}_{ce}) = \begin{cases} \frac{1+\dot{l}_{ce}{v_{max}}^{-1}}{1-\dot{l}_{ce}(a_f v_{max})^{-1}} & \dot{l}_{ce} < 0 \\ \frac{1+\alpha\dot{l}_{ce}{v_{max}}^{-1}}{1+\beta\dot{l}_{ce}{v_{max}}^{-1}} & \dot{l}_{ce} \geq 0 \end{cases} \tag{5.10}$$

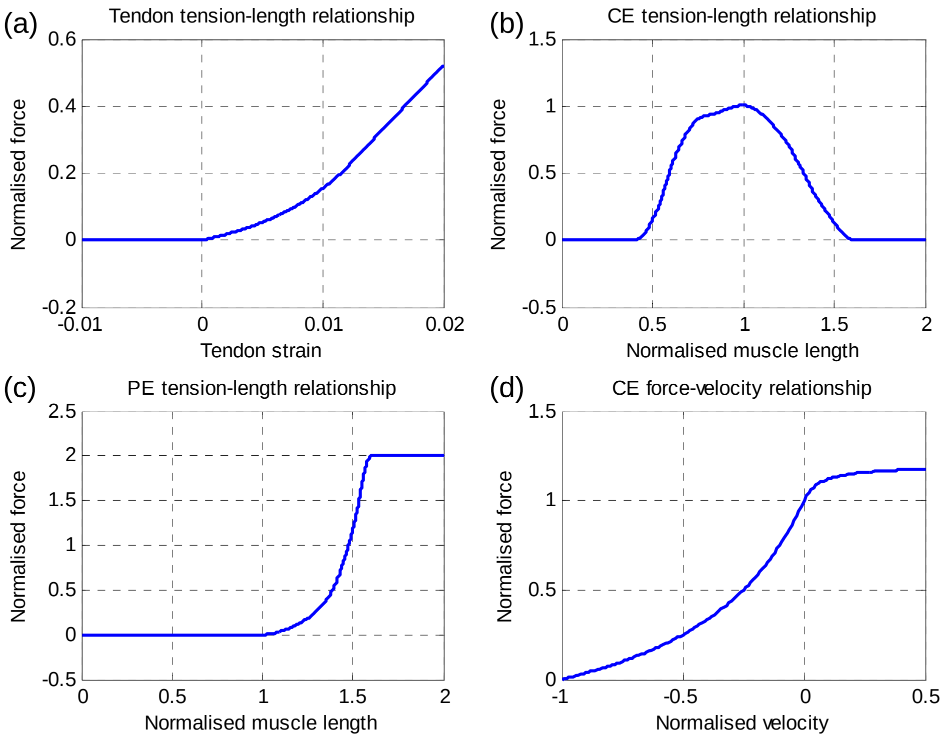

Figure 5.4: (a)Normalised tension-length relationship for the tendon. (b)Normalised tension-length relationship for the contractile element. (c)Normalised tension-length relationship for the parallel element. (d) Normalised force-velocity relationship for the contractile element (note that negative velocity signify contraction).

Using the above formulation, a state space model governing the dynamics of the muscle-tendon unit was established in this work, with the length of the contractile element as the state variable. This model can be derived by first considering the relationships between the lengths and forces of different components as shown in (5.11) and (5.12), where l_{mt} is the total length of the muscle-tendon unit and F_{MT} is the force along the muscle-tendon unit. Additionally, the force along the tendon, F_T and the force along the parallel element, F_{PE} can be represented by (5.13) and (5.14) respectively.

$$l_{mt} = l_t + l_{ce}\cos\theta \tag{5.11}$$

$$F_{MT} = F_T = (F_{CE} + F_{PE})\cos\theta \tag{5.12}$$

$$F_T = F_{max} f_t(l_t) \tag{5.13}$$

$$F_{PE} = F_{max} f_{pe}(l_{ce}) + c_{pe}\dot{l}_{ce} \tag{5.14}$$

Combination of (5.9) and (5.11) – (5.14) will then leads to (5.15), which describes how the contractile element length will evolve with time given the muscle activation and current length of the muscle-tendon unit. Although $\dot{l}_{ce}$ is not explicitly given in (5.15), unique solutions for it can be found by first expanding (5.15) into a piecewise quadratic function (5.16). The roots of the function can then be found and $\dot{l}_{ce}$ can be determined by selecting the solution with the appropriate sign. A first look at (5.15) suggests that the computation of $\dot{l}_{ce}$ will not be straight forward as this quantity is also used to determine the active segment of the piecewise function (5.10). A solution to this problem was devised in this work by taking into account the fact that $f_v(\dot{l}_{ce})$ is greater than unity for all positive contractile element velocities and less than unity when the muscle is contracting. Additionally, since A, F_{max}, f_{pe} and f_{ce} are all positive by definition, the difference between the tendon force and the static component of the muscle force as shown in (5.17) can only be positive if $\dot{l}_{ce}$ is positive and vice versa. This force difference was therefore used to ascertain the sign of $\dot{l}_{ce}$ and select the appropriate segment of (5.10) to be used in (5.16).

$$F_{max} f_t(l_{mt} - l_{ce}\cos\theta) = \left[A F_{max} f_v(\dot{l}_{ce}) f_{ce}(l_{ce}) + F_{max} f_{pe}(l_{ce}) + c_{pe}\dot{l}_{ce}\right]\cos\theta \tag{5.15}$$

$$F_{max} f_t(l_t) - \left[F_{max} f_{pe}(l_{ce}) + c_{pe}\dot{l}_{ce}\right]\cos\theta = \begin{cases} A F_{max}\cos\theta \, \frac{1+\dot{l}_{ce} v_{max}{}^{-1}}{1-\dot{l}_{ce}(a_f v_{max})^{-1}} & \tilde{F} < 0 \\ A F_{max}\cos\theta \, \frac{1+\alpha\dot{l}_{ce} v_{max}{}^{-1}}{1+\beta\dot{l}_{ce} v_{max}{}^{-1}} & \tilde{F} \geq 0 \end{cases} \tag{5.16}$$

$$\begin{aligned} \tilde{F} &= F_{max} f_t(l_t) - F_{max}\left[A f_{ce}(l_{ce}) + f_{pe}(l_{ce})\right]\cos\theta \\ &= A F_{max}\left[f_v(\dot{l}_{ce}) - 1\right] f_{ce}(l_{ce})\cos\theta + c_{pe}\dot{l}_{ce}\cos\theta \end{aligned} \tag{5.17}$$

5.3 Definition of Force Element Parameters

The lengths of ligaments and muscle-tendon units are governed by the paths that connect the origin and insertion points of the force elements. Two main factors that influence the length of such a path are the displacements of joints and locations of the insertion and origin points of the force element. While the ankle and subtalar joint displacements can be viewed as state variables in the overall ankle model, the insertion and origin points of force elements represents parameters which are specific to the anatomy of an individual. Since it is clear from previous sections that force along a ligament/muscle-tendon unit is highly dependent on its length, the definition of locations for origins and insertions of force elements is a prerequisite to the construction of a biomechanical model of the ankle.

Since all the foot bones from the calcaneus to the phalanges are treated as one rigid body in this biomechanical model, the only articulations of concern are the ankle and subtalar joints. As a result, only the main ligaments and muscle-tendon units which span these joints are considered in this model. The ligaments considered in this model are shown in Figure 5.5 while the muscles considered are similar to those used in the OpenSim software package [78] and are shown in Figure 5.6. The sites where ligaments and muscle-tendon units are attached to their respective bones can be found by referring to resources on human anatomy which provide information on the area of attachment for the force elements. In the model, the attachment sites are treated as points and the force elements are modelled as lines.

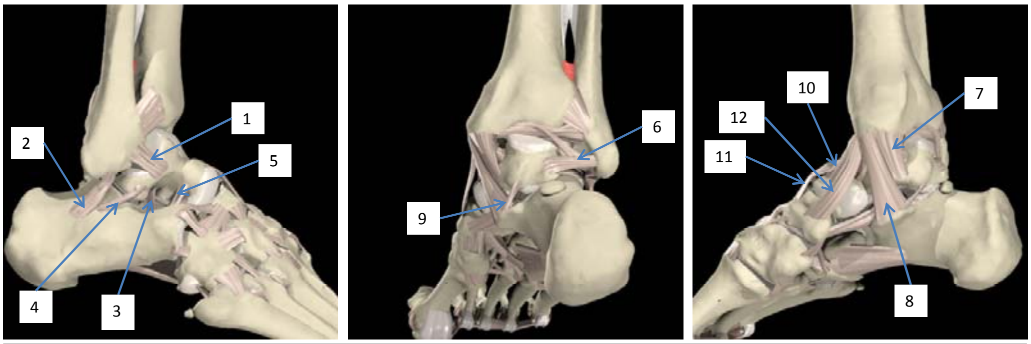

1: Anterior talofibular ligament
2: Calcaneofibular ligament
3: Interosseous talocalcaneal ligament
4: Lateral talocalcaneal ligament
5: Anterior talocalcaneal ligament
6: Posterior talofibular ligament
7: Posterior tibiotalar ligament
8: Tibiocalcaneal ligament
9: Medial talocalcaneal ligament
10: Anterior tibiotalar ligament
11: Talonavicular ligament
12: Tibionavicular ligament

Figure 5.5: ligaments of the ankle and subtalar joints considered in the ankle model. (Adapted from [119])

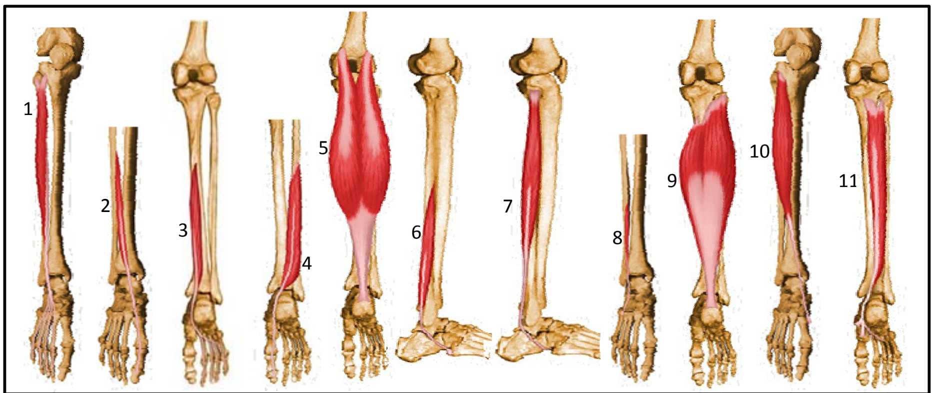

1: Extensor digitorum longus (EXTDIG)
2: Extensor hallucis longus(EXTHAL)
3: Flexor digitorum longus (FLEXDIG)
4: Flexor hallucis longus (FLEXHAL)
5: Gastrocnemius (GAS)
6: Peroneus brevis (PERBREV)
7: Peroneus longus (PERLONG)
8: Peroneus tertius (PERTERT)
9: Soleus (SOL)
10: Tibialis anterior (TIBANT)
11: Tibialis posterior (TIBPOST)

Figure 5.6: Foot muscles considered in the ankle model (Adapted from [120]).

Since the anatomical information above is typically presented through a visual medium, it must be converted to quantitative coordinates before it can be included in the model. A graphical user interface (GUI) had been developed in this research to facilitate this process. The developed GUI is capable of presenting the bone surface geometry in a graphical form and allows easy definition of the force element attachment points. In addition to the definition of the force element attachment points, the GUI developed can also be used to specify force relationship parameters of these elements. The ligament force-strain parameters used in this work are similar to those obtained from [115], while the muscle parameters used were similar to those in [78, 121]. These location and force parameters can then be stored in data files for use in the ankle model. The developed GUI therefore served as a tool to define and/or modify the force element parameters used in the biomechanical model. Screenshots of this GUI are shown in Figure 5.7.

The GUI in this work was developed in MATLAB and utilises a three-dimensional surface model of the lower limb skeleton [122] to provide the surface geometries for various bones around the ankle and subtalar joints. This data is given as a three dimensional point cloud with a connectivity matrix which designates the interconnection between these points to form the bone surface. Prior to the determination of the force element attachment points, the axes representing the ankle and subtalar joints were first defined. These axes were then used to define the joint coordinate frames. The ankle joint coordinate frame is fixed on the talus while the subtalar joint coordinate frame is anchored on the calcaneus.

Once the joint coordinate frames were established, the attachment points of the ligaments and tendons were determined by selecting points on the bone surface which corresponds to the attachment sites of the force elements shown in the anatomical resources [78, 119]. This is done with the aid of a rendered bone surface plot and the points collected were expressed in the coordinate frame of the dataset. The local coordinates of these points in their respective joint coordinate frames were subsequently computed and stored for use in the biomechanical model. Naturally, points located on the talus were expressed in the ankle joint coordinate frame and points on the remaining foot bones were given in the subtalar joint coordinates. As the tibia and fibula is assumed to be stationary, all points connected to these bones are expressed in the original dataset coordinate frame.

While it is convenient to consider the path of the force element to be a straight line connecting its origin to insertion points, this assumption can be inaccurate for longer force elements such as the muscle-tendon units since they typically wrap around other anatomical structures such as bones and ligaments. The incorporation the wrapping characteristics of muscle-tendon units are therefore important to produce more realistic simulation results. In this work, muscle wrapping is represented by requiring that the muscle path pass though certain intermediate points before ending at the insertion point. The locations of these intermediate points were again determined with reference to the anatomical resources and their local coordinates were also computed.

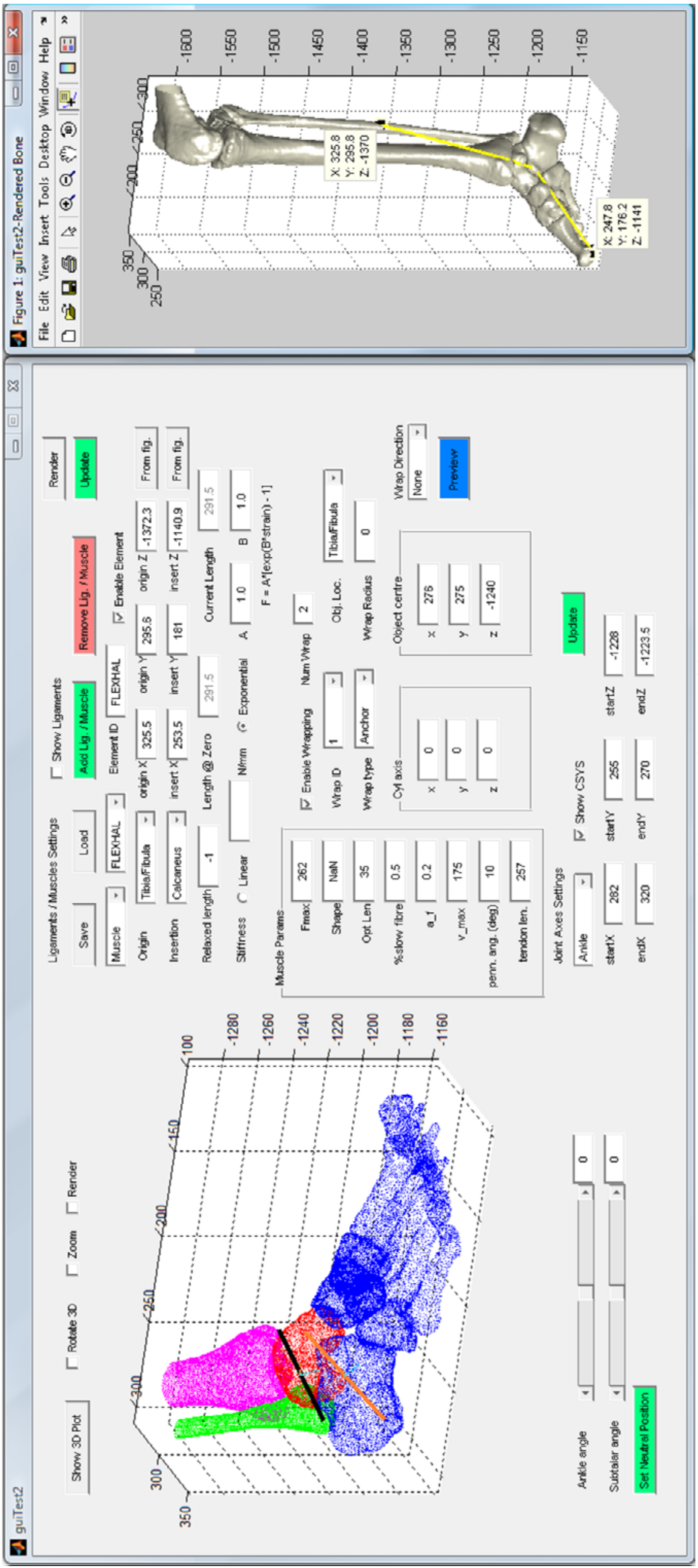

Figure 5.7: GUI developed to facilitate definition of force element parameters.

Using the defined local coordinates of the origin, insertion and intermediate points, the length of each force element can be computed using (5.18) and (5.19), where l_k is the length of the force element, n_k is the total number of attachment points, i is an index representing the attachment point being considered, $F_i = O, A, S$ is an identifier for the joint coordinate frame which corresponds to the i^{th} attachment point (where O, A and S are respectively used to denote the dataset frame, the ankle frame and the subtalar frame), T_{0F_i} is the homogeneous transformation matrix which transform the dataset coordinate frame to the corresponding joint coordinate frame; and $P_{k,F_i,i}$ is the position vector of the attachment point i for the k^{th} force element, expressed in the local coordinates of the F_i frame.

$$l_k = \sum_{i=1}^{i=n_k-1} \|v_{i,i+1}\| \tag{5.18}$$

$$v_{i,i+1} = [I_3 \quad 0_{3\times1}]\left(T_{0F_{i+1}} P_{k,F_{i+1},i+1} - T_{0F_i} P_{k,F_i,i}\right) \tag{5.19}$$

5.4 Modelling of Ankle-Foot Dynamics

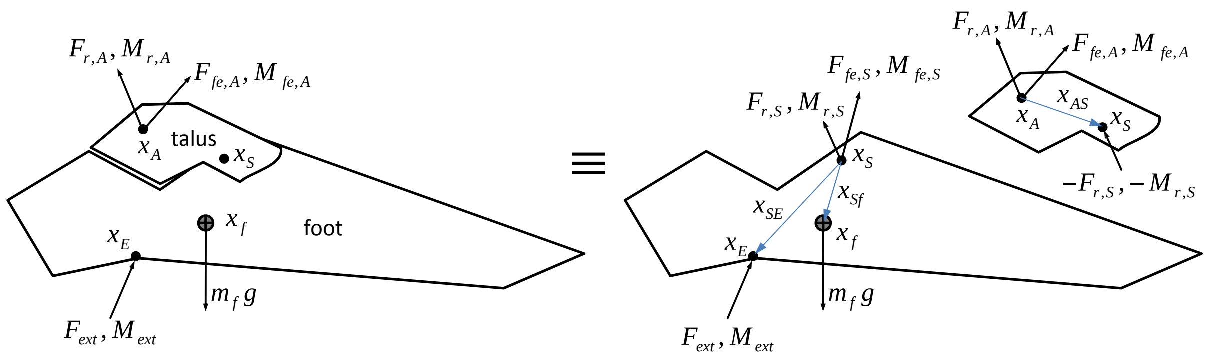

Figure 5.8: Free body diagram of the ankle-foot structure considered in the ankle model.

One of the main functions of this biomechanical model is to describe the dynamics of the ankle-foot structure under certain applied force and moment. The rigid body dynamics of the talus and foot used in this model can be summarised using the free body diagrams shown in Figure 5.8. In this diagram, $x_A \in \mathbb{R}^3$ and $x_S \in \mathbb{R}^3$ are respectively used to represent the locations of the ankle and subtalar joint centres in the global coordinate frame. The centre of mass of the foot with mass m_f is given by $x_f \in \mathbb{R}^3$ and the interaction point between the model and the external environment is represented by $x_E \in \mathbb{R}^3$. F is used to represent forces and M is used for moments, with subscripts r representing reaction force/moment, subscript fe representing the net force/moments produced by all force elements attached on the rigid body under consideration, and subscript ext denoting externally applied force/moment. Also, subscripts A and S are used to represent quantities relating to the ankle and subtalar joints. Lastly, the gravitational vector is given by g.

The rigid body dynamic equations governing the ankle-foot dynamics can be easily derived by considering the force and moment vectors shown in the free body diagrams. An inspection of Figure 5.8 shows that $F_{fe,A}$, $M_{fe,A}$, $F_{fe,S}$ and $M_{fe,S}$ (all of which are three-element column vectors) must first be found from the forces generated by these elements $f_k \in \mathbb{R}$ before they can be used in the overall dynamic equations. The relationship between these forces and moments at the talus is given by (5.20) and (5.21), where $F_{fe,A,k} \in \mathbb{R}^3$, $M_{fe,A,k} \in \mathbb{R}^3$ and $\hat{v}_{k,A,i} \in \mathbb{R}^3$ are respectively given by (5.22) – (5.24). Also, h_{norm} (5.25) is used to denote the function which normalises a given vector. Similar expressions can also be formed for $F_{fe,S} \in \mathbb{R}^3$ and $M_{fe,S} \in \mathbb{R}^3$ by replacing all variables relating to coordinate frame A with those relating to coordinate frame S.

$$F_{fe,A} = \sum_{k=1}^{k=N} F_{fe,A,k} \tag{5.20}$$

$$M_{fe,A} = \sum_{k=1}^{k=N} M_{fe,A,k} \tag{5.21}$$

$$F_{fe,A,k} = \sum_{i=1}^{i=n_k} f_k \hat{v}_{k,A,i} \tag{5.22}$$

$$M_{fe,A,k} = \sum_{i=1}^{i=n_k} \left(T_{0F_i} P_{k,F_i,i} \times f_k \hat{v}_{k,A,i} \right) \tag{5.23}$$

$$\hat{v}_{k,A,i} = \begin{cases} h_{norm}\left(v_{i,i+1}\right) & F_i = A, i = 1 \\ h_{norm}\left(v_{i,i+1}\right) - h_{norm}\left(v_{i-1,i}\right) & F_i = A, i \neq 1, i \neq n_k \\ -h_{norm}\left(v_{i-1,i}\right) & F_i = A, i = n_k \\ 0_{3\times 1} & \text{Otherwise} \end{cases} \tag{5.24}$$

$$h_{norm}(v) = \frac{v}{\|v\|} \tag{5.25}$$

The Newton Euler approach is a relatively simple method that can be used to derive the equations of motion for a system of rigid bodies [111]. In this approach, the equations of motion for each body in the system are first defined. It should be noted that due to the relatively small size of the talus, it had been assumed to be a body with negligible mass. The moment and force equations for the talus are given by (5.26) and (5.27) while those for the foot are shown in (5.28) and (5.29). Here, $I_f \in \mathbb{R}^{3\times 3}$ is the foot rotational inertia matrix in global coordinates and $\omega_f \in \mathbb{R}^3$ is the angular velocity of the foot in global coordinates. The rotational matrix is typically found in terms of some local coordinates as $I_{f,loc}$ and needs to be transformed as the orientation of the object changes. This relationship is given by $I_f = RI_{f,loc}R^T$, with R being the rotational transformation matrix describing the foot orientation.

$$F_{r,A} + F_{fe,A} - F_{r,s} = 0 \tag{5.26}$$

$$M_{r,A} + M_{fe,A} - M_{r,S} - x_{AS} \times \left(F_{r,A} + F_{fe,A}\right) = 0 \tag{5.27}$$

$$F_{r,S} + F_{fe,S} + F_{ext} + m_f g = m_f \ddot{x}_f \tag{5.28}$$

$$M_{r,S} + M_{fe,S} + M_{ext} - x_{Sf} \times \left(F_{fe,S} + F_{r,S}\right) + \left(x_{SE} - x_{Sf}\right) \times F_{ext} = I_f \dot{\omega} + \omega_f \times I_f \omega_f \tag{5.29}$$

By rearranging (5.26) and (5.28), (5.30) and (5.31) can be obtained. Substitutions of (5.30) and (5.31) into (5.27) – (5.29) and further manipulation will then lead to (5.32) and (5.33). If the ankle and subtalar joints are considered to be frictionless, the reaction moments $M_{r,A}$ and $M_{r,S}$ will only span the directions that are perpendicular to their respective revolute joints. This is to say that if the moment equations in (5.32) and (5.33) are projected back onto their corresponding revolute joints, the reaction moment terms will be eliminated, thus reducing the total number of equations to two. At first glance, it would appear that there is not enough information to solve this set of dynamic equations as there are six variables from the six accelerations and only two equations. However, certain kinematic constraints exist in the ankle model and this can be used to relate the general translational and rotational accelerations to the accelerations of the ankle and subtalar joints. These relationships can be obtained by differentiation of the global foot position x_f depicted by (5.34) – (5.36) and global angular velocity ω_f described by (5.37) – (5.39). The resulting derivatives are shown in (5.40) – (5.42). The notations of the rotational matrices in these equations are identical to those used in chapter 4. Also, $x_{AS,0}$ is used to represent the position vector (in global coordinates) from the ankle joint centre to the subtalar joint centre at the neutral orientation. Similarly, $x_{Sf,0}$ is the position vector from the subtalar joint centre to the foot centre of mass at the neutral orientation.

$$F_{r,A} = F_{r,S} - F_{fe,A} \tag{5.30}$$

$$F_{r,S} = m_f \ddot{x}_f - F_{fe,S} - F_{ext} - m_f g \tag{5.31}$$

$$\begin{aligned} M_{r,A} + M_{fe,A} + M_{fe,S} + M_{ext} + x_{AS} \times F_{fe,S} + x_{AE} \times F_{ext} + x_{Af} \times m_f g \\ = I_f \dot{\omega}_f + \omega_f \times I_f \omega_f + x_{Af} \times m_f \ddot{x}_f \end{aligned} \tag{5.32}$$

$$M_{r,S} + M_{fe,S} + M_{ext} + x_{Sf} \times m_f g + x_{SE} \times F_{ext} = I_f \dot{\omega}_f + \omega_f \times I_f \omega_f + x_{Sf} \times m_f \ddot{x}_f \tag{5.33}$$

$$x_f = x_A + R_A x_{AS,0} + R_f x_{Sf,0} \tag{5.34}$$

$$R_A = R_{0a,i} R_{x,a} {R_{0a,i}}^T \tag{5.35}$$

$$R_f = R_{0a,i} R_{x,a} {R_{as,i}}^T R_{0s,i} R_{x,s} {R_{0s,i}}^T R_{0f,i} \tag{5.36}$$

$$\omega_f = \begin{bmatrix} v_a & v_s \end{bmatrix} \begin{bmatrix} \dot{\theta}_a \\ \dot{\theta}_s \end{bmatrix} \tag{5.37}$$

$$v_a = R_{0a,i} [1 \;\; 0 \;\; 0]^T \tag{5.38}$$

$$v_s = R_{0a,i} R_{x,a} {R_{0a,i}}^T R_{0s,i} [1 \;\; 0 \;\; 0]^T \tag{5.39}$$

$$\dot{x}_f = \frac{\partial R_A}{\partial \theta_a} x_{AS,0} \dot{\theta}_a + \frac{\partial R_f}{\partial \theta_a} x_{Sf,0} \dot{\theta}_a + \frac{\partial R_f}{\partial \theta_s} x_{Sf,0} \dot{\theta}_s \tag{5.40}$$

$$\begin{aligned} \ddot{x}_f = {} & \frac{\partial R_A}{\partial \theta_a} x_{AS,0} \ddot{\theta}_a + \frac{\partial R_f}{\partial \theta_a} x_{Sf,0} \ddot{\theta}_a + \frac{\partial R_f}{\partial \theta_s} x_{Sf,0} \ddot{\theta}_s + \frac{\partial^2 R_A}{\partial {\theta_a}^2} x_{AS,0} {\dot{\theta}_a}^{\,2} + \frac{\partial^2 R_f}{\partial {\theta_a}^2} x_{Sf,0} {\dot{\theta}_a}^{\,2} \\ & + 2 \frac{\partial^2 R_f}{\partial \theta_a \theta_s} x_{Sf,0} \dot{\theta}_a \dot{\theta}_s + \frac{\partial^2 R_f}{\partial {\theta_s}^2} x_{Sf,0} {\dot{\theta}_s}^{\,2} \end{aligned} \tag{5.41}$$

$$\dot{\omega}_f = \begin{bmatrix} v_a & v_s \end{bmatrix} \begin{bmatrix} \ddot{\theta}_a \\ \ddot{\theta}_s \end{bmatrix} + \begin{bmatrix} 0_{3\times1} & \frac{\partial v_s}{\partial \theta_a} \dot{\theta}_a \end{bmatrix} \begin{bmatrix} \dot{\theta}_a \\ \dot{\theta}_s \end{bmatrix} \tag{5.42}$$

It is clear that $\ddot{x}_f$ and $\dot{\omega}_f$ can each be represented as in the form shown in (5.43) and (5.44). Substitution of these expressions into the projections of (5.32) onto v_a and (5.33) onto v_s will ultimately yield two equations and two unknowns in the form of $\ddot{\theta}_a$ and $\ddot{\theta}_s$, and can be represented by (5.45), where $\Delta_2 \in \mathbb{R}^{n_{lig}}$ is a vector of all the ligament state variables (total of n_{lig} ligaments), $L_{ce} \in \mathbb{R}^{n_{mus}}$ is a vector of all the muscle-tendon state variables(total of n_{mus} muscle-tendon units) and $\Gamma \in \mathbb{R}^{n_{mus}}$ is a vector of all the muscle activation levels. By referring to the force element dynamics equations given by (5.6) and (5.16), the time derivatives of Δ_2 and L_{ce} can also be represented as functions shown in (5.46) and (5.47). These equations therefore complete a state space model that represents the dynamics of the ankle-foot structure under certain applied force, moment and muscle activation. More specifically, the states of this model will include the ankle/subtalar displacements and velocities, as well as the ligament/muscle-tendon state variables. The inputs of this model on the other hand are the muscle activation levels and the externally applied forces and moments.

$$\ddot{x}_f = A_{xf} \begin{bmatrix} \ddot{\theta}_a \\ \ddot{\theta}_s \end{bmatrix} + b_{xf}\left(\theta_a, \theta_s, \dot{\theta}_a, \dot{\theta}_s, \Delta_2, L_{ce}, \Gamma, F_{ext}, M_{ext}\right) \tag{5.43}$$

$$\ddot{\omega}_f = A_{\omega f}\begin{bmatrix}\ddot{\theta}_a\\ \ddot{\theta}_s\end{bmatrix} + b_{\omega f}\left(\theta_a, \theta_s, \dot{\theta}_a, \dot{\theta}_s, \Delta_2, L_{ce}, \Gamma, F_{ext}, M_{ext}\right) \tag{5.44}$$

$$\begin{bmatrix}\ddot{\theta}_a\\ \ddot{\theta}_s\end{bmatrix} = f_{as}\left(\theta_a, \theta_s, \dot{\theta}_a, \dot{\theta}_s, \Delta_2, L_{ce}, \Gamma, F_{ext}, M_{ext}\right) \tag{5.45}$$

$$\dot{\Delta}_2 = f_{\Delta_2}\left(\theta_a, \theta_s, \dot{\theta}_a, \dot{\theta}_s, \Delta_2\right) \tag{5.46}$$

$$\dot{L}_{ce} = f_{L_{ce}}\left(\theta_a, \theta_s, \dot{\theta}_a, \dot{\theta}_s, L_{ce}, \Gamma\right) \tag{5.47}$$

5.5 Chapter Summary

A computational ankle model with a focus on ankle and subtalar joints was developed by considering the biomechanical characteristics of various ligaments and muscles around these joints. The model is a multi rigid body model that is more amenable for use in simulations involving longer durations. The decision to model the ligaments (which were not included in some of the existing rigid body based computational ankle models) and muscle-tendon units individually also allows the use of this model to investigate the effects of different motion trajectories on the force element tensions. The developed rigid body model had been expressed in the state space form to facilitate its use in forward dynamics simulations.

Chapter 6 Validation and Application of Ankle Model

The details relating to the computational ankle model developed in this research was presented in Chapter 5. Clearly, such a model has to be checked to ensure that it is suitable for its purpose. This chapter therefore details the validation of the developed model through comparison of the model data against experimental data obtained from literature as well as from the ankle rehabilitation robot prototype. Additionally, a sensitivity analysis of the developed model was also carried out to identify the influence of different model parameters on the interaction wrench required at the base of the foot to achieve equilibrium. Finally, to demonstrate the potential use of the resulting ankle model, the proposed model was applied in an optimisation problem formulated in this work for the selection of ankle rehabilitation trajectories which minimises a weighted sum of squares of force element tensions and joint reaction moments. Results of a simulation study using this proposed trajectory generation routine showed that differences in both performance and shape between a nominal straight line path and the optimised ankle rehabilitation trajectory can be rather significant.

6.1 Model Validation

It is important that the developed computational ankle model be compared against real clinical data to validate its ability to approximate the behaviour of the system of interest. As the ankle-foot properties are likely to vary considerably between individuals, accurate quantitative agreement of experimental and model simulation outputs should not be expected for non subject specific models. However, since the model is based on the biomechanical properties of the joints under consideration, the general trends of the model outputs should still follow those obtained from experimental studies. The focus of this section is therefore to evaluate whether the behaviour of the developed model is qualitatively comparable to observations on real human ankle-foot structures.

Several simulations involving the developed model has been carried out to allow its comparison with data available in the literature and data collected from experiments. Since an abundance of information is available on the passive moment-angular displacement relationship of the ankle, the model had been used in a “virtual experiment” to obtain this relationship. Additionally, to test the active muscle behaviour in the model, the response of the ankle foot model was recorded when certain muscle activation profiles were inputted to emulate application of flexion and inversion-eversion moments. Finally, the model was also compared with data obtained from the ankle rehabilitation robot. In this final validation trial, the forces measured by the robot were converted to appropriate moments and applied to the ankle model. The resulting motion of the ankle-foot model was then compared against the actual recorded foot motion.

6.1.1 Validation of Passive Moment-Displacement Characteristics

To approximate the passive moment-displacement relationships of the ankle under static conditions, a ramp input of external moment is applied along the *x*-axis of the global frame to simulate the scenario where external moments are being applied in the flexion direction. To minimise the contribution of damping, the ramp profile was chosen to have a small gradient. The results are shown in Figure 6.1a, while a typical ankle moment-displacement found in the literature is given in Figure 6.2. A comparison of both these graphs shows that the model does indeed produce a passive moment-displacement relationship similar to those found from experimental studies. Small moments were observed around the neutral foot orientation and these increased more rapidly as the foot moved further away from its neutral position. Another key feature of the simulated response is the higher stiffness and smaller motion range in the dorsiflexion direction when compared with those in the plantarflexion direction. This feature is also consistent with what is observed in the literature. The model was also simulated with moments being applied about the Y-Euler angle axis and the results of this is shown in Figure 6.1b. This plot suggests that the range of motion of the ankle model is in reasonable agreement with that observed in real ankles, with a greater range of motion in the inversion direction compared to the eversion direction.

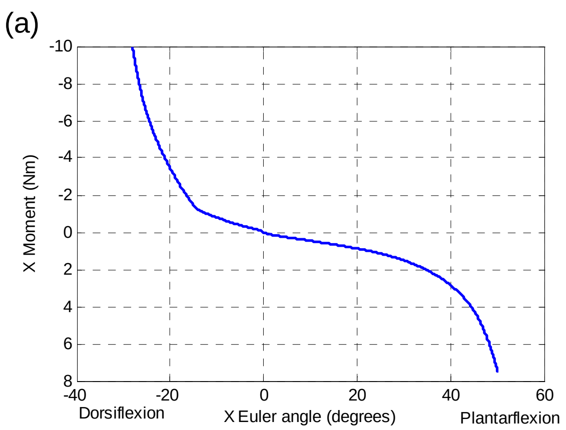

Figure 6.1: The moment-angular displacement relationship generated by applying a slow moment ramp input to the developed ankle model. Plot (a) shows the relationship for the flexion direction while plot (b) shows that for the inversion-eversion direction.

Figure removed due to third party copyright issues. Image can be accessed through Fig. 2 of [85]

Figure 6.2: Typical moment-angular displacement relationship in the flexion direction (Reproduced from[85]).

6.1.2 Simulation of Active Ankle-Foot Motion/Behaviour

The developed model has the ability to predict ankle-foot motion based on activation of different leg muscles. This feature of the model was also tested through simulations where a certain group of muscles responsible for a particular ankle-foot motion were activated to produce the corresponding foot motion. Four scenarios were considered and the resulting motions in terms of XYZ Euler angles are given in Figure 6.3. Among these simulations, case A involved the activation of plantarflexor muscles, case B involved the dorsiflexor muscles, case C involved the invertor muscles and case D involved the dorsiflexor and evertor muscles. Muscles recruited for each of these cases are shown inTable 6.1.

Table 6.1: Muscles recruited for different cases considered in simulation.

	Case A (PF)	Case B (DF)	Case C (INV & PF)	Case D (EV & DF)
Activated Muscles	FLEXDIG FLEXHAL GAS PERBREV PERLONG SOL TIBPOST	EXTDIG EXTHAL PERTERT TIBANT	TIBANT TIBPOST	EXTDIG EXTHAL PERBREV PERLONG PERTERT

Note: PF = Plantarflexion, DF = Dorsiflexion, INV = inversion, EV = Eversion.

The muscle activation signals were defined in such a way that a step activation is passed through a low pass filter prior to it being applied in the dynamic equations of the muscle-tendon units. In these simulations, the muscles were either fully activated or fully relaxed. The simulation results show that the model responses largely agreed with the expected foot behaviour, in the sense that activation of the muscles had produced the desired foot motion. For example, the steady state foot orientation observed in case A which involved activation of plantarflexor muscles had resulted in foot motion in predominantly the positive X Euler angle direction, which is equivalent to plantarflexion movement. Similar observations can also be made in the remaining three scenarios considered. Additionally, the extent of foot motion achieved with the different muscle activation patterns considered were also determined to be within the natural ankle range of motion.

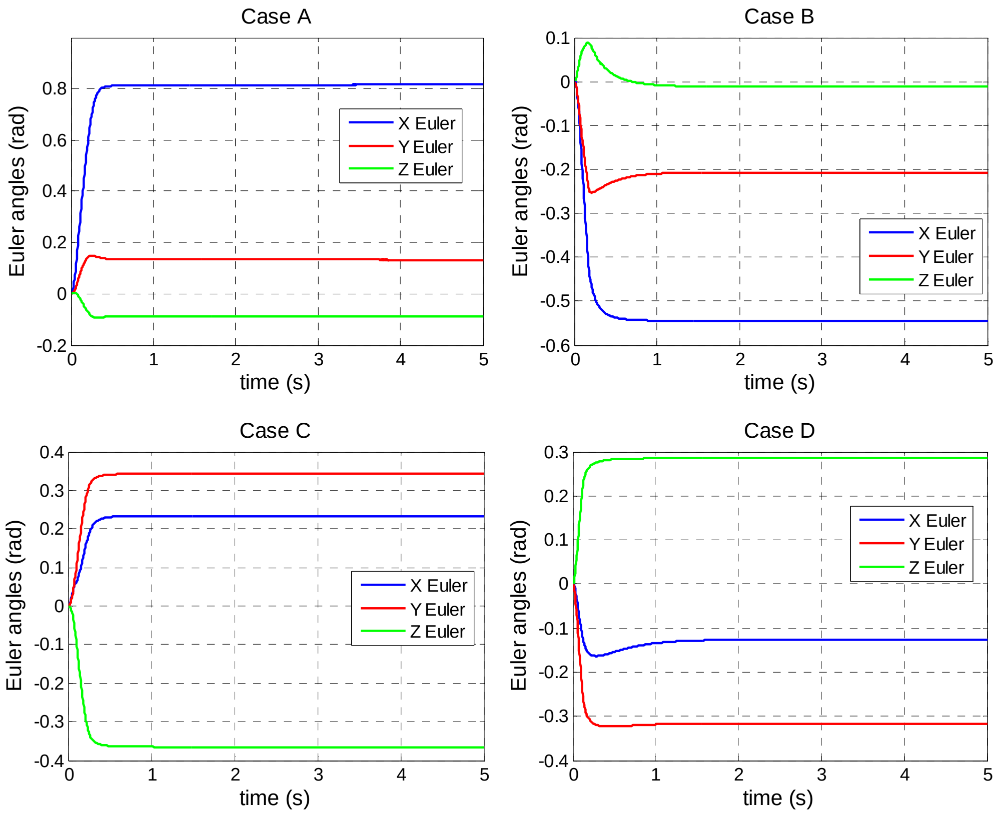

Figure 6.3: Time histories of the foot orientation in XYZ Euler angles obtained from simulations of the developed ankle model with muscle activations.

6.1.3 Comparison of Simulation and Experimental Results

The behaviour of the model was also compared with that observed in an experimental trial which involved the use of the ankle rehabilitation robot. The sole participant of this experiment is an adult male (1.75m height) with no prior ankle injuries and ethics approval had been granted by The University of Auckland Human Participants Ethics Committee (Ref. 2009/480). In the experiment, the robot was commanded to move the user's foot along certain desired path under impedance control while the user's foot is relaxed. Measurements were made on the forces applied in each actuator and the foot orientation throughout the experimental trial. The obtained data was then processed to extract the approximate moments that were applied to the ankle-foot structure. These moments were subsequently applied to the developed foot model. The resulting Euler angles of the model foot were then compared with the experimentally recorded foot Euler angles. Since the moments were not measured directly, some data processing was required to transform the raw actuator forces into moments that can be applied directly to the foot model. The details of the procedure involved in obtaining the moment are presented below.

Processing of actuator force data

The dynamic model can be considered to be made up of two parts, one which describes the rigid body dynamics of the shank and foot bones and another which describes the dynamic behaviour of the force elements. Any externally applied forces and moments at the base of the foot will only directly affect the ankle and subtalar joint accelerations but not the force element states, while the time derivatives of the force element states also have no instantaneous effects on the ankle and subtalar joint accelerations. Using this system characteristic, the external force and moment vector which is required to maintain zero joint accelerations can be easily computed from the rigid body dynamics of the ankle-foot model. In the developed model, this force and moment vector is applied at a point located at the base of the foot which is referred to as the interaction point. This point is assumed to be constant in the local subtalar coordinate frame.

When the robot prototype is used for the validation experiments, forces along the linear actuators are used to compute the effective moments applied to the ankle-foot complex. While the position of the interaction point relative to the robot can be precisely defined in a mathematical model, the same is difficult to achieve in real life. This means that there will most certainly be a positional deviation ($r_{NA} \in \mathbb{R}^3$) between the assumed and actual interaction point on the robot as shown in Figure 6.4. This deviation can cause errors between the moment component of wrenches taken about the assumed and actual interaction points. For clarity, the wrench taken about the actual interaction point will be referred to as the "actual wrench" ($w_A \in \mathbb{R}^6$) while the wrench taken about the assumed interaction point will be termed the "nominal wrench" ($w_N \in \mathbb{R}^6$). The relationship between these two wrenches is shown in (6.1), where $w = [F^T \ M^T]^T$, with $F \in \mathbb{R}^3$ being the force vector and $M \in \mathbb{R}^3$ being the moment vector. Also, I_n indicates an $n \times n$ identity matrix and $0_{m \times n}$ indicates an $m \times n$ zero matrix. Finally, $[r_{NA} \times] \in \mathbb{R}^{3\times3}$ is an anti symmetric matrix which satisfies the relationship $[r_{NA} \times]b = r_{NA} \times b$.

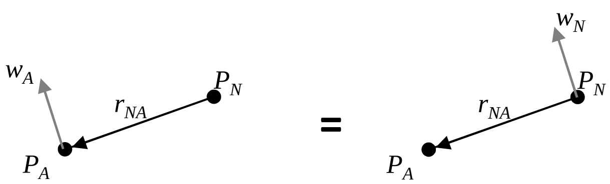

Figure 6.4: Schematic describing the nominal and actual interaction points on the robot and the equivalent wrenches applied at each of these points.

$$w_A = \begin{bmatrix} I_3 & 0_{3\times3} \\ -[r_{NA} \times] & I_3 \end{bmatrix} w_N \tag{6.1}$$

Clearly, the difference between these wrenches will become more significant when the magnitudes of the force or deviation vectors are large. As a result, if the nominal wrench is applied to the ankle model in simulation, the simulation results can differ substantially from the actual observed behaviour. To resolve the above issue, the deviation vector between the assumed and actual interaction points has to be found so that the nominal wrench can be reconciled to give the actual wrench, which is in turn used in simulation. The solution proposed in this work utilises stationary orientations observed during the experimental trials as snapshots where such reconciliations are made. By estimating the ankle and subtalar joint displacements that correspond to a stationary orientation, the ankle model can be used to establish whether a wrench applied at the interaction point on the foot will yield zero joint accelerations. The rigid body dynamics in the ankle model can be written as (6.2), with $A \in \mathbb{R}^{2\times 2}$ being the matrix coefficient of the joint accelerations, $N \in \mathbb{R}^2$ a vector containing information relating to force effects due to gravity, damping and resistances of force elements and $J \in \mathbb{R}^{2\times 6}$ a matrix which transforms the applied external wrench into the generalised forces considered in this equation. The minimal norm solution of a wrench that can result in zero joint accelerations can be obtained through (6.3), where $J^+ \in \mathbb{R}^{6\times 2}$ is used to denote the pseudo-inverse of J.

$$A\ddot{\theta} + N + Jw_A = 0 \tag{6.2}$$

$$w_{A,1} = J^+ N \tag{6.3}$$

Since the model is subjected to a six degree of freedom wrench but has only two degrees of freedom in motion, it is redundantly actuated. There is therefore a family of wrenches which can satisfy (6.2). This family is represented by (6.4), where $V_1 \in \mathbb{R}^{6\times 2}$ is a matrix of wrench bases which influences the joint accelerations and $V_0 \in \mathbb{R}^{6\times 4}$ is a matrix of wrench bases which do not. Naturally, $\eta_1 \in \mathbb{R}^2$ and $\eta_0 \in \mathbb{R}^4$ are vectors representing components of the wrench along these bases. It should be noted that $V_1\eta_1 = w_{A,1}$ is readily found in (6.3).

$$w_A = V_1\eta_1 + V_0\eta_0 \tag{6.4}$$

The actual wrench being applied can then be considered a member of this family which is consistent with the nominal wrench. In other words, the actual wrench will need to have an identical force component as the nominal wrench. Additionally, any difference in the moment component will need to be accounted for by a cross product between the negative deviation vector and the force component. In other words, the difference in moment will have to be orthogonal to the force vector. These conditions are stated in (6.5) and (6.6) respectively and when combined results in a system of simultaneous equations with four variables (three equations from (6.5) and one equation from (6.6)). Solution of this set of equations will yield η_0, and hence completes the description of w_A.

$$[I_3 \quad 0_{3\times 3}](V_1\eta_1 + V_0\eta_0) = [I_3 \quad 0_{3\times 3}]w_N \tag{6.5}$$

$$[0_{3\times3} \quad I_3](V_1\eta_1 + V_0\eta_0 - w_N) = \Delta M = -[r_{NA}\times]F_N$$
$$\{[0_{3\times3} \quad I_3](V_1\eta_1 + V_0\eta_0 - w_N)\}^T[I_3 \quad 0_{3\times3}]w_N = 0$$
$$w_N{}^T\begin{bmatrix}0_{3\times3} & I_3\\ 0_{3\times3} & 0_{3\times3}\end{bmatrix}(V_1\eta_1 + V_0\eta_0 - w_N) = 0 \tag{6.6}$$

After obtaining the actual wrench, the candidate solution for the deviation vector r_{NA} can be found by considering the difference in moment and the applied force. This candidate solution is parameterised by γ as shown in (6.7) since it cannot be uniquely defined. The possible solutions for (6.7) can be visualised as the dashed line in Figure 6.5.

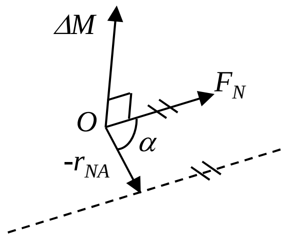

Figure 6.5: Possible solutions of r_{NA} includes all vectors that connects point O and any other point on the dashed line (which is parallel to the force vector F_N).

$$\Delta M = -[r_{NA}\times]F_N$$
$$\|\Delta M\| = \|r_{NA}\|\|F_N\|\sin\alpha\,, \quad \alpha = \frac{\pi}{2} - \tan^{-1}\gamma$$
$$\|\Delta M\| = \|r_{NA}\|\|F_N\|\cos(\tan^{-1}\gamma)$$
$$\|r_{NA}\| = \frac{\|\Delta M\|\sqrt{1+\gamma^2}}{\|F_N\|}$$
$$\frac{-r_{NA}}{\|r_{NA}\|} = \frac{1}{\sqrt{1+\gamma^2}}\left[\gamma\frac{F_N}{\|F_N\|} + \frac{F_N}{\|F_N\|}\times\frac{\Delta M}{\|\Delta M\|}\right]$$
$$-r_{NA} = \frac{\|\Delta M\|}{\|F_N\|}\left[\gamma\frac{F_N}{\|F_N\|} + \frac{F_N}{\|F_N\|}\times\frac{\Delta M}{\|\Delta M\|}\right] \tag{6.7}$$

By assuming that the deviation vector is constant in the local end effector coordinate frame, the rotational transformation matrix can be used to find the local deviation of the actual interaction point from its assumed position. Since the foot is placed flat on the end effector, it can also be assumed that the interaction point does not deviate in the vertical direction of the end effector. This condition can then be used to identify a unique solution for the deviation vector.

Simulation of the ankle model using wrenches adjusted by the approach discussed above continued to produce large differences between the observed and simulated outcomes. Closer inspection of the simulated system revealed that the effective moment generated by a force applied at the interaction point varied considerably with foot orientation. This means that differences in the simulated and observed orientations can lead to further discrepancies in terms of moments applied at the ankle and subtalar joints. This is particularly the case when large forces are applied at the interaction point. The model can therefore be subjected to vastly different moments in simulation compared to that applied during the real experiment.

To minimize the effect of orientation discrepancies on the moments applied to the joints, the force applied at the interaction point should ideally be made zero. However, if the force components are simply ignored, there would be large inconsistencies between the wrench applied to the model and the wrench actually experienced by the foot. A simplifying assumption can be made to make the wrench applied at the interaction point more indicative of the measured wrench while at the same time eliminating its dependency on the simulated platform orientation. This assumption requires that there exists a point on the foot (here referred to as the ankle centre, C_A) where the application of a force will produce little or no impact on the moments applied to the ankle and subtalar joints. This can be an acceptable assumption if the centres of both ankle and subtalar joints coincide or are closely located. It should be noted that the ankle centre is also assumed to be stationary in the foot coordinate frame. By taking the effective wrench about this ankle centre, the force component will have minimal influence on joint accelerations and can therefore be ignored. What remains is therefore the moment applied at the ankle centre, which can be directly transferred onto the foot interaction point.

The robot's generalised coordinates are the XYZ Euler angles and the generalised forces are moments along these axes taken about a nominal centre of rotation C_R. The wrench acting at the robot's nominal centre of rotation can be easily calculated and can be transformed into a wrench at the "actual" ankle centre, C_A through the use of (6.8). As with the previous scenario involving the actual and nominal interaction points, location of the ankle centre relative to the robot nominal centre of rotation, $r_{RA} \in \mathbb{R}^3$, is not known and once again a similar procedure is used to estimate the location of this point. The problem being considered is represented graphically in Figure 6.6.

$$w_A = \begin{bmatrix} I_3 & 0_{3\times3} \\ -[r_{RA}\times] & I_3 \end{bmatrix} w_R \tag{6.8}$$

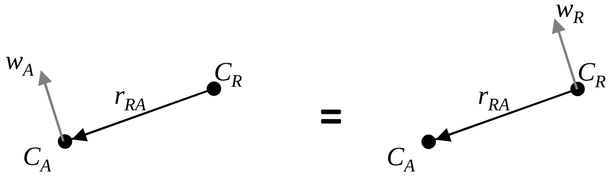

Figure 6.6: Schematic describing the nominal and actual centres of rotation of the ankle and the equivalent wrenches applied at each of these points.

The ankle model was also used here to obtain a zero-force wrench at the interaction point that can maintain equilibrium at the observed stationary orientation, thus leading to the relationship shown in (6.9).

$$[I_3 \quad 0_{3\times3}](V_1\eta_1 + V_0\eta_0) = 0_{3\times1} \tag{6.9}$$

Finally, the same orthogonality condition between the difference in moment and the overall force vector also holds. This can be represented by (6.10) and (6.11).

$$\Delta M = -[r_{RA} \times]F_R \tag{6.10}$$

$$\begin{gathered} \{[0_{3\times3} \quad I_3](V_1\eta_1 + V_0\eta_0 - w_R)\}^T [I_3 \quad 0_{3\times3}]w_R = 0 \\ {w_R}^T \begin{bmatrix} 0_{3\times3} & I_3 \\ 0_{3\times3} & 0_{3\times3} \end{bmatrix} (V_1\eta_1 + V_0\eta_0 - w_R) = 0 \end{gathered} \tag{6.11}$$

Solution of (6.9) and (6.11) will then fully define the wrench applied about the ankle centre and a similar procedure can be used to extract the deviation vector r_{RA}. To obtain a unique solution for r_{RA}, a similar condition as discussed previously can be used. Alternatively, if the vertical height of the ankle joint in the ankle used in the experiments can be estimated, say from observation of bony landmarks, a desired vertical offset for the local deviation vector can be calculated and used as the additional condition to be satisfied in the resolution of $\gamma \in \mathbb{R}$ (this alternative approach had been used to produce the simulation results presented below). Upon the solution of r_{RA}, wrenches computed about the robot's nominal centre of rotation w_R can be easily converted through (6.8) to the modified wrench that can be used in the model simulation.

Results

The ankle-foot model was simulated with the moments obtained via the procedures described in the previous section as inputs. The results of this simulation are shown in Figure 6.7. A comparison of the XYZ Euler angles obtained from measurement (blue lines) and simulation (red lines) are shown in Figure 6.7a, while the pure moments applied to the system are shown in Figure 6.7b.

It can be seen from the Figure 6.7a that rather large differences can be found between the two sets of Euler angles. Having said that however, the two sets of values can still be considered to be of the same order of magnitude and have a somewhat similar shape. The largest discrepancies in the X and Y Euler angles are observed at the start of the simulation, and this could be caused by frictions in the three degrees of freedom rotary joints located at the end of each robot actuator. The main indication for this is the fact that the measured X and Y Euler angles stayed rather constant in the measured data even as the X and Y moments increased gently from their initial levels. This suggests that frictions in the joints must had been impeding motion of the end effector and hence the user's foot. Additionally, the peaks of the measured Euler angles also appear to lag behind those of the applied moment, and this could once again be caused by the presence of friction as the direction of motion changes. Another notable difference in the measured and simulated data was the Z Euler angle displacement, where the simulated values were far larger in the internal rotation direction.

This could be caused by differences in kinematic constraints between the user and the model, as well as the larger magnitude of simulated inversion motion, which also influences internal rotation due to their coupling at the subtalar joint. Certainly, some of the errors can also be attributed to the fact that the model used was not customised to the user's ankle characteristics such as ankle and subtalar joint orientations as well as attachment points and properties of ligaments/tendons. Furthermore, parasitic motion between the foot and the end effector could also lead to variations in the modelled and measured data. Despite the presence of experimental errors and non subject specific nature of the model, qualitative agreement between the model and experimental data can still be observed. As a result, the developed model does appear to be able to give a reasonable description of ankle behaviour.

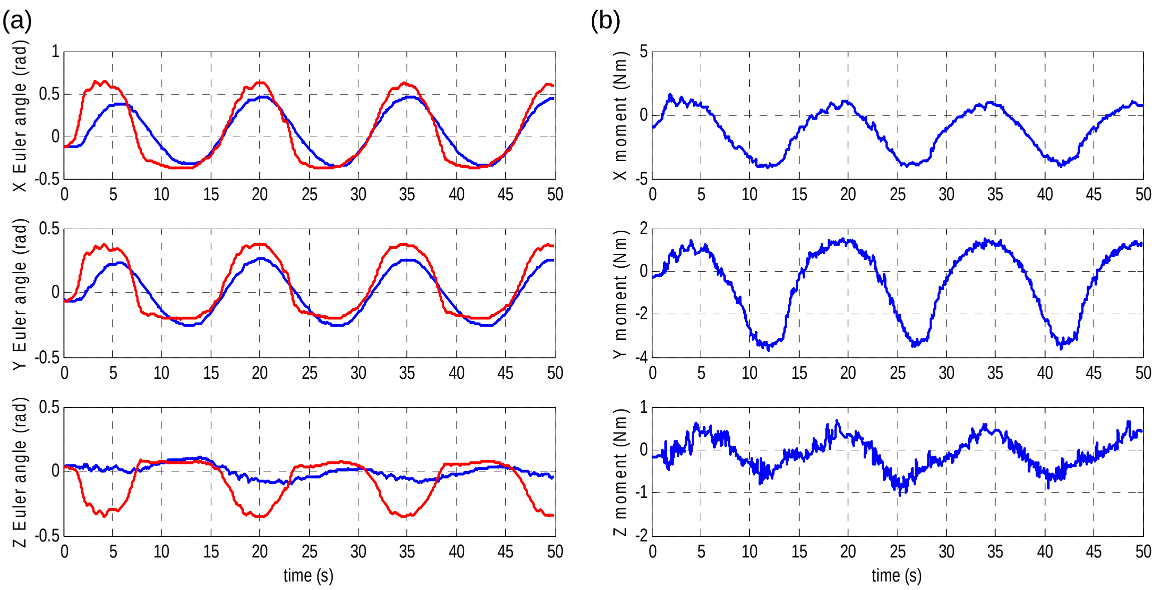

Figure 6.7: (a) Comparison of actual (blue) and simulated (red) foot orientations in terms of XYZ Euler angles. (b) Moments applied at the interaction point.

6.2 Sensitivity Analysis

Sensitivity analysis had been carried out to evaluate the robustness of the model with respect to changes in the model parameters. In order to limit the computational complexity of the problem, only the static behaviour of the model was analysed. As a result, model parameters which do not influence the static force and moment response of the model were excluded, thus leaving each ligament with three parameters (relaxed length of ligament, coefficients *A* and *B* used in the tension-strain relationship) and each muscle-tendon unit with four parameters (maximum muscle force, tendon slack length, optimal muscle fibre length and pennation angle of the muscle fibres).

In this study, 2000 sets of model parameters were obtained by randomly varying the model parameters within 5% of their respective nominal values. The minimal norm forces and moments required at the interaction point to maintain zero ankle and subtalar joint accelerations were then computed for each of these parameter sets at a particular foot configuration while all muscle activations were kept at zero (i.e. the foot is passively held in place with the applied forces and moments). The analysis was carried out at two different foot configurations, one where the foot is placed in a plantarflexed, inverted and adducted orientation ($\theta_a = 30°$, $\theta_s = 20°$), and another which placed the foot in a dorsiflexed, everted and abducted orientation ($\theta_a = -30°$, $\theta_s = -20°$).

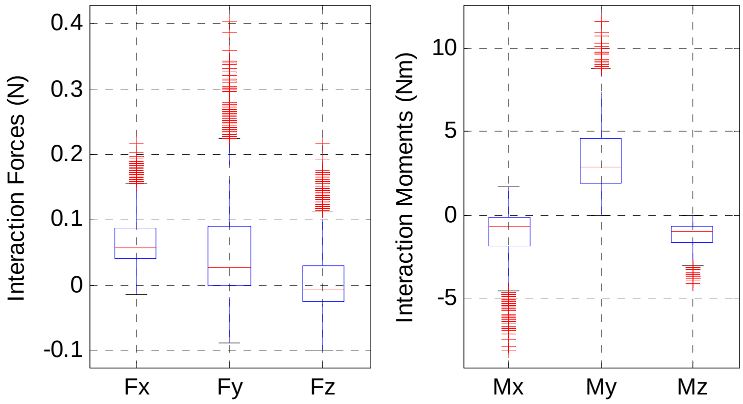

Figure 6.8: Box plots of the minimal norm interaction forces and moments computed for a variety of randomly selected ankle model parameters. The foot configuration is fixed at $\theta_a = 30°$, $\theta_s = 20°$ and muscle activations are set at zero. The values of the interaction forces and moments calculated for the nominal model parameters are F_x = 0.03N, F_y = 0N, F_z = 0.02N, M_x = -0.07Nm, M_y = 1.61Nm, M_z = -0.56Nm.

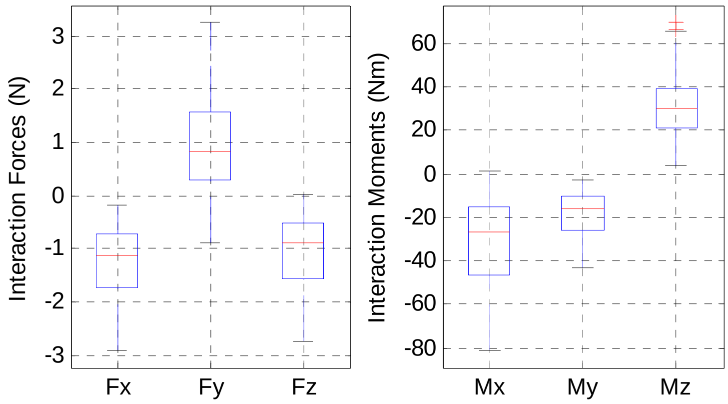

Figure 6.9: Box plots of the minimal norm interaction forces and moments computed for a variety of randomly selected ankle model parameters. The foot configuration is fixed at $\theta_a = -30°$, $\theta_s = -20°$ and muscle activations are set at zero. The values of the interaction forces and moments calculated for the nominal model parameters are F_x = -0.89N, F_y = 0.65N, F_z = -0.74N, M_x = -21.92Nm, M_y = -13.03Nm, M_z = 22.25Nm.

The results obtained from these analyses are presented in the box plots shown in Figure 6.8 and Figure 6.9. The results show that a large range of forces and moments can be observed when the model parameters are varied. However, it can be seen that the median values of these forces and moments are still reasonably similar to those obtained by applying the nominal model parameters. The large range observed in this study can be mainly attributed to variations in the ligament and tendon rest lengths due to the fact that their tension-length characteristics are governed by exponential functions. As a result, small changes in these rest lengths can potentially lead to large shifts in the force element tension, which in turn affects the level of resistive moments applied at the ankle and subtalar joints.

Further insights into the influence of individual parameters on the overall model behaviour can be obtained by computing the sensitivity gradient of the model. This sensitivity gradient is expressed in the form of a matrix and can be obtained by computing the ratio between the percentage change in the interaction wrench and the percentage change in a single model parameter. Clearly, a large ratio indicates that the particular model output is sensitive to changes in the model parameter being considered. The resulting sensitivity gradient matrix can therefore be sorted according to the magnitude of the matrix elements to determine the model parameters which have the most bearing on the interaction wrench around the considered conditions. The three most influential model parameters (in terms of interaction wrench sensitivity) are shown in Table 6.2 for each element of the interaction wrench, as well as for each of the two foot configurations considered in this study. Additionally, each element of the computed wrench is also plotted against the model parameter which is it most sensitive towards. The plots for both scenarios considered in this study are shown in Figure 6.10 and Figure 6.11.

Table 6.2: The three most influential model parameters (in terms of sensitivity) for each element of the interaction wrenches obtained from the two test scenarios.

		$\theta_a = 30°, \theta_s = 20°$			$\theta_a = -30°, \theta_s = -20°$		
	Rank	1	2	3	1	2	3
F_x	Sensitivity gradient	0.25	-0.22	0.12	-25.09	-6.18	-3.33
	Variable	$l_{lig0,CFL}$	$l_{tend0,PERLONG}$	$l_{tend0,EXTDIG}$	$l_{tend0,SOL}$	$l_{tend0,TIBPOST}$	$l_{opt,SOL}$
F_y	Sensitivity gradient	-16.99	13.20	-11.41	-44.364	-12.35	8.57
	Variable	$l_{tend0,PERLONG}$	$l_{tend0,EXTDIG}$	$l_{tend0,PERBREV}$	$l_{tend0,SOL}$	$l_{lig0,ATCL}$	$l_{lig0,ITCL}$
F_z	Sensitivity gradient	0.74	0.52	-0.35	-31.64	-5.68	-4.40
	Variable	$l_{tend0,PERLONG}$	$l_{tend0,EXTDIG}$	$l_{lig0,CFL}$	$l_{tend0,SOL}$	$l_{lig0,ATCL}$	$l_{tend0,TIBPOST}$
M_x	Sensitivity gradient	-4.24	4.22	-3.25	-31.95	-5.84	-4.31
	Variable	$l_{tend0,PERLONG}$	$l_{tend0,EXTDIG}$	$l_{tend0,PERBREV}$	$l_{tend0,SOL}$	$l_{lig0,ATCL}$	$l_{tend0,TIBPOST}$
M_y	Sensitivity gradient	0.26	0.15	0.14	-26.21	-5.87	-3.47
	Variable	$l_{tend0,PERLONG}$	$l_{lig0,CFL}$	$l_{lig0,TaNL}$	$l_{tend0,SOL}$	$l_{tend0,TIBPOST}$	$l_{opt,SOL}$
M_z	Sensitivity gradient	0.26	0.25	0.18	-16.86	-8.42	-7.44
	Variable	$l_{tend0,PERLONG}$	$l_{lig0,CFL}$	$l_{lig0,TaNL}$	$l_{tend0,SOL}$	$l_{tend0,TIBPOST}$	$l_{lig0,ITCL}$

l_{lig0} = ligament rest length, l_{tend0} = tendon rest length, l_{opt} = optimal fibre length

An inspection of Table 6.2 shows that the most influential variables are exclusively the ligament and tendon rest lengths, thus justifying the earlier attribution of the large force and moment variations to these variables. It can also be seen from the Table 6.2 that changes in tendons of the peroneus longus and extensor digitorum longus muscles, as well as the calcaneofibular ligament appear to contribute most to changes in ankle resistive moments when the foot is supinated. On the other hand, changes in tendon of the soleus, the tendon of the tibialis posterior and the anterior talocalcaneal ligament appears to contribute most to changes in ankle resistive moments when the foot is pronated. Figure 6.10 and Figure 6.11 also suggest that the sensitivities of the wrench elements towards these model parameters are rather nonlinear, with seemingly bigger changes when the rest lengths are reduced. This is as expected since shortening of the relaxed lengths will lead to higher force element tensions, which will ultimately result in larger resistive moments and reaction forces.

The sensitivity results indicate that the model output is highly dependent on the rest lengths of tendons and ligaments. The determination of such lengths in practice is clearly important to permit more accurate results. However, such a task is rather challenging and is anticipated to involve the use of medical imaging techniques whereby the appearance of the ligament or tendon of interest is monitored at various foot orientations to determine whether it is in tension. This can then allow the identification of the corresponding ligament/tendon rest length.

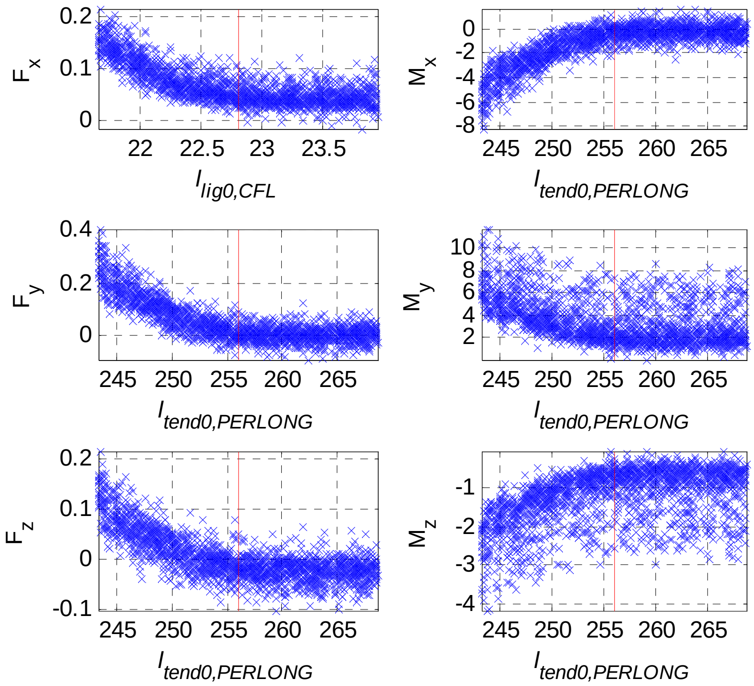

Figure 6.10: Scatter plots of different elements of the interaction wrench against their most influential model parameters when the foot is in supination. The vertical red lines are used to mark the nominal model parameters.

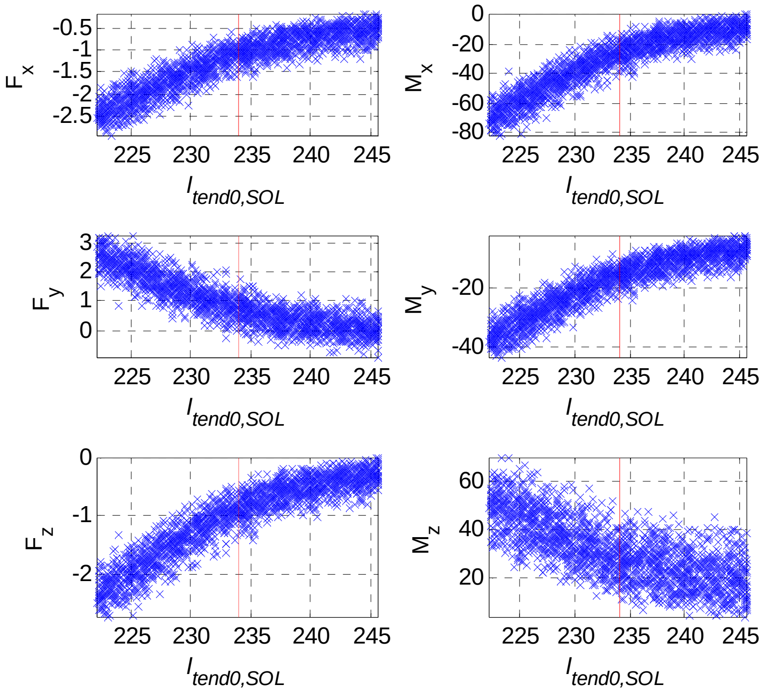

Figure 6.11: Scatter plots of different elements of the interaction wrench against their most influential model parameters when the foot is in pronation. The vertical red lines are used to mark the nominal model parameters.

6.3 Rehabilitation Trajectory Generation

Reference trajectory in rehabilitation robots is typically that of a predefined motion path which corresponds to limb trajectories encountered during activities of daily living. This motion trajectory is then altered during the operation of the robot through application of impedance or compliance control strategies to maintain a certain relationship between the user-robot interaction forces and the motion tracking error. More advanced trajectory generation strategies also utilises behaviour learnt from observing the interaction between therapists and patients [123], or from consideration of healthy limb movements in hemiplegic patients [124]. However, it appears that little work had been done to generate rehabilitation trajectories from biomechanical models of the musculoskeletal system, particularly in the area of ankle rehabilitation.

One of the main motivations for developing a biomechanical model of the ankle that takes into account actions of individual ligaments and muscle-tendon units instead of lumping these into a single resistive moment-joint displacement relationship is that it can be used to provide an indication of the forces along such force elements. This information can be used to analyse how different motion trajectories influence tensions in the force elements. A potential application of the biomechanical model, apart from its use in controller simulation, is in the evaluation of rehabilitation trajectories. As ankle sprains are caused by excessive tensioning of ligaments, forces along weaker ligaments should be kept low to avoid any injuries. Another quantity of interest is the reaction moments applied at the ankle joint. Since the tibia and fibula are held together by ligaments instead of being rigidly fused, the assumption that the ankle joint can be treated as a rigidly fixed revolute joint may become invalid when large moments are applied in directions perpendicular to the joint axis. As a result, large reaction moments at the ankle joint can also be interpreted as an increased likelihood of joint dislocation. It can be seen from the above discussion that suitability of different rehabilitation trajectories can be evaluated by investigating the force element tensions and joint reaction moments associated with them. Such information can then be incorporated into a cost function to allow easier comparison and optimisation methods can also be used to improve the "performance" of a given nominal trajectory.

6.3.1 Formulation of Optimisation Problem

To simplify the optimisation problem, the rehabilitation trajectory was defined using cubic splines rather than allowing the trajectory to take the form of an arbitrary function. This means that the trajectories considered in this work are parameterised by several key points on the trajectory. Instead of specifying the ankle or subtalar displacement as a function of the other, a common independent variable λ is used to define the cubic splines representing each of the ankle and subtalar displacements. The advantage of this approach is that there is no restriction on the trajectory so that there is only a one-to-one mapping between the ankle and subtalar joints. This formulation is shown in more detail in (6.12) – (6.19), where $f_{ij}(\lambda)$ are cubic functions used to represent the value of the ankle or subtalar displacements at a given value of λ, $i = a, s$ is used to denote the ankle or subtalar trajectory and $j = 1, \dots, N$ is an index of the cubic spline segment used to define the trajectory. Also, c_{ijk} are constant scalar coefficients of the k^{th} power term in the cubic functions that can be obtained by solving (6.16) – (6.19) simultaneously for the corresponding $f_{ij}(\lambda)$. These conditions basically require that the trajectory be continuous up to its first derivative. Additionally, it is also required that the gradient at any data point located between two other data points be parallel to a straight line connecting these two outer data points. The reason for this is to ensure that the trajectory will not deviate too far from the general direction of travel.

$$\theta_a = f_a(\lambda) \tag{6.12}$$

$$\theta_s = f_s(\lambda) \tag{6.13}$$

$$f_i(\lambda) = \begin{cases} f_{i1}(\lambda) & \lambda_0 \le \lambda < \lambda_1 \\ \vdots & \\ f_{ij}(\lambda) & \lambda_{j-1} \le \lambda < \lambda_j \\ \vdots & \\ f_{iN}(\lambda) & \lambda_{N-1} \le \lambda < \lambda_N \end{cases} \tag{6.14}$$

$$f_{ij}(\lambda) = c_{ij0} + c_{ij1}\lambda + c_{ij2}\lambda^2 + c_{ij3}\lambda^3 \tag{6.15}$$

Where:

$$f_{ij}(\lambda_{j-1}) = p_{i,j-1} \tag{6.16}$$

$$f_{ij}(\lambda_j) = p_{i,j} \tag{6.17}$$

$$\frac{df_{ij}(\lambda_{j-1})}{d\lambda} = \begin{cases} \frac{p_{i,N}-p_{i,0}}{\lambda_N-\lambda_0} & j = 1 \\ \frac{p_{i,j}-p_{i,j-2}}{\lambda_j-\lambda_{j-2}} & 1 < j \leq N \end{cases} \tag{6.18}$$

$$\frac{df_{ij}(\lambda_j)}{d\lambda} = \begin{cases} \frac{p_{i,j+1}-p_{i,j-1}}{\lambda_{j+1}-\lambda_{j-1}} & 1 \leq j < N \\ \frac{p_{i,N}-p_{i,0}}{\lambda_N-\lambda_0} & j = N \end{cases} \tag{6.19}$$

The parameters used to form the above ankle and subtalar trajectories are therefore the key points of the ankle and subtalar trajectory given by p_{ij}. The exact set of parameters however is dependent on the specific scenario being considered. For instance, if the start and end points of the trajectory is fixed, then the parameters will simply be the points between the initial and final trajectory points. Alternatively, one may wish to vary one or both of the displacement values at the end point. Under this condition, the parameters would include the displacement values being varied. Upon definition of the trajectory points, the independent variables λ_j was computed automatically by considering the cumulative and normalised Euclidean distance between two adjacent key points on the θ_a-θ_s plane (normalisation was done with respect to the total Euclidean distance). This means that λ_0 will always be zero and λ_N will always be unity.

Since the quantities to be minimised are the force element tensions and the joint reaction forces, a cost function can be defined in a rather straight forward manner as (6.20), where t_{fe} is a vector of the steady state force element tensions at a given set of joint displacements, μ_{AS} is a vector of the magnitudes for the ankle and subtalar joint reaction moments and γ is a variable used to denote the Euclidean distance traversed along the prescribed trajectory. The steady state tensions can be computed by ignoring the dynamic components of the ligament and muscle-tendon models, while the magnitude of the reaction moments can be obtained by first computing the minimal norm external wrench required to maintain the ankle-foot dynamic model in steady state, and then substituting the resulting wrench in the moment equations to calculate the reaction moment vector.

$$C = \int \begin{bmatrix} {t_{fe}}^T & {\mu_{AS}}^T \end{bmatrix} W \begin{bmatrix} t_{fe} \\ \mu_{AS} \end{bmatrix} d\gamma \tag{6.20}$$

By taking into consideration the relationship between γ and λ given in (6.21), the cost function (6.20) can be rewritten as (6.22). The value for the cost function can then be obtained by numerical integration of (6.22). However, this could be computationally intensive if the integral step size is too small as the ligament and muscle-tendon tensions will have to be solved repeatedly at each integration step. A simpler alternative is to obtain an approximation of this cost function by assuming that the tensions and reaction moments are constant over a small segment of the trajectory. These segments can be prescribed to be of a fixed and uniform length, where the segmental length can be computed by numerical integration of (6.21) with respect to λ.

$$\frac{d\gamma}{d\lambda} = \sqrt{\left(\frac{d\theta_a}{d\lambda}\right)^2 + \left(\frac{d\theta_s}{d\lambda}\right)^2} = \sqrt{\left(\frac{df_a(\lambda)}{d\lambda}\right)^2 + \left(\frac{df_s(\lambda)}{d\lambda}\right)^2} \tag{6.21}$$

$$C = \int \left[{t_{fe}}^T \quad {\mu_{AS}}^T\right] W \begin{bmatrix} t_{fe} \\ \mu_{AS} \end{bmatrix} \sqrt{\left(\frac{df_a(\lambda)}{d\lambda}\right)^2 + \left(\frac{df_s(\lambda)}{d\lambda}\right)^2}\, d\lambda \tag{6.22}$$

In addition to the cost function to be minimised, definition of parameter constraints is also important to complete the formulation of the optimisation problem. At the basic level, these constraints take the form of upper and lower bounds of the trajectory parameters as shown in (6.23). Other possible constraints include:

1) The straight line distance between a key point at λ_j and the end point of the trajectory at λ_N must be shorter than that computed using the previous key point at λ_{j-1}. This constraint can be expressed as (6.24).
2) A trajectory point must be within certain distance of the nominal point. This constraint can be expressed as (6.25), where δ is the proximity within which the parameters are constrained.

$$lb_i \le p_{i,j} \le ub_i \tag{6.23}$$

$$\sqrt{\left(p_{a,N} - p_{a,j}\right)^2 + \left(p_{s,N} - p_{s,j}\right)^2} < \sqrt{\left(p_{a,N} - p_{a,j-1}\right)^2 + \left(p_{s,N} - p_{s,j-1}\right)^2} \tag{6.24}$$

$$\text{Where: } 1 < j \le N-1$$

$$\sqrt{\left(p_{a,j,nom} - p_{a,j}\right)^2 + \left(p_{s,j,nom} - p_{s,j}\right)^2} \le \delta_j \qquad 1 \le j \le N \tag{6.25}$$

It can be seen that constraint 1 will only be appropriate for trajectories which resemble straight line paths. For paths which involve significant deviation from straight lines such as elliptic or circular paths, constraint 1 can be applied on points located between several critical points upon which constraint 2 is imposed.

6.3.2 Results

Using the above formulation, an optimisation of a test problem was carried out using the `fmincon` function in MATLAB to improve a trajectory which moves the foot from its neutral position ($\theta_a = 0°$, $\theta_s = 0°$) to a more supinated position ($\theta_a = 40°$, $\theta_s = 25°$). The initial trajectory was selected so that the entire set of trajectory points is located on a straight line passing through the start and end positions on the θ_a-θ_s displacement plane. The trajectory was defined with a total of four segments, where in addition to the intermediate points, the subtalar displacement of the trajectory end point was also allowed to vary within 5° of its initial value. The weights in the cost function used in this test problem were selected so that only the forces along some of the lateral ankle ligaments were considered together with the reaction moment magnitudes of the ankle and subtalar joints. The weighting for all other force elements were set to be zero. This had been done to focus on minimisation of forces along the lateral ligaments which are more prone to injuries. The cost weightings used for this test problem and the values of the initial and optimised trajectories are presented in Table 6.3, where w is used to denote the weights along the diagonal of the weighting matrix W (note that weights are set to zero unless otherwise specified). Also, C_0 and C_f are used to represent the cost of the initial and improved trajectories.

Table 6.3: Weightings for ligament tensions/joint reaction moments and the cost of initial and final trajectories.

w_{ATaFL}	w_{CFL}	w_{LTaCL}	w_{PTaFL}	w_{μ_A}	w_{μ_S}	C_0	C_f
$(1/300)^2$	$(1/600)^2$	$(1/300)^2$	$(1/550)^2$	$(1/10)^2$	$(1/10)^2$	0.7846	0.6180

ATaFL: Anterior TaloFibular Ligament; CFL: Calcaneofibular Ligament; LTaCL: Lateral Talocalcaneal Ligament; PTaFL: Posterior TaloFibular Ligament

The initial and improved trajectories are shown in Figure 6.12a where the circular markers denote the key points used to define the trajectories. The values of the instantaneous cost function to be integrated for both trajectories are also shown in Figure 6.12b. Additionally, a comparison of the ligament forces and reaction moments are provided in Figure 6.13. In all these plots, the green lines represent quantities associated with the initial trajectory while the blue lines denote quantities relating to the improved trajectory.

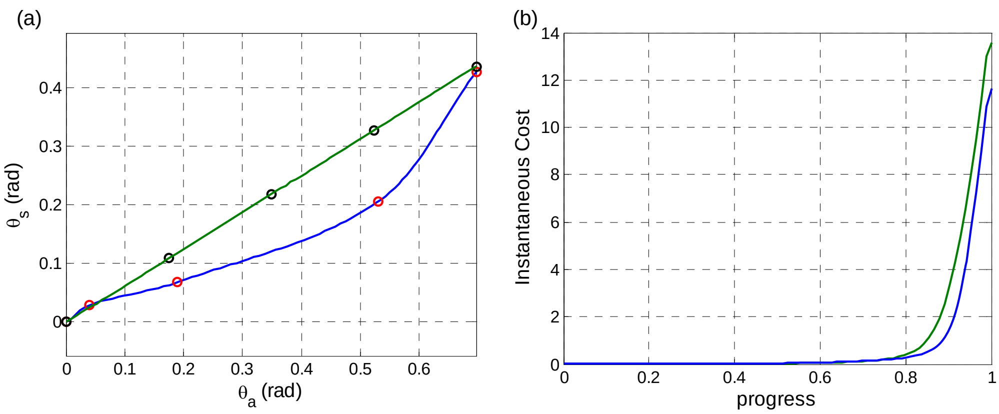

Figure 6.12: (a) Initial (green) and improved (blue) rehabilitation trajectories. (b) Instantaneous costs related to the initial (green) and improved (blue) trajectories.

It can be seen from Table 6.3 that the use of the optimised trajectory can lead to approximately 20% reduction in the cost function when compared with the nominal straight line trajectory. Figure 6.12a shows that the improved trajectory had deviated considerably from the initial trajectory. It should also be noted that the subtalar displacement of the end point had decreased slightly to reduce the peak ligament tensions and joint reaction moments. It can be seen from Figure 6.13 that although the trajectory produced from the optimisation is longer in terms of path length, it still has a cost function which is about 20% lower than that of the shortest path. Since the cost function indirectly penalises longer trajectories, this shows that an appreciable reduction in ligament tensions and joint reaction moments can be achieved by deviation from the path of minimal distance, and that there are merits associated with the use of an optimisation based approach to generate rehabilitation trajectories.

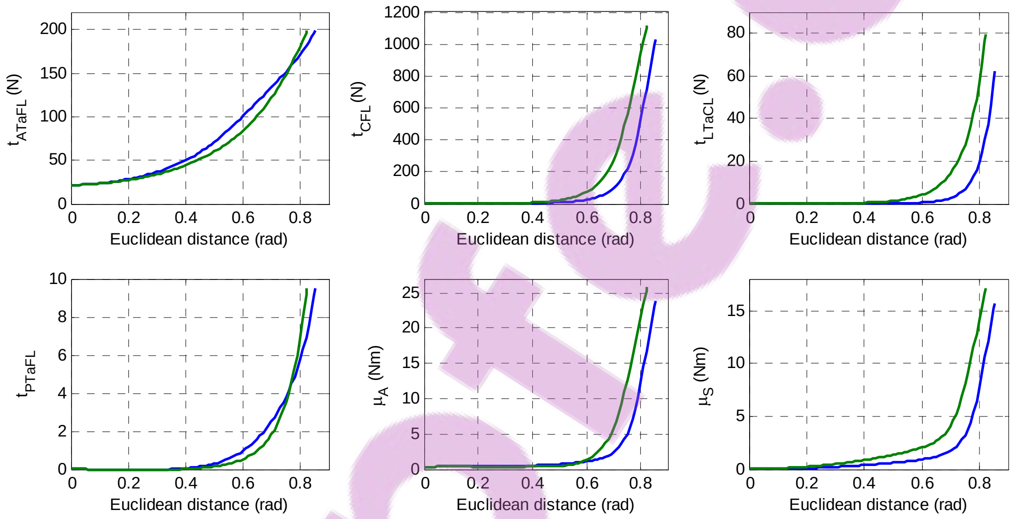

Figure 6.13: Ligament tensions and joint reaction moment magnitudes for the intial (green) and improved (blue) trajectories.

6.4 Chapter Summary

Validation of the computational ankle model presented in Chapter 5 suggested that the model behaviour is largely in agreement with observations obtained from the real ankle in terms of trend of motion and movement range of the ankle foot. A more quantitative validation approach however showed some discrepancies between the model and experimental data, but this can be attributed to several potential sources of errors in the experimental setup and also the fact that the biomechanical model is not built around the subject involved in the experimental trials. Taking this into consideration, the model and actual response can still be considered as a reasonable match.

The application of the developed model in the rehabilitation trajectory generation routine proposed in this research had suggested that a path with minimal length is not necessarily the ideal path between two foot configurations. It therefore supports the idea that a biomechanical ankle model can be used to help improve an initial path to better satisfy certain desired performance/safety requirements.

Chapter 7 Multi-Input Multi-Output Actuator Force Control

Operation of the developed rehabilitation robot relies on implementation of a suitable interaction controller, and a force based impedance control approach had been taken in this research, whereby the desired robot impedance is realised through actuator level force control. This chapter details the development of the multi-input multi-output (MIMO) actuator force controller devised in this work. As will be shown later in this chapter, preliminary experimental trials carried out in this research had revealed that independent application of actuator force control schemes on each actuator yielded undesired oscillatory behaviour. Consequently, a MIMO actuator force controller which takes into account the coupling effects introduced by kinematic constraints of the parallel manipulator had been proposed in this work to improve the force control performance.

The motivation for the development of an actuator force controller is first presented in this chapter, followed by a discussion on the approach taken to decouple the actuator forces using information related to the manipulator configuration. To enable a more thorough analysis, higher order dynamics were included in the actuator force models by inclusion of the actuator resonance, force sensor dynamics and environmental dynamics into an overall actuator-sensor-environment model. The stability analysis of this combined system is also presented, where a transfer function based frequency domain analysis is used to estimate the gain margins for the proposed decoupling control scheme while a state space model of the linearised system is utilised in the robust stability analysis. A final actuator force controller is then proposed based on observations obtained from these analyses. Finally, simulation and experimental results are analysed and discussed, with particular emphasis on disturbance rejection and backdriveability.

7.1 Motivation for a MIMO Actuator Force Controller

Interaction control of manipulators can typically be implemented through either a position based or a force based approach. The position based method utilises force information as measured or estimated from available sensors to compute a reference trajectory for the robot according to the desired impedance relationship, and is typically applied on systems with good position tracking capability such as industrial robots [125-127]. Advanced control techniques developed for position control can therefore be used to track the generated reference trajectory and produce the desired force or impedance relationship [34]. Force based approaches on the other hand requires the robot to directly apply the necessary force/torque to the environment to give it the prescribed mechanical behaviour. This latter approach therefore necessitates a force controlled inner loop, which is typically realised through accurate control of the actuator forces/torques [128]. The force based approach is therefore suitable for use in devices which utilise actuators with low transmission ratios and thus lower effective friction [12, 24, 30]. However, as large forces are needed in this work to cater for ankle resistive exercises and to support the weight of the user's lower limb during operation, actuators with high gear ratios had been used to increase the force capacity of the robot. An undesired consequence of this is that the frictional torque within the motor was also amplified due to the high transmission ratio. This suggests that a force based implementation of the impedance control algorithm would be challenging.

Even though the above presents a strong case for the adoption of a position based impedance control strategy, the fact that the user's ankle will form part of the robot kinematic constraint and the presence of actuation redundancy (when the ankle is assumed to have three rotational degrees of freedom) had led to the consideration of an inner force control loop. Since redundantly actuated parallel manipulators are over constrained mechanisms, the use of position control strategies which typically involve high controller gains can lead to generation of large forces or torques within the mechanism when discrepancies exist between the actual robot kinematic parameters and those used to compute the inverse kinematic solution for the position controller. Such a problem was discussed in [129] where controller gains were tuned to minimise mutually competing actuator actions. Additionally, due to the uncertainties involved in the actual ankle kinematics and its incorporation into the robot kinematic constraints, it is also inappropriate to implement position control strategies which rely on independent control of actuator displacements due to the inexact knowledge of the relationship between task space (actuator lengths) and joint space (end effector orientation) variables. Also, other torque/force based position control strategies such as inverse dynamics or computed torque control will still ultimately lead to the need to regulate forces/torques at the actuator level.

It is therefore clear from the above discussion that an actuator force control scheme is crucial for the implementation of interaction control strategies on the proposed ankle rehabilitation robot. An additional motivation for the use of a force based impedance controller in this research is the intention to regulate the level of actuator forces applied in the vertical direction at the ankle joint using the redundant actuation degree of freedom. In order to achieve this, the null space actuator forces which have no influence on the task space dynamics must be controlled to complement other components of the actuator forces so that the desired net vertical force is realised. Last but not least, the ability for pure force or torque control is also an important feature for rehabilitation robots as it is required to implement strength training exercises, and this can be easily accomplished upon the establishment of a suitable actuator force controller.

Based on the above reasons, the design of a force controlled inner loop had been considered in this research. While various actuator force/torque control techniques are available in literature [104-106, 130], they are mainly focused on the control of a single actuator as a single-input single-output (SISO) system, and does not consider the overall kinematics of the mechanism being driven. These schemes also often require measurements of velocities and good knowledge of the robot dynamics. As significant force coupling can be found among the actuator forces in a parallel robot, independent actuator force control may lead to performance degradation as force interactions between various actuators will simply be treated as additional disturbances in the SISO force controllers. A MIMO approach for actuator force control that takes into account the kinematic and inertial information of the parallel manipulator was therefore investigated in this research.

7.2 Actuator Force Control by Decoupling of Inertia Matrix

The dynamics of the actuators used in this research has to be considered to gain a better understanding of the coupling that arises when these actuators are installed on the parallel robot. The equation governing the dynamics of the brushed DC motor driven linear actuators used in this research is given in (7.1), where F_{act} is the actuator force resisting the actuator motion, i is the actuator current, l is the actuator length, K_t is the torque constant of the motor, K_a is the transmission ratio between the rotary and linear displacements, J_{eff} is the effective motor rotational inertia, b_{eff} is the effective motor viscous damping coefficient and F_{fric} is the effective Coulomb friction acting on the actuator rod.

$$F_{act} = K_t K_a i - {K_a}^2 J_{eff} \ddot{l} - {K_a}^2 b_{eff} \dot{l} - F_{fric} \tag{7.1}$$

Provided that the actuators share the same characteristics, (7.1) will be equally applicable for the case where the actuators are coupled through the four link parallel mechanism used in this work. In such a scenario, the variables F_{act}, i, l and F_{fric} can simply be treated as four element column vectors. This relationship can therefore be integrated with the task space dynamics to give the overall actuator and robot dynamics. As with many manipulators, the robot task space dynamics considered in this work can be represented in the form shown in (7.2), where $\Theta \in \mathbb{R}^3$ is the task space coordinates in XYZ Euler angles, $M(\Theta) \in \mathbb{R}^{3\times3}$ is a configuration dependent inertia matrix, $N(\Theta, \dot{\Theta}) \in \mathbb{R}^3$ is a vector gathering all the centripetal, Coriolis and gravitational forces, $\tau_{ext} \in \mathbb{R}^3$ is the external torque applied to the robot manipulator and $J \in \mathbb{R}^{4\times3}$ is the manipulator Jacobian. Using this manipulator Jacobian, the task space and joint space velocities and accelerations can also be related through (7.3) and (7.4) respectively.

$$M(\Theta)\ddot{\Theta} + N(\Theta, \dot{\Theta}) + \tau_{ext} = J^T F_{act} \tag{7.2}$$

$$\dot{l} = J\dot{\Theta} \tag{7.3}$$

$$\ddot{l} = J\ddot{\Theta} + \dot{J}\dot{\Theta} \tag{7.4}$$

The actuator accelerations can be obtained by substituting the task space accelerations obtained from rearranging (7.2) into (7.4). The resulting actuator accelerations and the actuator velocities can then be further incorporated into (7.1) to give (7.5), where the matrix D is used to describe the coupling between the actuator currents and the resulting actuator forces. The expression for this matrix is given in (7.6). It should be noted that dependencies on the task space coordinates and velocities are dropped hereafter for brevity. Additionally, since the manipulator Jacobian is not square for redundantly actuated robots, the pseudo-inverse (denoted by the operator $^+$) has been used in place of the conventional matrix inverse operation. More specifically, the pseudo-inverse of the manipulator Jacobian is computed using (7.7). It is also worth noting that $J^T(J^+)^T = I$ and $(J^+)^T J^T = I - v_0 {v_0}^T$, where v_0 is a column-wise collection of the null space vector(s) of J^T.

$$F_{act} = K_t K_a D i + (I - D)(J^+)^T(N + \tau_{ext}) - D\underbrace{\left[{K_a}^2\left(J_{eff}\dot{J} + b_{eff}J\right)\dot{\Theta} + F_{fric}\right]}_{F_{distb}} \tag{7.5}$$

$$D = \left(I + {K_a}^2 J_{eff} J M^{-1} J^T\right)^{-1} \tag{7.6}$$

$$J^+ = (J^T J)^{-1} J^T \tag{7.7}$$

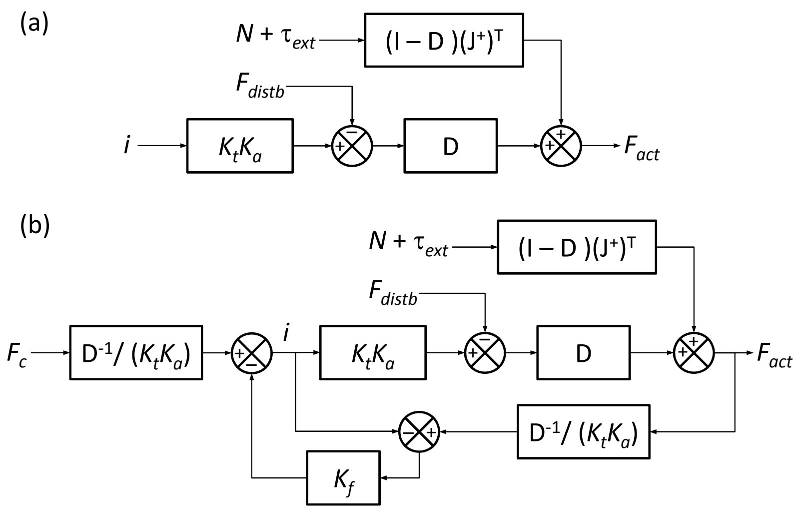

Figure 7.1: Block diagrams of the actuator dynamics (a) and block diagram of the system under disturbance observer based control (b).

Disturbance observer based controllers had been used by several researchers for position and force control of electrical actuators [97, 98, 104, 105, 130]. Due to its relative simplicity and good performance, this control structure had been used in this work as the basis for further analysis and development. By treating last two terms in (7.5) as disturbances, the plant which relates the actuator current to the actuator force can be viewed as a simple gain matrix. The actuator force control problem can therefore be represented using the block diagram as shown in Figure 7.1a. By applying the typical disturbance observer based control scheme to this system, the resulting closed loop system is given in Figure 7.1b. It can be seen from Figure 7.1b that the feedback block used in this scenario need only be a gain matrix instead of a low pass filter as often used in other applications. This is the result of allocating the other dynamical terms as system disturbances to be rejected. Using the proposed controller, the commanded actuator current can be written as (7.8), with K_f being the scalar controller gain used in the feedback path of the disturbance observer, $F_c \in \mathbb{R}^4$ being the vector of commanded force, $G \in \mathbb{R}^{4\times4}$ being the gain matrix in the forward path and $H \in \mathbb{R}^{4\times4}$ being the gain matrix in the feedback path. This gain K_f can take on values between zero and unity, and better disturbance rejection can be achieved as the gain approaches unity. The proposed control law can be seen as a simpler version of other similar disturbance observer based approaches found in the literature as it does not require measurement of actuator velocity or acceleration. This is because the robot inertia matrix and manipulator Jacobians are purely dependent on the configuration of the manipulator end effector.

$$\begin{aligned} i_c &= \frac{1}{K_t K_a \left(1 - K_f\right)} D^{-1} F_c - \frac{K_f}{K_t K_a \left(1 - K_f\right)} D^{-1} F_{act} \\ &= \frac{1}{K_t K_a} \left(G F_c - H F_{act}\right) \end{aligned} \tag{7.8}$$

7.2.1 Benefits of Decoupling

Substitution of the control law (7.8) into (7.5) then yields (7.9), which shows no coupling between the commanded force and the actual actuator force. An additional benefit of application of the decoupling gain matrix can be seen by considering the effect that the control law (7.8) has on task space accelerations. One of the fundamental uses of actuator force control is to provide improved backdriveability to the rehabilitation robot. This is equivalent to having a zero vector as the commanded force. Substituting (7.8) with zero commanded force into the original actuator force dynamics (7.1) then yields (7.10), with F_{distb} being a disturbance force which includes frictional and velocity dependent components of the actuator dynamics. Combination of (7.10) and (7.2) will further lead to (7.11), which shows that the effective inertia matrix of the mechanism is dependent on the feedback gain matrix H. It can be shown (refer to Appendix B) that the effective inertia matrix in (7.11) can be eventually simplified to the form shown in (7.12) if H is a multiple of the decoupling matrix D^{-1}, with $m_a = {K_a}^2 J_{eff}$ and $h = K_f / \left(1 - K_f\right)$.

$$F_{act} = F_c + \left(1 - K_f\right)(I - D)(J^+)^T (N + \tau_{ext}) - \left(1 - K_f\right) D F_{distb} \tag{7.9}$$

$$F_{act} = (I + H)^{-1}\left[-K_a{}^2 J_{eff} J \ddot{\Theta} - F_{distb}\right] \tag{7.10}$$

$$\left[M + K_a{}^2 J_{eff} J^T (I + H)^{-1} J\right]\ddot{\Theta} + N + \tau_{ext} = -J^T (I + H)^{-1} F_{distb} \tag{7.11}$$

$$M + m_a J^T (I + H)^{-1} J = M + \left[\frac{(1+h)}{m_a} V_J \Sigma_J{}^{-2} V_J{}^T + hM^{-1}\right]^{-1} \tag{7.12}$$

Closer inspection of (7.12) reveals that the second term on the right hand side of (7.12) is mainly dominated by the term hM^{-1} if m_a is large, which means that the effective inertia matrix would be very similar to a scaled version of the original manipulator inertia matrix. As a result, provided that the robot inertia matrix is diagonally dominant and has a relatively small condition number (this was found to be the case with the developed robot), externally applied torques will mainly contribute to accelerations along similar directions. Since the externally applied torque represents the interaction between the user and the robot, the above implies that the use of the decoupling matrix in the feedback path will allow more intuitive motion of the robot when the user is applying an effort to backdrive the manipulator. On the other hand, if an identity matrix is used in the feedback path instead, the resulting effective inertia matrix of the controlled manipulator will be heavily influenced by the manipulator Jacobian, particularly when the feedback gain is small. In fact, the condition number of the second term in the effective inertia matrix will be the square of that for the manipulator Jacobian, indicating that coupling will be amplified in general even with relatively well conditioned manipulator Jacobians.

7.2.2 Generalisation of the Decoupling Force Controller

The control law in (7.8) can be further generalised to allow a variation in the level of "decoupling" and the application of additional control action in the null space of the manipulator Jacobian transpose. This modified control law is given in (7.13), where n is the power to which the matrix D^{-1} is raised to $(0 \leq n \leq 1)$ and K_{v0} is the scalar gain for the additional disturbance observer applied along the null vector $v_0 \in \mathbb{R}^4$ of the manipulator Jacobian. The main rationale for the addition of a disturbance observer loop in the null space is as follows. Since forces along the null space do not influence the task space moments and motion, its control parameters can be chosen independently. Furthermore, in this particular application, the singular value of the matrix D^{-1} along the null vector is significantly lower than that of the other directions due to the large actuator transmission ratio. The result of this is smaller control action and a corresponding decrease in disturbance rejection capability along the null space. The addition of the disturbance observer in the null space therefore aims to compensate for the above shortcoming.

$$i_c = \frac{1}{K_t K_a}\left[\left(\frac{1}{(1-K_f)}D^{-n} + \frac{1}{(1-K_{v0})}v_0 {v_0}^T\right)F_c - \left(\frac{K_f}{(1-K_f)}D^{-n} + \frac{K_{v0}}{(1-K_{v0})}v_0 {v_0}^T\right)F_{act}\right] \tag{7.13}$$

The main motivation for the introduction of partial decoupling through variation of the negative power applied to the D matrix is discussed below. Due to the presence of unmodelled dynamics, there exists a limit for K_f above which the system will become unstable. The introduction of partial decoupling therefore allows the controller to be further fine tuned so that the relative gains applied along each decoupled directions can be changed to strike a balance between the disturbance rejection capability and extent of decoupling while maintaining the overall system stability. The above can be illustrated more clearly by considering a simplified problem. By making the assumption that the force control problem can be perfectly decoupled into four single degree of freedom systems (each lying in one of the decoupled directions or output basis vectors of the D matrix), it can be seen that each of these degrees of freedom will have its own gain margin or critical gain. Clearly, the ratios of these gain margins may not be identical to those of the singular values obtained from the decoupling matrix D^{-1}. It is easy to see that a stable system can only be achieved if the effective gains along all the decoupled directions are less than their corresponding critical gains. Since the effective gains along each of these decoupled directions are dependent on both the singular value of D^{-1} along that direction and the overall controller gain K_f, the restriction of the relative ratios of singular values in H to that found in D^{-1} will generally lead to the case where effective gains along the decoupled directions are not maximised. A possible approach to alleviate this problem is through the introduction of partial decoupling, which provides an additional controller parameter that can be adjusted so that the effective gains can be pushed closer to their critical values while also maintaining some level of decoupling.

Clearly, to maximise performance in terms of disturbance rejection, the ideal approach would be to allow individual selection of the gains along each of these decoupled directions. However, the downside to this method is that the critical gain values may completely ignore the trend found in the singular values of the decoupling matrix. The partial decoupling method can therefore be viewed as an acceptable compromise. One issue with the above analysis is the applicability of the simplifying assumption. This will be further explored in the following sections where the initially unmodelled dynamics are incorporated into the overall system. The control law with individual gain selection along different decoupled directions is also further investigated in this chapter.

7.3 Higher Order Dynamic Model of Actuator-Sensor-Environment System

As discussed previously and as pointed out by researchers, stability of force feedback controllers are often compromised due to the presence of unmodelled dynamics and non-collocation of sensor and actuator [99]. The main implication of this phenomenon is the existence of an upper force feedback gain limit. The higher order dynamics introduced by compliance of the force sensor and actuator must therefore be considered to obtain a better understanding of the stability of a force feedback controlled system. Higher order dynamics in the force sensor based actuator force control problem was modelled in [102, 103] as a three-mass system with two masses representing the actuator and one representing the force sensor. This had been done to describe both the first resonance mode of the actuator and the compliance introduced by the force sensor. By assuming a rigid interface between the force sensor and the interacting mechanical environment, the environmental dynamics can also be integrated into the three-mass model to allow for an analysis on the overall system stability. For the purpose of this section, this combined system is referred to as the actuator-sensor-environment system. It should also be noted that when viewed from the perspective of the actuators, the end effector dynamics of the parallel manipulator as well as any associated kinematic coupling are considered as part of the environment.

7.3.1 General Three-Mass Model for Unidirectional Actuator- Sensor-Environment Systems

Prior to conducting a full scale stability analysis of the actuator force controller through integration of kinematic coupling and dynamics of the parallel mechanism, it is helpful to gain a general understanding of how a unidirectional three-mass system behaves. This can be done by considering the frequency response of a typical three degree of freedom mass-spring-damper system. Such a system can be represented graphically as Figure 7.2, where variables m , b and k are used to represent mass, damping and stiffness values while subscripts a, f and e are respectively used to denote quantities relating to the actuator, force sensor and environment. Lastly, F_a represents the force generated by the actuator.

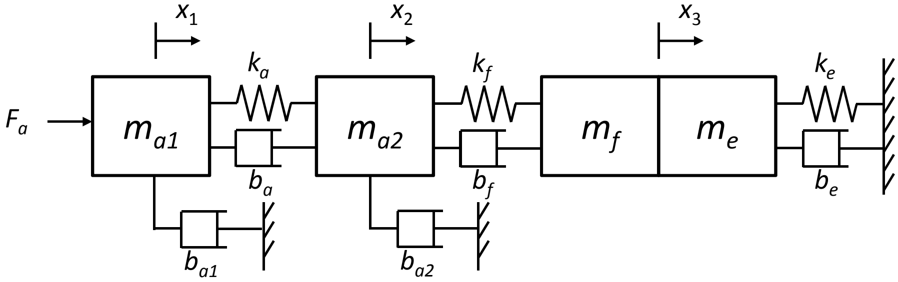

Figure 7.2: A three degree of freedom mass-spring-damper system.

The Laplace transform for each motion degree of freedom of the system depicted in Figure 7.2 can be stated as (7.14), (7.15) and (7.16). The force as obtained from the force sensor can also be assumed to be proportional to the deformation found in the force sensor, and by taking compression as positive, the force sensor reading is given by (7.17).

$$[m_{a1}s^2 + (b_{a1} + b_a)s + k_a]X_1(s) = F_a(s) + (b_a s + k_a)X_2(s)$$
$$\Rightarrow d_1(s)X_1(s) = F_a(s) + n_{21}(s)X_2(s) \tag{7.14}$$

$$\left[m_{a2}s^2 + \left(b_a + b_{a2} + b_f\right)s + k_f + k_a\right]X_2(s)$$
$$= (b_a s + k_a)X_1(s) + \left(b_f s + k_f\right)X_3(s)$$
$$\Rightarrow d_2(s)X_2(s) = n_{12}(s)X_1(s) + n_{32}(s)X_3(s) \tag{7.15}$$

$$\left[(m_f + m_e)s^2 + \left(b_e + b_f\right)s + k_f + k_e\right]X_3(s) = \left(b_f s + k_f\right)X_2(s)$$
$$\Rightarrow d_3(s)X_3(s) = n_{23}(s)X_2(s) \tag{7.16}$$

$$F_{meas}(s) = k_f[X_2(s) - X_3(s)] \tag{7.17}$$

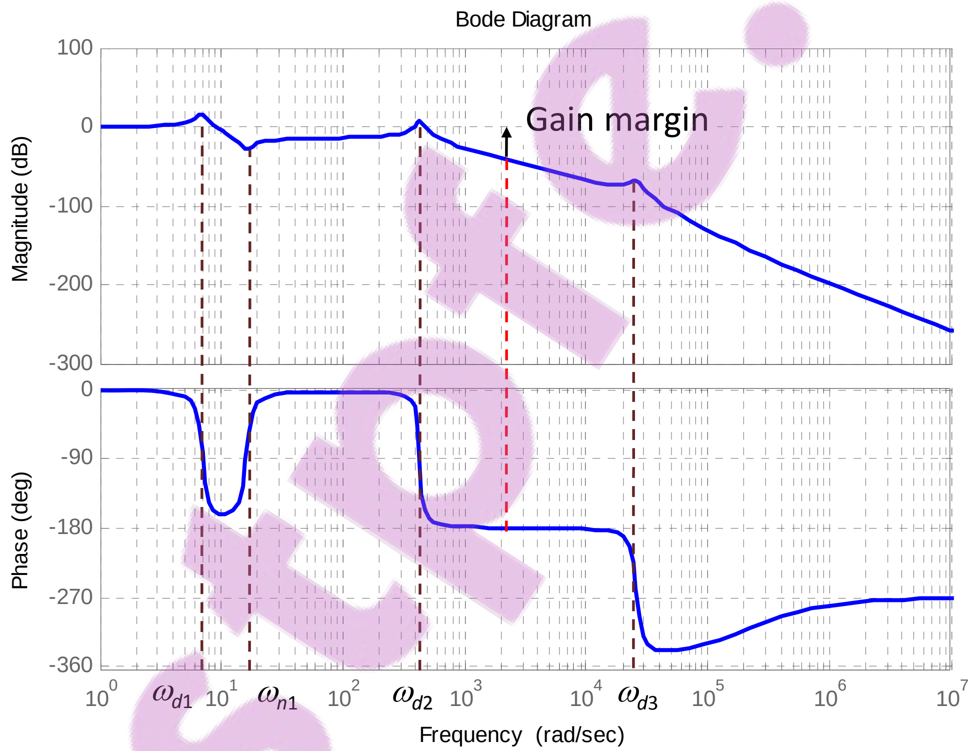

Figure 7.3: Bode diagram of the transfer function between applied actuator force and the interaction force as measured by the force sensor.

Combining the dynamic equations above to yield a single transfer function with actuator generated force as input and the measured force as output then yields (7.18). Since stability of the close loop systems can be evaluated by considering the frequency response of the open loop transfer function, this information is presented as a set of Bode plots in Figure 7.3. It should be noted that the system parameters used to obtain this frequency response were those assumed for the actuators used in this research (see Appendix C). Where possible, the values of these parameters were chosen by considering the physical dimensions and data sheets of the hardware components used. Some parameters were also selected so that they take on similar values to what is used in existing literature. It can be seen from Figure 7.3 that due to the presence of higher order dynamics, there is a limiting proportional gain above which the closed loop force feedback controlled system will become unstable (as denoted by the gain margin).

$$\frac{F_{meas}(s)}{F_a(s)} = \frac{n_{12}(s)[d_3(s) - n_{23}(s)]}{d_3(s)[d_1(s)d_2(s) - n_{12}(s)n_{21}(s)] - d_1(s)n_{32}(s)n_{23}(s)} \tag{7.18}$$

7.3.2 Sensitivity of the General Three-Mass Model to Parameter Variation

It is clear from the Bode plot shown in Figure 7.3 that there are several resonant and anti-resonant frequencies which corresponds to the local maxima and local minima of the magnitude response curve. Rapid phase changes are also expected at these frequencies. Clearly, the gain margin and its corresponding frequency can be altered significantly when these resonant and anti-resonant frequencies are changed through the use of different system parameters. More insights of the system can therefore be obtained by analysing how these resonant and anti-resonant frequencies changes with variation in system parameters. This can be done by factorising the open loop transfer function in (7.18) to give (7.19), where α and β are the coefficients of the first and zeroth order terms in each second order factor. The subscript n is used to denote the factor obtained from the numerator while subscript d is used to denote the factors obtained from the denominator. Additionally, K is the gain of the transfer function (unity in this case) and T is the time constant for the first order factor in the numerator.

$$\begin{aligned} \frac{F_{meas}(s)}{F_a(s)} &= K(Ts+1)\left(\frac{s^2 + \alpha_n s + \beta_n}{\beta_n}\right)\prod_{i=1}^{i=3}\left(\frac{\beta_{d,i}}{s^2 + \alpha_{d,i}s + \beta_{d,i}}\right) \\ &= K(Ts+1)G_n(s)\prod_{i=1}^{i=3}G_{d,i}(s) \end{aligned} \tag{7.19}$$

The frequencies corresponding to the local minima and local maxima on the magnitude plot can be approximated by considering separately the individual second order transfer functions which are denoted by $G_n(s)$ and $G_{d,i}(s)$ in (7.19). When converted to the frequency domain, the magnitudes of the second order polynomials can be represented as (7.20). Clearly, any stationary points (including local maximum and local minimum) in the frequency response of these second order transfer functions must occur at frequencies where the frequency derivative of (7.20) becomes zero. The positive and non-zero frequency which satisfy the above condition is given by (7.21). If a real solution is identified, the maximum or minimum magnitude of the transfer function under consideration can then be easily computed using this frequency.

$$|(j\omega)^2 + j\alpha\omega + \beta|^2 = (\beta - \omega^2)^2 + \alpha^2\omega^2 \tag{7.20}$$

$$\omega^* = \sqrt{\beta - \frac{\alpha^2}{2}} \tag{7.21}$$

Using the above information, a sensitivity analysis can be carried out to investigate how different system parameters influence the resonant/anti-resonant frequencies and the magnitudes associated with them. Such an analysis would involve the computation of the ratio between the percentage change of the quantities of interest to the percentage change of the parameter being varied. This is expressed mathematically as (7.22) [131], where S_ρ^y is the sensitivity of the quantity y with respect to the parameter ρ, and Δ is used to indicate small changes. The quantities that y represent in this analysis include the magnitudes and resonant/anti-resonant frequencies of the factorised terms presented in (7.19), while ρ is used to refer to the system parameters such as the mass, viscous damping and stiffness attached to each body shown in Figure 7.2. By utilising the parameters used to construct the Bode diagram in Figure 7.3 as the nominal system parameters, a sensitivity analysis was carried out numerically. The results of this analysis are summarised in Table 7.1 and Table 7.2, where the top four most influential parameters for each variable of interest are shown with their respective sensitivity values.

$$S_\rho^y = \frac{\frac{\Delta y}{y}}{\frac{\Delta \rho}{\rho}} = \frac{\rho}{y}\frac{\partial y}{\partial \rho} \tag{7.22}$$

Table 7.1: Results summary of sensitivity analysis for the first two resonant frequencies.

ρ	$S_\rho^{\lvert G_{d1}(j\omega_{d1})\rvert}$	ρ	$S_\rho^{\omega_{d1}}$	ρ	$S_\rho^{\lvert G_{d2}(j\omega_{d2})\rvert}$	ρ	$S_\rho^{\omega_{d2}}$
b_e	-0.55267	k_e	0.50328	b_f	-0.93345	k_f	0.49847
k_e	0.49832	m_{a1}	-0.3952	k_f	0.50476	m_e	-0.4008
b_{a1}	-0.4341	m_e	-0.09589	m_e	0.42034	m_{a1}	-0.09551
m_{a1}	0.39712	m_{a2}	-0.00452	m_{a1}	0.077129	b_f	-0.0027

Table 7.2: Results summary of sensitivity analysis for the last resonant frequency and the anti-resonant frequency.

ρ	$S_\rho^{\lvert G_{d1}(j\omega_{d3})\rvert}$	ρ	$S_\rho^{\omega_{d3}}$	ρ	$S_\rho^{\lvert G_{d1}(j\omega_{n1})\rvert}$	ρ	$S_\rho^{\omega_{n1}}$
b_a	-0.85918	k_a	0.5032	b_e	0.99371	k_e	0.50619
k_a	0.49482	m_{a2}	-0.4884	k_e	-0.49649	m_e	-0.49233
m_{a2}	0.49435	b_a	-0.00981	m_e	-0.4955	b_e	-0.01264
b_f	-0.13423	m_{a1}	-0.00556	m_f	-0.00099	m_f	-0.00099

It can be seen from the above results that the first resonant frequency is relatively low (less than 10Hz) and is highly dependent on the environmental stiffness and the first actuator mass. Its associated magnitude can also be seen to be heavily influenced by the environmental damping and stiffness, as well as the viscous damping and mass applied on the first actuator mass. The second resonant frequency is almost two orders of magnitude higher than the first resonant frequency and is more reliant on the values of the force sensor stiffness and environmental mass, while the magnitude at this frequency is mainly controlled by the sensor damping, sensor stiffness and environmental mass. The third resonant frequency can be seen to occur at a very high frequency (>10kHz) and is largely controlled by the actuator stiffness and the second actuator mass. The magnitude of the peak at this frequency is sensitive to the damping and stiffness that exist between the two actuator masses, as well as the second actuator mass. Lastly, the anti-resonant frequency can be seen to be most sensitive to the environmental stiffness and mass. Its magnitude is also largely controlled by the environmental parameters, thus showing that this feature on the frequency response is essentially independent of other actuator and sensor parameters. A general trend that can be observed within the results is that the magnitude at the resonant frequencies will decrease with larger damping and increase with larger mass or stiffness. An opposing trend is however observed for the anti-resonant frequency. As expected, the values of the resonant/anti-resonant frequencies can also be seen to increase with higher stiffness and lower mass.

It can be concluded from the Bode diagram that for the set of parameters considered, the second resonant frequency and its associated magnitude appear to have the most influence on the system gain margin since the cross-over frequency (the lowest frequency at which the phase response equates to -180°) lies between the second and third resonant frequencies. The gain margin of the system is thus dependent on the magnitude of the peak introduced by this second resonant frequency. This magnitude will have an even larger influence when additional phase delay is introduced to the system, which will result in the cross over frequency moving closer towards the second resonant frequency.

It should be noted however that changes in the environmental characteristics can also make the magnitude at the first resonant frequency more important in terms of determining the gain margin. This is because as the environmental damping factor reduces, the peak and trough which occurs at these frequencies will become more prominent. This is also accompanied by more rapid phase changes (since an instantaneous phase shift of 180° can be observed in systems with no damping). The effect of this is that the phase response between these two frequencies will approach -180°. Although it will never go below this threshold in the ideal system analysed in the Bode diagram, any additional delay can certainly decrease the phase response further to bring the cross-over frequency to this frequency segment. Since a decrease in environmental damping factor can be realised through increase of environmental stiffness, increases in the environmental stiffness can potentially alter the gain margin of the system. Having considered the above however, it is important to note that that the environment with which the actuators interacts in this research is that of the human foot which has a relatively large compliance when compared with other more rigid materials. The damping factor associated with such an environment is also expected to be relatively large. Furthermore, as the first resonant and anti resonant frequencies are significantly smaller than the second resonant frequency, any phase lag introduced by low pass filters or constant time delays will also be less significant due to the lower frequencies. Consequently, the main factor influencing the gain margin is still considered to be the magnitude of the second resonant frequency.

7.3.3 Three-Mass Model of the Actuator and Force Sensor Hardware

After establishing the generic three-mass model, the higher order actuator dynamics can be found by fitting the actual system into the general model structure. The actual actuator and force sensor hardware used in this research can be modelled as a three-mass system by considering the actuator compliance, sensor compliance and environmental dynamics. Formation of this three-mass model therefore requires a more detailed look into the actuator hardware to identify the source of its compliance.

The linear actuators used in this research are powered by brushed DC motors where the motor torque is transmitted to a ball screw via a 5:1 belt drive. The rotational motion is in turn converted into linear motion through the ball screw with a 3.175mm (1/8") pitch. Taking into account the compliance of the belt drive, the vibration mode between the motor and the ball screw can be represented graphically in Figure 7.4, where the variables θ, ω , J, r are used to denote angular displacements, angular velocities, rotational inertias and pulley radii in that order. The above variables are also used with subscripts m and s to respectively represent quantities relating to the motor and the ball screw. Additionally, k_b and b_b are the stiffness and damping of the transmission belt while b_m and b_s are damping introduced by viscous friction on the motor and ball screw. Lastly, K_t, i and τ_{load} are respectively used to refer to the motor torque constant, motor current and the load torque applied at the ball screw. Taking the Laplace transform of the motor and ball screw dynamics then leads to (7.23) and (7.24).

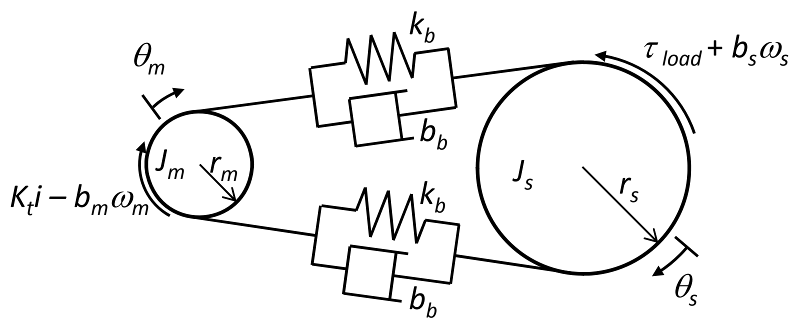

Figure 7.4: Loading conditions between the motor rotor and the ball screw.

$$[J_m s^2 + (b_m + 2{r_m}^2 b_b)s + 2{r_m}^2 k_b]\theta_m(s) = K_t I(s) + 2(r_m r_s b_b s + r_m r_s k_b)\theta_s(s) \qquad (7.23)$$

$$[J_s s^2 + (b_s + 2{r_s}^2 b_b)s + 2{r_s}^2 k_b]\theta_s(s) = -\tau_{load}(s) + 2(r_m r_s b_b s + r_m r_s k_b)\theta_m(s) \qquad (7.24)$$

Assuming a perfectly rigid transmission between the ball screw and the linear actuator rod, the belt drive compliance would become the sole source of actuator compliance, thus resulting in a two mass model for the actuator. Addition of the force sensor onto the end of the actuator rod then results in the setup shown in Figure 7.5, where x_r and x_f are the displacements of the actuator rod and force sensor, $G_s = \frac{2\pi}{\text{pitch}}$ is the transmission ratio of the ball screw, m_r is the mass of the actuator rod, b_r is the viscous friction acting on the actuator rod and F_{int} is the interaction force between the force sensor and the environment. Also, m_f, b_f and k_f are the mass, damping and stiffness of the force sensor. Analysis of the dynamics of this system then leads to (7.25) and (7.26). It should be noted that for completeness, a force F_{fric} is also applied onto the rod to represent Coulomb friction. This force however is neglected in further analysis within this section as the relationship of interest is that between the input current and measured force.

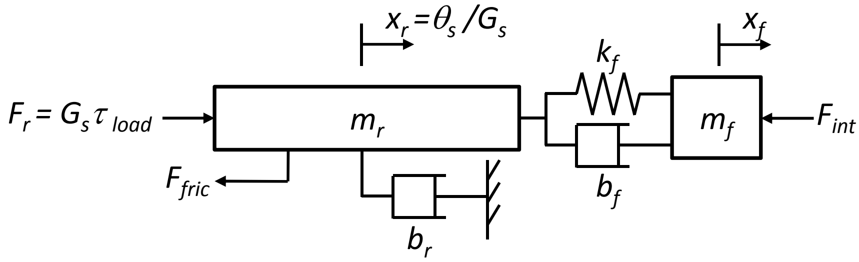

Figure 7.5: Loading conditions between the actuator rod and force sensor.

$$\left[m_r s^2 + \left(b_r + b_f\right)s + k_f\right]X_r(s) = G_s\tau_{load}(s) + \left(b_f s + k_f\right)X_f(s) - F_{fric}(s) \qquad (7.25)$$

$$\left[m_f s^2 + b_f s + k_f\right]X_f(s) = -F_{int}(s) + \left(b_f s + k_f\right)X_r(s) \qquad (7.26)$$

To complete the definition of the actuator-sensor-environment system, the interaction force shown in Figure 7.5 has to be related to dynamics of the interacting environment. In reality, this environment would involve the kinematic coupling imposed by the parallel mechanism. However, for the purpose of illustrating the relationships between the actual actuator parameters and the system parameters of the three-mass model given in the previous section, the force sensor is considered to be rigidly coupled to a single degree of freedom environment through a certain transmission ratio as shown in Figure 7.6. The reason for the introduction of this transmission ratio σ is to allow incorporation of the manipulator Jacobian singular values in the unidirectional model. This arrangement basically considers the unidirectional system to be acting along one of the output basis vectors of the manipulator Jacobian, with the transmission ratio being a factor which scales the task space motion to joint space motion. As the motion variable shown in Figure 7.6 is that of the task space displacement, the associated environmental parameters are also given in the task space. The Laplace transform of the environmental dynamics can be written as (7.27).

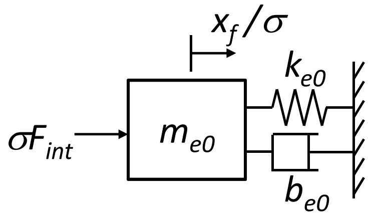

Figure 7.6: Environment dynamics along one of the output basis vectors of the manipulator Jacobian.

$$\frac{1}{\sigma^2}[m_e s^2 + b_e s + k_e]X_f(s) = F_{int}(s) \tag{7.27}$$

By considering all the dynamic equations above and using the parameterisation shown in (7.28), the actuator-sensor-environment system can be restated as the three equations shown in (7.29) – (7.31). Comparing these equations with those found in (7.14) – (7.16) shows that they share a similar structure, with $X_m = X_1$, $X_r = X_2$ and $X_f = X_3$. Equating the coefficients found in these equations then allow the establishment of relationships between the hardware parameters and the general three-mass model parameters. These relationships are summarised in Table 7.3, where the top row shows the system parameters of the general three-mass model while the bottom row gives the corresponding actuator and environmental parameters obtained from the real system. A noteworthy implication of the result obtained in Table 7.3 is that although the belt stiffness may be significantly less than the stiffness of the force sensor, the large transmission ratio of the actuator has the effect of amplifying its effective stiffness when viewed in the linear direction of motion. A consequence of this is that the natural frequency controlled by the actuator stiffness and mass is the highest among the three resonance modes considered in this model, and it can be seen in the following analyses that the system stability is much less reliant on the actuator compliance when additional delay is modelled in the system.

$$\frac{r_s}{r_m} G_s X_m(s) = \theta_m(s) \tag{7.28}$$

$$\begin{aligned} &\left[G_s{}^2 \frac{r_s{}^2}{r_m{}^2} J_m s^2 + G_s{}^2 \left(\frac{r_s{}^2}{r_m{}^2} b_m + 2r_s{}^2 b_b\right) s + 2G_s{}^2 r_s{}^2 k_b\right] X_m(s) \\ &\qquad = \frac{r_s}{r_m} K_t G_s I(s) + 2G_s{}^2 (r_s{}^2 b_b s + r_s{}^2 k_b) X_r(s) \\ &\qquad \Rightarrow d_m(s) X_m(s) = \frac{r_s}{r_m} K_t G_s I(s) + n_{rm}(s) X_r(s) \end{aligned} \tag{7.29}$$

$$\begin{aligned} &\left[(m_r + G_s{}^2 J_s)s^2 + \left(b_r + b_f + b_s G_s{}^2 + 2G_s{}^2 r_s{}^2 b_b\right)s + k_f + 2G_s{}^2 r_s{}^2 k_b\right] X_r(s) \\ &\qquad = 2G_s{}^2 (r_s{}^2 b_a s + r_s{}^2 k_a) X_m(s) + \left(b_f s + k_f\right) X_f(s) \\ &\qquad \Rightarrow d_r(s) X_r(s) = n_{mr}(s) X_m(s) + n_{fr}(s) X_f(s) \end{aligned} \tag{7.30}$$

$$\left[\left(m_f + \frac{m_{e0}}{\sigma^2}\right)s^2 + \left(b_f + \frac{b_{e0}}{\sigma^2}\right)s + k_f + \frac{k_{e0}}{\sigma^2}\right]X_f(s) = \left(b_f s + k_f\right)X_r(s) \tag{7.31}$$

Table 7.3: Relationship between the system parameters of the general three-mass model and the hardware parameters.

m_{a1}	b_{a1}	b_a	k_a	m_{a2}	b_{a2}	m_e	b_e	k_e
${G_s}^2 \frac{{r_s}^2}{{r_m}^2} J_m$	${G_s}^2 \frac{{r_s}^2}{{r_m}^2} b_m$	$2{G_s}^2{r_s}^2\, b_b$	$2{G_s}^2{r_s}^2\, k_b$	$m_r + {G_s}^2 J_s$	$b_r + b_s {G_s}^2$	$\frac{m_{e0}}{\sigma^2}$	$\frac{b_{e0}}{\sigma^2}$	$\frac{k_{e0}}{\sigma^2}$

7.3.4 Inclusion of Kinematic Coupling

The model of the actuator-sensor-environment system discussed thus far had been restricted to motion along a unidirectional path. The extension of this model to one that can be representative of the actuator force control on the developed parallel mechanism therefore requires the incorporation of the manipulator kinematics and dynamics as part of the mechanical environment. To simplify this task, the manipulator can be linearised about a particular operating point so that the manipulator Jacobian matrix J can be used to relate the task space and joint space motion variables as shown in (7.32), where Θ is the task space coordinates and X_f is a vector of force sensor displacements for all the actuating links. The combined dynamics of the manipulator and the task space mechanical environment can also be approximated in a linear form as in (7.33), where M_e, B_e and K_e are the inertia, damping and stiffness matrices of the manipulator and task space environment.

$$X_f(s) = J\Theta(s) \tag{7.32}$$

$$(M_e s^2 + B_e s + K_e)\Theta(s) = J^T F_{int}(s) \tag{7.33}$$

Since the matrix J is rectangular with more rows than columns due to the use of a redundantly actuated manipulator, by substituting $\Theta(s) = J^+ X_f(s)$ into (7.33) and pre-multiplying the resulting equation by $(J^+)^T$, (7.34) can be obtained. As before, v_0 is used to denote the null space of J^T and superscript $^+$ is used to represent the pseudo-inverse operation.

$$[\underbrace{(J^+)^T M_e J^+}_{M_e{}'} s^2 + \underbrace{(J^+)^T B_e J^+}_{B_e{}'} s + \underbrace{(J^+)^T K_e J^+}_{K_e{}'}]X_f(s) = (I - v_0 {v_0}^T)F_{int}(s) \tag{7.34}$$

To obtain the overall dynamics for all four actuators, the equations (7.29) and (7.30) can still be reused with variables X_m, X_r and X_f now being four element vectors. The dynamic equations for the force sensor masses however have to be re-evaluated due to the coupling which exists between the task space and joint space motion variables. The force sensor dynamics prior to consideration of the interaction force exerted by the environment is given by (7.35). Due to the redundant actuation, the joint space motion along the null space of J^T is constrained to be zero (i.e. ${v_0}^T X_f(s) = 0$). This fact can then be used to produce (7.36). Combination of (7.34), (7.35) and (7.36) then results in

(7.37). This equation, together with (7.29) and (7.30) can then be used to fully describe the dynamics of the coupled actuator-sensor-environment system.

$$\begin{aligned}(m_f s^2 + b_f s + k_f)X_f(s) &= -F_{int}(s) + (b_f s + k_f)X_r(s)\\ \Rightarrow d_f(s)X_f(s) &= -F_{int}(s) + n_{rf}(s)X_r(s)\end{aligned} \tag{7.35}$$

$$v_0 {v_0}^T F_{int}(s) = n_{rf}(s) v_0 {v_0}^T X_r(s) \tag{7.36}$$

$$\left[(M_e' s^2 + B_e' s + K_e') + d_f(s)I\right]X_f(s) = n_{rf}(s)(I - v_0 {v_0}^T)X_r(s) \tag{7.37}$$

7.3.5 Decoupled Transfer Functions of Actuator-Sensor-Environment System

Due to the coupling present in the actuator-sensor-environment system, transfer functions in the transfer function matrix may be of a much higher order than what was found in the unidirectional case. Additionally, stability analysis of the system also cannot be done by simply considering the frequency response of individual elements of the transfer function matrix. However, if the system can be fully decoupled into independent degrees of freedom, the use of frequency response methods to study the system stability will become a much more straightforward task.

It is clear from the system model developed in previous sections that if all actuators and sensors share the same parameters, the coupling is caused by the kinematic constraints of the parallel mechanism and any coupling within the task space environment. However, if the environmental dynamics are coupled in the same manner, or in other words, the environmental damping and stiffness matrices are proportional to the environmental inertia matrix, full decoupling of (7.37) will be possible. When the above condition is satisfied, the matrices M_e', B_e' and K_e' will all share the same output basis vectors. Additionally, since these matrices are rank deficient with a common null space (v_0) as that of J^T, the output basis vectors (or decoupled directions) obtained from the singular value decomposition of the M_e' matrix can be used to diagonalise (7.37). The diagonalised version of (7.37) is given in (7.38), where $\Sigma_m' \in \mathbb{R}^{3\times 3}$ is a diagonal matrix containing the non-zero singular values as shown in (7.39); while α_b and α_k are the proportionality constants for B_e' and K_e'. Also, the decoupled variables X_f' and X_r' are obtained by pre-multiplying X_f and X_r with $[U_m' \quad v_0]^T$. A similar transformation can also be applied to (7.29) and (7.30) so that the motion variables X_m and X_r are converted into X_m' and X_r' which align with the output basis vectors of M_e'. Combining these resulting equations with (7.38) and solving for the decoupled sensor force measurement given in (7.40) will then yield the transfer function (7.41) for the force in the null space direction and the transfer function (7.42) for forces along other decoupled directions, where the polynomial $d_{ef,i}(s)$ is different for each non-null decoupled direction and is defined as (7.43), with $\sigma_{m,i}$ being the i^{th} largest singular value of M_e'.

$$\begin{bmatrix} (s^2 + \alpha_b s + \alpha_k)\Sigma_m{}' + d_f(s)I_3 & 0_{3\times1} \\ 0_{1\times3} & d_f(s) \end{bmatrix} X_f{}'(s) = \begin{bmatrix} n_{rf}(s)I_3 & 0_{3\times1} \\ 0_{1\times3} & 0 \end{bmatrix} X_r{}'(s) \tag{7.38}$$

$$M_e' = [U_m{}' \quad v_0] \begin{bmatrix} \Sigma_m{}' & 0_{3\times1} \\ 0_{1\times3} & 0 \end{bmatrix} [U_m{}' \quad v_0]^T \tag{7.39}$$

$$F_{meas}{}'(s) = k_f \left[X_r{}'(s) - X_f{}'(s) \right] \tag{7.40}$$

$$\frac{F_{meas,0}{}'(s)}{I_0'(s)} = \frac{\frac{r_s}{r_m} K_t G_s k_f n_{mr}(s)}{d_m(s)d_r(s) - n_{mr}(s)n_{rm}(s)} \tag{7.41}$$

$$\frac{F_{meas,i}{}'(s)}{I_i'(s)} = \frac{\frac{r_s}{r_m} K_t G_s k_f n_{mr}(s)\left[d_{ef,i}(s) - n_{rf}(s)\right]}{d_{ef,i}(s)[d_m(s)d_r(s) - n_{mr}(s)n_{rm}(s)] - d_m(s)n_{rf}(s)n_{fr}(s)} \tag{7.42}$$

$$d_{ef,i}(s) = \left[\sigma_{m,i}(s^2 + \alpha_b s + \alpha_k) + d_f(s)\right] \tag{7.43}$$

It should be noted that full decoupling of the transfer functions is still possible when the assumption that the stiffness and damping matrices be proportional to the inertial matrix is relaxed to one which requires that all three matrices share the same basis vectors. This would of course alter the coefficients in the decoupled transfer functions which corresponds to the environmental stiffness and damping, its effect on the gain margin is not expected to be significant as the sensitivity results in Table 7.1 suggests that these environmental stiffness and damping parameters are mainly responsible for changes in the magnitude and frequency of the first resonance while the system gain margin is largely dependent on the characteristics of the second resonance.

7.3.6 State Space Model of the Linearised Actuator-Sensor-Environment System

A more general approach in analysing the stability of the overall actuator-sensor-environment system under closed loop control would be to analyse the roots of its characteristic equation. This can be a rather difficult task if approached from the consideration of the coupled transfer function matrix. However, when the system is expressed as differential equations in time domain and formulated as a state space model, solution of the system poles simply becomes an eigenvalue problem for the state transition matrix.

The state space model for the coupled system can be easily formulated from the kinematic and dynamic relationships of the motor, ball screw, force sensor and the parallel manipulator as presented in (7.23) – (7.26), (7.32) and (7.33). It is therefore convenient to select the state variables x as the angular displacements and velocities of the motors (θ_m, $\dot{\theta}_m$), the displacements and velocities of the actuator rod (x_r, $\dot{x}_r$) and the displacement and velocity of the task space coordinates $(\Theta, \dot{\Theta})$. The inputs u of this model on the other hand are the actuator currents and the effective frictional forces along the actuator rod. Lastly, the outputs y of the system are chosen as the force output of the force sensors. This means that the state space model can be represented in the form shown in (7.44), where the state, input and output vectors are respectively defined as $x = \left[\Theta^T \;\; {x_r}^T \;\; \theta_m \;\; \dot{\Theta}^T \;\; {\dot{x}_r}^T \;\; {\dot{\theta}_m}^T\right]^T \in \mathbb{R}^{22}$, $u = \left[i^T \;\; {F_{fric}}^T\right]^T \in \mathbb{R}^8$ and $y = F_{meas} \in \mathbb{R}^4$.

$$\begin{aligned} \dot{x} &= Ax + Bu \\ y &= Cx \end{aligned} \tag{7.44}$$

While the above state space model represents the system exactly as described by the linearised dynamic equations, it is possible that the real system would have additional delays. For instance, the actuator current is assumed to be an ideal input variable in the above model. In reality however, the current is in fact controlled using a pulse width modulation based motor driver. Consequently, discrepancies will exist between the commanded and actual actuator current. This discrepancy can be modelled as a first order low pass filter with unity gain and a small time constant to reflect the fact that such delay is expected to be relatively low. The introduction of this low pass filter into the above state space model will require the augmentation of the state vector to include additional states which describes the filter dynamics given in (7.45), with i_c being the commanded current issued by the actuator force controller.

$$\tau_{LP}\frac{di}{dt} + i = i_c \tag{7.45}$$

The incorporation of the current dynamics into the above state space model will then result in another state space system with the augmented state vector $x' = [x^T \;\; i^T]^T \in \mathbb{R}^{26}$ and a modified input vector $u' = \left[{i_c}^T \;\; {F_{fric}}^T\right]^T \in \mathbb{R}^8$. This system is represented as (7.46), with $B_i \in \mathbb{R}^{22\times4}$ and $B_{fric} \in \mathbb{R}^{22\times4}$ being submatrices of the original B matrix which correspond to the current and actuator friction inputs.

$$\begin{aligned} \dot{x}' &= \underbrace{\begin{bmatrix} A & B_i \\ 0_{4\times22} & -\frac{1}{\tau}I_4 \end{bmatrix}}_{A'} x' + \underbrace{\begin{bmatrix} 0_{22\times4} & B_{fric} \\ \frac{1}{\tau}I_4 & 0_{4\times4} \end{bmatrix}}_{B'} u' \\ y &= \underbrace{[C \quad 0_{4\times4}]}_{C'} x' \end{aligned} \tag{7.46}$$

7.4 Stability Analysis of the Coupled Actuator-Sensor-Environment System

The stability of the coupled actuator-sensor-environment system under closed loop force feedback can be evaluated by examining the higher order dynamic models presented in Sections

7.3.5 and 7.3.6. Even though these models were obtained from a linearised system, they can still be utilised to give a good indication on the system behaviour around its linearisation point. One additional point to keep in mind is that while the model consisting of the decoupled transfer functions assumes that environmental stiffness and damping is proportional to the environmental inertia matrix, no such restriction is placed on the state space model. The state space model can therefore be used to give a more general analysis of the coupled system. Having stated this however, the decoupled transfer functions do have an advantage as they can be easily analysed in the frequency domain to yield gain margins which is expected to be indicative of the actual gain margins when the proportionality assumption is not severely violated. This section will therefore consider the stability of the closed loop system using both models.

7.4.1 Stability Analysis using Decoupled Transfer Functions

Stability analysis of the simplified system can be carried out by applying the Nyquist criterion on the frequency response of the open loop decoupled transfer functions given by (7.41) and (7.42). This can be done by simultaneously considering the Bode diagram of these transfer functions. An interesting observation which can be made about the decoupled transfer functions is that the dynamics along the null space of the manipulator Jacobian transpose is of a lower order compared to the other decoupled directions of $M_e{}'$ in (7.34). For brevity, initial analysis was focused on evaluating the frequency response of forces along the null space and one other decoupled direction. Additionally, the issue of imperfect realisation of the commanded current was also considered by cascading a low pass filter as described in (7.45) to the overall transfer functions. Figure 7.7 shows four Bode plots in two colours. These Bode plots present the frequency responses of the decoupled transfer functions, two along the decoupled direction with the largest singular value (blue) and two along the null space direction (red). For each direction, the frequency response obtained without the application of a low pass filter is given as a solid line while that obtained with low pass filtering is given as a dotted line.

It can be seen from the Bode magnitude plot that there are only two peaks for forces along the null space (red) as opposed to three in the force response along the other decoupled direction considered (blue). Another noticeable difference between the frequency responses of these two directions is that the magnitude of the first peak observed in the null space direction is considerably higher than that of the second peak of the alternative direction. Further examination of the Bode plots shows that the main effects of adding a low pass filter are more rapid decrease of phase and additional magnitude attenuation at high frequencies. Of these two effects, the former appears to have a greater impact on the gain margins. This is because the additional phase delay introduced by the low pass filter has significantly shifted the cross-over frequencies for both force directions to lower values. Consequently, the gain margins for both directions are also greatly reduced since the additional magnitude attenuation contributed by the low pass filtering has yet to take effect at the cross-over frequencies. This is believed to be the main reason limiting the stable force feedback gain on the ankle rehabilitation robot developed in this research. To allow the use of larger gains, a proportional derivative (PD) controller can be used to counter the phase decrease caused by the low pass filter.

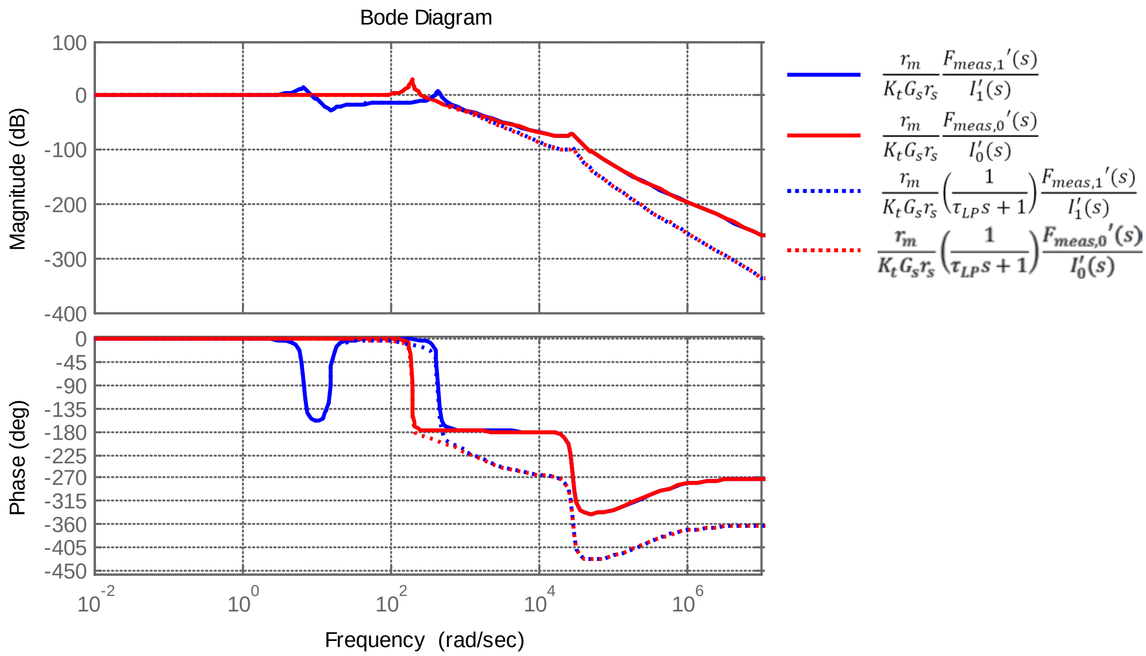

Figure 7.7: Bode diagrams of the frequency responses for the actuator-sensor-environment system along the decoupled direction with the largest singular value (blue lines) and along the null vector (red lines). Solid lines indicate that no low pass filter is added to the system while dotted line indicates otherwise.

One point worth noting here is that due to the relatively high cut-off frequency of the low pass filter, the second resonance peak in the non-null space directions would appear to have the most impact on the directional gain margins. By referring back to the sensitivity analysis results in Table 7.1, and noting the relationships between parameters in the general three-mass model and the actual hardware parameters given in Table 7.3, it is clear that the magnitude and frequency of the peak is largely dependent on the force sensor stiffness and damping, as well as the environmental mass. While the stiffness and damping of the force sensor is largely fixed, variations can be found in the environmental mass. The sensitivity results indicate that the peak magnitude will increase with increasing environmental mass. As the environmental mass is basically represented by the singular values of M_e', it is expected that gain margins will be smaller in coupled directions with larger singular values. This is an interesting result since the ratios between the singular values of matrix M_e' is actually very similar to that coupling matrix D shown in (7.6). In fact, these two matrices share the same decoupled directions when $M_e = M$. This observation therefore provides more support for the implementation of partial decoupling control since this control law actually applies larger gains along the decoupled directions of D which have smaller singular values. On a slightly different note, the gain margin for the null space direction should be independent from the task space environmental parameters as it is isolated from the task space.

Since the force feedback controller is carried out in discrete time due to the use of an embedded controller, a more appropriate analysis would involve the conversion of the continuous time transfer functions in the s-domain into their equivalent discrete time counterparts in the z-domain by assuming zero order hold of the system input. This was accomplished using the `c2d` command in MATLAB. To analyse system stability under discrete proportional derivative control, the discretised transfer function can be cascaded with a unity gain discrete proportional derivative filter. The transfer function of such a filter in the z-domain is given by (7.47), with K_d being the normalised derivative gain and T being the sampling interval. The feedback control system along the decoupled directions can then be represented as in Figure 7.8.

$$G_{PD}(Z) = \frac{Y(z)}{U(z)} = \frac{\left(1 + \frac{K_d}{T}\right)z + \frac{K_d}{T}}{z} \tag{7.47}$$

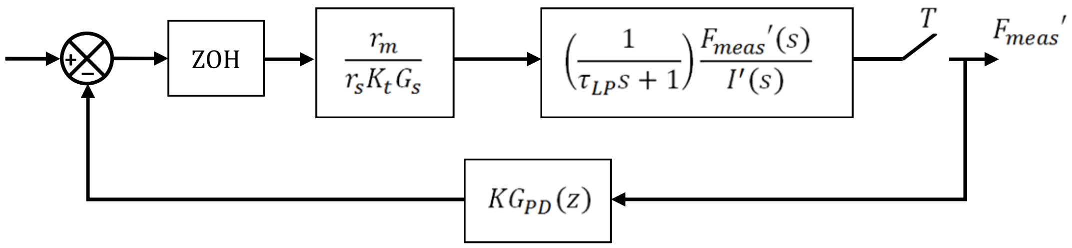

Figure 7.8: Block diagram showing discrete proportional derivative force feedback control along the decoupled directions.

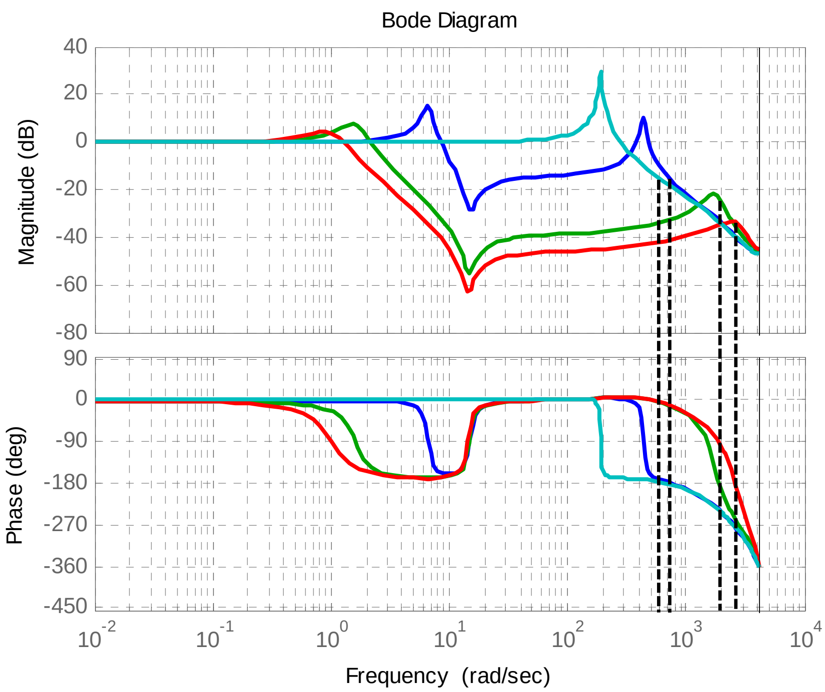

Figure 7.9: The discrete Bode plots of the input force to output force frequency responses along all decoupled directions. The cross-over frequencies of these responses are marked using the thick vertical dashed lines.

The gain margins available for all the decoupled force directions under proportional derivative control can then be found by considering the discrete Bode plots of the open loop transfer function of the block diagram shown in Figure 7.8, with K set to unity. These Bode diagrams are shown in Figure 7.9, where the cross-over frequencies of each of the decoupled directions are indicated on the plot. The cyan line is used to represent the response in the null space direction while the blue, green and red lines are used to represent responses for the decoupled directions with decreasing singular values in $M_e{}'$. In other words, the blue lines represent the magnitude and phase responses for the direction with the largest singular value while the red line shows the same information for the direction with the smallest singular value. Inspection of the Bode diagrams reveals that as predicted previously, the gain margins for the decoupled directions with the smaller singular values are generally larger.

As the Bode plots shown in Figure 7.9 are those obtained by assuming a particular $M_e{}'$, the gain margins computed from these plots will only apply around the particular linearisation point. In order to obtain the gain margins over a larger range of operating points using the above approach, it is important to identify how matrix $M_e{}'$ varies with the operating range of the robot. By definition, $M_e{}'$ is dependent on both the manipulator Jacobian and environmental inertia, it is therefore dependent on the task space coordinates. Assuming that the environmental inertia is an inertia tensor with constant principal components, the matrix $M_e{}'$ can be expressed as (7.48), where $R_\Theta \in \mathbb{R}^{3\times 3}$ is the rotational transformation matrix indicating the orientation of the manipulator end effector and M_{e0} is the environmental inertia tensor at zero task space coordinates.

$$M_e' = (J^+)^T R_\Theta M_{e0} R_\Theta{}^T J^+ \tag{7.48}$$

Once this is established, the gain margins can be numerically computed over a range of task space coordinates which lies within the operating range of the robot while applying constant environmental stiffness and damping matrices. Details of the parameters used in this analysis are similar to those used to create the Bode diagram in Figure 7.3 and are provided in Appendix C. Consideration of the resulting gain margins had shown for directions orthogonal to the null space that a clear trend exists between the value of the critical gain and the singular value of the decoupled direction under consideration. These relationships are shown in Figure 7.10. The gain margin along the null space however was found to be a constant (with a value of 7.6). This is an expected observation as the null space force is isolated from the task space environment. Its gain margin must therefore also be independent of the environmental dynamics.

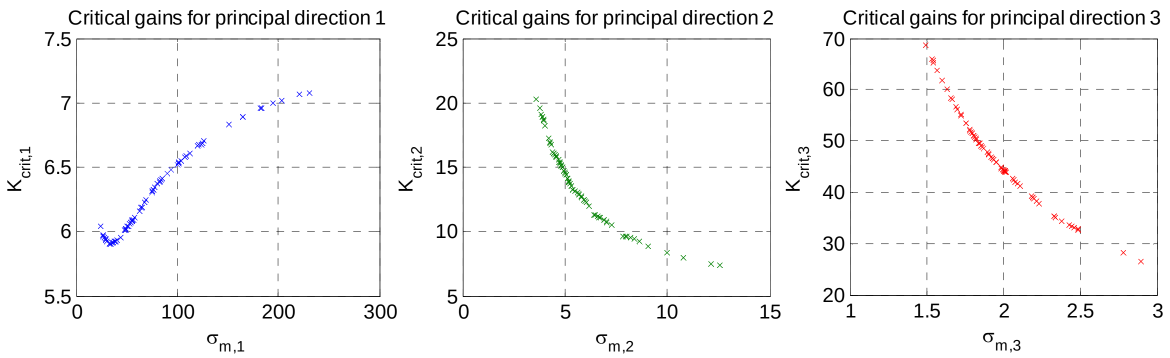

Figure 7.10: Plots of the critical gains in non-null decoupled directions against their corresponding singular values.

It can be seen from the critical gain values that the gain margins tend to increase for the second and third decoupled directions when the singular values along these directions decreases. This is in line with the trend reasoned from the sensitivity results. This trend however was not observed in the critical gains along the decoupled direction with the largest singular value (or largest effective mass/inertia), where larger singular values are accompanied with small increase in critical gain. This is believed to be caused by the phase lead introduced by the PD action which pushes the cross-over frequency higher for this direction, the gain margin in this direction will therefore be less reliant on the peak magnitude. This effect was not observed in the other decoupled directions because their cross-over frequencies occur at higher values, where the effect of the PD phase lead is cancelled out by the phase lag effected by the low pass filtering of actuator currents.

The gain margins obtained from this analysis can be used a starting point for tuning the controller gains along these decoupled directions. A more important result from this analysis however, is that it supports the concept of applying a different gain along different decoupled directions of the $M_e{}'$ matrix. As shown in this analysis, this would allow significant performance improvements over controllers which apply a constant gain across all directions (as the maximum stable gain is limited by the lowest critical gain).

7.4.2 Stability and Robustness Analysis in State Space

The decoupled transfer functions can only be used if the damping and stiffness matrices are scaled versions of the inertia matrix or if all these matrices share the same decoupled directions. To study more general environments, a state space model can be used as it does not require the above simplification. The basic state space model considered here is that of the actuator-sensor-environment system with low pass current filtering as presented in Section 7.3.6. Due to the use of a digital controller, the stability of the system is analysed in discrete time. Again, the `c2d` MATLAB command had been used to convert the continuous state space model to its discrete counterpart given in (7.49).

$$\begin{aligned} x'_{k+1} &= A'_z x'_k + B'_z u'_k \\ y_k &= C'_z x'_k \end{aligned} \tag{7.49}$$

To incorporate the effect of the PD control action into the state space system, the dynamics of discrete time PD control must be considered. This dynamic relationship can be expressed using the difference equation (7.50), where backward differentiation is done with k indicating the current sample number. Note that the variable $F = y$ is used to represent the force sensor measurement as outputted from the discrete state space model in (7.49) while F^* is the resulting force after application of the unity gain PD filter. To allow its integration into the state space model, an alternative but equivalent difference equation as shown in (7.51) can be considered.

$$F_k^* = F_k + \tfrac{K_d}{T}(F_k - F_{k-1}) \tag{7.50}$$

$$\begin{aligned} F_{k+1}^* &= \left(1 + \tfrac{K_d}{T}\right) F_{k+1} - \tfrac{K_d}{T} F_k \\ &= \left(1 + \tfrac{K_d}{T}\right) y_{k+1} - \tfrac{K_d}{T} y_k \\ &= \left[\left(1 + \tfrac{K_d}{T}\right) C'_z A'_z - \tfrac{K_d}{T} C'_z\right] x'_k + \left(1 + \tfrac{K_d}{T}\right) C'_z B'_z u'_k \end{aligned} \tag{7.51}$$

Equation (7.51) shows that additional states of F_k^* can be added to the discrete state space model and that the state transition of this variable is purely dependent on other states x'_k and inputs u'_k of the current sample. The augmented state space model is represented in (7.52).

$$\begin{aligned} \overbrace{\begin{bmatrix} x'_{k+1} \\ F_{k+1}^* \end{bmatrix}}^{x''_{k+1}} &= \overbrace{\begin{bmatrix} A'_z & 0_{26\times4} \\ \left(1 + \tfrac{K_d}{T}\right) C'_z A'_z - \tfrac{K_d}{T} C'_z & 0_{4\times4} \end{bmatrix}}^{A''_z} \overbrace{\begin{bmatrix} x'_k \\ F_k^* \end{bmatrix}}^{x''_k} + \overbrace{\begin{bmatrix} B'_z \\ \left(1 + \tfrac{K_d}{T}\right) C'_z B'_z \end{bmatrix}}^{B''_z} u'_k \\ \underbrace{F_k^*}_{y'_k} &= \underbrace{\begin{bmatrix} 0_{4\times26} & I_4 \end{bmatrix}}_{C''_z} x''_k \end{aligned} \tag{7.52}$$

When a feedback law with a constant gain matrix K as shown in (7.53) is used on the system, the closed loop difference equation for the system states becomes (7.54). Computing the eigenvalues of the $A''_{z,cl} \in \mathbb{R}^{30\times30}$ matrix can then reveal the pole locations of the system and stability can be verified if all poles are located within the unit circle on the z-plane (i.e. magnitude of the poles are all less than unity).

$$u'_k = -K y'_k \tag{7.53}$$

$$x''_{k+1} = (A''_z - B''_z K C''_z) x''_k = A''_{z,cl} x''_k \tag{7.54}$$

The above state space model can also be used to test for the robust stability of the system when uncertainties are incorporated into the original system model. For the purpose of this analysis, all the uncertainties are assumed to be located in the environment and the actual environmental parameters are taken to be the summation of the nominal parameters with an additional uncertain term. Using the above approach and considering (7.35), (7.33) can be modified to give (7.55), where quantities accented with ~ are used to denote the uncertain terms. The introduction of uncertainties to the task space dynamics can also be graphically represented using the block diagram shown in Figure 7.11.

$$\begin{aligned}&\left(M_e + \widetilde{M}_e\right)\ddot{\Theta} + \left(B_e + \tilde{B}_e\right)\dot{\Theta} + \left(K_e + \widetilde{K}_e\right)\Theta = J^T F_{int} \\ \Rightarrow &\left(M_e + m_f J^T J + \widetilde{M}_e\right)\ddot{\Theta} + \left(B_e + b_f J^T J + \tilde{B}_e\right)\dot{\Theta} + \left(K_e + k_f J^T J + \widetilde{K}_e\right)\Theta \\ &= b_f J^T \dot{x}_r + k_f J^T x_r\end{aligned} \tag{7.55}$$

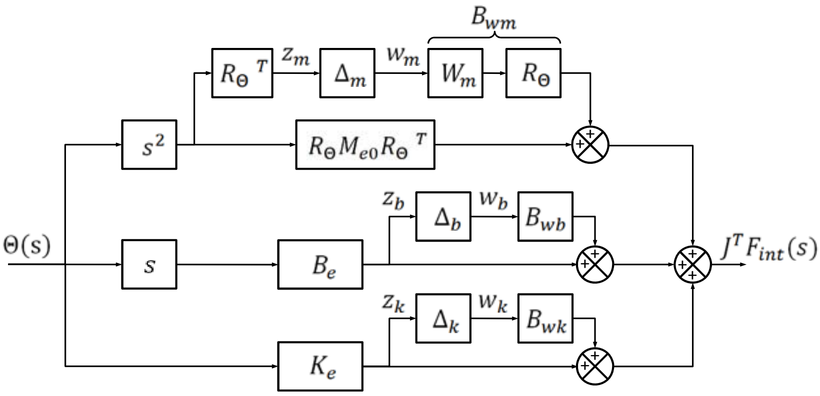

Figure 7.11: Uncertainty formulation of the task space environment.

It can be seen that the uncertainty terms $\widetilde{M}_e$, $\tilde{B}_e$ and $\widetilde{K}_e$ in (7.55) were in turn broken down into several blocks in the uncertainty model structure shown in Figure 7.11. The main reason for this was to make the problem more amenable to application of existing robust stability analysis methods. The relationships between the uncertainty matrices in (7.55) and the uncertain terms shown in Figure 7.11 are shown in (7.56) – (7.58). It should be noted that for the remaining of this section, the terms Δ_m, Δ_b and Δ_k will be referred to as uncertainty matrices while the terms B_{wm}, B_{wb} and B_{wk} will be referred to as uncertainty weighting matrices.

$$\widetilde{M}_e = R_\Theta W_m \Delta_m R_\Theta{}^T = B_{wm} \begin{bmatrix} \delta_{m1} & 0 & 0 \\ 0 & \delta_{m2} & 0 \\ 0 & 0 & \delta_{m3} \end{bmatrix} R_\Theta{}^T \tag{7.56}$$

$$\tilde{B}_e = B_{wb} \Delta_b B_e \tag{7.57}$$

$$\widetilde{K}_e = B_{wk} \Delta_k K_e \tag{7.58}$$

It can be seen from (7.56) – (7.58) that the method used to model uncertainties in the inertia tensor was slightly different compared to that for the environmental stiffness and damping. By assuming that uncertainties in the environmental inertia tensor only affect values of its principal components, and that the principal component axes are aligned with the global reference frame at zero task space coordinates, the inertia uncertainty can be written in the form shown in (7.56), with Δ_m being a real diagonal matrix and W_m also a diagonal and real weighting matrix. As less information can be assumed about the environmental stiffness and damping, the uncertainties in these parameters were left in a more general form as shown in (7.57) – (7.58), where both the uncertainty matrix and the uncertainty weighting matrix were general 3×3 complex matrices. Note also that the uncertainties for the stiffness and damping were given in multiplicative terms, as opposed to the additive approach used for the inertia parameter. This means that quantities in the W_m matrix must be selected so that they share the same units as that of the inertia tensor, while B_{wb} and B_{wk} are simply dimensionless weightings.

Robust stability is generally analysed by first grouping all uncertainty matrices into one block and the remaining closed loop system into another. Using the uncertainty assignment presented in Figure 7.11, the overall closed loop force control system can be put into such a structure and this is shown in Figure 7.12, where the 9×9 matrix M_{sys} is used to represent the dynamics of the nominal system under closed loop force control. This particular form will then allow straight forward application of methods such as small gain theorem and structured singular value analysis for the determination of robust stability.

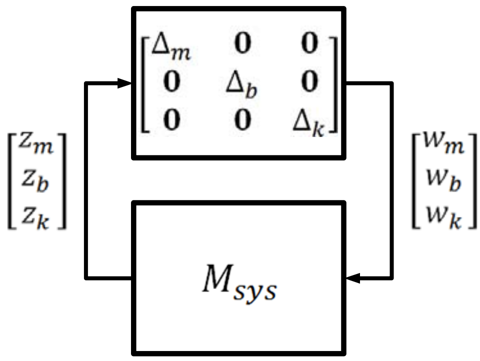

Figure 7.12: Typical representation of systems with uncertainties where the uncertainty block is separated from the overall system.

The M_{sys} block shown in Figure 7.12 can be obtained by discretising an extended version of the state space model given in (7.46) and closing the loop with the discrete PD force control law. The extension is required to incorporate additional inputs and outputs to M_{sys}. The inputs of M_{sys} are the outputs of the uncertainty matrices $\varepsilon = [{w_m}^T \quad {w_b}^T \quad {w_k}^T]^T$, while the outputs of M_{sys} are the inputs to the uncertainty matrices $\zeta = [{z_m}^T \quad {z_b}^T \quad {z_k}^T]^T$. It should be noted that the reason behind the disappearance of the commanded current and PD filtered force measurements (the original inputs and outputs of the state space system) from the input and output ports of M_{sys} was due to the completion of the force feedback loop within M_{sys}. Extension of the state space model as described above had led to the representation of M_{sys} as given in (7.59). Construction of the output and direct feed through matrices ($C_{z\zeta}$ and $D_{z\zeta}$) can be done by considering relationships $z_m = {R_\Theta}^T \ddot{\Theta}$, $z_b =$

$B_e\dot{\Theta}$ and $z_k = K_e\Theta$. Additionally, since (7.60) is true by definition and (7.61) can be obtained from (7.55) and (7.60), the continuous input matrix for ε (B_ε) will only have non-zero entries at rows corresponding to $\ddot{\Theta}$.

$$\begin{aligned} x''_{k+1} &= A''_{z,cl}x''_k + \begin{bmatrix} B_{z\varepsilon} \\ \left(1+\frac{K_d}{T}\right)C'_zB_{z\varepsilon} \end{bmatrix}\varepsilon_k \\ \zeta_k &= C_{z\zeta}x''_k + D_{z\zeta}\,\varepsilon_k \end{aligned} \tag{7.59}$$

$$\begin{aligned} \widetilde{M}_e\ddot{\Theta} + \widetilde{B}_e\dot{\Theta} + \widetilde{K}_e\Theta &= B_{\varepsilon,\ddot{\Theta}}\varepsilon \\ &= \begin{bmatrix} B_{wm} & B_{wb} & B_{wk} \end{bmatrix}\begin{bmatrix} w_m \\ w_b \\ w_k \end{bmatrix} \end{aligned} \tag{7.60}$$

$$\left(M_e + m_fJ^TJ\right)\ddot{\Theta} = b_fJ^T\dot{x}_r + k_fJ^Tx_r - \left(B_e + b_fJ^TJ\right)\dot{\Theta} - \left(K_e + k_fJ^TJ\right)\Theta - B_{\varepsilon,\ddot{\Theta}}\varepsilon \tag{7.61}$$

The small gain theorem is a relatively simple method of analysing the robust stability of systems which are expressed in the form shown in Figure 7.12. It states that the closed loop system shown in Figure 7.12 will be stable as long as the product of the maximum singular value for the uncertainty block and that for M_{sys} is less than unity over all frequencies. Typically, the uncertainty weighting is "factorised" out of the uncertainty matrix and included in M_{sys} so that the norm of the uncertainty block can be set to unity. With this condition, the stability of the closed loop system will be fully reliant on the maximum singular value of M_{sys}. As long as M_{sys} is stable, stability of the closed loop system will be guaranteed if this maximum singular value is less than one. Although relatively simple to compute, the small gain theorem has the disadvantage of being overly conservative [132, 133] as it allows all elements in the uncertainty block to take on arbitrary values so long as it satisfies the unity norm condition.

An improved analysis method is the structured singular value, which does consider the structure within the uncertainty block. Formally, the structure singular value is defined as (7.62) [132], where μ is the structured singular value, $\widetilde{\Delta}$ is the set of uncertainty matrix which satisfies the desired structure and $\sigma_{max}(\Delta)$ is used to denote the maximum singular value of Δ. In other words, the structured singular value is inversely related to the size/norm of the smallest uncertainty matrix Δ (which shares the same structure as $\widetilde{\Delta}$) that can cause the system M_{sys} to become unstable by making $det\left(I - M_{sys}\Delta\right) = 0$. Based on this definition, a smaller structured singular value indicates higher robust stability. When the uncertainty weightings have been selected to allow a maximum norm of one for Δ, it can be seen that as long as μ is smaller than unity, the system will be robustly stable for all possible systems which falls within the chosen uncertainty bounds. It should be noted however that analytical solutions to μ can only be obtained for certain special cases and it is in general estimated numerically. The `mu` function in MATLAB is one such function and it had been used in this work.

$$\mu(M_{sys}) = \frac{1}{\inf_{\Delta \in \widetilde{\Delta}}\{\sigma_{max}(\Delta) | det(I - M_{sys}\Delta) = 0\}} \tag{7.62}$$

As M_{sys} is frequency dependent, computation of the structured singular value will also need to be done at all frequencies and the largest result should be returned. In order to do so, the frequency response of M_{sys} must be obtained. By considering the discrete state space model in (7.59), the z-transform of ζ can be related to the z-transform of ε through (7.63). Since $z = e^{sT}$ and the substitution of $s = j\omega$ is used to obtain frequency response of transfer functions, the frequency response $M_{sys}(j\omega)$ is given by (7.64).

$$M_{sys}(z) = \frac{\zeta(z)}{\varepsilon(z)} = \left\{C_{z\zeta}\left(zI - A''_{z,cl}\right)^{-1}\left[\frac{B_{z\varepsilon}}{\left(1 + \frac{K_d}{T}\right)C'_z B_{z\varepsilon}}\right] + D_{z\zeta}\right\} \tag{7.63}$$

$$M_{sys}(j\omega) = \frac{\zeta(j\omega)}{\varepsilon(j\omega)} = \left\{C_{z\zeta}\left(e^{j\omega T}I - A''_{z,cl}\right)^{-1}\left[\frac{B_{z\varepsilon}}{\left(1 + \frac{K_d}{T}\right)C'_z B_{z\varepsilon}}\right] + D_{z\zeta}\right\} \tag{7.64}$$

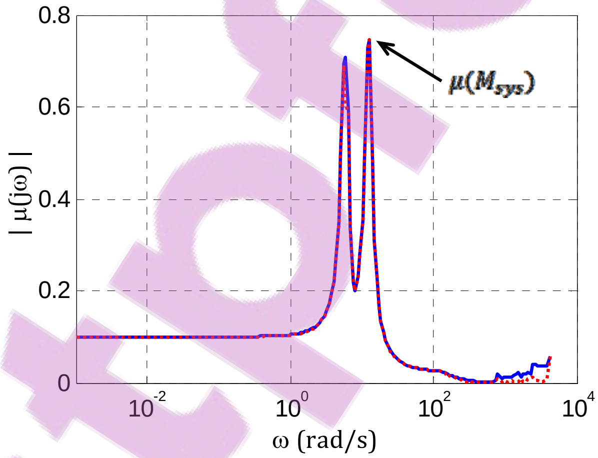

Figure 7.13: The structured singular values of the system at different frequencies. Solid line indicates the upper bound and dotted line indicate the lower bound.

The result in (7.64) can then be computed on a frequency grid to produce $M_{sys}(j\omega)$ at discrete intervals. This information can then be passed into the `mu` function to obtain an upper and lower bound on $|\mu(j\omega)|$ over the considered frequencies. The maximum of the upper bound of $|\mu(j\omega)|$ can then be used as an estimate for the structured singular value of M_{sys}. The result of the structured singular value analysis of the system linearised about the zero task space coordinates is plotted in Figure 7.13 to give an indicative example of $|\mu(j\omega)|$. The highest peak which is considered to be the structured singular value for M_{sys} is also marked on the plot. In this work, the frequency grid used to compute $M_{sys}(j\omega)$ spans from 10^{-3} rad/s to $\frac{\pi}{T}$ rad/s (the frequency beyond which aliasing will occur in the discrete control system). The final frequency grid used is uniformly spaced on the logarithmic frequency scale with 200 intervals. The choice of the number of intervals was selected by trial and error and is done by gradually decreasing the number of frequency intervals while observing the peak values of $|\mu(j\omega)|$ obtained from the `mu` function. The smallest number of intervals which preserves the value of the peaks was chosen for use in the final analysis. For simplicity, the uncertainty weighting matrices were not chosen to be frequency dependent and were simply selected as scaled identity matrices. Additionally, environmental stiffness and damping had also been chosen to be the same as the scaled identity matrices used to obtain the gain margins in Section 7.4.1.

7.5 Proposed Actuator Force Controller

Based on the above analyses, a gain scheduled actuator joint force controller was proposed and implemented on the ankle rehabilitation robot. The structure of this controller is shown in Figure 7.14, where F_c is a vector of the commanded forces and F_{meas} is a vector of forces as provided by the force sensors. K is the gain matrix which is given by (7.65), where $U_m{}'$ and v_0 are the output basis vectors of $M_e{}'$ that can be obtained from the singular value decomposition of $M_e{}'$. Furthermore, $\mathrm{diag}(.)$ is a function that forms a diagonal matrix using its argument and k_i are the controller gains applied to the i^{th} basis vector, with $i = 0$ referring to the gain along the null space direction and $i = 1,2,3$ referring to gains along decoupled directions with the first, second and third largest singular values respectively.

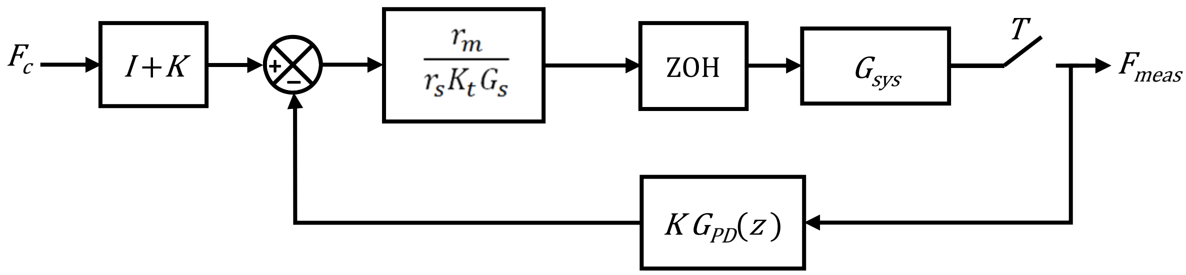

Figure 7.14: Structure of the final actuator force control law.

$$K = [U_m{}' \quad v_0]\mathrm{diag}([k_1 \quad k_2 \quad k_3 \quad k_0])[U_m{}' \quad v_0]^T \tag{7.65}$$

Gain scheduling for the controller gains in two of the three non-null decoupled directions were done using piecewise linear functions fitted below the critical gain values obtained in Section 7.4.1. These relationships are shown as solid lines in Figure 7.15, together with the critical gain values for comparison. The remaining non-null direction on the other hand was assigned a constant gain since the critical gain variation over the range of singular values considered is relatively small. Additionally, as the null direction is not influenced by the configuration of the manipulator, it is also assigned a constant gain which is below its gain margin.

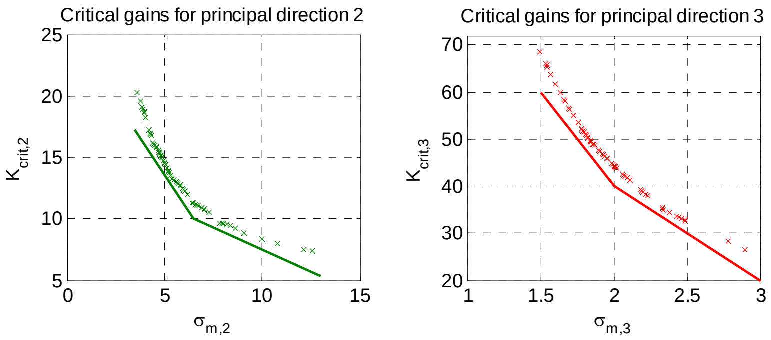

Figure 7.15: Linear piecewise functions used for gain scheduling in different decoupled directions of M_e'.

As the gain margins obtained in Section 7.4.1 was computed with environmental stiffness and damping which are proportional to the assumed environmental inertia, gains which will result in a stable system under the considered circumstances may no longer be suitable when the environmental parameters deviate from these nominal values. In order to obtain a more realistic evaluation on the stability of the proposed controller, the analysis should be carried out using parameters which can reflect the actual operating conditions. While the determination of gain margins using the method shown in Section 7.4.1 is not possible for systems with general environmental stiffness and damping matrices (i.e. does not share the same decoupled directions with the environmental inertia), the stability of such systems can still be validated using the state space formulation. Additionally, by incorporating the robustness analysis, one can obtain a range of operating environment which will allow stable operation of the controller.

The computational ankle model developed in chapter 5 was used to obtain a more realistic operating environment for the ankle rehabilitation robot. The environmental stiffness experienced during passive ankle motion was estimated from the static torque observed at different ankle and subtalar joint displacements. These torque profiles were then numerically differentiated with respect to the ankle and subtalar displacements to produce the stiffness matrix K_{as}, which is a 2×2 matrix. This matrix was subsequently transformed into the manipulator task space to give a 3×3 stiffness matrix K_e, using a procedure which will be discussed in more detail in chapter 9. The environmental damping matrix B_e on the other hand was assumed to have the form shown in (7.66), with both a constant and a variable component. In (7.66), b_e is a scalar constant which gives a base level of damping while $\gamma \ll 1$ is a proportionality constant between the damping and stiffness parameters. The variable component had been included to introduce additional damping in a proportional manner to the ankle stiffness and is mainly used to reduce the damping factor experienced at foot orientations with very high stiffness.

$$B_e = b_e I + \gamma K_e \tag{7.66}$$

A structured singular value analysis of the proposed actuator force controller was carried out to determine its stability and robustness properties. This analysis was carried out at discrete points in the task space which corresponds to different combinations of ankle and subtalar joint displacements within a certain range ($\pm 40°$ at 4° interval for the ankle displacement and $\pm 30°$ at 3° interval for the subtalar displacement). At each of these task space coordinates, the environmental stiffness and damping matrices were obtained and used to form the nominal external environment. The environmental inertia matrix was also modified accordingly using (7.48) and by assuming constant principal components in the inertia tensor. The uncertainty weighting matrices used in this analysis is given in Table 7.4. The uncertainties considered represents about 5% of the total nominal mass parameter and 10% variations in the stiffness and damping parameters. Note that the environmental mass includes that of the manipulator and as a result of that, 5% uncertainty in the total nominal mass parameters actually relates to a higher proportion (about 10%) of the foot rotational inertia according to estimates derived from [134].

Table 7.4: Uncertainty weighting matrices used in the robust stability analysis.

Uncertainty Weighting	B_{wm}	B_{wb}	B_{wk}
Value/expression	$0.002R_{\Theta}$ kgm^2	$0.1I_3$	$0.1I_3$

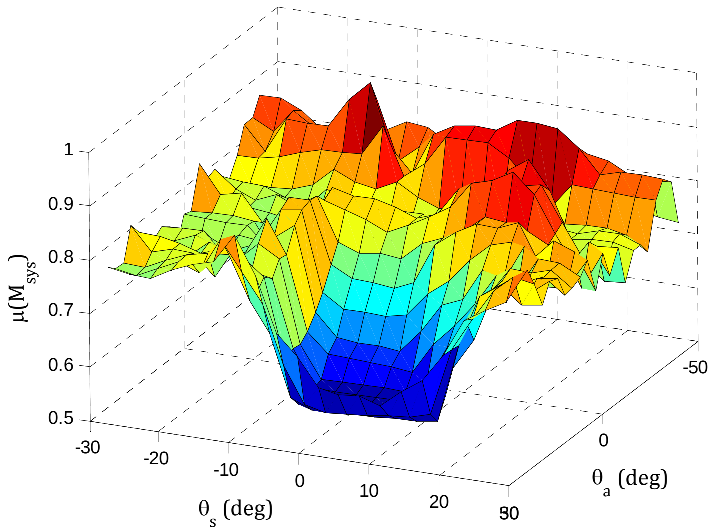

Figure 7.16: Values of $\mu(M_{sys})$ computed over a range of foot orientations defined by the ankle (θ_a) and subtalar (θ_s) joint displacements.

Stability analysis of the $A''_{z,cl}$ matrix in M_{sys} had shown that all system poles are located within the unit circle on the z-plane for the foot configurations tested, thus proving system stability and ensuring that structure singular values can be used to evaluate the robust stability of the system. The results of the structured singular value analyses are summarised in Figure 7.16, where the computed values of $\mu(M_{sys})$ are plotted over their corresponding ankle and subtalar joint displacements. It can be seen from this figure that all the structured singular values are below unity, thus indicating that the system will remain stable as long as the environmental uncertainties remain within the prescribed bounds.

It should be noted that although the final force controller used is not exactly the same as the partial decoupling controller presented in Section 7.2, they do have considerable similarities. The main feature shared by these two controllers is the application of different control gains along different decoupled directions of the M_e'matrix (recall that the output basis vectors of M_e' can be shown to be identical to that of the coupling matrix D when the same task space mass matrix is used). Secondly, the relative magnitudes of the controller gains in the non-null decoupled directions can also be sorted in the same order for both these control laws, thus indicating that the final force control law will still achieve some level of decoupling. Furthermore, as with the partial decoupling controller, the final control law also allows independent gain selection along the null space of the manipulator Jacobian transpose (which is also the null space of M_e').

7.6 Simulation Results

Simulations using the simplified state space models discussed above were carried out to evaluate the efficacy of the proposed actuator force controller. A linear state space model had been used in this simulation, where the linearisation point was taken to be the origin of the task space coordinates. This means that the manipulator Jacobian used to construct the state space model was that corresponding to this orientation. Two sets of tests were carried out to evaluate the performance improvements of the proposed controller over a force controller with uniform gains across all directions (hereafter referred to as the uniform gain controller). The first involves a test on disturbance rejection capability while the second centres on the backdriveability of the controlled manipulator. Both these simulations were carried out in the Simulink environment and continuous state space models were used to describe the plant while the PD filter and controller was implemented as discrete time blocks. The system and parameters used are similar to those employed throughout this chapter while the controller gain matrices used are defined according to (7.65). Details of these parameters can again be found in Appendix C.

7.6.1 Test for Disturbance Rejection

In the first test, frictional forces along the actuator rod were included as inputs to the continuous state space model to introduce disturbances into the system. A simple friction model had been used whereby the friction force F_{fric} is a saturation function of the rod velocity as shown in (7.67), with $F_{f,max}$ being the maximum friction and η being a large constant. The simulation is run with a sinusoidal profile for the desired force and different gain matrices were applied in two separate simulations, both with the PD filter in place. The desired and actual force profiles for each actuator, along with the force errors are shown for both the proposed controller and the uniform gain controller in Figure 7.17. In the first four plots of each column, the desired force profiles are shown as dotted lines while actual measured forces are given as solid lines. The final plot on the other hand presents the force errors obtained from all four actuators.

$$F_{fric} = F_{f,max}\min(\max(\eta\dot{x}_r, -1), 1) \tag{7.67}$$

Discussion

It is clear from the results above that the proposed controller showed much better force tracking accuracy, thus indicating its ability to better reject disturbances. This is not surprising as the gain of the uniform gain controller is limited by the least stable decoupled direction whereas the proposed method permits the use of higher gains (and hence better disturbance rejection) in more stable directions.

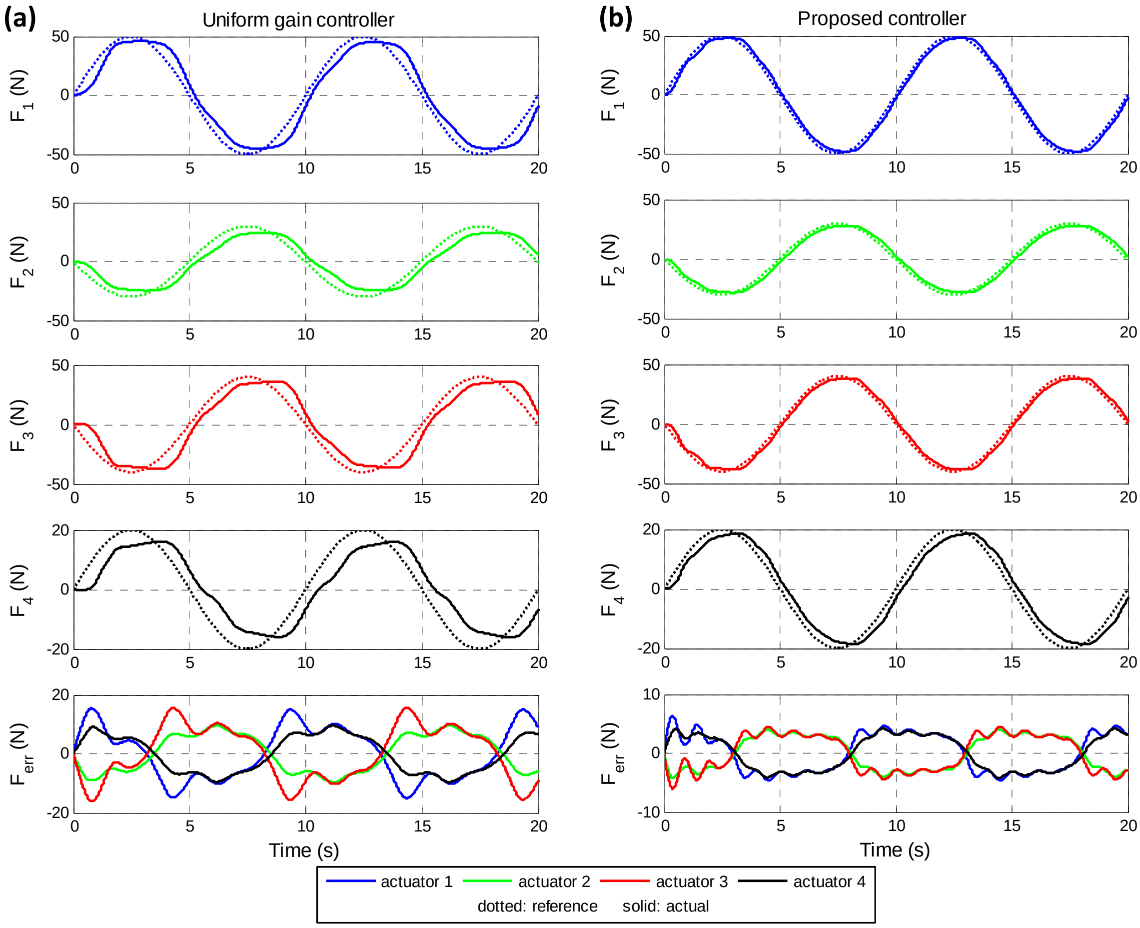

Figure 7.17: Desired (dotted lines) and measured (solid lines) actuator force profiles, as well as force errors F_{err} for (a) the uniform gain controller and (b) the proposed controller.

7.6.2 Test for Backdriveability

The second test involved a study of the backdriveability of the force controlled manipulator. In this test, the main aim was to verify that the proposed controller can partially decouple the system and result in an effective inertia matrix (see equation (7.12)) which is more similar to the actual environmental inertia. This investigation therefore requires the incorporation of an external torque into the inputs of the state space system and can be easily accomplished by considering the rows of the input matrix which corresponds to the task space accelerations. The desired forces were set to be zero in this test to allow “maximum” backdriveability of the manipulator and equal levels of external torques were applied in all three task space directions. The stiffness of the environment used in this simulation was also decreased to improve the damping factor of the system and reduce oscillations to facilitate inference of acceleration from the task space displacements. Plots relating to the task space displacements are shown in Figure 7.18.

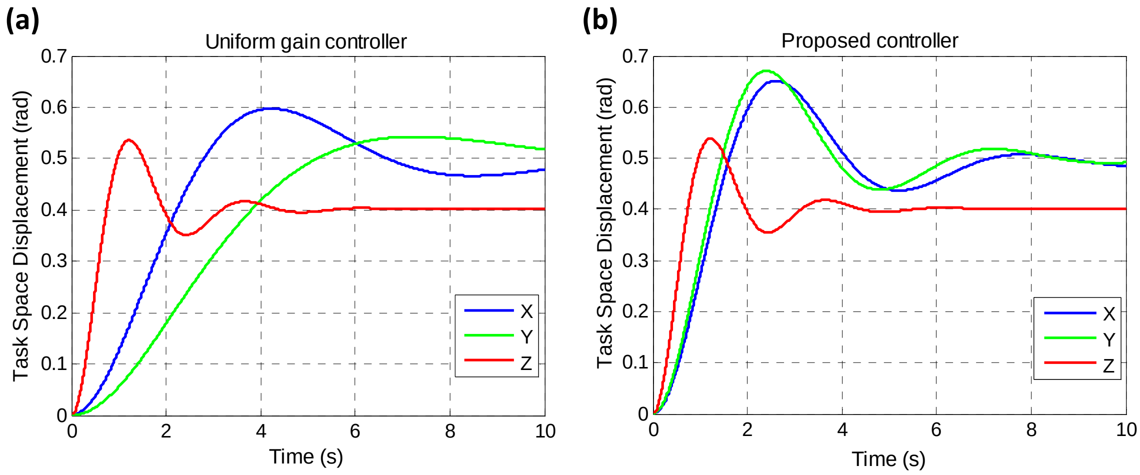

Figure 7.18: Task space displacements of the system obtained in the backdriveability simulation with (a) the uniform gain controller and (b) the proposed controller.

Discussion

For the proposed controller, motion in the Z direction appears to have the greatest acceleration for the same applied torque. Movements in the X and Y directions on the other hand can be considered to have similar responsiveness to an applied torque. A significantly larger spread in terms of responsiveness however can be observed from results obtained using the uniform gain controller, with the Z direction being the “fastest”, followed by the X and Y directions.

The behaviours observed above can be better explained when considering the effective inertia matrix. Using the notations of the higher order dynamic model, this effective mass matrix can be represented as (7.68), where K is the controller gain matrix. The effective mass matrix for both the proposed controller and the uniform gain controller, together with the original environmental inertia matrix are given in Table 7.5. It is immediately clear from the consideration of these matrices that the effective inertia of the force controlled system is significantly larger than that of the original environment. This is mainly due to the large effective actuator mass contributed by the high transmission ratios. However, by making a comparison between the effective inertia matrices of both the controllers, it can be concluded that the proposed control strategy is capable of producing an effective inertia matrix which is more uniform along the diagonal, with smaller off diagonal elements. Since the inertia matrix is organised in such a way that its first, second and third columns corresponds respectively to accelerations in X, Y and Z directions, it can be seen that the responsiveness observed in Figure 7.18 can be inversely correlated to the magnitude of elements along the diagonally dominant inertia matrix, thus confirming that the effective inertia matrix given in (7.12) is still applicable on systems with higher order dynamics.

$$M_{eff} = M_e + (m_{a1} + m_{a2})J^T(I + K)^{-1}J \tag{7.68}$$

Table 7.5: The environmental inertia matrix and the effective inertia matrices for the force controllers considered in the backdriveability simulation

M_e	M_{eff} of final controller	M_{eff} of uniform gain controller
$\begin{bmatrix} 0.047 & 0 & 0 \\ 0 & 0.045 & 0 \\ 0 & 0 & 0.04 \end{bmatrix}$	$\begin{bmatrix} 0.2714 & 0 & 0 \\ 0 & 0.2308 & 0.0014 \\ 0 & 0.0014 & 0.0642 \end{bmatrix}$	$\begin{bmatrix} 0.6455 & 0 & 0 \\ 0 & 1.4691 & 0.0120 \\ 0 & 0.0120 & 0.0643 \end{bmatrix}$

7.7 Experimental Results

Several experimental trials had been carried out on the ankle rehabilitation robot developed in this research to evaluate the effectiveness of the proposed actuator force controller. The sole participant of these experiments is an adult male (1.75m height) and ethics approval had been granted by The University of Auckland Human Participants Ethics Committee (Ref. 2009/480). These experiments can be classified into two groups, one to highlight the effects that different force controllers have on system stability and another to evaluate and compare the force control performance of different controllers in executing tasks required by the rehabilitation exercises.

7.7.1 Stability Experiment

Since one of the main motivations behind the development of the proposed force controller is to improve the system stability, one of the experimental trials carried out in this work was centred on demonstrating the stability improvement brought on through the application of the proposed control scheme. This experimental trial involved the operation of the ankle rehabilitation robot under pure force control, where the force commands were selected by requiring that the vertical component of the null space forces be summed to a desired value to provide support for the user's lower limb, while all remaining non-null space forces are set to be zero. The reader is referred to chapter 8 for more details on this redundancy resolution scheme. The subject was then prompted to move his foot freely in primarily the plantar/dorsi-flexion direction. This experiment was done for four different actuator force controllers, which are listed and described in Table 7.6. The results of this experiment are presented in Figure 7.19. Note that only the forces measured along one of the actuators are shown for brevity, and forces along other directions behave in a similar manner.

Table 7.6: Actuator force controllers considered in the stability experiments.

Controller	Description
P control, uniform gain of 10	Measured force is fed directly into disturbance observer, the gain matrix K in (7.65) is obtained by selecting $k_1 = k_2 = k_3 = k_4 = 10$
PD control, uniform gain of 16	Measured force is fed into disturbance observer through a proportional-derivative filter $G_{PD}(z)$, the gain matrix K in (7.65) is obtained by selecting $k_1 = k_2 = k_3 = k_0 = 16$
Proposed controller	Measured force is fed into disturbance observer through a proportional-derivative filter $G_{PD}(z)$, the gain matrix K in (7.65) is obtained by observing the gain margins given in Figure 7.15
Proposed controller + minimum gain of 14	Measured force is fed into disturbance observer through a proportional-derivative filter $G_{PD}(z)$, the gain matrix K in (7.65) is obtained by setting $k_1 = k_0 = 14$, while k_2 and k_3 are obtained by observing the gain margins given in Figure 7.15

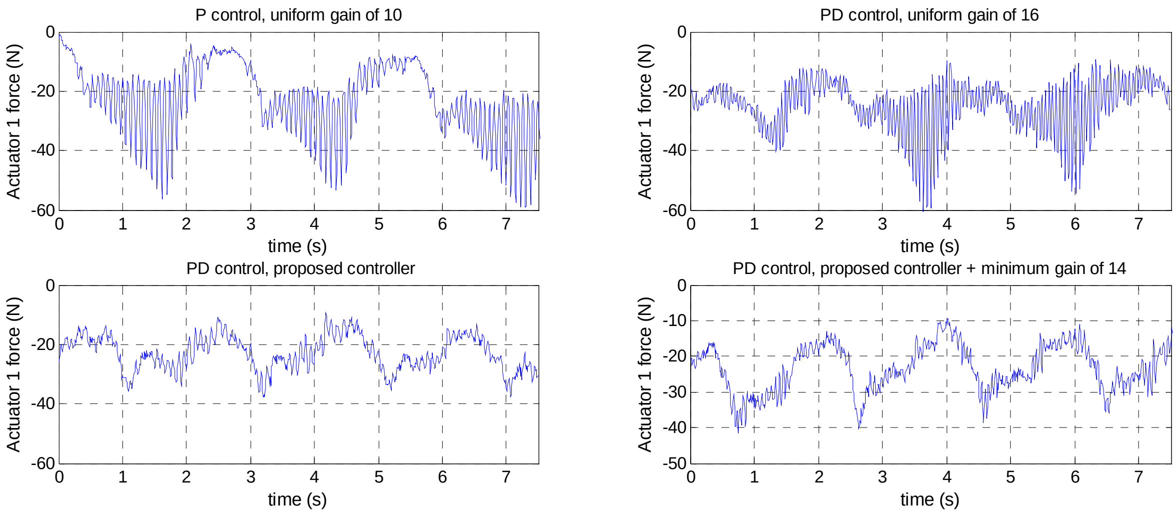

Figure 7.19: Forces measured along actuator 1 using different actuator force controllers.

Discussion

From the experiments, motions obtained using the first two controllers showed clear signs of instability with significant levels of oscillation. This is backed up by the actuator force measurements given in Figure 7.19. Since the gains of the uniform gain controllers were selected to be the lowest gains that will result in perceptible oscillations in the robot, it can be seen that the addition of the proportional derivative term in the feedback loop does indeed improve the stability of the system and allow better performance through application of larger controller gains. Additionally, Figure 7.19 also shows that although some of the gains applied along certain decoupled directions of the third and fourth controllers considered were larger in value than that of the second uniform gain controller, these controllers remained stable during operation. This supports the idea that there are directions which are less stable and that these directions are ultimately limiting the maximum gain that can be applied in a controller with uniform gains. Consequently, the important conclusion that can be drawn from this experiment is that when actuators are independently controlled with its own disturbance observer (the uniform gain control approach), the maximum performance achievable would be limited due to the upper gain limit imposed by system stability. However, when the coupling introduced by the manipulator kinematics and inertia is taken into account, it is possible to manage stability through application of different gains along different decoupled directions of M_e'. This allows higher gains in more stable directions, and thus results in an improved overall performance.

7.7.2 Experiments for Performance Evaluation

In additional to the stability experiment, further trials were also carried out using both a uniform gain controller and the proposed controller to illustrate the performance improvements afforded through incorporation of the coupling information into the controller. These experiments were again done on the developed ankle rehabilitation robot and involve three main tasks which are considered important for implementation of ankle rehabilitation exercises. The first is the ability to maximise the backdriveability of the robot by commanding zero task space moments (such as that done in the stability experiment), the second is to move the foot passively using impedance control (see Chapter 8 for details), while the third is explicit control of the robot-user interaction moment. All these tasks were carried out using a uniform gain actuator force controller with a gain of 5, and the proposed controller (note that the gain of 5 is also used along the output basis vector of M_e' which has the largest singular value). The results for the first two tasks described above are summarised in Figure 7.20 and Figure 7.21, while the root mean square values of the actuator force errors are provided in Table 7.7. Additionally, results obtained from the third task are also presented in Figure 7.22 and Figure 7.23.

Table 7.7: Root mean squares of actuator force errors for both the uniform gain controller and the proposed controller during free and passive motion tasks.

Controller	Task	RMS force errors for actuator			
		1	2	3	4
Uniform gain	Free motion	18.1557 N	13.8108 N	13.9476 N	22.0288 N
	Passive motion	17.4053 N	8.7092 N	12.8562 N	19.5321 N
Proposed	Free motion	9.2550 N	8.0545 N	7.0205 N	13.0206 N
	Passive motion	8.2829 N	7.2636 N	5.6524 N	10.9297 N

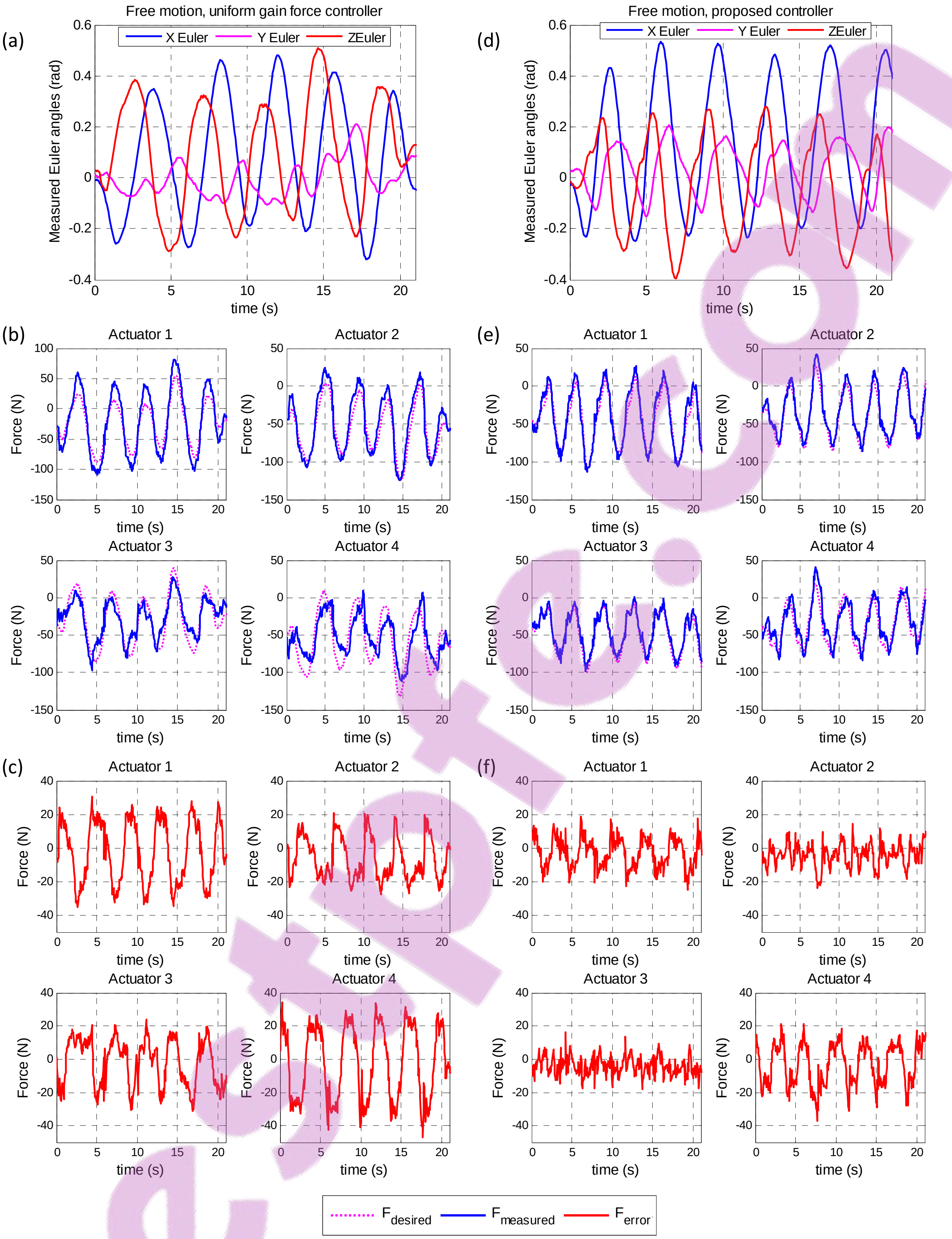

Figure 7.20: Experimental results obtained during free motion of the user's foot on the ankle rehabilitation robot. The Euler angle trajectories for the uniform gain controller is shown in (a) while the associated actuator forces and force errors are given in (b) and (c). Similarly, the motion trajectories obtained using the proposed controller is given in (d) and its associated forces and force errors are shown in (e) and (f).

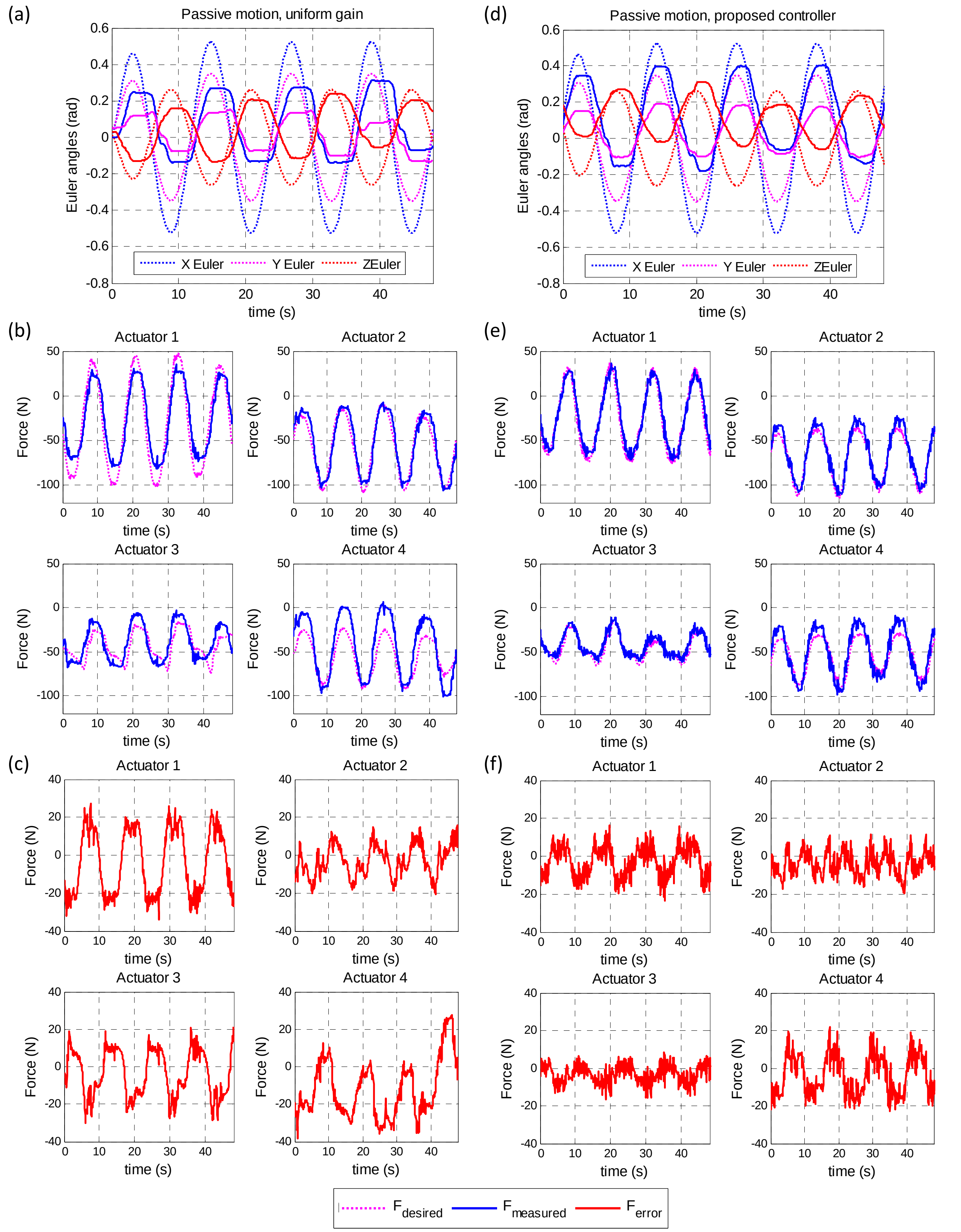

Figure 7.21: Experimental results obtained when foot of the user is moved passively by the ankle rehabilitation robot. The Euler angle trajectories for the uniform gain controller is shown in (a) while the associated actuator forces and force errors are given in (b) and (c). Similarly, the motion trajectories obtained using the proposed controller is given in (d) and its associated forces and force errors are shown in (e) and (f).

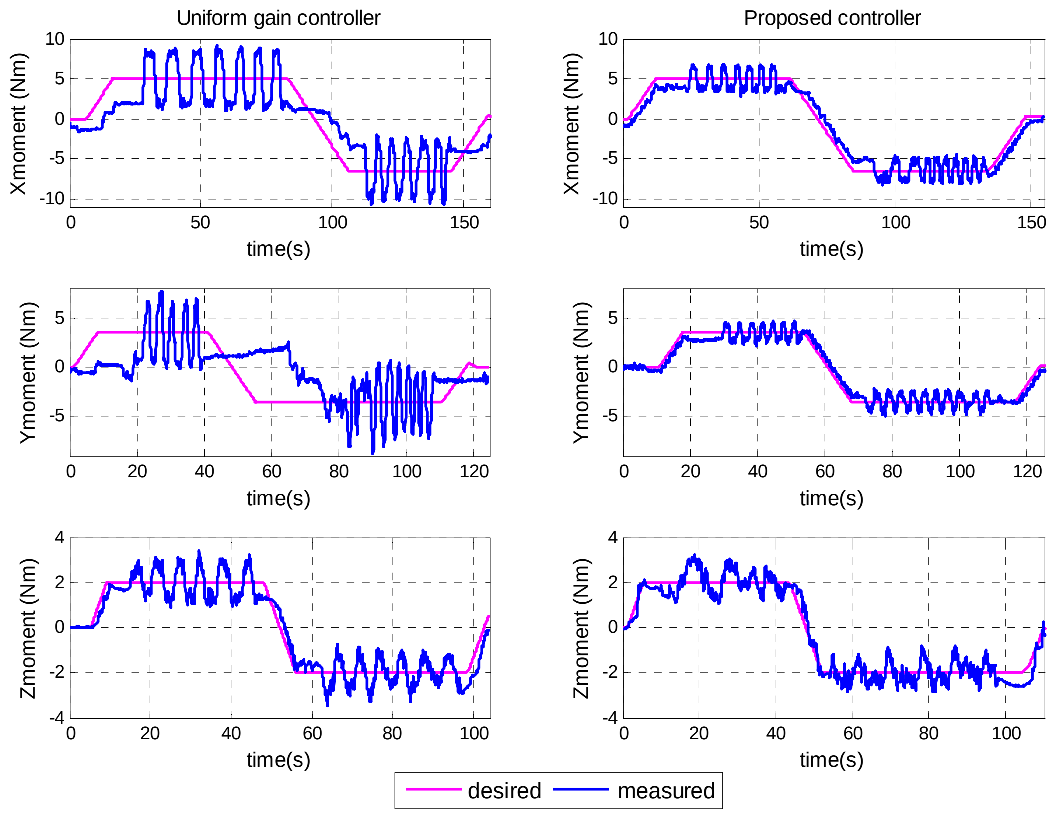

Figure 7.22: Desired and measured ankle moments about the ankle as obtained from the torque control experiment.

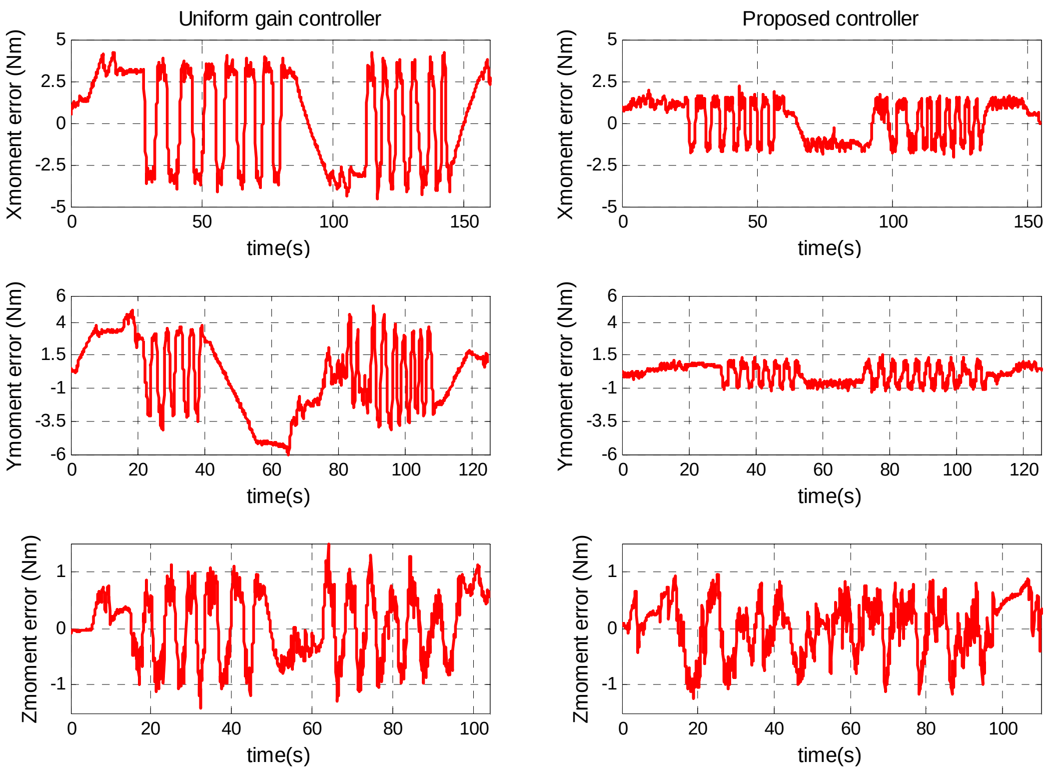

Figure 7.23: Moment errors as obtained from the torque control experiment.

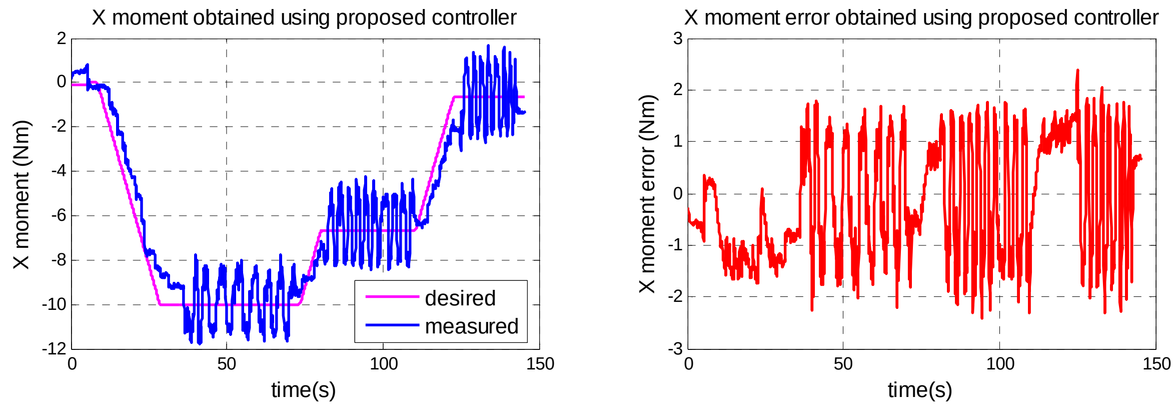

Figure 7.24: Experimental results obtained by using the proposed controller in regulation of the X interaction moment about three different levels.

Discussion

It can be seen from the results obtained in the free and passive motion trials that utilisation of the proposed control scheme over the uniform gain controller can significantly reduce the actuator force errors, with some of the actuators experiencing a force error reduction of about 50%. Comparison of Figure 7.20a and Figure 7.20d also suggests that the force proposed controller is more capable in terms of maximising the compliance of the ankle rehabilitation robot since it appears that motion recorded using the proposed controller are of larger amplitudes and velocities relative to that of the uniform gain controller. For the case of passive motion, examination of Figure 7.21a and Figure 7.21d indicates that the reference trajectory used in the impedance controller is tracked more closely with a smaller time delay when the proposed controller is used in place of the uniform gain controller. This indicates that rejection of disturbance forces such as friction is considerably improved in the proposed control scheme, thus allowing more accurate rendering of the desired robot impedance.

Inspection of results from the torque control trials also showed similar trends, where moment tracking capability of the robot is markedly improved in the X and Y directions when the proposed controller is used over the uniform gain controller. The moment performance along the Z direction however is similar between the two controllers. This can be explained by how the task space moments are related to the actuator forces through the manipulator Jacobian transpose J^T. Singular decomposition of J^T can be used to show that the output basis vector of J^T with the most influence on the Z direction is linked to an input basis vector which is closely aligned with the basis vector of K with the smallest gain. Since this smallest gain is also of the same magnitude as the gain used in the uniform gain controller, it is not surprising that similar moment errors were observed along the z-direction. Similarly, the X and Y task space moments can also be found to be more closely linked to the directions where gains k_2 and k_3 are applied in the proposed controller. This further agrees with the observation that smaller moment errors were recorded in the Y direction.

The results of the torque control trials have suggested that the moment errors are rather large, even with the use of the proposed controller. It should be noted however that this error is mainly caused by frictional effects and does not vary significantly with the amplitude of the commanded torque levels. This is shown through Figure 7.24, where the moment regulation performance of the robot in the X direction was tested at three different levels. It is clear from the moment error plot that the magnitude of the errors remained relatively constant regardless of the value of the reference moment. This implies that the robot is not capable of realising the desired moment in a very precise manner. Given that low moment commands are used mainly to improve robot backdriveability, the above results means that an effective frictional moment of approximately 1.5Nm is to be expected on the robot. While not ideal, this is considered to be acceptable for this application, as the user should be able to easily overcome such resistance. For tasks involving larger moment commands such as strengthening exercises, the moment error will become less significant and will not severely degrade the performance of the robot.

7.7.3 Comparison of Simulation and Experimental Results

It is worth noting that the critical gain values observed in the experiments are significantly larger than those observed from the Bode diagrams (and hence the model used in simulation). The reason for this could be that there are discrepancies between the assumed and the actual system parameters. However, an additional cause for this could be that the frictional forces along the actuators (which are left out of the actuator model for simplicity) are providing additional nonlinear damping to the system, therefore allowing the use of larger controller gains. Furthermore, the assumption used in the design of the MIMO controller which specifies that the environmental stiffness and damping be proportional to the environmental inertia may also not hold in the real experimental trial. This would have an effect of the validity of the gain margins. The actual changes to the gain margins caused by deviations from such an assumption will be rather difficult to explore due to the increased complexity of the problem when the transfer functions cannot be fully decoupled. Nonetheless, since larger gains were permitted in the experiments compared with the controller designed based on the system model, the violation of this assumption does not appear to pose significant safety concerns to the operation of the ankle rehabilitation robot.

A comparison of the simulation (Figure 7.17) and experimental (Figure 7.21) results involving the passive motion task shows that the motion variables recorded in the simulation differed considerably from those obtained from experiments. Clearly, differences in the motion trajectories are caused mainly by the fact that a linearised model is used in simulation which assumes a constant and isotropic environmental stiffness, while in real life the ankle stiffness is anisotropic and varies with foot configuration. Further, friction is modelled in a simple manner in the simulation using a saturation function while in reality is it more complex and can vary along the actuator. Nonetheless, the pattern of the force errors does somewhat agree between the simulation and experimental results. It can be seen that the force errors obtained experimentally using the proposed controller is indeed more oscillatory compared to that obtained using the uniform gain controller, as predicted from the simulation. Additionally, the experimental results also shows an approximately 50% reduction in force errors for certain actuators, and this trend is shared by the results obtained from simulation. This indicates that despite the simplifications, the model used in the simulation and analysis does indeed capture some of the characteristics of the real system. Consequently, observations obtained from analysis of the actuator model should be equally applicable to the actual system.

7.8 Chapter Summary

This chapter detailed the development of a multi-input multi-output actuator force controller for the ankle rehabilitation robot used in this research. The coupling between actuator forces was first identified and an initial design of a disturbance observer based decoupling force control scheme which considers the kinematic and inertial characteristics of the robot was presented. While this decoupling control scheme cannot be implemented directly on the robot due to stability issues originating from the presence of unmodelled dynamics, it had provided valuable insights into the coupled force dynamics by highlighting the possibility of transforming the force control problem into a separate force coordinate frame which bases are spanned by the output basis vectors or decoupled directions of the coupling matrix D.

Using this transformation, further analyses were carried out on a higher order model of the actuator which includes the actuator and force sensor compliance. By applying certain simplifying assumptions, the force control problem was completely decoupled along these decoupled directions and stability analyses were independently conducted on these different directions. Based on these analyses, an additional proportional derivative filter was included into the disturbance observer and gain margins along these decoupled directions were established for different orientations of the robot end effector. It was found that the gain margins vary rather significantly among different decoupled directions as well as across different end effector orientations of the ankle rehabilitation robot. This had led to the proposal of a gain scheduled MIMO actuator force controller in this research. This controller was subsequently tested for robust stability through the use of structured singular value analysis, with the nominal environmental stiffness and damping matrices estimated from the computational ankle model developed in Chapter 5, and the nominal robot inertia matrix taken from consideration of the robot CAD model. The result of the analysis have shown that the proposed controller will remain stable with 10% perturbation in environmental stiffness or damping, and a variation in the combined robot-foot inertia matrix which is equivalent to about 10% of the .typical foot rotational inertia matrix according to anthropometric data.

Simulations using a linearised state space model of the actuator-robot dynamics had shown the proposed method to be effective in improving the performance of the force controller over the uniform gain approach (which is also the approach where each actuator is controlled independently from one another). Additionally, as the computed gain margins allow partial decoupling of the actuator-robot system, the condition number of the effective end effector inertia is also significantly reduced in the proposed control scheme, thus making the backdriveability of the robot more uniform in different directions. Finally, experimental results have also reiterated the performance advantages brought on by the use of the proposed control scheme over a uniform gain force controller.

Chapter 8 Model Integration and Elementary Robot Control

Since it is important to obtain a description of the overall system being controlled for the purpose of controller design and simulation, a discussion on controller development would be incomplete without the establishment of a suitable dynamic model. The first half of this chapter is therefore dedicated to the development of a model of the overall operating environment. As the dynamic model of the human ankle had been covered in chapter 5, the modelling section in this chapter will focus on capturing the manipulator dynamics and integrating it with the ankle model to produce a description of the overall system dynamics.

While the actuator force controller developed in chapter 7 is essential for providing the desired forces at the joint level, it must be used in conjunction with an outer control loop to execute physical interaction tasks, where the outer control loop is required to provide coordination between the manipulator configuration and the robot-user interaction forces. The basic formulation of the outer impedance control loop used in this research is therefore also presented in this chapter. In addition to the general impedance control law, issues relating to the development and implementation of this impedance controller are also addressed. Further, as the robot used in this research is redundantly actuated, its redundancy resolution scheme is also discussed. Finally, simulation and experimental results are presented to demonstrate the efficacy of the proposed system.

8.1 Dynamic Modelling of Parallel Mechanism

The dynamics of the overall parallel mechanism can be obtained by combining the dynamics of the actuating links and the dynamics of the end effector through application of the mechanism's kinematic constraints. The dynamics of individual actuating links are first presented in this section, followed by that of the end effector. These dynamic models are then combined to give the overall dynamic model of the mechanism.

8.1.1 Actuating Link Dynamics

The structure of the actuating link used in the developed ankle rehabilitation robot is represented graphically in Figure 8.1a. Each actuating link is connected to the base platform of the robot through a universal joint (denoted as U_i) and attached to the end effector platform through an effective spherical joint (denoted as S_i). The actual actuator can be separated into two parts; a lower segment which only rotates about the universal joint, and the actuator rod segment which is constrained to move linearly relative to the lower segment. The end of the actuator rod is in turn attached to a force sensor, which is ultimately connected to the effective spherical joint. The centres of mass of the lower actuator segment, the actuator rod and the force sensor are denoted by A_i, B_i and C_i respectively. The deformation in the load cell is represented by δ_i while the length of the actuating link (considered to be the distance between the centres of the universal and effective spherical joints) is represented by l_i. It should be noted that the inclusion of the force sensor dynamics in this actuating link model was based on the analysis carried out in Chapter 7, which suggests that the force sensor dynamics is more important in determining the system stability compared to the actuator compliance (which mainly contributes to dynamics at very high frequencies).

Having established a system of rigid bodies to represent various components of the actuating link, its dynamics can be obtained by considering the forces applied on each of these rigid bodies. The actions of the internally generated actuator force ($F_{act,i} \in \mathbb{R}^3$), the interaction force between the actuating link and the end effector ($F_{f,i} \in \mathbb{R}^3$), the reaction forces and moments between the different segments (denoted by variables with the subscript R), and the gravitational forces for each of these rigid bodies are shown in the free body diagrams in Figure 8.1b – Figure 8.1d. Based on these free body diagrams, the Newton-Euler approach was used to obtain the overall dynamic equations that govern the movement of an individual actuating link.

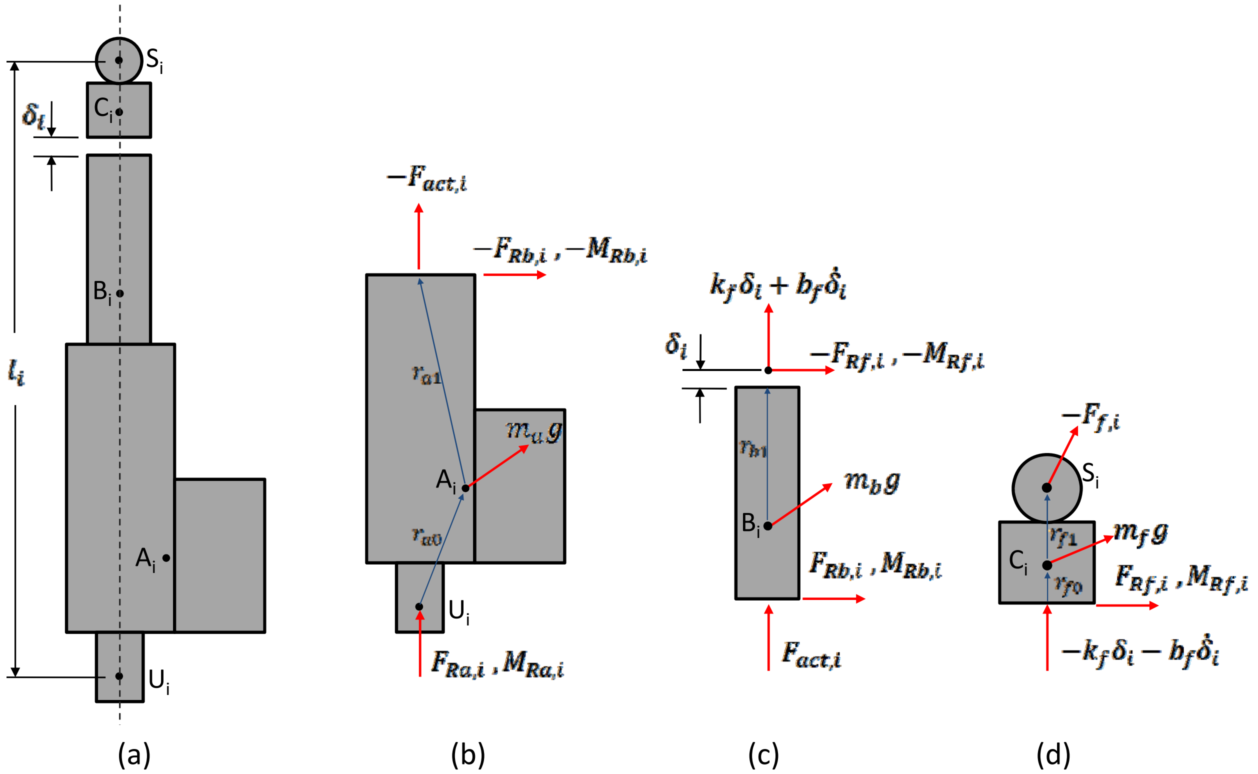

Figure 8.1: Graphical representation of an actuating link (a) and free body diagrams of the lower actuator segment (b), actuator rod (c), and force sensor (d).

The force and moment equations for each of these three rigid bodies had been derived from the free body diagrams shown in Figure 8.1b – Figure 8.1d. These dynamic relationships are shown in

(8.1) – (8.6), with x_a, x_b and x_f respectively representing the locations of the centres of mass for the lower actuator segment, the actuator rod and the force sensor (relative to U_i but expressed in global coordinates). Other variables used in these dynamic equations are also defined in

Table **8.1**, using i as the identifier for the actuating link being considered. In this table, R_i is the rotational transformation matrix which transforms vectors in the local actuating link coordinates to the global coordinates. This matrix is dependent on the angular displacements along the universal joint U_i and can be defined as (8.7), with $R_{z,\phi_i} \in \mathbb{R}^{3\times3}$ being the rotational transformation matrix describing a z-rotation that transforms the x-axis of the global coordinate frame to the x-axis of the actuating link coordinate frame, which is also aligned with the axis of the first revolute joint in U_i. $R_{x,\alpha_i} \in \mathbb{R}^{3\times3}$ ($R_{y,\beta_i} \in \mathbb{R}^{3\times3}$) on the other hand is a rotational transformation which produces a rotation of α_i (β_i) about the x-axis (y-axis), with α_i (β_i) being the angular displacement about the first (second) revolute joint in U_i. Additionally, $\hat{L}_i$ is the unit vector representing the direction of action of the i^{th} actuating link in global coordinates. It should also be noted that notation of the moment arm vectors in

Table 8.1 is defined in such a manner where the subscript prior to the ':' symbol is the origin of the vector while the subscript following the ':' symbol is the end point of the vector. Consequently, $r_{a:a0} = -r_{a0:a}$. Additionally, subscript $a0$ is used to indicate the base point while subscript $a1$ is used to indicate the follower point, both on the rigid body a. Lastly, $\hat{k}$ is used to represent the unit vector along the z-axis of the local actuating link coordinate frame.

$$m_a\ddot{x}_{a,i} = F_{Ra,i} - F_{Rb,i} + m_a g - F_{act,i} \tag{8.1}$$

$$I_a\dot{\omega}_i + \omega_i \times I_a\omega_i = M_{Ra,i} - M_{Rb,i} + r_{a:a0,i} \times F_{Ra,i} + r_{a:a1,i} \times (-F_{Rb,i} - F_{act,i}) \tag{8.2}$$

$$m_b\ddot{x}_{b,i} = F_{act,i} + F_{Rb,i} - F_{Rf,i} + \left(k_f\delta_i + b_f\dot{\delta}_i\right)\hat{L}_i + m_b g \tag{8.3}$$

$$\begin{aligned} I_b\dot{\omega}_i + \omega_i \times I_b\omega_i \\ &= M_{Rb,i} - M_{Rf,i} + r_{b:b0,i} \times \left(F_{Rb,i} + F_{act,i}\right) + \left(r_{b:b1,i} + \delta\hat{L}_i\right) \\ &\times \left[-F_{Rf,i} + \left(k_f\delta_i + b_f\dot{\delta}_i\right)\hat{L}_i\right] \end{aligned} \tag{8.4}$$

$$m_f\ddot{x}_{f,i} = -F_{f,i} + F_{Rf,i} - \left(k_f\delta_i + b_f\dot{\delta}_i\right)\hat{L}_i + m_f g \tag{8.5}$$

$$I_f\dot{\omega}_i + \omega_i \times I_f\omega_i = M_{Rf,i} + r_{c:c0,i} \times \left[F_{Rf,i} - \left(k_f\delta_i + b_f\dot{\delta}_i\right)\hat{L}_i\right] + r_{c:c1,i} \times -F_{f,i} \tag{8.6}$$

$$R_i = R_{z,\phi_i}R_{x,\alpha_i}R_{y,\beta_i} \tag{8.7}$$

Table 8.1: Definition of Moment arm vectors and motion variables for an actuating link.

Variable	Expression
$r_{a:a0,i} \in \mathbb{R}^3$	$-R_i r_{a0}$
$r_{a:a1,i} \in \mathbb{R}^3$	$R_i r_{a1}$
$r_{b:b0,i} \in \mathbb{R}^3$	$-R_i\left[(l_i - \delta_i)\hat{k} - r_{f1} - r_{f0} - r_{b1} - r_{a1} - r_{a0}\right]$ $= -\left(l_i - \delta_i - \lVert r_{f1}\rVert - \lVert r_{f0}\rVert - \lVert r_{b1}\rVert - \lVert r_{a1} + r_{a0}\rVert\right)\hat{L}_i$
$r_{b:b1,i} \in \mathbb{R}^3$	$R_i r_{b1} = \lVert r_{b1}\rVert \hat{L}_i$
$r_{c:c0,i} \in \mathbb{R}^3$	$-R_i r_{f0} = -\lVert r_{f0}\rVert \hat{L}_i$
$r_{c:c1,i} \in \mathbb{R}^3$	$R_i r_{f1} = \lVert r_{f1}\rVert \hat{L}_i$
$x_{a,i} \in \mathbb{R}^3$	$-r_{a:a0,i}$
$x_{b,i} \in \mathbb{R}^3$	$x_{a,i} + r_{a:a1,i} - r_{b:b0,i}$
$x_{f,i} \in \mathbb{R}^3$	$x_{b,i} + r_{b:b1,i} + \delta_i \hat{L}_i - r_{c:c0,i}$
$x_{s,i} \in \mathbb{R}^3$	$l_i R_i \hat{k}_i = l_i \hat{L}_i$
$\omega_i \in \mathbb{R}^3$	$R_{z,\phi_i}[\dot{\alpha}_i \;\; 0 \;\; 0]^T + R_{z,\phi_i} R_{x,\alpha_i}[0 \;\; \dot{\beta}_i \;\; 0]^T$

By noting that the force transmitted by the force sensor is parallel to the vector $\hat{L}_i \in \mathbb{R}^3$, summation of moment equations (8.2), (8.4) and (8.6) will yield (8.8). Additionally, (8.9), (8.10) and (8.11) can respectively be obtained through rearranging (8.5); the sum of (8.3) and (8.5); and the sum of (8.1), (8.3) and (8.5). By substituting (8.9) – (8.11) into (8.8) and grouping the moment arm vectors, (8.12) can also be obtained. Note that the rotational inertias of all the rigid bodies are lumped as a single inertia tensor given by $I_{tot} \in \mathbb{R}^{3\times3}$.

$$\begin{aligned} I_{tot}\dot{\omega}_i + \omega_i \times I_{tot}\omega_i \\ &= M_{Ra,i} + r_{a:a0,i} \times F_{Ra,i} + r_{a:a1,i} \times \left(-F_{Rb,i} - F_{act,i}\right) + r_{b:b0,i} \\ &\times \left(F_{Rb,i} + F_{act,i}\right) - \left(r_{b:b1,i} + \delta_i \hat{L}_i\right) \times F_{Rf,i} + r_{c:c0,i} \times F_{Rf,i} \\ &+ r_{c:c1,i} \times -F_{f,i} \end{aligned} \tag{8.8}$$

$$F_{Rf,i} = m_f \ddot{x}_{f,i} - m_f g + F_{f,i} + \left(k_f \delta_i + b_f \dot{\delta}_i\right)\hat{L}_i \tag{8.9}$$

$$F_{Rb,i} = m_b \ddot{x}_{b,i} + m_f \ddot{x}_{f,i} - \left(m_b + m_f\right) g + F_{f,i} - F_{act,i} \tag{8.10}$$

$$F_{Ra,i} = m_a \ddot{x}_{a,i} + m_b \ddot{x}_{b,i} + m_f \ddot{x}_{f,i} - \left(m_a + m_b + m_f\right) g + F_{f,i} \tag{8.11}$$

$$\begin{aligned} I_{tot}\dot{\omega}_i + \omega_i \times I_{tot}\omega_i \\ &= M_{Ra,i} - x_{s,i} \times F_{f,i} - x_{a,i} \times m_a\left(\ddot{x}_{a,i} - g\right) - x_{b,i} \times m_b\left(\ddot{x}_{b,i} - g\right) \\ &- x_{f,i} \times m_f\left(\ddot{x}_{f,i} - g\right) \end{aligned} \tag{8.12}$$

It should be noted that although the reaction forces $F_{Rb,i}$ and $F_{Rf,i}$ have three components, they are in fact two degree of freedom force vectors as their component along the line of action of the actuating link is zero by definition. This means that $\hat{L}_i^T F_{Rb,i} = \hat{L}_i^T F_{Rf,i} = 0$ and additional equations as shown in (8.13) and (8.14) can also be obtained by finding the inner product between $\hat{L}_i$ and (8.5), as well as the inner product between $\hat{L}_i$ and (8.3).

$$m_f \hat{L}_i^T \ddot{x}_{f,i} = -\hat{L}_i^T F_{f,i} - \left(k_f \delta_i + b_f \dot{\delta}_i\right) + m_f \hat{L}_i^T g \tag{8.13}$$

$$m_b \hat{L}_i^T \ddot{x}_{b,i} = \hat{L}_i^T F_{act,i} + \left(k_f \delta_i + b_f \dot{\delta}_i\right) + m_b \hat{L}_i^T g \tag{8.14}$$

Since the reaction moment experienced at the universal joint can only act along one direction (the direction perpendicular to both the revolute axes of the universal joint), it can be expressed as $M_{Ra,i} = \mu_{a,i} \hat{L}_i$. By keeping this in mind, the variable $M_{Ra,i}$ can be eliminated from (8.12) by pre-multiplying (8.12) with $I - \hat{L}_i \hat{L}_i^T$. The result of this operation is shown in (8.15). By recognising that the cross product operation can be replaced by a matrix multiplication involving a 3×3 skew symmetric matrix as shown in (8.16), (8.15) can be represented by (8.17) instead.

$$\begin{aligned} &\left(I - \hat{L}_i \hat{L}_i^T\right)[I_{tot}\dot{\omega}_i + \omega_i \times I_{tot}\omega_i] \\ &\quad = \left(I - \hat{L}_i \hat{L}_i^T\right)\left[-x_{s,i} \times F_{f,i} - x_{a,i} \times m_a\left(\ddot{x}_{a,i} - g\right)\right. \\ &\quad \left. - x_{b,i} \times m_b\left(\ddot{x}_{b,i} - g\right) - x_{f,i} \times m_f\left(\ddot{x}_{f,i} - g\right)\right] \end{aligned} \tag{8.15}$$

$$x_{s,i} \times F_{f,i} = \begin{bmatrix} x_{s,i,x} \\ x_{s,i,y} \\ x_{s,i,z} \end{bmatrix} \times F_{f,i} = \underbrace{\begin{bmatrix} 0 & -x_{s,i,z} & x_{s,i,y} \\ x_{s,i,z} & 0 & -x_{s,i,x} \\ -x_{s,i,y} & x_{s,i,x} & 0 \end{bmatrix}}_{X_{s,i}} F_{f,i} \tag{8.16}$$

$$\begin{aligned} &\left(I - \hat{L}_i \hat{L}_i^T\right)[I_{tot}\dot{\omega}_i + \omega_i \times I_{tot}\omega_i] \\ &\quad = \left(I - \hat{L}_i \hat{L}_i^T\right)\left[-X_{s,i} F_{f,i} - m_a X_{a,i}\left(\ddot{x}_{a,i} - g\right) - m_b X_{b,i}\left(\ddot{x}_{b,i} - g\right)\right. \\ &\quad \left. - m_f X_{f,i}\left(\ddot{x}_{f,i} - g\right)\right] \end{aligned} \tag{8.17}$$

It can be seen that the matrix coefficient for $F_{f,i}$, the interaction force between the end effector and the actuating link, is rank deficient in (8.17), which prevents it from being rewritten with $F_{f,i}$ as the subject. However, if (8.13) is pre-multiplied by $\hat{L}_i$ and added to (8.17), it can be shown that the matrix coefficient for $F_{f,i}$ will become $X_{s,i} + \hat{L}_i \hat{L}_i^T$. As this is a full rank matrix (due to $x_{s,i}$ being parallel to $\hat{L}_i$), a valid matrix inversion operation can be done to restate $F_{f,i}$ as a vector function of the other terms. This expression can then be used to integrate the actuating link dynamics into the end effector dynamics.

8.1.2 End Effector Dynamics

The dynamic equations governing the motion of the end effector can be derived by considering the free body diagram shown in Figure 8.2. In the free body diagram, point E is used to denote the centre of mass of the end effector and mass of the end effector is represented by m_p. Point D on the other hand is used to denote an interaction port on the end effector where external forces and moments ($F_{ext} \in \mathbb{R}^3$ and $M_{ext} \in \mathbb{R}^3$) are applied. The vectors $P_i' \in \mathbb{R}^3$ are position vectors in the local end effector coordinates which connects the end effector centre of mass to the i^{th} actuating link while $r_{ed} \in \mathbb{R}^3$ is a similar position vector which connects the end effector centre of mass to the interaction port. Lastly, R is a rotational transformation matrix which describes the orientation of the end effector in global coordinates. Based on the free body diagram, the linear and rotational acceleration terms of the end effector can be written as (8.18) and (8.19) respectively.

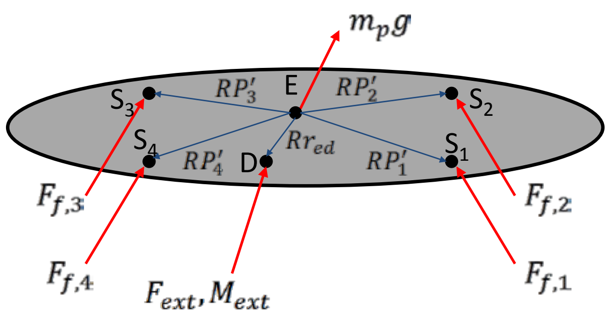

Figure 8.2: Free body diagram of the end effector.

$$m_p \ddot{x}_p = \sum_{i=1}^{i=4} F_{f,i} + m_p g + F_{ext} \tag{8.18}$$

$$I_p \dot{\omega}_p + \omega_p \times I_p \omega_p = \sum_{i=1}^{i=4} \left(RP_i' \times F_{f,i}\right) + Rr_{ed} \times F_{ext} + M_{ext} \tag{8.19}$$

8.1.3 Formation of Overall Mechanism Dynamics

While the approach for obtaining $F_{f,i}$ was established in Section8.1.1, the resulting relationship is expressed in terms of the actuating link motion variables. This means that direct substitution of these relationships into the end effector dynamic equations will lead to an excessive amount of variables and an insufficient number of equations to provide a definite solution to the forward dynamics problem. Relationships between the task space motion variables and the actuating link motion variables must therefore be incorporated to reduce the number of variables in the overall system of dynamic equations. These relationships can be derived by considering the kinematic constraints within the parallel mechanism.

The formation of the mechanism kinematic constraints first requires the definition of a set of generalised coordinates to describe the configuration of the end effector. Even though the parallel mechanism used in this research had been treated as a manipulator with pure rotational degrees of freedom in its design, the end effector dynamics described above is still defined by assuming that the end effector is capable of general six degree of freedom motion. This had been done to ensure generality of the model, thus allowing it to be applied regardless of the type of kinematic constraints present in the environment. This is an important feature as the foot motion depicted by the commonly used biaxial ankle model (see Chapter 4) is in fact not purely rotational. In this work, the generalised coordinates used to define the end effector configuration was selected to be the location of the end effector centre of mass x_p and the XYZ Euler angles Θ used to describe the end effector orientation. It should be noted that both these quantities are observed in the global coordinate frame and are grouped together as the generalised coordinate vector given in (8.20).

$$\xi = \begin{bmatrix} x_p \\ \Theta \end{bmatrix} \tag{8.20}$$

Having decided on the generalised coordinates, the kinematic constraints imposed by the parallel mechanism can be established by observing the collocation of the S_i points. This means that the locations of the S_i points as obtained from the task space generalise coordinates must be equivalent to those found using the actuating link coordinates. This relationship can be represented as (8.21), with u_i being a position vector describing the location of the universal joint U_i in the global frame and $x_{s,i}$ is as defined in

Table **8.1**. A mapping from the generalised coordinates $\xi \in \mathbb{R}^6$ to three of the actuating link coordinates (α_i, β_i and l_i) can therefore be obtained from (8.21). The time derivative of this relationship can then be used to obtain a Jacobian matrix $J_i \in \mathbb{R}^{3\times 6}$ which relates the derivatives of the actuating link coordinates to the generalised coordinate derivatives as shown in (8.22).

$$x_p + RP_i' = x_{s,i} + u_i \tag{8.21}$$

$$\begin{bmatrix} \dot{\alpha}_i \\ \dot{\beta}_i \\ \dot{l}_i \end{bmatrix} = J_i \dot{\xi} \tag{8.22}$$

By considering the sensor deformations as additional state variables, the expressions for the centres of mass of the actuating link segments were represented in the general form given in (8.23), with $\varsigma = a, b, f, s$. Similarly, the angular velocities of the actuating links were also written in the form given in (8.24). Repeated differentiation of (8.23) and (8.24) then leads to the actuating link acceleration terms being represented by ξ, δ_i and their higher order time derivatives (up to the second order). With this in mind, the actuating link-end effector interaction forces were restated as $F_{f,i} = h_i(\ddot{\xi}, \ddot{\delta}_i, \dot{\xi}, \dot{\delta}_i, \xi, \delta_i)$. It follows that the dynamic equations given in (8.18) and (8.19) can be combined and viewed as (8.25), with $w_{ext} = [{F_{ext}}^T \; {M_{ext}}^T]^T \in \mathbb{R}^6$ and $\delta = [\delta_1 \; \delta_2 \; \delta_3 \; \delta_4]^T \in \mathbb{R}^4$.

Additionally, $M_1 \in \mathbb{R}^{10\times10}$ is the configuration dependent matrix coefficient for the state acceleration variables, $N_1 \in \mathbb{R}^{10}$ is the grouping of nonlinear terms and $A_1 \in \mathbb{R}^{10\times6}$ is the matrix coefficient for the external wrench applied to the end effector.

$$x_{\varsigma,i} = f_{\varsigma,i}(\xi, \delta_i) \tag{8.23}$$

$$\omega_i = g_i(\xi, \dot{\xi}) \tag{8.24}$$

$$M_1(\xi)\begin{bmatrix}\ddot{\xi}\\ \ddot{\delta}\end{bmatrix} + N_1(\dot{\xi}, \dot{\delta}, \xi, \delta) + A_1(\xi)w_{ext} = 0 \tag{8.25}$$

Even with the reparameterisation, there are still only six equations available from (8.25) while there are ten unknown accelerations. Additional equations are therefore required to obtain a definite solution to the mechanism dynamics. This can be obtained by taking into account the reparameterised version of (8.14) for each actuating link. Appending these equations to (8.25) will then lead to the complete model of the mechanism dynamics as shown in (8.26), with $F_{act} = [F_{act,1}\ F_{act,2}\ F_{act,3}\ F_{act,4}]^T$, $M \in \mathbb{R}^{10\times10}$ being the matrix coefficient of the acceleration terms, $N \in \mathbb{R}^{10}$ being the nonlinear dynamic terms, $A \in \mathbb{R}^{10\times6}$ being the matrix coefficient for the interaction wrench and $B \in \mathbb{R}^{10\times4}$ being the matrix coefficient for the actuator force vector.

$$M(\xi)\begin{bmatrix}\ddot{\xi}\\ \ddot{\delta}\end{bmatrix} + N(\dot{\xi}, \dot{\delta}, \xi, \delta) + A(\xi)w_{ext} = B(\xi)F_{act} \tag{8.26}$$

8.2 Integration of Manipulator Model with Foot and Actuator Dynamics

As discussed previously, the mechanism dynamic model had been formulated in more general terms to allow its coupling to a larger range of environments. For the application of ankle rehabilitation, this environment is that of the user's foot. The ankle model described in Chapter 5 must therefore be integrated with the mechanism dynamics to give a more complete description of the overall system dynamics. Furthermore, as the actuating link dynamics discussed previously does not take into account the dynamics of the electrical actuators, this information must also be incorporated in the final model. These issues are further discussed in this section.

8.2.1 Integration of foot dynamics

The integration of the foot model and the mechanism model can be done by first ensuring that the interaction ports on the foot and on the end effector are collocated. If this criterion in satisfied, the wrenches acting on the interaction port of the end effector will simply be equal but opposite of that acting on the foot model. This condition can therefore be used to combine the two models. In addition to the above condition, the kinematic relationship between generalised coordinates of the ankle model and the generalised coordinates of the end effector must also be found to allow further reparameterisation of the combined dynamic equations to yield a compact state space model which can be solved exactly. Clearly, as ankle model introduces additional kinematic constraints on the end effector, the final generalised coordinate would involve the ankle and subtalar joint displacements.

It can be seen from Chapter 5 that the ankle model can be represented in the form shown in (8.27), where θ_{as} is the ankle and subtalar joint displacement, z_f is a vector of additional state variables of the ankle model (which includes ligament and muscle-tendon states), Γ a vector of muscle activation levels and $w_{ext,f}$ is the external wrench applied to the interaction port of the foot. Note also that the subscript ft is used to denote the matrix coefficients and nonlinear dynamic terms relating to the ankle model, with $M_{ft} \in \mathbb{R}^{2\times 2}$, $N_{ft} \in \mathbb{R}^{2}$ and $A_{ft} \in \mathbb{R}^{2\times 6}$.

$$M_{ft}(\theta_{as})\ddot{\theta}_{as} + N_{ft}\left(\theta_{as}, \dot{\theta}_{as}, z_f, \Gamma\right) + A_{ft}(\theta_{as})w_{ext,ft} = 0 \tag{8.27}$$

The kinematic relationship between θ_{as} and ξ can be easily defined using the ankle kinematic model defined in Chapter 4 as long as the relative position of the end effector centre of mass with respect to the subtalar joint centre is known at the neutral position of the ankle (by definition, this should also correspond to the end effector orientation with zero XYZ Euler angles). This relationship was represented as (8.28), and was further differentiated with respect to time to give (8.29) and (8.30).

$$\xi = f_{\xi}(\theta_{as}) \tag{8.28}$$

$$\dot{\xi} = J_{\xi}\dot{\theta}_{as} \tag{8.29}$$

$$\ddot{\xi} = J_{\xi}\ddot{\theta}_{as} + \dot{J}_{\xi}\dot{\theta}_{as} \tag{8.30}$$

By considering (8.28) – (8.30), (8.26) was reparameterised with θ_{as} and its time derivatives as (8.31). Note that the matrix coefficient of the acceleration terms ($M' \in \mathbb{R}^{10\times 6}$) and the nonlinear dynamic terms ($N' \in \mathbb{R}^{10}$) are different from those given in (8.26) due to the substitution of the task space acceleration vector in (8.31).

$$M'(\theta_{as})\begin{bmatrix}\ddot{\theta}_{as}\\ \ddot{\delta}\end{bmatrix} + N'\left(\dot{\theta}_{as}, \dot{\delta}, \theta_{as}, \delta\right) + A(\theta_{as})w_{ext} = B(\theta_{as})F_{act} \tag{8.31}$$

By recognising that $w_{ext} = -w_{ext,f}$, (8.27) can be rewritten as (8.32). Note that the dependencies of the nonlinear terms and matrix coefficients will be dropped hereafter for brevity. It can be seen that pre-multiplication of (8.32) by ${A_{ft}}^{+} = {A_{ft}}^{T}\left(A_{ft}{A_{ft}}^{T}\right)^{-1} \in \mathbb{R}^{6\times 2}$ will result in (8.33), with $v_{0,A_{ft}} \in \mathbb{R}^{6\times 4}$ being the null space matrix of A_{ft} (with the null vectors occupying the columns of $v_{0,A_{ft}}$). Equation (8.33) was then further expanded as (8.34), which showed that the actual interaction wrench can be represented by the summation of the right hand side of (8.33) with an additional four degree of freedom vector $v_{0,A_{ft}}\rho$, with $\rho = {v_{0,A_{ft}}}^T w_{ext} \in \mathbb{R}^4$. Substituting this result into (8.31) then yields (8.35).

$$M_{ft}\ddot{\theta}_{as} + N_{ft} - A_{ft}w_{ext} = 0 \tag{8.32}$$

$$(I - v_{0,A_{ft}}{v_{0,A_{ft}}}^T)w_{ext} = {A_{ft}}^+ M_{ft}\ddot{\theta}_{as} + {A_{ft}}^+ N_{ft} \tag{8.33}$$

$$\begin{aligned} w_{ext} &= {A_{ft}}^+ M_{ft}\ddot{\theta}_{as} + {A_{ft}}^+ N_{ft} + v_{0,A_{ft}}{v_{0,A_{ft}}}^T w_{ext} \\ &= {A_{ft}}^+ M_{ft}\ddot{\theta}_{as} + {A_{ft}}^+ N_{ft} + v_{0,A_{ft}}\rho \end{aligned} \tag{8.34}$$

$$\begin{aligned} &M' \begin{bmatrix} \ddot{\theta}_{as} \\ \ddot{\delta} \end{bmatrix} + N' + A{A_{ft}}^+ M_{ft}\ddot{\theta}_{as} + A{A_{ft}}^+ N_{ft} + Av_{0,A_{ft}}\rho = BF_{act} \\ &\Longrightarrow M" \begin{bmatrix} \ddot{\theta}_{as} \\ \ddot{\delta} \end{bmatrix} + N' + A{A_{ft}}^+ N_{ft} + Av_{0,A_{ft}}\rho = BF_{act} \end{aligned} \tag{8.35}$$

Since the solution of ρ is of no interest, (8.35) was further pre-multiplied by $N_A = \left[Null\left({v_{0,A_{ft}}}^T A^T\right)\right]^T$ to yield (8.36), where the function $Null(.)$ returns a matrix which columns are filled by the null vectors of the function argument (i.e. $N_A \in \mathbb{R}^{6\times10}$). Inspection of (8.36) reveals that there are now six acceleration variables and six equations, which means that the acceleration variables can be solved exactly given certain actuator forces and muscle activation levels. Clearly, the state space model of the foot-manipulator system will only be complete when the state transition equations for the ligament and muscle-tendon states are included.

$$N_A M" \begin{bmatrix} \ddot{\theta}_{as} \\ \ddot{\delta} \end{bmatrix} + N_A N' + N_A A{A_{ft}}^+ N_{ft} = N_A BF_{act} \tag{8.36}$$

8.2.2 Integration of actuator electrical dynamics

Based on the actuating link coordinates used in section 8.1.1, the actuator dynamics was expressed as (8.37), with $i_{act,i}$ being the actuator current, K_t being the motor torque constant, K_a being the actuator transmission ratio, J_{eff} being the effective motor inertia, b_{eff} being the effective viscous damping of the motor and $F_{fric,i}$ being the Coulomb friction experienced by the actuator. Since $\ddot{l}_i$ and $\dot{l}_i$ can ultimately be related to the accelerations and velocities of the ankle and subtalar joints, (8.37) was reorganised as (8.38). Substitution of (8.38) into (8.36) will then lead to the set of equations which describes the rigid body dynamics of the actuator, parallel mechanism, and foot.

This set of equations is given in (8.39), with $M_{F_{act}} \in \mathbb{R}^{4\times6}$ being a matrix which rows are consisted of $M_{F_{act,i}} \in \mathbb{R}^{1\times6}$ and $N_{F_{act}} \in \mathbb{R}^{4}$ being a vector which rows are consisted of $N_{F_{act,i}}$.

$$F_{act,i} = K_t K_a i_i - K_a{}^2 J_{eff}\left(\ddot{l}_i - \ddot{\delta}_i\right) - K_a{}^2 b_{eff}\left(\dot{l}_i - \dot{\delta}_i\right) - F_{fric,i} \tag{8.37}$$

$$F_{act,i} = K_t K_a i_{act,i} - M_{F_{act,i}} \begin{bmatrix} \ddot{\theta}_{as} \\ \ddot{\delta} \end{bmatrix} - N_{F_{act,i}} - F_{fric,i} \tag{8.38}$$

$$\begin{aligned} \left(N_A M'' + N_A B M_{F_{act}}\right) \begin{bmatrix} \ddot{\theta}_{as} \\ \ddot{\delta} \end{bmatrix} + N_A N' + N_A B N_{F_{act}} + N_A B F_{fric} + N_A A A_{ft}{}^{+} N_{ft} \\ = K_t K_a N_A B i_{act} \end{aligned} \tag{8.39}$$

8.3 Elementary Robot Control

Any robot used to facilitate physical therapy must physically interact in some way with the user or patient. This often requires the robot to move the user's limb along certain rehabilitation trajectories while maintaining a safe level of interaction force. Alternatively, the robot may be required to provide resistance to the user's motion for the purpose of muscle strengthening. There is therefore a need for control schemes capable of regulating both force and position variables on rehabilitation robots. One of these control strategies is impedance control, a general approach for motion control where it aims to regulate a dynamic relationship between the force and motion variables of the manipulator so that it can exhibit the desired mechanical behaviour.

In the context of rehabilitation robots, the force variable is the user-robot interaction force while the motion variable is simply the movement of the joint or limb under rehabilitation. It should also be noted that the dynamic relationships described above are typically represented as a second order mechanical system as shown in (8.40) with inertial (M_d), damping (B_d) and stiffness (K_d) parameters. Additionally, the variables f, f_d, x and x_d are respectively used to denote the force applied to the environment, the desired force, the actual position of the end effector and the desired end effector position. The advantage of having the force and motion variables in relative terms is that it allows variation in the equilibrium position about which the impedance relationship is based, thus allowing the use of this control strategy for a wider range of tasks. In fact, when put in this form, pure motion control and pure force control can simply be viewed as special cases of impedance control, where pure motion control can be achieved with infinitely large impedance and pure force control with zero impedance. Due to its versatility, the interaction control scheme developed for the ankle rehabilitation robot is based on this general impedance control law.

$$f - f_d = M_d(\ddot{x}_d - \ddot{x}) + B_d(\dot{x}_d - \dot{x}) + K_d(x_d - x) \tag{8.40}$$

8.3.1 Basic Impedance Control

It is easy to see that implementation of the impedance control law can be done by issuing f as a force command to the actuator force controller. This means that an outer motion control loop is required to complete the impedance control scheme. Since the actuator force controller is defined in joint space while the impedance control law is applied in task space to allow more intuitive description of the desired manipulator behaviour, the actual input to the outer impedance loop would be the motion variables in terms of end effector orientation and the output will be that of the torques along the task space coordinates. This torque must therefore be transformed into their corresponding actuator forces prior to it being used as force commands for the inner force control loop. In order to derive this force command, it is necessary to first consider the desired impedance relationship in task space as shown in (8.41), where τ_{ext} is the robot-user interaction torque, $\tau_d$is the desired interaction torque, Θ is the task space coordinates in XYZ Euler angles and Θ_d is the desired task space position. Note that the desired task space acceleration is deliberately left off the inertial component of the impedance relationship to simplify the control law. As the main focus of the impedance control law is not to achieve pure position control, this simplification is acceptable.

$$\tau_{ext} - \tau_d = -M_d\ddot{\Theta} + B_d\left(\dot{\Theta}_d - \dot{\Theta}\right) + K_d(\Theta_d - \Theta) \tag{8.41}$$

By considering the influence of the inner actuator force control law, the effective dynamics of the manipulator can be rewritten as (8.42), where M_{eff} is the effective inertia matrix as obtained from Chapter 7 and $K \in \mathbb{R}^{4\times 4}$ is the gain matrix used in the inner force controller. Also, F_{distb} is used to refer to the actuator disturbance forces as defined in (7.5) of Chapter 7, C is used to represent the centripetal and Coriolis forces in the manipulator dynamics, and G is used to represent the gravitational forces in the manipulator dynamics. Finally, F_c represents the force command issued to the inner force controller. By considering (8.41) and (8.42), as well as the fact that $J^T(J^+)^T = I$, a suitable impedance control law can be constructed. This is shown in (8.43). The dynamics of the impedance controlled manipulator (8.44) was then obtained by substituting (8.43) into (8.42). This shows that the desired manipulator impedance is almost entirely recreated by using the proposed impedance control law, with the exception of an additional disturbance term introduced by the inner force control loop (note however that this term will be small for a sufficiently large K). Another point worth noting is that this control law is not used to modify the inertia of the "original" manipulator (in this case original is used to refer to the force controlled manipulator).

$$M_{eff}\ddot{\Theta} + C + G + \tau_{ext} = J^T F_c - J^T(I + K)^{-1}F_{distb} \tag{8.42}$$

$$F_c = (J^+)^T\left[\tau_d + B_d\left(\dot{\Theta}_d - \dot{\Theta}\right) + K_d(\Theta_d - \Theta) + C + G\right] \tag{8.43}$$

$$\tau_{ext} - \tau_d = -M_{eff}\ddot{\Theta} + B_d\left(\dot{\Theta}_d - \dot{\Theta}\right) + K_d(\Theta_d - \Theta) - J^T(I + K)^{-1}F_{distb} \tag{8.44}$$

Gravitational compensation

It can be seen from the impedance control law (8.43) that the gravitational, centripetal and Coriolis terms of the robot dynamics are required for cancellation of the system nonlinearities. Unfortunately, due to imperfect knowledge of the system properties, particularly those of the user's foot, complete cancellation of the nonlinear terms is difficult to achieve. Even with a perfect dynamic model, computation of these terms in real time may not be computationally tractable due to the complex dynamics of the parallel mechanism and this may require a larger sampling time which can then lead to performance degradation or even system instability. A compromise between perfect cancellation of nonlinearities and computational tractability must therefore be found when implementing the proposed controller.

One possible approach is to compute only the gravitational component of the nonlinear dynamics for the manipulator [15]. This has been proposed because motion of the robot is expected to be relatively slow due to its use in rehabilitation tasks such as passive range of motion and strength training exercises. As such, dynamic terms which are velocity dependent are also anticipated to be small compared to the gravitational effects. Another problem associated with the computation of the centripetal and Coriolis terms in the manipulator dynamics is the need to numerically differentiate the task space coordinates. Due to the fast sampling rate and presence of sensor noise, the corresponding terms being computed is expected to be noisy and can lead to sudden changes in force commands. This potential problem is therefore circumvented by excluding velocity dependent dynamics in the control law.

Further simplifications were also made to provide a more computationally efficient evaluation of the gravitational terms. This was done by considering the gravitational forces acting on the robot end effector and actuators in the manner shown in Figure 8.3. Here, R is the rotational transformation matrix which describes the orientation of the end effector with respect to the neutral orientation. P_i ($i = 1,2,3,4$) on the other hand is the position vector (in local end effector coordinates) which connects the assumed ankle centre of rotation to the effective spherical joint centres of each actuating link. Also, t_{og} is the position vector going from the assumed centre of rotation to the centre of mass of the end effector, again in local end effector coordinates. Additionally, m_i, m_p and g are respectively the mass of the actuating link distal to the force sensor, the mass of the end effector and the gravitational acceleration vector. Finally, since the centres of mass of m_i are assumed to be located on the lines of action of their respective actuating links, the variable l (taken to be constant across all actuating links) is used to denote the distance from the effective spherical joint centre to these centres of mass. The moments generated by gravitational forces acting on the system shown in Figure 8.3 can be obtained from (8.45), where $\hat{L}_i$ are unit vectors denoting the line of action of the actuating links, pointing towards the effective spherical joints. Note that these unit vectors are also dependent on the task space coordinates and can be obtained by solving the inverse kinematics of the parallel manipulator as described in Chapter 3. Using the gravitational moments computed in this manner, the actual impedance control law implemented is given by (8.46).

$$\hat{G} = Rt_{og} \times m_p g + \sum_{i=1}^{i=4} \left[(RP_i - l\hat{L}_i) \times m_i g \right] \tag{8.45}$$

$$F_c = (J^+)^T \left[\tau_d + B_d(\dot{\Theta}_d - \dot{\Theta}) + K_d(\Theta_d - \Theta) + \hat{G} \right] \tag{8.46}$$

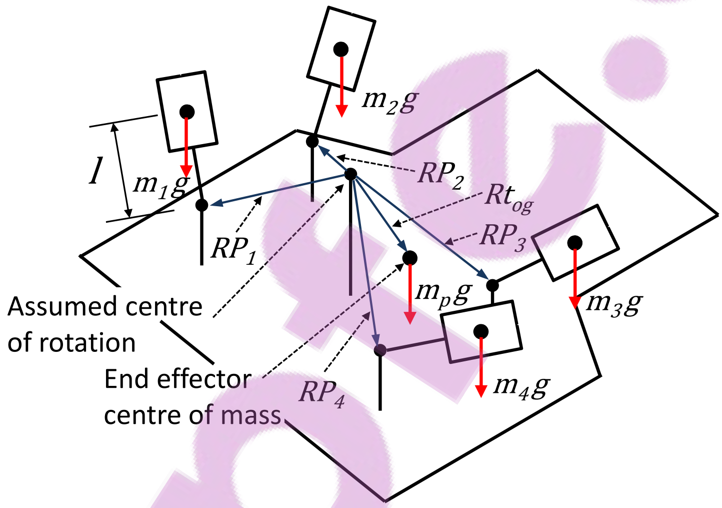

Figure 8.3: Action of gravitational forces on the robot end effector and distal segments of the actuating links.

8.3.2 Redundancy Resolution

The relationship between the task space moments and joint space forces of the parallel manipulator can be expressed as (8.47). Computation of the joint space forces which can produce a particular task space moment vector therefore involves finding the inverse to (8.47). However, by considering the task space as a three degree of freedom system, the use of four actuators on the parallel robot means that the manipulator Jacobian matrix is not square and there will be an infinite number of actuator force vectors which can satisfy (8.47). Consideration of the singular value decomposition of $J^T \in \mathbb{R}^{3\times4}$ shows that this family of force vectors can be represented as (8.48), where v_0 is the null vector of J^T. It can therefore be seen that the force command obtained through the use of (8.46) is simply a special case of (8.48) which is void of any force components along the null vector, hence making it the minimal norm solution [135].

$$\tau_c = J^T F_c = V_J [\Sigma_J \quad 0_{3\times1}] {U_J}^T F_c \tag{8.47}$$

$$F_c^* = U_J \begin{bmatrix} {\Sigma_J}^{-1} {V_J}^T \tau_c \\ \lambda \end{bmatrix} = (J^+)^T \tau_c + \lambda v_0 \tag{8.48}$$

Since the additional component of null space forces can be selected arbitrarily without influencing the actual task space torque, it can be utilised to meet additional control objectives which are not in conflict with the task space torque requirements. For the purpose of this research, this additional control requirement is the regulation of total vertical actuator forces. The main motivation for the selection of this control requirement is to incorporate the ability to control the vertical forces being applied to the lower limb of the user. By regulating the vertical force, different levels of weight bearing can be simulated on the rehabilitation robot. This will allow the robot to operate in a wider range of conditions to suit the rehabilitation requirements of the user. For instance, the desired level of weight bearing for patients in their initial phase of rehabilitation may be kept small to prevent excessive stresses on healing tissues. However, as the patient's condition improves, the level of weight bearing will have to be increased to better simulated real life scenarios.

The combined vertical force $f_{vert} \in \mathbb{R}$ applied by all four actuators is given by (8.49), where f_i is the compressive force along each actuator, v_z is a column vector containing the z-components of the unit actuating link vectors, and F is the actuator force vector. This means that a positive vertical force will result in the end effector being pulled downward, which in turn causes a tension force to be applied to the user's ankle. The vertical force applied by the family of force commands capable of producing the desired task space torque can therefore be represented as (8.50). It is clear from this relationship that as long as v_z is not orthogonal to the null vector v_0, a value of λ can be chosen to realise any desired vertical force $f_{vert,d}$. This value of λ can be computed from (8.51) and used to obtain the final force command issued to the actuator force controller through (8.48).

$$f_{vert} = \sum_{i=1}^{i=4} \left([0 \quad 0 \quad 1] f_i \hat{L}_i \right) = {v_z}^T F \tag{8.49}$$

$$f_{vert} = {v_z}^T F_c^* = {v_z}^T (J^+)^T \tau_c + \lambda {v_z}^T v_0 \tag{8.50}$$

$$\lambda = \frac{f_{vert,d} - {v_z}^T (J^+)^T \tau_c}{{v_z}^T v_0} \tag{8.51}$$

8.4 Implementation Issues

While main control laws concerning the elementary robot control had been outlined above, additional modules were also developed to facilitate the actual implementation of the above control laws. One of these modules is used to compute the end effector orientation by combining information obtained from position sensors on the robot, while another module was developed to estimate the actual centre of rotation of the user's foot. The development of these modules will be discussed below to provide a complete description of the basic robot controller.

8.4.1 Estimation of End Effector Orientation

One feature which can be used to distinguish between parallel manipulators with their serial counterparts is that solution of the inverse kinematics of parallel robots is typically much easier in parallel robots, where the joint space coordinates of the parallel robot can usually be expressed explicitly in terms of the task space coordinates. Conversely, solution of the forward kinematics problem for parallel robots is in general more challenging, and often involves the use of numerical algorithms. Since it is more intuitive to express the desired mechanical impedance of the manipulator in task space, the impedance control law will require the motion variables to be expressed in task space. While this can be done relatively easily in serial robots, the use of a parallel manipulator in this research means that special attention must be placed on obtaining an effective means for solving the forward kinematics problem.

In this research, the forward kinematics problem is solved through application of a numerical algorithm based on the Gauss-Newton method. This method is essentially a numerical optimisation algorithm which aims to minimise the discrepancies between the actual measured actuator link lengths and the actuator link lengths as obtained from the inverse kinematics model by varying the task space coordinates governing the end effector orientation. For convenience, the inverse kinematic model (previously presented in Chapter 3) is restated here as (8.52). Where R is the rotational transformation matrix which describes the end effector orientation, t_0 is the location of the nominal centre of rotation in the global coordinates, P_i are the position vectors (in end effector coordinates) connecting this centre of rotation to the effective spherical joints at the end of the actuating links, and B_i are the position vectors connecting the origin of the global coordinate frame to the universal joint centres of the actuating link on the base platform. Since the adopted task space coordinates is that of the XYZ Euler angles, this rotational matrix was defined as (8.53), with R_x, R_y and R_z being rotational transformation matrices about the x, y and z axes respectively, and the angle of rotation in each of these matrices is given in the same order by elements in the task space coordinate $\Theta = [\theta_x \;\; \theta_y \;\; \theta_z]^T$.

$$(l_i)^2 = {L_i}^T L_i = (t_0 + RP_i - B_i)^T (t_0 + RP_i - B_i) \tag{8.52}$$

Using the kinematic relationship (8.52) and the definition of the end effector orientation given in (8.53), it is easy to see that the actuator length is a function of the task space variable. The forward kinematics of the manipulator can therefore be solved by finding the task space coordinates that minimises (8.54), where $l_{m,i}$ is the measured length of actuator i, L_m is a vector of these measured lengths and L is a vector of the computed actuator lengths. Applying the Gauss-Newton algorithm [136] to this problem then allows the estimates of the task space coordinates to be updated as shown in (8.55), where k is the iteration number and J is the Jacobian matrix relating the changes in computed lengths with respect to changes in the task space coordinates (note that this is identical to the manipulator Jacobian). Specifically, the matrix J is defined by (8.56). The numerical algorithm therefore involves the repeated update of the task space parameters using (8.55) until the cost C_{fk} falls below a certain tolerance threshold. This threshold should be chosen sufficiently small to provide a good level of accuracy but not too small to reduce the number of iterations required for the solution algorithm. A tolerance threshold of 10^{-6} m^2 had been used for the purpose of this research.

$$R(\Theta) = R_x(\theta_x) R_y(\theta_x) R_z(\theta_x) \tag{8.53}$$

$$C_{fk} = \frac{1}{2} \sum_{i=1}^{i=4} \left(l_{m,i} - l_i\right)^2 = \frac{1}{2} (L_m - L)^T (L_m - L) \tag{8.54}$$

$$\Theta_{k+1} = \Theta_k + \left({J_k}^T J_k\right)^{-1} {J_k}^T (L_m - L_k) \tag{8.55}$$

$$J = \begin{bmatrix} \frac{\partial l_1}{\partial \theta_x} & \frac{\partial l_1}{\partial \theta_y} & \frac{\partial l_1}{\partial \theta_z} \\ \vdots & \vdots & \vdots \\ \frac{\partial l_4}{\partial \theta_x} & \frac{\partial l_4}{\partial \theta_y} & \frac{\partial l_4}{\partial \theta_z} \end{bmatrix} \tag{8.56}$$

The forward kinematics algorithm would work well as long as the kinematic parameters of the parallel manipulator are accurately known. However, since the ankle rehabilitation robot used in this research is designed to operate with the user’s lower limb forming part of the robot’s kinematic constraint, the centre of rotation of the end effector may not coincide with the nominal centre of rotation used in the kinematic design. In fact, the motion of the end effector may not even be purely rotational. This therefore introduces additional difficulties in the solution of the end effector orientation as the kinematic parameters required for the above algorithm are not fully available. To overcome this problem, a two axis inclinometer was installed on the end effector to provide information regarding the pitch and roll of the end effector. This therefore provides two of the three degrees of freedom needed to describe the end effector orientation. By noting that the correct solution of the end effector orientation is actually not reliant on the end effector motion being purely rotational, the end effector can be assumed to be “rotating” about an instantaneous pivot point which has the same relative position to the end effector coordinate frame as that of the nominal centre of rotation used in the above forward kinematics algorithm (i.e. P_i remains the same). The location of this pivot, together with the yaw angle of the end effector therefore forms four unknown variables. Using the four nonlinear equations relating the lengths of the actuating links to the end effector orientation and pivot location, all these unknowns can be solved exactly through application of the Gauss-Newton algorithm.

As the measurements returned by the inclinometer are expressed in the ZXY instead of the XYZ Euler angle convention, the rotational matrix used here must therefore be redefined as (8.57), with ϕ_x being the pitch angle and ϕ_y being the roll angle provided by the inclinometer. The remaining angle ϕ_z then is used to represent the unknown yaw angle. In the problem described above, the instantaneous pivot is represented by t_0. The vector of unknowns can therefore be defined as $\rho = [\phi_z \;\; {t_0}^T]^T \in \mathbb{R}^4$ and the parameter update law is now given by (8.58), with (8.59) as the gradient matrix. Once the yaw angle is obtained from this algorithm, the ZXY Euler angles can be converted back into the XYZ Euler angle convention for use in the control algorithm. This can be done in a rather straight forward manner by comparing the terms found in different elements of the rotational transformation matrix.

$$R(\Phi) = R_z(\phi_z)R_x(\phi_x)R_y(\phi_y) \tag{8.57}$$

$$\rho_{k+1} = \rho_k + \left({J'_k}^T J'_k\right)^{-1} {J'_k}^T (L_m - L_k) \tag{8.58}$$

$$J' = \begin{bmatrix} \frac{\partial l_1}{\partial \phi_z} & \frac{\partial l_1}{\partial t_{0x}} & \frac{\partial l_1}{\partial t_{0y}} & \frac{\partial l_1}{\partial t_{0z}} \\ \vdots & \vdots & \vdots & \vdots \\ \frac{\partial l_4}{\partial \phi_z} & \frac{\partial l_4}{\partial t_{0x}} & \frac{\partial l_4}{\partial t_{0y}} & \frac{\partial l_4}{\partial t_{0z}} \end{bmatrix} \tag{8.59}$$

It should be noted however that due to limitations of the inclinometer, the pitch and roll of the end effector can only be sampled at a maximum rate of 40Hz. Consequently, the availability of the pitch and roll angles may not be fast enough to allow effective outer loop control. This issue is addressed by combining the use of the original forward kinematics algorithm with the modified algorithm described above. This final algorithm updates the instantaneous pivot and computes the yaw angle whenever data is available from the inclinometer. For all other time instances however, the previously calculated pivot is used as the available kinematic parameters and the original forward kinematics algorithm is executed to obtain all three task space coordinates. Using this method, a sampling interval of 3ms was achieved in the outer impedance control loop.

8.4.2 Estimation of Centre of Rotation

As discussed previously, the ankle rehabilitation robot developed in this research utilises the actual human ankle joint as part of the kinematic constraints of the parallel mechanism. The actual centre of rotation for the end effector may therefore be different from the nominal centre of rotation used in the design. This is mainly due to uncertainties of the user's ankle kinematics and the variability in terms of the exact location of the foot on the end effector. Even though it was highlighted in the previous section that precise knowledge of the end effector centre of rotation is not necessary for the correct computation of the end effector orientation, the manipulator Jacobian is still computed with reference to this nominal centre of rotation. Since the manipulator Jacobian plays an important role in the controller by mapping the motion and force variables between task and joint space, a grossly incorrect centre of rotation of the end effector can have a negative impact on system performance and stability (since the null vector and the decoupled directions used in the proposed actuator force controller are derived from the manipulator Jacobian).

An appreciation of the potential problems caused by a mismatch between the assumed and actual centre of rotation can be obtained by considering the problem of task space torque control. Since the controller obtains the desired force commands through the use of the manipulator Jacobian, the resulting force commands will only apply the desired torque about the assumed centre of rotation. Any deviation of the actual centre of rotation from this assumed centre will therefore lead to a discrepancy between the desired and actual moment experienced at the true centre of rotation. Since this true centre of rotation is also the ankle joint centre, an incorrect assumption of the centre of rotation can lead to the "wrong" moment being applied to the ankle. This problem can be exacerbated when the redundancy resolution scheme is used to generate vertical force of large magnitude as the controller will apply additional forces along the null vector based on the assumption that these forces will not influence the task space moment about the nominal centre of rotation. Clearly, any deviation of the actual centre of rotation from its nominal value will violate this assumption and result in an additional moment about the actual centre of rotation.

The above discussion have emphasised the importance of obtaining a good estimate for the actual ankle/end effector centre of rotation. Given the sensor information available, such an estimate can be obtained by considering the t_0 vectors computed during the solution of the manipulator kinematics. Assuming that the end effector is indeed rotating about a fixed point, the locus of the computed t_0 will lie on a sphere centred about the actual centre of rotation. This can be written as (8.60), with R being the rotational transformation matrix which describes the end effector orientation, I being a 3×3 identity matrix, Δ_{t0} being the position vector connecting the actual centre of rotation to the assumed centre of rotation in the end effector coordinate frame and t_0^* being the actual location of the centre of rotation in the global coordinate frame. The above problem formulation is shown diagrammatically in Figure 8.4, with P_i^* being the vector connecting the actual centre of rotation to the spherical joint at the end of the i^{th} actuating link.

$$t_0 = R\Delta_{t0} + t_0^* = [R \quad I]\left[{\Delta_{t0}}^T \quad t_0^{*T}\right]^T \tag{8.60}$$

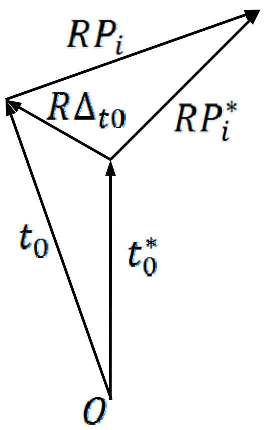

Figure 8.4: Relationships between the nominal and actual end effector centre of rotation.

It is easy to see that this relationship can also be represented in a linear in parameter form with Δ_{t0} and t_0^* being the unknowns. This therefore simplifies the identification of these parameters as methods such as recursive least squares can be applied to obtain an online estimate of these parameters. Once estimates of these parameters are obtained, adjustments can be made to the P_i vectors used in the computation of the manipulator Jacobian. From Figure 8.4, the relationship between P_i and P_i^* can be expressed as (8.61). Additionally, each element of the nominal manipulator Jacobian can be computed through (8.62), with i representing the actuator number and θ_j ($j = x, y, z$) denoting the corresponding Euler angle. By noting that vectors L_i remain unchanged even through the parameter adjustment, the manipulator Jacobian with the updated parameters was written as the summation of the nominal Jacobian and an additional update term as shown in (8.63).

$$P_i^* = P_i + \Delta_{t0} \tag{8.61}$$

$$J_{ij} = \left(\frac{L_i}{l_i}\right)^T \frac{\partial R}{\partial \theta_j} P_i \tag{8.62}$$

$$J_{ij}^* = \left(\frac{L_i}{l_i}\right)^T \frac{\partial R}{\partial \theta_j} P_i^* = J_{ij} + \left(\frac{L_i}{l_i}\right)^T \frac{\partial R}{\partial \theta_j} \Delta_{t0} \tag{8.63}$$

A problem associated with the implementation of the above estimation and adjustment algorithm on the actual ankle rehabilitation robot is that the lower limb of the user is not rigidly fixed to the robot and can shift slightly during operation. This is particularly the case for the interface between the base platform and the user's shank. A consequence of this is that the centre of rotation of the ankle will not remain constant in the global coordinate frame, thus violating the implicit assumption of constant parameters and making the use of recursive least squares unsuitable. However, it can be seen from (8.63) that only the parameter Δ_{t0} is needed in the adjustment of the manipulator Jacobian, and since the fixture of the foot on the end effector is considered to be more secure than that between the shank and the robot base platform, Δ_{t0} can be treated as a constant vector. A short preliminary trial which involves the movement of the user's foot throughout a wide range of orientation (ideally in a zero torque mode to minimise the actuator forces) can therefore be carried out on the robot at the start of the robot's operation. The recursive least squares algorithm can be run during this initial trial to identify the Δ_{t0} parameter. This result can then be treated as a constant adjustment parameter and applied in (8.63) to give the adjusted manipulator Jacobian for subsequent operation of the robot.

8.5 Simulation Results

In order to evaluate the efficacy of the proposed elementary control scheme on the ankle rehabilitation robot, the developed impedance controller, the redundancy resolution scheme and an inner actuator force controller were all applied to the integrated foot-robot model presented earlier in this chapter. The simulation was carried out to emulate the scenario where the robot is used to guide the patient's foot under impedance control along certain rehabilitation trajectory while the user remains passive (i.e. no muscle activation). The trajectory used in the simulation was chosen to resemble pronation-supination motion of the foot and are given in (8.64), where the angles are expressed in radians and the variable t is the simulation time. The reference moment τ_d in the basic impedance control law was also set to be zero throughout the duration of the simulation.

$$[\theta_x \quad \theta_y \quad \theta_z]^T = \left[\frac{\pi}{6}\sin\left(\frac{\pi t}{6}\right) \quad \frac{\pi}{9}\sin\left(\frac{\pi t}{6}\right) \quad -\frac{\pi}{12}\sin\left(\frac{\pi t}{6}\right)\right]^T \tag{8.64}$$

8.5.1 Simulation with Rigid Biaxial Ankle Kinematics

Preliminary simulations have shown that the actuator force controller developed in Chapter 7 cannot be applied directly to the integrated model without causing system instability. Investigation into the problem revealed that the gains used in the proposed gain scheduling force controller were too large. Additionally, the set of stable gain values (found through trial and error using the simulation model) was also found to follow a pattern which differed from that established in Chapter 7 if the decoupled directions were determined using the originally proposed method. Further analysis showed that the cause for this problem lied in the fact that the ankle kinematic model used was of only two degrees of freedom (dof). The result of this is an altered manipulator Jacobian and hence also a variation in the decoupled directions and their associated singular values. Since the gain margin along the null vector was relatively low for the three dof manipulator model used to formulate the proposed controller, direct application of the proposed force controller to a two dof system had resulted in an unstable system. This is because the presence of an additional vector in the null space means that some of the higher gains applied in other directions will be projected onto the null vectors instead, thus increasing the effective gains beyond the critical gain and ultimately causing system instability. A similar phenomenon can also occur for the least stable decoupled direction in the two degree of freedom model due to the mismatch of assumed and actual decoupled directions.

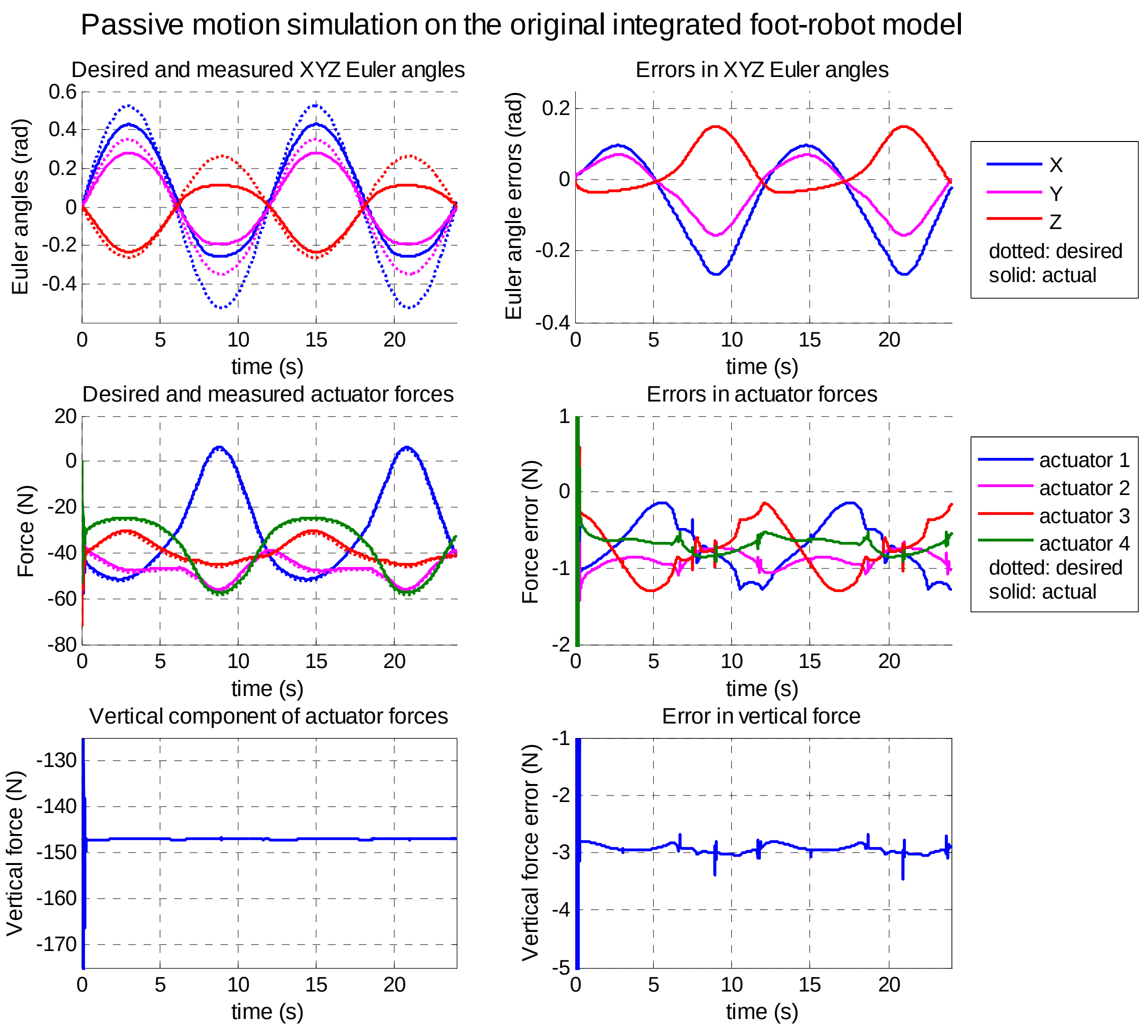

Figure 8.5: Simulation results of a passive motion trial on the ankle rehabilitation robot. This simulation applies the proposed basic impedance controller, redundancy resolution scheme and a modified actuator force controller on the integrated foot-robot model.

The above notion is supported by the fact that system stability can be restored when the force controller is redesigned by taking into account the manipulator Jacobian and inertia matrix of the two dof system. Using constant gains along the principal directions computed from the newly formulated coupling term, it was found that higher gains can be applied along directions with smaller singular values. Results of the simulation carried out using this modified inner force controller is given in Figure 8.5. An isotropic robot stiffness of 10Nm/rad and a robot damping of

2Nms/rad were used in the simulation. Additionally, a desired vertical force of -150N was also used in the redundancy resolution scheme.

8.5.2 Simulation with Added Yaw Compliance

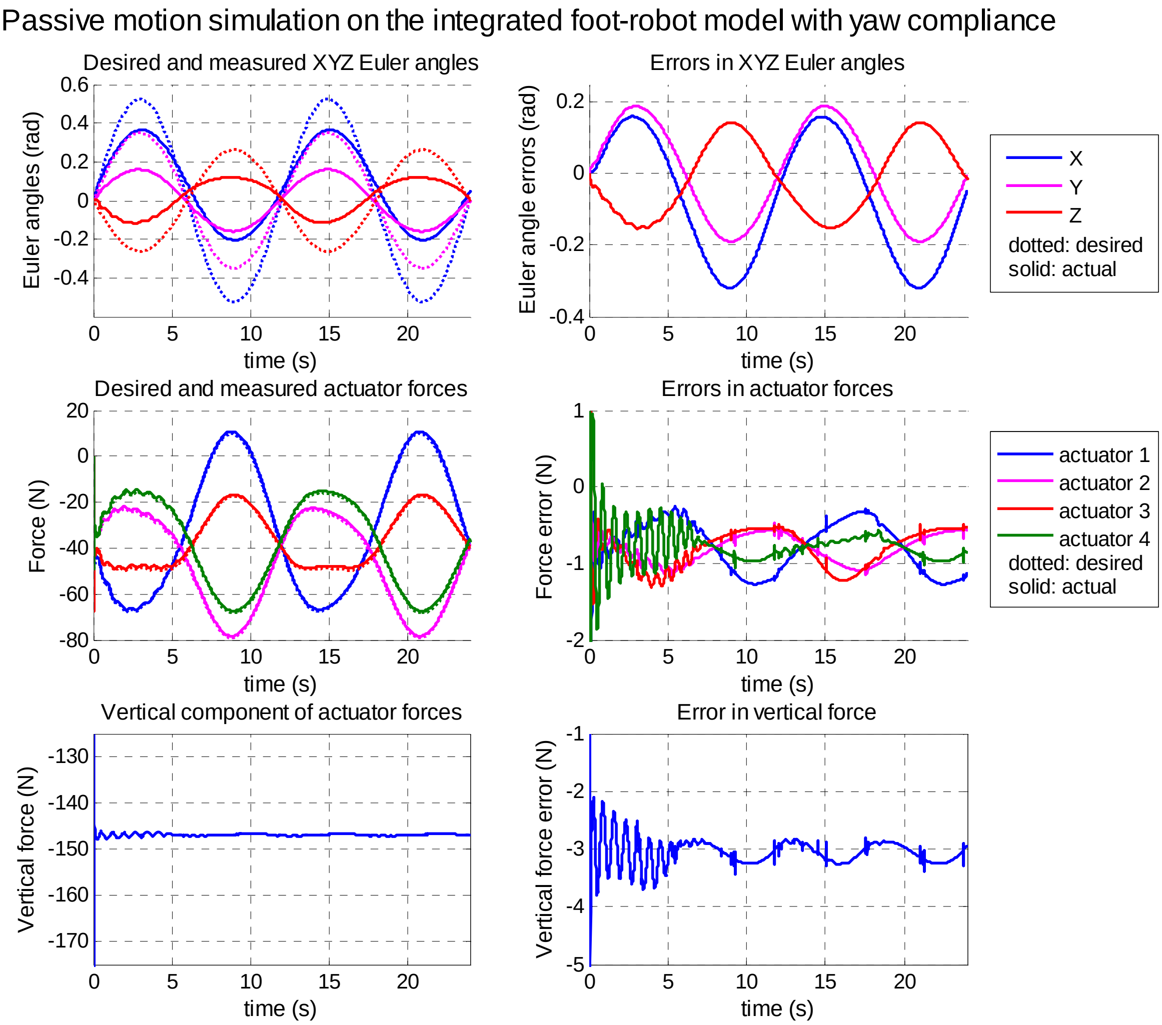

Figure 8.6: Simulation results of a passive motion trial on the ankle rehabilitation robot. This simulation applies the proposed basic impedance controller, redundancy resolution scheme and actuator force controller on the integrated foot-robot model with added yaw compliance.

Based on the findings obtained from the above simulation, an important point which needs to be addressed is whether the proposed actuator force controller can be applied to the actual ankle rehabilitation robot. Since the biaxial ankle model is only an approximation to the complex ankle kinematics, the actual motion available at the ankle is most likely not strictly constrained to be of only two degrees of freedom. Furthermore, the foot and shank of the user is also not rigidly attached to the robot as assumed in the integrated model, which means that the ankle motion will not be that of a pure two dof mechanism. To represent this in the simulated system, an additional degree of freedom had been included in the ankle model through addition of an extra revolute joint at the talus. This revolute joint is fixed in the vertical (yaw) direction, and the talus was allowed to rotate about this joint. A set of linear rotational spring and damper units with reasonably large stiffness and damping (k_z = 5Nm/rad, b_z = 2Nms/rad) were also added along this joint. These parameters had been chosen manually to prevent large angular deflections about this axis while maintaining a well damped system. A simulation similar to the one described above was then carried out using the proposed force controller and this modified foot model. It should be noted that due to added complexities in the kinematic structure of the integrated foot-robot system, there exists discrepancies between the inertia matrices used in Chapter 7 to obtain the gain margins and the actual inertia matrices of the integrated system. Consequently, the gains of the proposed controller were reduced (to approximately 75% of their original values) to ensure stability. The relative magnitudes of these gains however still followed the same trend as that used in the proposed controller. The results of this simulation are summarised in Figure 8.6.

8.5.3 Discussion

The results obtained from the simulation trials show a comparable level of force tracking capability in both systems. This however does not translate to a similar position following capability, with errors in the yaw compliant model much larger than that of the original foot-robot model. By noting that the same impedance controller has been used and that the force tracking capability in both systems are similar, the difference in the position errors must be caused by the addition of the yaw axis compliance. This is also believed to be partly the cause of the initial oscillations observed in the second simulation trial. Despite these differences, it is clear from both simulations that larger position errors can be found in the negative x-direction, an observation that is in line with greater ankle stiffness in the dorsiflexion direction. The simulation results also show that the redundancy resolution scheme is working well, with the total vertical force regulated to about 3N of the desired set point in the absence of friction along the actuators.

One other point to be noted is that high frequency force oscillations were observed at the start of both simulations. This is most likely due to the selection of initial states of the integrated system, where the initial force sensor deformations were set to be zero while in reality a certain force is required along the actuator to maintain equilibrium. There is therefore a period during the start of the simulation where the “correct” force sensor deformation is reached, thus leading to the observed transient oscillations. However, as the simulation progresses, these oscillations quickly decays and does not have significant impact on the overall simulation results.

8.6 Experimental Results

In addition to the simulations, the basic impedance controller was also tested experimentally using the actual ankle rehabilitation robot with a healthy test subject. The subject is an adult male (1.75m height) and ethics approval had been granted by The University of Auckland Human

Participants Ethics Committee (Ref. 2009/480). The robot was commanded to move the subject's right foot over the same trajectory using the basic impedance controller developed above. The foot of the user is attached onto the robot end effector platform using Velcro strips while the shank of the subject is attached through a shin guard to the shank brace on the ankle rehabilitation robot. The subject remained relaxed throughout the trial to minimise muscle activations, and thus the resulting motion can be considered passive. A segment of the results obtained from this experiment is shown in Figure 8.7. Note that the inner actuator force controller used in the experiment is that of the originally proposed force controller with no gain reduction as it was found to be stable in preliminary trials on the robot and thus higher gains were used to improve force tracking performance.

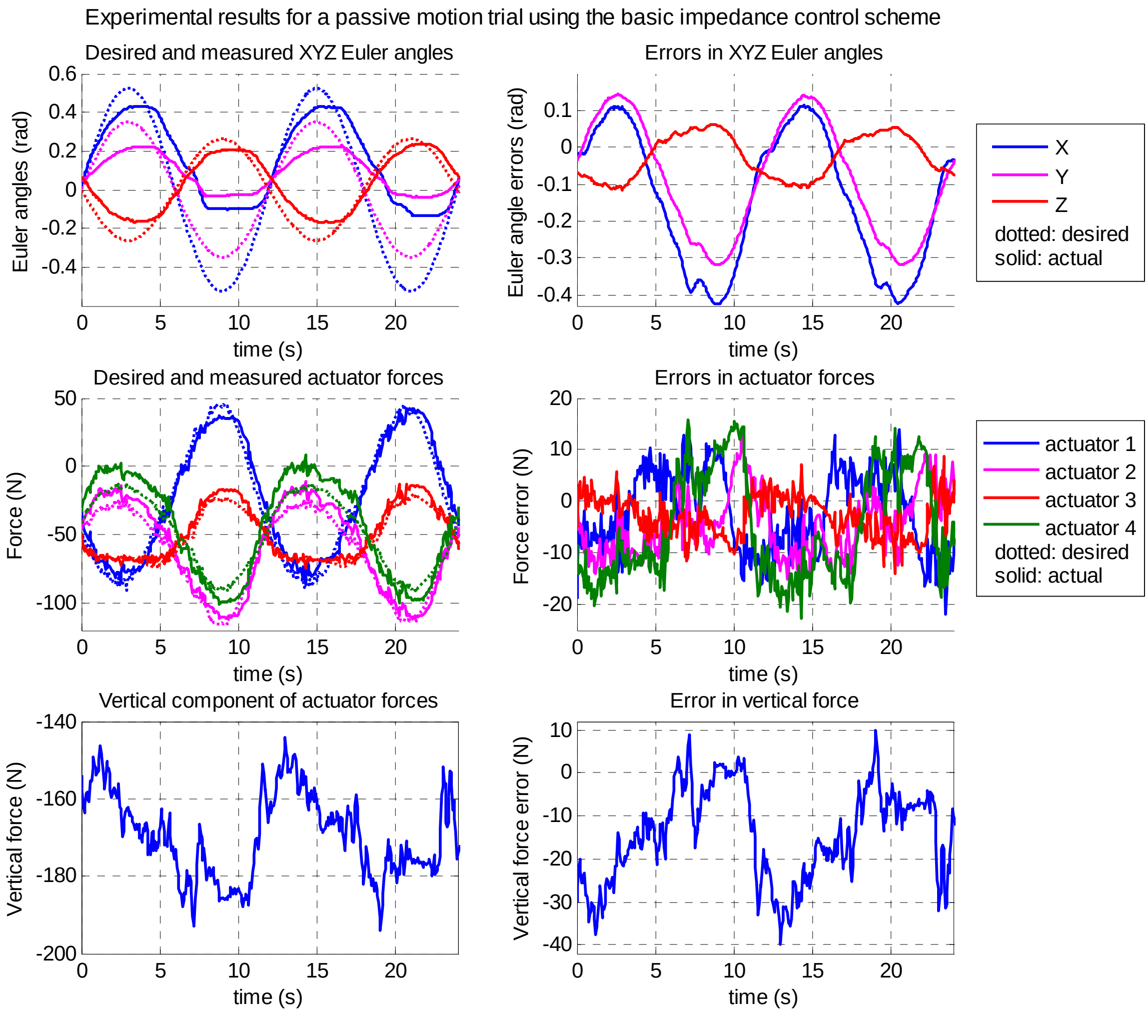

Figure 8.7: Experimental results of a passive motion trial on the ankle rehabilitation robot. This simulation applies the proposed basic impedance controller, redundancy resolution scheme and actuator force controller on the actual ankle rehabilitation robot.

8.6.1 Discussion

It can be seen from the experimental results that the force tracking capability on the robot was worse than that observed in the simulation. This was expected since friction was not included in the integrated model. Focusing on the performance of the basic impedance control scheme, it can be seen that the errors in X Euler angle did follow a very similar trend to those obtained from simulations, again with much larger errors in the negative X Euler (or dorsiflexion) direction. The motion in the Y Euler angle direction however was rather different from those seen in simulations as there was hardly any movement in the negative y direction. This can be due to several factors, one of which is the difference between the actual ankle stiffness and the stiffness of the ankle model used in simulation. Secondly, frictions within the actuators and passive robot joints can also contribute to smaller effective moments being applied to the foot. Lastly, imperfect attachment of the shank to the robot can also lead to the robot coordinate frame not being aligned perfectly with the ideal foot coordinate frame. The results however suggest that the first two factors could be more dominant here due to the small amount of negative y motion observed, while if the third factor is dominant then there should only be some form of bias/offset in the trajectory. Motion along the Z Euler angle shows that the measured motion in the z direction is actually tracking the desired trajectory quite closely compared to the simulations. This again can be due to discrepancies between the stiffness characteristics of the ankle model and the actual foot, or it can also be due to the fact that the yaw compliance is greater than assumed in the model used for the second simulation.

Considering that the desired vertical force is set to be about -180N, it can be seen that the robot is capable of regulating the total vertical force to within approximately 30N of the set point during most parts of the motion. This relatively large error (compared to the simulation) was the result of the larger force tracking error found in the actual ankle rehabilitation robot. By noting that a negative vertical force is equivalent to application of a compressive load on the ankle joint, and that the measured vertical force is predominantly greater than the desired force, it can be seen that the compressive load applied to the ankle is typically below that of the desired value. Since a compressive load is typically required to support the weight of the lower limb and to emulate different levels of weight bearing, a smaller compressive load means that it is less likely for the robot to “over-burden” the ankle joint. The larger vertical force error observed in the robot is therefore not likely to compromise the safety of the user.

From the experimental results, it can be seen that while the robot performance is not ideal due to hardware limitations such as friction and fixture issues, it is still capable of executing general rehabilitation tasks. The experimental trial had also shown that the proposed impedance and force control laws which represent the motion of the end effector (and hence also the foot) in three rotational degrees of freedom can be safely applied to the actual human ankle.

8.7 Chapter Summary

The first half of this chapter detailed the dynamic model of the parallel mechanism developed in this research and provided a description of the integration of this dynamic model with the actuator force and ankle dynamics to form a model of the overall system. Additionally, this chapter also presented the basic impedance controller used in the interaction control of the ankle rehabilitation device, as well as the redundancy resolution scheme used to achieve regulation of the total vertical force applied by the linear actuators. Issues surrounding the implementation of the proposed control schemes onto the actual robot were also discussed, with particular emphasis on the computation of end effector/foot orientation using redundant sensing and the estimation of the actual ankle centre of rotation.

The overall system model developed in this chapter was used to simulate the behaviour of the proposed interaction controller and it was shown that while the actuator force controller proposed in the previous section cannot be used directly on a system with a rigid biaxial ankle model, it can be adapted to work with a system with added rotational compliance in the yaw direction. Since the latter case is considered to be more representative of the real operating condition of the robot, the proposed control scheme is still considered suitable for use on the actual ankle rehabilitation robot. This notion is further verified by results obtained from the experimental trials, although the presence of significant actuator friction means that the performance of the overall system is still not ideal. The efficacy of the redundancy resolution scheme had also been demonstrated through the simulations while experimental results suggested that it is capable of offering an acceptable level of vertical force regulation at the ankle joint.

Chapter 9 Adaptive Interaction Control via Variable Impedance Control

While the rehabilitation robot can be programmed to carry out fundamental rehabilitation operations such as passive range of motion and resistive exercises using the basic robot interaction controller described in the previous chapter, one of the main aims of this research is to go one step further and improve the safety and performance of the rehabilitation robot through development of adaptive control strategies. Such strategies can involve automatic adjustments of the controller parameters or the adaptation of controller reference signals. In this work, the basic impedance control law presented in Chapter 8 had been extended to yield a more advanced interaction control scheme for passive range of motion and active assistive exercises. One of these extensions involves the incorporation of an impedance parameter adjustment module in the overall interaction control scheme. This impedance adjustment rule is designed to utilise the biomechanical information provided by the ankle model developed in Chapter 5 to improve the performance of the ankle rehabilitation robot. This chapter details the formulation of this impedance adjustment scheme and evaluates the efficacy of the proposed scheme through both simulation and experimental results.

9.1 Biomechanical Model Based Impedance Adjustment

It can be seen from the definition of the basic impedance control law that it is essentially a proportional-derivative controller for the end effector orientation, where the desired manipulator stiffness and damping are respectively represented by the proportional and derivative gain matrices. Typically, the selection of these gain matrices can be done through manual tuning of the PD controller to yield the desired performance. For instance, the value of the proportional gain matrix can be increased to give a stiffer robot and better position tracking while a decrease in the same parameter will make the robot more compliant and thus allows better force control. It should be noted however that apart from manual tuning, the impedance parameters of the robot can also be selected by considering the optimisation of certain objective functions [29].

The robot impedance also need not be held constant during robot operation. In fact, researchers had developed more advanced impedance control schemes which vary the robot impedance parameters according to the environmental characteristics [137] or to the task being carried out [125]. An example of the above in the area of physical human robot interaction includes the variation of robot damping during human-robot cooperative tasks to improve coupled stability [138]. Additionally, the impedance robot control scheme developed in [139] for an upper limb rehabilitation robot also varies its impedance parameters according to the arm configuration to limit extensions of a ligament connecting the radius and ulna.

It can be seen from the above that more systematic approaches are available for tuning of impedance parameters and this had been further explored in this research. Hogan had shown that the weighted sum of the position error and robot-environment interaction forces can be minimised by selecting the manipulator impedance to be proportional to the environmental admittance (inverse of the environment impedance) [29]. This impedance selection scheme can therefore be used to find a balance between accurate positioning and "gentle" interaction between the user and robot. Because of the uncertainties that are present in the kinematics of the human limbs/joints, portions of a given reference trajectory may in fact be inadmissible for the limb/joint under consideration. Consequently, by choosing the robot impedance to be proportional to the limb/joint admittance, the controller will be able to trade off positional accuracy for lower interaction forces at regions with higher stiffness, thus ensuring safe operation of the rehabilitation robot.

The above feature is particularly important for the ankle rehabilitation robot developed in this research. The biaxial kinematic model of the human ankle is discussed in Chapter 4, and it is clear that this model describes the ankle motion using only two degrees of freedom. This therefore prompts a question on the validity of designing a three degree of freedom outer loop position controller to regulate the orientation of the robot end effector. The response to this question is that the design of a controller to handle motion in three degrees of rotational motion is in fact intentional. This is because a more general controller will be able to handle the variability of ankle kinematics among different users. By applying impedance control in the three rotational degrees of freedom, all possible orientations of the ankle kinematic model can be accommodated. The possible downside of this however, is that the commanded orientation trajectory may consist of points or segments which are not realisable by the ankle kinematics of the current user. This problem is precisely the issue being addressed by the implementation of this environmental admittance based manipulator impedance adjustment rule. Due to its ability to balance safety and performance as well as its applicability to the developed device, this controller parameter selection scheme had been investigated in this research.

9.1.1 Formulation of Environment Based Stiffness Adaptation Scheme

Clearly, knowledge of the environmental admittance is essential to allow implementation of the adopted impedance selection rule. This information can be estimated by considering the computational ankle model developed in Chapter 5. Since the robot is expected to operate in low velocity conditions, only the steady state behaviour of the ankle model was used to estimate the environmental characteristics. This means that only the stiffness/compliance of the environment is observed in the development of this impedance adaptation scheme. Additionally, the environmental characteristics were also obtained in the absence of any muscular activation, or in other words, when the foot is completely passive.

In order to estimate the environmental stiffness, the developed ankle model was used to compute the resistive moments applied by the various force elements (ligaments and muscle-tendon units) on the ankle and subtalar joints at various points on the θ_a-θ_s plane, where θ_a and θ_s are respectively used to denote displacements about the ankle and subtalar joints. The ankle and subtalar moments obtained through this exercise are shown in Figure 9.1.

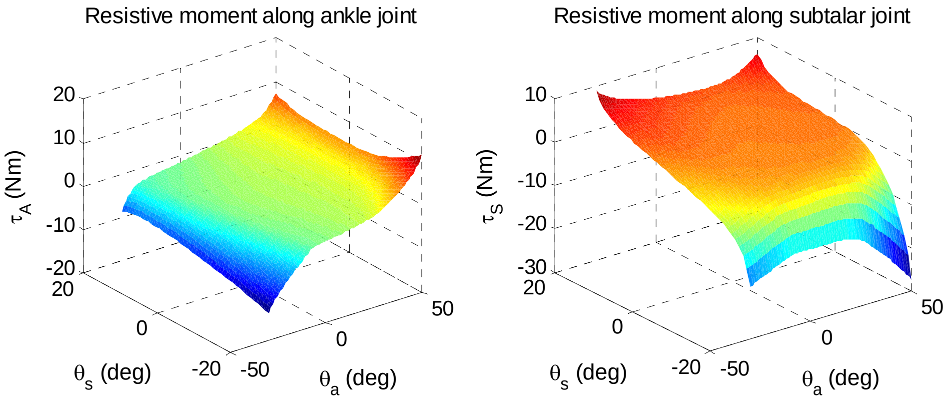

Figure 9.1: Resistive moments contributed by the ligaments and muscle-tendon units on the ankle and subtalar joints. These moments are obtained from the computational ankle model by assuming steady state behaviour of the force elements.

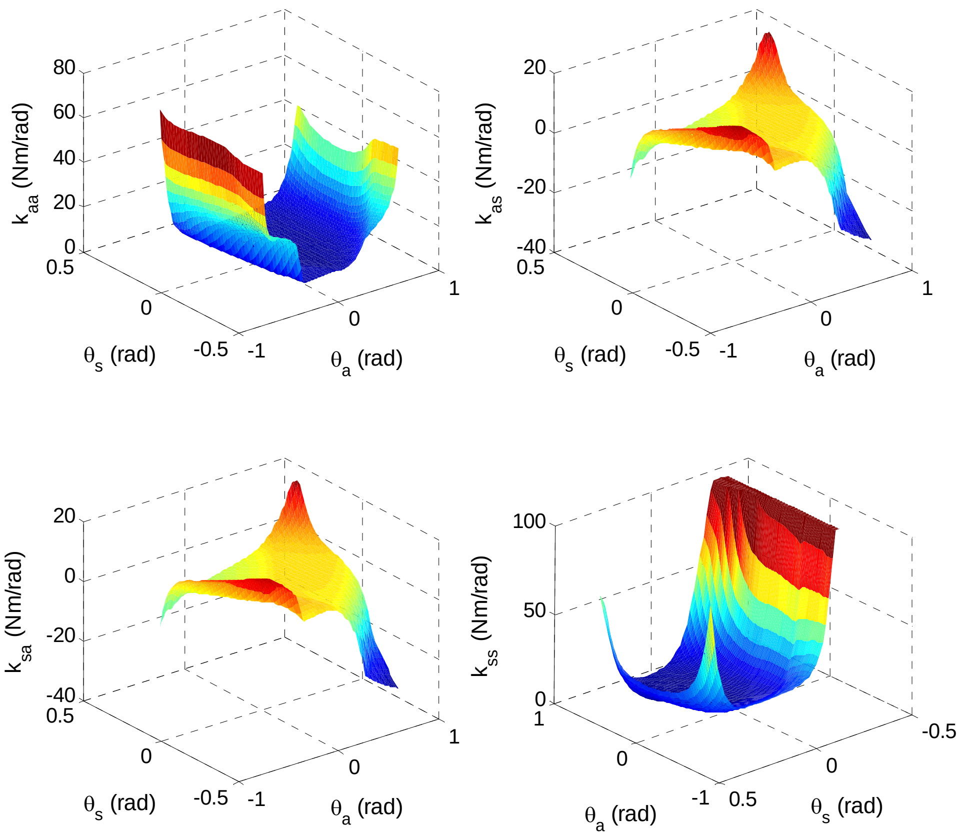

Figure 9.2: Surface plots for different elements of the ankle stiffness matrix computed across a range of ankle and subtalar joint displacements.

The available moment-displacement data can then be numerically differentiated to obtain the stiffness matrix in the ankle and subtalar coordinates as shown in (9.1), where τ_A and τ_S are respectively the resistive moments observed along the ankle and subtalar axes. The results of these numerical differentiations are summarised in Figure 9.2. Note that stiffness values shown are saturated at 100Nm/rad to ensure that details on the plots are not lost to accommodate the inclusion of extreme values. It can be seen from Figure 9.2 that the stiffness matrix varies quite significantly over the range of ankle and subtalar displacements considered. The results have also verified that the computed stiffness matrix is symmetric as expected.

$$K_{as} = \begin{bmatrix} k_{aa} & k_{as} \\ k_{sa} & k_{ss} \end{bmatrix} = \begin{bmatrix} \frac{\partial \tau_A}{\partial \theta_a} & \frac{\partial \tau_A}{\partial \theta_s} \\ \frac{\partial \tau_S}{\partial \theta_a} & \frac{\partial \tau_S}{\partial \theta_s} \end{bmatrix} \approx \begin{bmatrix} \frac{\Delta \tau_A}{\Delta \theta_a} & \frac{\Delta \tau_A}{\Delta \theta_s} \\ \frac{\Delta \tau_S}{\Delta \theta_a} & \frac{\Delta \tau_S}{\Delta \theta_s} \end{bmatrix} \tag{9.1}$$

Contour plots of the elements in the stiffness matrix are also given in Figure 9.3. It can be concluded from these contour plots that there is a large region of points with relatively low stiffness near the neutral orientation. The ankle stiffness however increases much more rapidly as the foot is moved further away from the neutral orientation. It can also be seen that the magnitudes of off-diagonal elements in the stiffness matrix are also typically smaller than the diagonal elements, which suggests that the stiffness matrix will remain positive definite throughout the ankle's range of motion. This is confirmed by the fact that determinants of the computed stiffness matrices are all greater than zero.

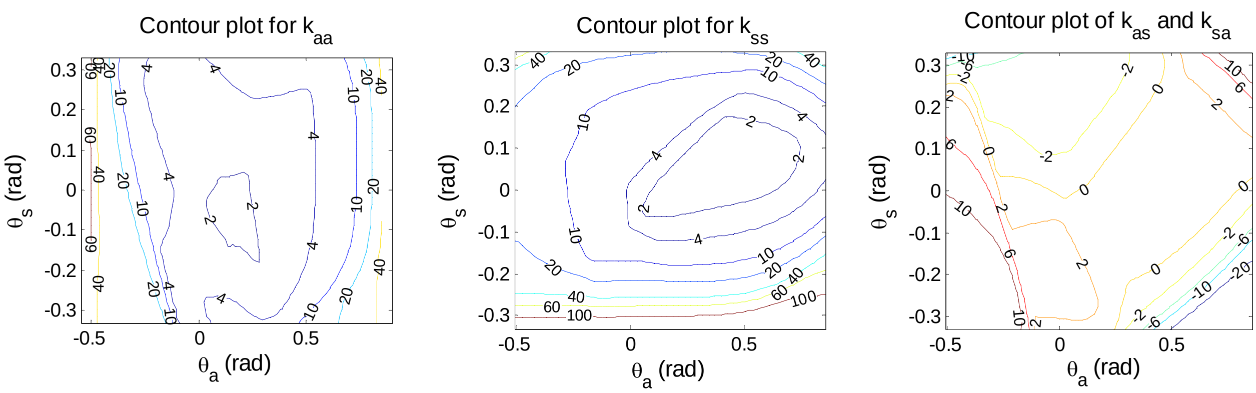

Figure 9.3: Contour plots for different elements of the ankle stiffness matrix computed across a range of ankle and subtalar joint displacements

As the impedance adaptation rule considered requires that the robot impedance parameters be selected in proportion to the environmental admittance, the robot stiffness parameter should be chosen to be proportional to the environmental compliance. However, as the ankle stiffness matrix K_{as} obtained above is a 2×2 matrix while the robot stiffness matrix K_d is a 3×3 matrix, computation of the suitable robot stiffness matrix is not a straightforward task and requires the ankle stiffness matrix to be converted into an equivalent task space compliance matrix. The procedure involved in this conversion can be derived by first considering the relationship between torques/velocities in the global coordinate frame and the generalised forces/velocities of the XYZ Euler angle/ankle-subtalar coordinates. Equation (9.2) can be used to relate the time derivatives of the XYZ Euler angle ($\dot{\Theta}$) and of the ankle-subtalar joint displacements ($\dot{\theta}_{as}$) to angular velocities in the global frame (ω) through the linear mappings $H_\Theta \in \mathbb{R}^{3\times 3}$ and $H_{as} \in \mathbb{R}^{3\times 2}$. The same equation can therefore also be used to obtain an approximate relationship between small changes in XYZ Euler angles and in ankle-subtalar joint displacements. On the other hand, torques about the Euler angle axes and the ankle-subtalar joints can be related to the equivalent torque in the global coordinate frame through (9.3) and (9.4) respectively. Further, by noting that the compliance matrix in the ankle-subtalar coordinates S_{as} can be computed from (9.5), and that it can be used to produce an estimate of the change in ankle-subtalar joint displacements given a small change in the moments applied along these joint axes as in (9.6), the equivalent ankle compliance relationship can be restated in the coordinates of XYZ Euler angles as (9.7), with S_Θ being the compliance matrix in XYZ Euler angle coordinates.

$$\begin{gathered} \omega_{glob} = H_\Theta \dot{\Theta} = H_{as}\dot{\theta}_{as} \\ \Longrightarrow H_\Theta \Delta\Theta = H_{as}\Delta\theta_{as} \end{gathered} \tag{9.2}$$

$$\begin{gathered} \tau_\Theta = {H_\Theta}^T \tau_{glob} \\ \Longrightarrow \Delta\tau_\Theta = {H_\Theta}^T \Delta\tau_{glob} \end{gathered} \tag{9.3}$$

$$\begin{gathered} \tau_{as} = {H_{as}}^T \tau_{glob} \\ \Longrightarrow \Delta\tau_{\mathrm{as}} = {H_{\mathrm{as}}}^T \Delta\tau_{glob} \end{gathered} \tag{9.4}$$

$$S_{as} = {K_{as}}^{-1} \tag{9.5}$$

$$\Delta\theta_{as} = S_{as}\Delta\tau_{as} \tag{9.6}$$

$$\Delta\Theta = \underbrace{{H_\Theta}^{-1} H_{as} S_{as} {H_{\mathrm{as}}}^T {H_\Theta}^{-T}}_{S_\Theta} \Delta\tau_\Theta \tag{9.7}$$

It is clear from (9.7) that the S_Θ matrix is at most of rank two. This means that the compliance along the null vector is zero, thus indicating that the environment is perfectly rigid along the direction orthogonal to both the ankle and subtalar joint axes (denoted by unit vector v_p). This is a result of representing the two degree of freedom ankle compliance in three degrees of freedom. According to the impedance adaptation rule described above, the robot stiffness should be proportional to the environmental compliance. This means that the ankle compliance matrix obtained using this rule will be rank deficient with a null vector along ${H_\Theta}^{-1} v_p$. In the event where a full rank controller gain matrix is required (for instance to satisfy stability/performance criteria such as that shown in section 10.1.4), a small but constant level of compliance can be assumed along ${H_\Theta}^{-1} v_p$ and the robot stiffness matrix can be obtained in the form shown in (9.8). Note that this stiffness matrix is consisted of a stiffness component obtained from application of the impedance adaptation rule with the proportionality constant η, and an additional stiffness component along the direction of v_p with a singular value of κ.

$$K_p = \eta S_\Theta + \kappa {H_\Theta}^{-1} v_p {v_p}^T {H_\Theta}^{-T} \tag{9.8}$$

As shown previously, the ankle stiffness and therefore compliance can vary significantly with the foot orientation. It follows that different controller gain matrices must be used at different orientations. While the ankle stiffness matrix presented above can be computed with reference to the ankle and subtalar joint displacements, such displacements cannot be directly measured on the ankle rehabilitation robot. Consequently, the estimates for these displacements as obtained from the ankle kinematic estimation algorithm described in Chapter 4 are used instead. Since calculation of the stiffness matrix is a computationally intensive task and thus not suitable for real time implementation, a lookup table for individual elements of the ankle stiffness matrix K_{as} had been created to adjust the controller parameters in a gain scheduled manner. These lookup tables can then be used to approximate the ankle stiffness matrix during the operation of the controller through linear interpolation of the tabulated values. Note that the linear interpolation is only done when the estimated ankle and subtalar joints are within the range provided by the lookup table and stiffness values. Stiffness values for orientations located beyond this range are saturated at the values observed at the range boundaries. Since the robot stiffness matrix is positively correlated to the inverse of the ankle stiffness values, the occurrence of out of range ankle and subtalar displacements will simply result in the robot stiffness matrix being saturated at a lower bound value. As this lower bound value is typically small due to the already large values observed at the range boundaries, this saturation is not expected to impose significant concerns on user safety.

Another point worth noting is that the application of this gain scheduling approach assumes that the stiffness variation of a typical user varies in a similar manner to that observed in the computational ankle model. The use of the ankle and subtalar joint displacements as independent variables in the lookup table means that this stiffness variation is represented with respect to displacements about the functional joints of the ankle rather than the overall foot orientation in the global frame. Since the stiffness of the ankle considered is ultimately caused by tensions within ligaments and tendons located around the functional joints, the stiffness variations observed in the adopted displacement parameterisation is considered to be more suitable in capturing, for a general foot, the underlying relationship between ankle stiffness and ankle configuration.

9.1.2 Limitations of the Proposed Impedance Adjustment Scheme

As large variability can be found in the physical properties of the ankle and foot, it is acknowledged that the ankle stiffness relationship used in the parameter adjustment module is most likely not quantitatively identical to that observed in a particular user. However, due to the use of an anatomically based model, it is believed that the trend observed in the computational ankle model would still be applicable for a general ankle and can be used as a good starting point for the proposed impedance adjustment module.

In addition to the above, the anatomical structure/characteristics of a patient suffering from ankle sprain injuries could also be significantly different from that considered in the healthy ankle model due to the presence of damaged ligaments and swelling. As a result, additional work will be required to identify and classify the anatomical changes associated with different types and grades of injury. These observations can then be used to alter the underlying ankle model used to generate a more patient specific set of stiffness lookup tables.

9.2 Simulation Results for Impedance Adjustment Module

Simulations were carried out to verify the effectiveness of the proposed impedance adjustment rule. These simulations were done using a simplified version of the integrated foot-robot model. This simplified model leaves the force sensor and actuator dynamics out of the system to allow evaluations to be made on the fundamental concept of adapting the robot impedance according to the environmental admittance. These simulations again involved emulation of passive motion trials using the same reference trajectories as the previous chapter. Two simulation runs were carried out, a control run with the basic impedance control scheme proposed in the previous chapter, where robot stiffness and damping parameters were set to be constant (uniform stiffness and damping of 10Nm/rad and 2Nms/rad respectively) and a second trial which utilised the proposed impedance adjustment rule to allow variable impedance control (η=20, chosen so that the larger robot impedance parameters obtained using this rule is similar in magnitude to that of the constant impedance case). These simulation results are presented in Figure 9.4.

To facilitate the evaluation of the performance of each of these two controllers, a cost function similar to that used by Hogan to derive the optimality of the impedance selection approach used in this research was also evaluated from the simulation results. More specifically, the cost function considered at each sample C_k is given by (9.9), with k being the sample number, Θ_e being the errors in the XYZ Euler angle coordinates, τ_k being the applied torque and η is a constant weighting which is also the same as the proportionality constant that relates the manipulator impedance to the environmental admittance. The cost index can then be computed from this function as (9.10), where $\delta_{t,k} = t_{k+1} - t_k$ is the time between two successive samples, T_{tot} is the total time elapsed between the first and the last sample and N is the total number of samples available.

$$C_k = \eta {\Theta_{e,k}}^T \Theta_{e,k} + {\tau_k}^T \tau_k \tag{9.9}$$

$$C = \frac{1}{T_{tot}} \sum_{k=1}^{k=N-1} C_k \delta_{t,k} \tag{9.10}$$

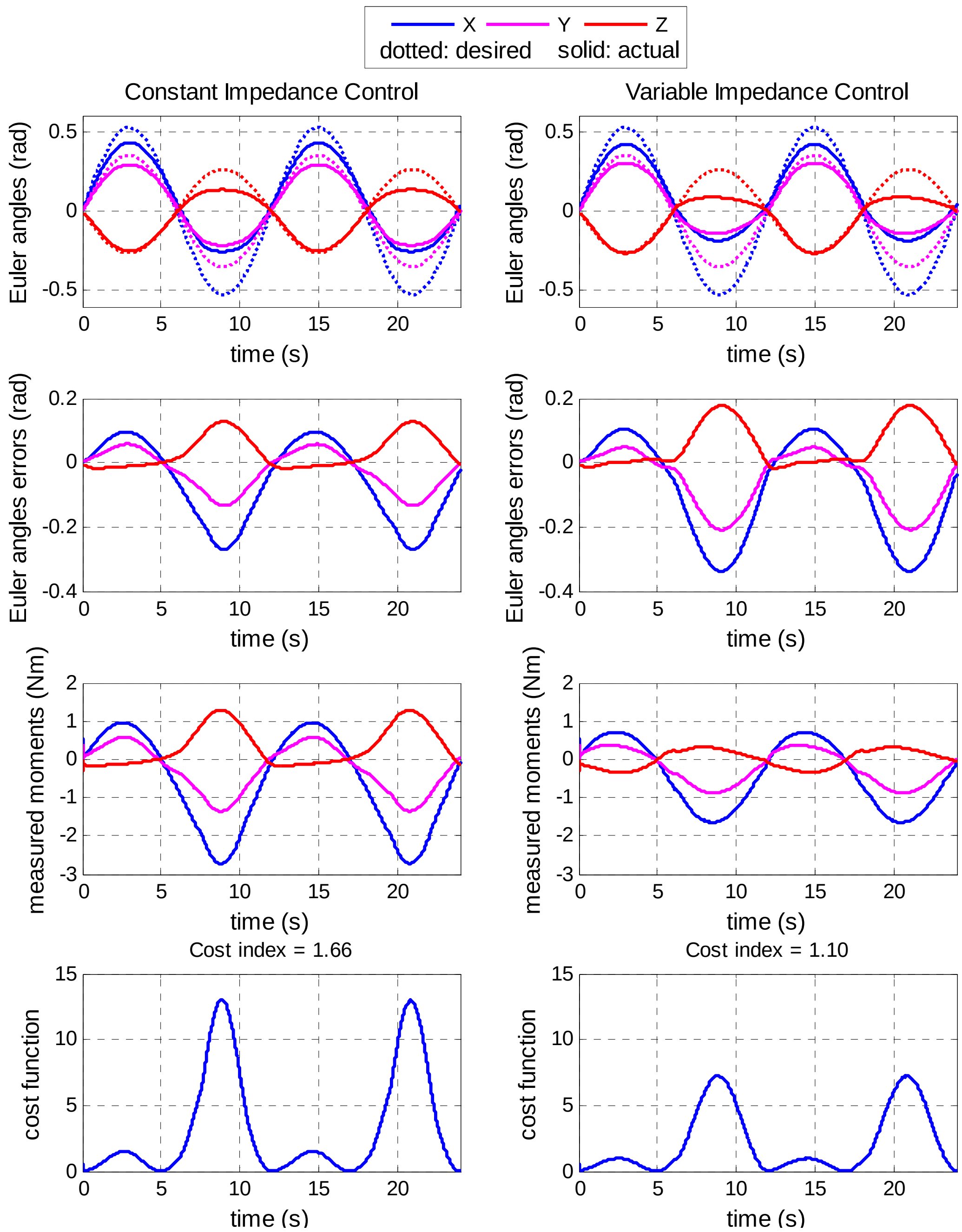

Figure 9.4: Simulation results of passive moment trials using the constant and variable impedance control schemes.

9.2.1 Discussion

The simulation results clearly show that the variable impedance controller does indeed have a smaller cost function when compared with the constant controller. Closer inspection of the position errors and the task space moment shows that while the constant impedance case offers greater positional accuracy, it does so at the expense of significantly larger task space moments. This is particularly noticeable when the foot is moving in the pronation direction (combination of dorsiflexion, eversion and external rotation/abduction), where it is clear that the variable impedance control has considerably reduced its actuation effort compared to the constant impedance controlled system. In rehabilitation tasks, it is necessary to limit the moments applied to the user's limb or joint in order to minimise the likelihood of injuries. The proposed impedance adaptation rule is therefore well suited for this type of tasks. A disadvantage of the variable impedance approach is that it may not be able to produce sufficient motion in stiffer directions due to its low gains. A solution to this is to apply the impedance adjustment rule with a suitable moment reference profile in the impedance controller. The additional desired torque will then act to drive the foot further in stiffer directions, while the reduction of robot impedance in stiff regions will ensure that greater emphasis is placed on torque control in these regions. As a result, as long as the provided moment reference is within tolerable limits, the robot will be able to operate safely with little risk of causing any injuries or discomfort to the user.

9.3 Experimental Results for Impedance Adjustment Module

In addition to the above simulations, the impedance adjustment rule was also implemented and tested in practice on the actual ankle rehabilitation robot. Two experimental trials were conducted, on a single subject (healthy adult male of 1.75m height, ethics approval reference 2009/480) using the same reference trajectories as those used in the simulations. The subject's foot was kept in a relaxed state during the trials to study the effect the control schemes have on passive foot motion. The constant impedance parameters were identical to those used in the simulation while an additional term ($\kappa H_{\Theta}{}^{-1} v_p v_p{}^T H_{\Theta}{}^{-T}$, κ = 0.5) was added to the stiffness matrix of the variable impedance control to provide some control along the direction orthogonal to both the estimated ankle and subtalar joint axes. The results from these trials, together with the computed cost functions and cost indices, are summarised in Figure 9.5.

9.3.1 Discussion

The experimental results have again shown the variable impedance controlled case to be better in terms of a lower cost index, albeit to a much smaller extent in relative terms. Examination of the motion trajectories revealed that while the foot is moved to a similar position in supination in both controllers, the variable impedance controlled trial resulted in a much lesser degree of pronation motion (negative x, negative y, positive z). This can be attributed to the smaller moments being applied in the x and y directions during pronation movements.

It can be seen from the results that the cost index obtained from both experiments are much larger than those found in simulation. This is most likely caused by the considerably larger errors encountered in the actual ankle rehabilitation robot due to frictional forces and torques within the actuator-robot mechanism. This larger error also causes larger moment commands and since some of the moments are used to overcome friction in the mechanism rather than acting directly on the foot, the overall cost function values will also appear larger. The above issues provide more motivation for the use of a feed-forward moment command in conjunction with the variable impedance controller, where additional moment components can be added to overcome the frictional effects.

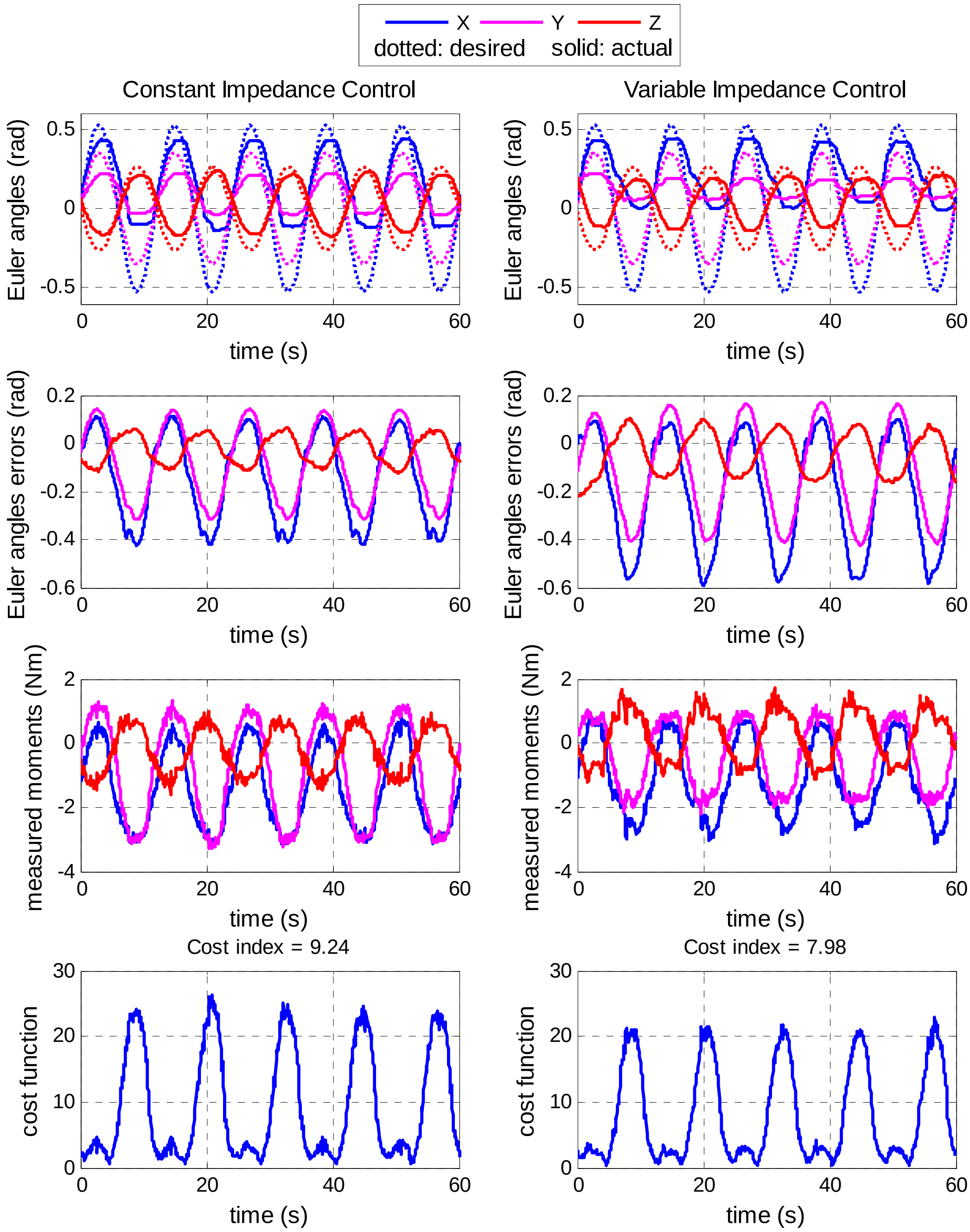

Figure 9.5: Experimental results of passive moment trials using the constant and variable impedance control schemes.

Since the ankle model was formed without using subject specific data, another source for discrepancies between simulation and experimental results comes in the form of a mismatch between stiffness characteristics of the subject's ankle and that obtained from the ankle model. The effect of this is that the robot impedance may be reduced to small values even when the actual compliance at that region is relatively high. This suggests that the stiffness or compliance characteristic should ideally be acquired online or adapted to the patient’s characteristics to allow better controller performance. However, the above can be difficult to achieve, particularly as the stiffness of the ankle is not only dependent on the foot configuration but also the levels of muscle activation. This makes estimation of the instantaneous ankle stiffness challenging and is the reason for the use of a lookup table based approach which considers only the passive foot stiffness. Nonetheless, this can still be the subject of future research.

9.4 Chapter Summary

This chapter presented the variable impedance control approach proposed in this research to achieve adaptive interaction control. The environment based stiffness adaptation module is used to adapt the robot stiffness in proportion to the environmental compliance, which is computed from the ankle and subtalar joint displacement estimates produced by the kinematic estimation algorithm presented in Chapter 4, as well as a foot configuration to ankle stiffness mapping obtained using the ankle model developed in Chapter 5. Simulation and experiments using the proposed adaptation scheme had shown that the proposed robot impedance adaptation scheme does decrease the performance cost function which is computed as a weighted sum of applied moment and motion tracking error, thus indicating that the proposed method can be used to trade off positional accuracy to maintain safety of the rehabilitation robot.

Chapter 10 Adaptive Interaction Control via Assistance Adaptation

While the previous chapter presents the incorporation of adaptability in an interaction control scheme through use of variable impedance, additional means can also be utilised to further enhance the capability of the controller to accommodate users of different joint characteristics and capabilities. This chapter explores the use of an assistance adaptation scheme to achieve the above and presents the implementation of a control module to facilitate active user participation in the rehabilitation exercises while considering the possibilities of a constrained workspace. Additionally, the proposed assistance adaptation scheme is also designed to reduce the amount of resistance applied by the robot when the user is moving ahead of the reference position. The formulation, simulation case study and experimental investigation of such a scheme are first presented in this chapter. The chapter then ends with an overview of the interaction control framework developed in this research and a discussion on how different ankle rehabilitation exercises can be implemented using this interaction control framework.

10.1 Assistance Adaptation

One of the important functionality of rehabilitation robots is to guide the user's affected limb or joint through certain rehabilitation trajectories. For severely affected joints or limbs, the effort required to realise the motion will be completely provided by the rehabilitation robot, and the user's limb will act as a passive environment. As commercially available devices in the form of continuous passive movement (CPM) machines can already be used to generate purely passive motion, support for motion therapy in rehabilitation robots should go beyond that of pure passive movements to justify its use in rehabilitation. A common operation of rehabilitation robots therefore involves the cooperation of both the user and robot to achieve the desired motion. The main idea used in the literature to achieve active assistance is to adapt either a feed forward force or the parameters of the interaction controller based on certain performance measures, typically in the form of a position tracking error [2, 14, 49]. One main emphasis of such adaptation algorithms is that the assistance provided by the robot should decrease over time so as to continually challenge the users to exert their own effort and thus actively participate in the exercises.

While active assistance exercises are primarily aimed at neuromotor training of patients suffering from neurological disorders, adaptive control schemes developed for such exercises are still highly relevant for general rehabilitation tasks. This is particularly the case for approaches based on adaptation of a feed forward force/moment. This is because the variable impedance controller would integrate well with such a feed forward force adaptation scheme as it can be used to provide a suitable moment reference trajectory. Furthermore, even if the main emphasis of the current research is in the rehabilitation of sprained ankles, the developed robot and control scheme can also be potentially applied in physical therapy of other injuries/disorders. The inclusion of an assistance adaptation scheme on the robot will therefore ready the developed robot for future extensions. Based on the above rationale, a feed forward force/moment based assistance adaptation scheme had been included in the overall robot interaction controller.

10.1.1 Impedance Control with Adaptive Feed Forward Force

Generally, when pure impedance control is used in the interaction control scheme, large impedance parameters will be required to provide sufficient motion in stiff environments. Two problems can arise with this arrangement. Firstly, larger robot impedance equates to higher position feedback gains, and can lead to system instability in non-passive interaction controllers. More importantly, higher impedance parameters also lead to reduced compliance of the rehabilitation robot, thus potentially compromising the safety of the user since it is possible that the desired trajectory is in fact outside the range of motion of the user’s limb or joint. However, with a feed forward force term in the controller, the additional effort contributed by this term will allow greater movements to be made and provided that the magnitude of this feed forward term is kept at safe levels, the risk of injury will also be minimal. An advantage of a feed forward force based adaptation scheme is therefore the ability to obtain better motion tracking while still maintaining relatively low robot impedance.

Wolbretch et al. had proposed an interaction controller with both a feed forward force component and an impedance control component to accomplish the active assistance task [50]. The feed forward force is used to capture information relating to the gravitational terms of the robot and user dynamics, as well as the capability of the user in producing motion at different positions. This force can therefore be set to be a sufficiently large value in a manner which is not directly related to the position error. The impedance component can then be chosen with small impedance parameters to permit deviations from the commanded trajectories.

The control and adaptation laws for the interaction controller given in [50] is represented by (10.1) and (10.2) respectively, where $F_r \in \mathbb{R}^m$ is the assistive force applied by the robot in the m dimensional workspace and $Y\hat{a}$ is the feed forward component of the force. $Y \in \mathbb{R}^{m\times n}$ is the regression matrix which is obtained from the activation levels of a set of n spatially distributed Gaussian radial basis functions and $\hat{a} \in \mathbb{R}^n$ is a vector of the weightings associated with these Gaussian functions. Additionally, $K_P \in \mathbb{R}^{m\times m}$ and $K_D \in \mathbb{R}^{m\times m}$ are the stiffness and damping matrices used in the impedance component of the control law and x_e is the position error. Lastly,

$\Gamma \in \mathbb{R}^{n\times n}$ is a symmetric positive definite matrix and τ is the time constant of the parameter adaptation law. This control scheme had also been proven stable in the Lyapunov sense, where it was shown that the system error is bounded [50].

$$F_r = Y\hat{a} + K_P x_e + K_D \dot{x}_e \tag{10.1}$$

$$\dot{\hat{a}} = -\frac{1}{\tau} Y^T (YY^T)^{-1} Y\hat{a} + \Gamma^{-1} Y^T (\dot{x}_e + \Lambda x_e) \tag{10.2}$$

An inspection of the adaptation law shows that the feed forward assistive force is controlled by two terms, one relating to the existing parameter values and another which depends on the position tracking error. It can be seen that the matrix Γ is used to control how the position tracking error will increase the feed forward force adaptation rate while the time constant τ determines how quickly the feed forward assistance reduces over time in the absence of any position tracking errors.

This adaptation law appears to be suitable for the scenario where the workspace is free of kinematic constraints or stiff regions as the adaptation law will adjust the feed forward assistive force until the rate of decay of the force is balanced out by the position tracking error, at which stage a steady state assistive force will be obtained. However, when uncertain kinematic constraints are present in the operating environment and engaged by the robot, such an adaptation law would continue to increase the forces applied in the constrained directions until the adaptation law reaches the steady state assistive force. Such behaviour is considered to be undesirable as the increase in interaction force serves little to improve the trajectory following capability of the user-robot system. Additionally, the above control and adaptation law will also act to correct the position of the end effector regardless of whether the current position is behind or ahead of the current reference position in the desired trajectory. In assistive rehabilitation exercises, users are typically allowed to move ahead of the desired trajectory with little or no resistance. This issue has been addressed by some researchers such as in [2] where the potential function used to define the corrective forces applied to the user is defined in such a manner that resistance will not be exerted on the user when the end effector position is further along the desired exercise path. In this work, modifications are proposed to the control and adaptation laws shown in (10.2) to accommodate the two issues discussed above.

10.1.2 Alternative Error Dependency Functions

In order to reduce the force increase due to constraints and high stiffness in the environment, the tracking error dependent term in the parameter adaptation law (10.2) can be modified so that it does not continue to increase proportionately with the error magnitude as large tracking errors are encountered. Two approaches to limit the contribution of large tracking errors in the force adaptation law have been investigated and will be discussed in this section. For both methods, the adaptation law will retain a similar form as that used in (10.2). A more intuitive representation of the adaptation law in terms of the feed forward force is shown in (10.3), where $F_{ff} = Y\hat{a}$ is the feed forward force and k is a scalar which determines the influence of the error dependent term. It should be noted that this form is selected so that its minimal norm solution for $\dot{\hat{a}}$ is equivalent to (10.2) when the time rate of change of the regression matrix Y is ignored and when the matrix Γ is a multiple of the identity matrix, with $\Gamma^{-1} = kI$. Using the formulation shown in (10.3), it can be seen that the relationship (10.4) holds for the adaptation law (10.2). This relationship will be referred to hereafter as the error dependency function (EDF), and two alternative error dependency functions were considered in this work.

$$\dot{F}_{ff} = -\frac{1}{\tau}F_{ff} + kYY^T\varepsilon$$
$$\dot{\hat{a}} = -\frac{1}{\tau}Y^T(YY^T)^{-1}Y\hat{a} + kY^T\varepsilon \tag{10.3}$$

$$\varepsilon = \dot{x}_e + \Lambda x_e \tag{10.4}$$

The first alternative EDF is rather intuitive and involves limitation of the error component used in the adaptation law by saturating the error coefficient to a certain threshold before applying it to the normalised error vector. This saturated EDF can be represented by (10.5) below, where $x_{e,thres} \in \mathbb{R}$ is a positive error threshold, $x_{e0} \in \mathbb{R}^m$ is the position error normal to the direction of motion and $x_{e1} \in \mathbb{R}^m$ is the position error along the direction of motion. The separation of error into these two components is intended to allow independent treatment of the errors between the direction where motion is possible (unconstrained) and other directions where no motion is observed (possibly constrained).

$$\varepsilon = \Lambda\left[\min(\|x_{e0}\|, x_{e,thres})\frac{x_{e0}}{\|x_{e0}\|} + \min(\|x_{e1}\|, x_{e,thres})\frac{x_{e1}}{\|x_{e1}\|}\right] + \dot{x}_e \tag{10.5}$$

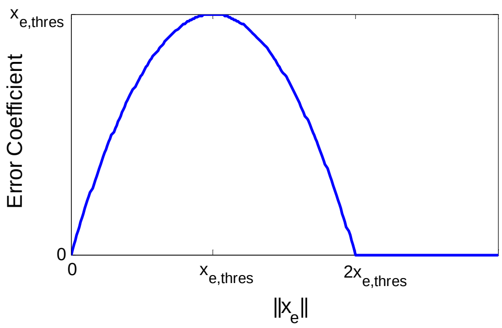

Figure 10.1: The proposed parabolic error dependency function.

The second alternative EDF investigated in this work makes use of the piecewise function shown in Figure 10.1 to scale the coefficient of the normalised error vector. The expression for this parabolic EDF is given in (10.6). In contrast to the saturated EDF described above which holds the error coefficient constant at large error magnitudes, this approach reduces the error coefficient as it grows beyond the error threshold. As a result, smaller feed forward forces should be observed in directions with large position errors.

$$\varepsilon = \Lambda\left[\max\left(\frac{\|x_{e0}\|}{x_{e,thres}}\left(2x_{e,thres} - \|x_{e0}\|\right), 0\right)\frac{x_{e0}}{\|x_{e0}\|} + \max\left(\frac{\|x_{e1}\|}{x_{e,thres}}\left(2x_{e,thres} - \|x_{e1}\|\right), 0\right)\frac{x_{e1}}{\|x_{e1}\|}\right] + \dot{x}_e \tag{10.6}$$

A comparison of (10.4), (10.5) and (10.6) shows that all these EDFs can be described using the same structure as shown in (10.7), where i = 0, 1, and 2 are used to enumerate the different EDFs discussed above. The terms used to describe the different EDFs considered in this work according to the structure given in (10.7) are summarised in Table 10.1, where the direction of motion is represented by a unit vector v.

$$\varepsilon = \begin{bmatrix}\Lambda A_i & \varsigma_i I\end{bmatrix}\begin{bmatrix}x_\varepsilon \\ \dot{x}_\varepsilon\end{bmatrix} \tag{10.7}$$

Table 10.1: Relationship between the feed forward adaptation rule parameters and the types of error dependency functions.

EDF	i	A_i	ς_i
Linear	0	I	1
Saturated	1	$A_1 = \min\left(1, \frac{x_{e,thres}}{\|x_{e0}\|}\right)(I - vv^T) + \min\left(1, \frac{x_{e,thres}}{\|x_{e1}\|}\right)vv^T$	1
Parabolic	2	$A_2 = \max\left(0,2 - \frac{\|x_{e0}\|}{x_{e,thres}}\right)(I - vv^T) + \max\left(0,2 - \frac{\|x_{e1}\|}{x_{e,thres}}\right)vv^T$	1

10.1.3 Work based Stiffness Adaptation

The environment in which the robot operates is not necessarily passive as the user can actively apply forces to generate movement. The power or incremental work done by the robot can therefore take on both positive and negative values, where positive work indicates that the robot is providing assistance to the desired motion. In contrast, negative work indicates that the robot is impeding motion of the user. The incremental work done by the robot can therefore be used to identify when the motion of the patient is being resisted and appropriate changes to the control parameters can be made to reduce this resistance during assistive exercises. In this work, it is proposed that this be achieved through modification of the desired robot stiffness matrix as in (10.8) – (10.10), where $\gamma \in \mathbb{R}$ is a state variable used to control the reduction of stiffness along the desired direction of motion given by the unit vector $\hat{v}_d \in \mathbb{R}^m$, $0 < \gamma_{max} < 1$ is the maximum permitted value for γ, $w \in \mathbb{R}$ the amount of incremental work done by the robot and c is a positive coefficient which governs how quickly γ changes. Additionally, $f(w)$ is a monotonic function which saturates at 0 and 1 and provides the driving force for the change in γ, with $b \in \mathbb{R}$ being a positive scaling factor for the incremental work.

$$K_P' = \left[I - \gamma \hat{v}_d \hat{v}_d^{\,T}\right] K_P \tag{10.8}$$

$$\dot{\gamma} = c\left[-\frac{\gamma}{\gamma_{max}} + f(w)\right] \tag{10.9}$$

$$f(w) = \max(0, \min(1, -bw)) \tag{10.10}$$

10.1.4 Stability Analysis of Adaptive Control Scheme for Active Assistance

Stability analysis is important in evaluating the feasibility of the proposed modifications to the assistance adaptation scheme. This is because a stable system is essential to ensure the safe operation of the robot. The stability analysis can therefore be used to identify suitable control or adaptation parameters for use as a starting point for further tuning of the control system. In this research, the stability analysis approach taken in [50] was extended to accommodate the proposed modifications made in the assistance adaptation rule. This section will begin with the stability analysis of the overall system when different error dependency functions as described in Table 10.1 are used in the feed forward force adaptation law. This analysis is then extended in the latter part of this section by including the incremental work based robot stiffness adjustment rule.

The robot dynamics considered in the stability analysis is represented as (10.11), where $M \in \mathbb{R}^{m \times m}$ is a symmetric positive definite inertia matrix of the robot, $C_{dyn} \in \mathbb{R}^{m \times m}$ is the Coriolis terms in the robot dynamics, $N \in \mathbb{R}^m$ represents other nonlinear terms in the robot dynamics, $F_h \in \mathbb{R}^m$ is the forces applied to the robot by the user and $F_r \in \mathbb{R}^m$ is the forces generated by the robot actuators.

$$M\ddot{x} + C_{dyn}\dot{x} + N = F_r + F_h \tag{10.11}$$

To facilitate the stability analysis, the feed forward term is considered to be learning or adapting to the expression shown in (10.12), with a being the ideal or optimal parameters and q is given by $q = \dot{x}_d + \Lambda x_e$. Note that x_d denotes the reference position. By rearranging (10.11) and substituting the result into (10.12), the overall system dynamics was rewritten as (10.13), with $s = \dot{x}_e + \Lambda x_e$.

$$Ya = M\dot{q} + C_{dyn}q + N - F_h \tag{10.12}$$

$$Ya - F_r = M(\dot{q} - \ddot{x}) + C_{dyn}(q - \dot{x}) = M\dot{s} + Cs \tag{10.13}$$

The Lyapunov candidate function as shown in (10.14) was considered to further the stability analysis. The time derivative of (10.14) can then be computed as (10.15).

$$V = \tfrac{1}{2}\left[s^T M s + (a - \hat{a})^T \Gamma (a - \hat{a}) + x_e^{\,T}(K_P + \Lambda K_D)x_e\right] \tag{10.14}$$

$$\begin{aligned}\dot{V} &= \tfrac{1}{2}s^T\dot{M}s + s^T M\dot{s} - (a-\hat{a})\Gamma\dot{\hat{a}} + x_e{}^T(K_P + \Lambda K_D)\dot{x}_e \\ &= \tfrac{1}{2}s^T\dot{M}s + s^T MM^{-1}\left(Ya - F_r - C_{dyn}s\right) - (a-\hat{a})\Gamma\dot{\hat{a}} + x_e{}^T(K_P + \Lambda K_D)\dot{x}_e \\ &= \tfrac{1}{2}s^T\left(\dot{M} - 2C_{dyn}\right)s + s^T Ya - s^T F_r - (a-\hat{a})\Gamma\dot{\hat{a}} + x_e{}^T(K_P + \Lambda K_D)\dot{x}_e \qquad (10.15)\end{aligned}$$

Due to the skew symmetric property of the term $\dot{M} - 2C_{dyn}$ in robot dynamic equations, the first term in (10.15) is equivalent to zero. By further substituting the control law shown in (10.1) in (10.15), (10.16) was obtained, with $e = [x_e{}^T \quad \dot{x}_e{}^T] \in \mathbb{R}^{2m}$ and $Q = \begin{bmatrix}\Lambda K_P & 0 \\ 0 & K_D\end{bmatrix} \in \mathbb{R}^{2m\times 2m}$.

$$\begin{aligned}\dot{V} &= s^T Ya - s^T Y\hat{a} - s^T(K_P x_e + K_D\dot{x}_e) - (a-\hat{a})\Gamma\dot{\hat{a}} + x_e{}^T(K_P + \Lambda K_D)\dot{x}_e \\ &= (a-\hat{a})^T\left(Y^T s - \Gamma\dot{\hat{a}}\right) - (\Lambda x_e + \dot{x}_e)^T(K_P x_e + K_D\dot{x}_e) + x_e{}^T(K_P + \Lambda K_D)\dot{x}_e \\ &= (a-\hat{a})^T\left(Y^T s - \Gamma\dot{\hat{a}}\right) - x_e{}^T\Lambda K_P x_e - \dot{x}_e{}^T K_D\dot{x}_e \\ &= (a-\hat{a})^T\left(Y^T s - \Gamma\dot{\hat{a}}\right) - e^T Qe \qquad (10.16)\end{aligned}$$

By considering the adaptation law (10.2), the rate of change of the Lyapunov candidate function was further expanded as (10.17). This expression was then used to analyse the conditions for a decreasing Lyapunov candidate function. Matrices $B \in \mathbb{R}^{n\times 2m}$ and $C \in \mathbb{R}^{n\times n}$ had been used to simplify the notations used, where $B = Y^T[\Lambda(I - A_i)\ (1 - \varsigma_i)I]$ and $C = \frac{1}{\tau}\Gamma Y^T(YY^T)^{-1}Y$.

$$\begin{aligned}\dot{V} &= (a-\hat{a})^T\left(Y^T s + \tfrac{1}{\tau}\Gamma Y^T(YY^T)^{-1}Y\hat{a} - Y^T\varepsilon\right) - e^T Qe \\ &= (a-\hat{a})^T Y^T(s-\varepsilon) + \tfrac{1}{\tau}(a-\hat{a})^T\Gamma Y^T(YY^T)^{-1}Y\hat{a} - e^T Qe \\ &= (a-\hat{a})^T(Be + C\hat{a}) - e^T Qe \qquad (10.17)\end{aligned}$$

To ensure a decreasing Lyapunov candidate function, (10.18) must hold. Additionally, to obtain a more conservative estimate on this condition the term on the right hand side of the inequality (10.18) must be maximised with respect to $\hat{a}$. The partial derivative of the right hand term in (10.18) with respect to $\hat{a}$ is given by (10.19). The optimal parameter vector, $\hat{a}_{opt}$ is given in (10.20), with $^+$ being the pseudo-inverse operator. The maximum right hand term was therefore expressed as (10.21).

$$\dot{V} < 0 \Rightarrow e^T Qe > (a-\hat{a})^T(Be + C\hat{a}) \qquad (10.18)$$

$$\frac{\partial}{\partial\hat{a}}[(a-\hat{a})^T(Be + C\hat{a})] = -Be - 2C\hat{a} + Ca \qquad (10.19)$$

$$\hat{a}_{opt} = \tfrac{1}{2}a - \tfrac{1}{2}C^+ Be \qquad (10.20)$$

$$\max_{\hat{a}}[(a-\hat{a})^T(Be+C\hat{a})] = \frac{1}{4}(a+C^+Be)^T(Be+Ca)$$
$$= \frac{1}{4}(a^TCa + e^TB^TC^+Be + 2a^TBe) \qquad (10.21)$$

The condition that must be satisfied for decreasing V is therefore given by (10.22).

$$e^T\left(Q - \frac{1}{4}B^TC^+B\right)e > \frac{1}{4}a^TCa + \frac{1}{2}a^TBe \qquad (10.22)$$

It can be shown (see Appendix B) that (10.23) holds, with $Y = U_Y\Sigma_Y{V_Y}^T$ being the result obtained from the singular value decomposition of Y and $\Sigma_{Y1} \in \mathbb{R}^{m\times m}$ is a square matrix which is related to the singular value matrix Σ_Y via $\Sigma_Y = [\Sigma_{Y1}\ \mathbf{0}]$.

$$B^TC^+B = \tau k\begin{bmatrix} \Lambda(I-A_i)U_Y{\Sigma_{Y1}}^2{U_Y}^T(I-A_i)\Lambda & (1-\varsigma_i)\Lambda(I-A_i)U_Y{\Sigma_{Y1}}^2{U_Y}^T \\ (1-\varsigma_i)U_Y{\Sigma_{Y1}}^2{U_Y}^T(I-A_i)\Lambda & (1-\varsigma_i)^2U_Y{\Sigma_{Y1}}^2{U_Y}^T \end{bmatrix} \qquad (10.23)$$

It should be noted that the maximum singular value of $I - A_i$ is bounded by unity and this can be seen from the definition of A_i used in Table 10.1. A similar bound also exists for the regression matrix Y, where it was written in the form as shown in (10.24), with y being a column vector of the activation levels of the radial basis functions, normalised so that the sum of all elements in y will always be unity. It can therefore be seen that all singular values of Y are identical and must be less than unity, and that $U_Y{\Sigma_{Y1}}^2{U_Y}^T = {\sigma_y}^2I$.

$$Y = \begin{bmatrix} y^T & 0 & 0 \\ 0 & y^T & 0 \\ 0 & 0 & \ddots \end{bmatrix} \qquad (10.24)$$

This bound was taken into account when determining the positive definiteness of the matrix coefficient on the left hand side of (10.22). This matrix coefficient, denoted as P, is given in (10.25). It can be seen that when ς_i is chosen as unity and K_D is positive definite, the positive definiteness of P can be guaranteed if (10.26) holds.

$$P = Q - \frac{1}{4}B^TC^+B$$
$$= \begin{bmatrix} \Lambda K_P & 0 \\ 0 & K_D \end{bmatrix} - \frac{\tau k}{4}{\sigma_y}^2\begin{bmatrix} \Lambda(I-A_i)^2\Lambda & (1-\varsigma_i)\Lambda(I-A_i) \\ (1-\varsigma_i)(I-A_i)\Lambda & (1-\varsigma_i)^2I \end{bmatrix} \qquad (10.25)$$

$$\lambda_{min}\left(\Lambda\left[K_P - \frac{\tau k}{4}{\sigma_y}^2(I-A_i)^2\Lambda\right]\right) > 0 \qquad (10.26)$$

The condition (10.22) was further reduced to that given in (10.27). If the adaptation parameters are chosen in such a manner that matrix P is positive definite, then there will be an error norm above which the Lyapunov candidate function will be decreasing (note that C is positive semi-definite). For the case where $i = 0$ (linear error dependency), matrix B will reduce to a zero matrix and the error norms which will lead to decrease in V is given by (10.28) [50].

$$\lambda_{min}(P)\|e\|^2 - \tfrac{1}{2}\sigma_{max}(B)\|a\|\|e\| - \tfrac{1}{4}\lambda_{max}(C)\|a\|^2 > 0 \tag{10.27}$$

$$\|e\| > \frac{1}{2}\|a\|\sqrt{\frac{\frac{1}{\tau}\lambda_{max}(\Gamma)}{\lambda_{min}(Q)}} \tag{10.28}$$

Inclusion of Incremental Work Based Robot Stiffness Adjustment

The effect of the proposed incremental work based stiffness adjustment rule on system stability was studied by analysing the same Lyapunov candidate function used in (10.14). The only modification required was the replacement of K_P with K_P' . This had introduced an additional term in the time derivative of the candidate function as in (10.29), with the time derivative of the matrix K_P' given in (10.30). The Q matrix in this case is given by (10.31), and this expression will determine whether a decreasing Lyapunov candidate function can be obtained.

$$\dot{V} = (a-\hat{a})^T\left(Y^T s - \Gamma\dot{\hat{a}}\right) - {x_e}^T \Lambda K_P' x_e - {\dot{x}_e}^T K_D \dot{x}_e + \tfrac{1}{2}{x_e}^T \dot{K}_P' x_e \tag{10.29}$$

$$\begin{aligned}\dot{K}_P' &= \left\{-\dot{\gamma}\hat{v}_d{\hat{v}_d}^T - \tfrac{\gamma}{\sqrt{{v_d}^T v_d}}\left[\left(I-\hat{v}_d{\hat{v}_d}^T\right)\dot{v}_d{\hat{v}_d}^T + \hat{v}_d{\dot{v}_d}^T\left(I-\hat{v}_d{\hat{v}_d}^T\right)\right]\right\}K_P \\ &= \left\{-c\left[f(w) - \tfrac{\gamma}{\gamma_{max}}\right]\hat{v}_d{\hat{v}_d}^T \right.\\ &\qquad \left. - \tfrac{\gamma}{\sqrt{{v_d}^T v_d}}\left[\left(I-\hat{v}_d{\hat{v}_d}^T\right)\dot{v}_d{\hat{v}_d}^T + \hat{v}_d{\dot{v}_d}^T\left(I-\hat{v}_d{\hat{v}_d}^T\right)\right]\right\}K_P\end{aligned} \tag{10.30}$$

$$Q = \begin{bmatrix}\Lambda K_P' - \frac{1}{2}\dot{K}_P' & 0 \\ 0 & K_D\end{bmatrix} \tag{10.31}$$

The matrix from the top left corner of the Q matrix was written as (10.32), and was further analysed to establish the condition required for a decreasing V. It can be shown that the inequality given in (10.33) holds (see Appendix B). Based on the bounds obtained from this inequality, the lower bound of the quadratic expression obtained using the first two terms on the right hand side of (10.32) are given in (10.34). A similar lower bound obtained by considering the last term on the right side of (10.32) is also shown in (10.35).

$$\begin{aligned}\Lambda K_P' - \tfrac{1}{2}\dot{K}_P' &= \left\{\Lambda I - \left[\Lambda\gamma + \tfrac{c}{2}\left(\tfrac{\gamma}{\gamma_{max}} - f(w)\right)I\right]\hat{v}_d{\hat{v}_d}^T \right.\\ &\qquad \left. + \tfrac{\gamma}{\sqrt{{v_d}^T v_d}}\left[\left(I-\hat{v}_d{\hat{v}_d}^T\right)\dot{v}_d{\hat{v}_d}^T + \hat{v}_d{\dot{v}_d}^T\left(I-\hat{v}_d{\hat{v}_d}^T\right)\right]\right\}K_P\end{aligned} \tag{10.32}$$

$$-1 \le \tfrac{\gamma}{\gamma_{max}} - f(w) \le 1 \tag{10.33}$$

$$\min\left(x_e{}^T\left\{\Lambda I-\left[\Lambda\gamma+\frac{c}{2}\left(\frac{\gamma}{\gamma_{max}}-f(w)\right)I\right]\hat{v}_d\hat{v}_d{}^T\right\}K_Px_e\right)$$
$$>x_e{}^T\left\{\Lambda I-\left[\Lambda\gamma_{max}+\frac{c}{2}I\right]\hat{v}_d\hat{v}_d{}^T\right\}K_Px_e \tag{10.34}$$

$$\min\left(\frac{\gamma}{\sqrt{v_d{}^Tv_d}}x_e{}^T\left[\left(I-\hat{v}_d\hat{v}_d{}^T\right)\dot{v}_d\hat{v}_d{}^T+\hat{v}_d\dot{v}_d{}^T\left(I-\hat{v}_d\hat{v}_d{}^T\right)\right]K_Px_e\right)$$
$$>\frac{-2\gamma_{max}}{\sqrt{v_d{}^Tv_d}}\lambda_{max}(K_P)\left\|\left(I-\hat{v}_d\hat{v}_d{}^T\right)\dot{v}_d\right\|\|x_e\|^2 \tag{10.35}$$

Even with a different Q matrix, bounded error can still be attained in the system as long as the P matrix given in (10.25) is positive definite. If ς_i is again chosen as unity, this condition was reduced to (10.36).

$$x_e{}^T\Lambda\left[K_P'-\frac{1}{2}\Lambda^{-1}\dot{K}_P'-\frac{\tau k}{4}\sigma_y{}^2(I-A_i)^2\Lambda\right]x_e>0 \tag{10.36}$$

Substitution of $\Lambda=dI$ in (10.36) then resulted in (10.37).

$$x_e{}^T\left(dK_P'-\frac{1}{2}\dot{K}_P'\right)x_e-\frac{\tau kd^2}{4}\sigma_y{}^2x_e{}^T(I-A_i)^2x_e>0 \tag{10.37}$$

By taking into account both (10.34) and (10.35), the inequality (10.38) was obtained as a more conservative version of (10.37). Additionally, by using the fact that $\sigma_y\le 1$, $\sigma_{max}(I-A_i)\le 1$ and assuming that there exist an upper bound for the norm of the projection of the desired acceleration on the velocity, (10.38) was further simplified to (10.39), with $\|a\|_{max}$ denoting the maximum L2 norm of vector a.

$$x_e{}^T\left\{dI-\left[d\gamma_{max}+\frac{c}{2}I\right]\hat{v}_d\hat{v}_d{}^T\right\}K_Px_e-\frac{2\gamma_{max}}{\sqrt{v_d{}^Tv_d}}\lambda_{max}(K_P)\left\|\left(I-\hat{v}_d\hat{v}_d{}^T\right)\dot{v}_d\right\|\|x_e\|^2$$
$$-\frac{\tau kd^2}{4}\sigma_y{}^2x_e{}^T(I-A_i)^2x_e>0 \tag{10.38}$$

$$\left\{\left[d(1-\gamma_{max})-\frac{c}{2}\right]-2\gamma_{max}\frac{\lambda_{max}(K_P)}{\lambda_{min}(K_P)}\left\|\frac{\left(I-\hat{v}_d\hat{v}_d{}^T\right)\dot{v}_d}{\sqrt{v_d{}^Tv_d}}\right\|_{max}-\frac{\tau kd^2}{4\lambda_{min}(K_P)}\right\}\|x_e\|^2>0$$
$$\Rightarrow\frac{\tau k}{4\lambda_{min}(K_P)}d^2-(1-\gamma_{max})d+\left[\frac{c}{2}+2\gamma_{max}\frac{\lambda_{max}(K_P)}{\lambda_{min}(K_P)}\left\|\frac{\left(I-\hat{v}_d\hat{v}_d{}^T\right)\dot{v}_d}{\sqrt{v_d{}^Tv_d}}\right\|_{max}\right]<0 \tag{10.39}$$

Since variables used in (10.39) are all positive, it can be seen that as long as real roots exist for the quadratic equation on the left hand side, then it is possible to obtain a decreasing Lyapunov candidate function by choosing an appropriate value of d. The roots of the quadratic equation on the right hand side of (10.39) are given in (10.40), with $\xi=1-\gamma_{max}$. It can be seen that for real solutions to exist, the discriminant must be greater than zero. This can be achieved for sufficiently small values of τ, c, γ_{max} and k. When real solutions exist, the range of d that can satisfy the condition for decreasing V is given by (10.41). It should be noted that in practice, the value of d is not critical since it does not directly appear in the control and adaptation laws. It can therefore take on any positive values which can ensure a stable system. The parameters τ, c, γ_{max} and k however have larger impacts on the performance of the controller. Consequently, the design of a stable controller will mainly involve finding a set of these parameters which can produce a positive discriminant in the quadratic equation in (10.39). It should be noted that the analysis presented in this section is based on the "worst case scenario". The resulting stability criterion is therefore conservative in the sense that it is a sufficient but not necessary condition, meaning that adaptation laws which violate these conditions may still be stable in the actual system. Nonetheless, the parameters deemed to be stable from this criterion can still be used as a good starting point for further tuning of the adaptation law.

$$d_{1,2} = \frac{2\lambda_{min}(K_P)}{\tau k}\left\{\xi \pm \sqrt{\xi^2 - \frac{\tau k}{\lambda_{min}(K_P)}\left[\frac{c}{2} + 2\gamma_{max}\frac{\lambda_{max}(K_P)}{\lambda_{min}(K_P)}\left\|\frac{\left(I-\hat{v}_d\hat{v}_d{}^T\right)\dot{v}_d}{\sqrt{v_d{}^T v_d}}\right\|_{max}\right]}\right\} \tag{10.40}$$

$$d_1 < d < d_2 \tag{10.41}$$

10.1.5 Reference Trajectory Modification

An additional measure that can be used to limit the forces being applied in stiff or constrained direction is to modify the reference trajectory so that the desired position is moved in the opposite direction of the position error. When used in conjunction with impedance control, this can help reduce the forces applied to the environment. However, if such an adjustment is made regardless of the magnitude of the error, the amount of forces being applied may be limited to a value which is too low to allow any useful motion. In order to address this issue, a minimum error threshold (below which no trajectory adaptation will occur) can be used in the trajectory modification rule. This will permit the desired trajectory to be followed more closely when the stiffness or resistive force in the environment is small. At the same time, it will also allow modification of the reference trajectory when the position error magnitude is sufficiently large to indicate that the desired position is located in a stiff or kinematically constrained region of the workspace. The proposed trajectory modification rule can be expressed as (10.42), where x_d' is the modified trajectory, x_d is the original reference trajectory and Δx_d is a correction term defined using (10.43), where the regression matrix Y is the same as that used in the feed forward force adaptation law and $\hat{\rho} \in \mathbb{R}^n$ is the parameter vector. Using the terms defined above, the adaptation law for the trajectory correction term can be expressed as (10.44), where x_e is the position error vector and $x_{e,th}$ is the minimum error threshold as discussed previously. It should be noted that the pseudo-inverse is again used to obtain the minimal norm solution for the parameter time derivative in (10.44).

$$x'_d = x_d - \Delta x_d \tag{10.42}$$

$$\Delta x_d = Y\hat{\rho} \tag{10.43}$$

$$Y\hat{\rho} = -\alpha Y\hat{\rho} + \beta(YY^T)\max\left(0{,}1 - \frac{x_{e,th}}{\|x_e\|}\right)x_e$$
$$\dot{\hat{\rho}} = -\alpha Y^T(YY^T)^{-1}\Delta x_d + \beta Y^T \max\left(0{,}1 - \frac{x_{e,th}}{\|x_e\|}\right)x_e \tag{10.44}$$

10.2 Simulated Case Study for Assistance Adaptation

The adaptation laws discussed above have been tested in simulation using a two dimensional virtual environment. The stiffness characteristic of the virtual environment is defined through the superposition of several potential functions. These potential functions were selected in such a manner that there exist a region around the origin of the workspace where there is constant potential energy and therefore zero stiffness. Additionally, the environment was designed to be anisotropic with different stiffness along different directions while a constant viscous damping was also applied. The directions along which the potential functions are defined were also rotated about the controller and world reference frame. More specifically, the potential function of the environment is given by (10.45). It should be noted that u and v are the generalised coordinates of the environment. Furthermore, u_{01} and u_{02} are respectively the lower and upper bounds within which the potential function is constant along the u direction (a similar notation applies for the v direction). Finally, the angle Φ is used to denote the rotation which transformed the global reference frame into the principal reference frame used to define the environment. Resistive forces within the environment were obtained through partial differentiation of the potential function p_{tot} along the directions of interest.

$$p_{tot} = \sum_i p_i \tag{10.45}$$

Where:

$$p_1 = \frac{1}{2}k_1[\min(0, u - u_{01})]^2$$

$$p_2 = \frac{1}{2}k_2[\max(0, u - u_{02})]^2$$

$$p_3 = \frac{1}{2}k_3[\min(0, v - v_{01})]^2$$

$$p_4 = \frac{1}{2}k_4[\max(0, v - v_{02})]^2$$

$$\begin{bmatrix} u \\ v \end{bmatrix} = \begin{bmatrix} \cos\Phi & \sin\Phi \\ -\sin\Phi & \cos\Phi \end{bmatrix} \begin{bmatrix} x \\ y \end{bmatrix}$$

As some of the modifications proposed to the adaptation law are aimed at reducing the robot forces when kinematic constraints are encountered, such a constraint was also imposed on the environment during some of the simulation trials. In these trials, the kinematic constraints were given in the form of an ellipse which is centred and rotated about the global reference frame. The constraint to be satisfied is therefore given by (10.46), with l_a and l_b respectively being the minor and major radii, φ being the angle of the semi-minor axis with respect to the x-axis, while C_φ and S_φ are short for the cosine and sine of φ in that order.

$$\left[\left(\frac{C_\varphi}{l_a}\right)^2+\left(\frac{S_\varphi}{l_b}\right)^2\right]x^2 + 2\left(\frac{1}{{l_a}^2}-\frac{1}{{l_b}^2}\right)C_\varphi S_\varphi xy + \left[\left(\frac{S_\varphi}{l_a}\right)^2+\left(\frac{C_\varphi}{l_b}\right)^2\right]y^2 \le 1 \tag{10.46}$$

To facilitate the simulation of the constrained system, a large stiffness was introduced when the point under consideration ventures outside the constraint boundary. This approach was preferred over the application of a hard constraint because it can eliminate the need to reset the velocity and position states and thus simplifies the definition of a state space model for the system. In order to compute the resistive forces applied to the point under consideration when the system violates (10.46), the point on the ellipse that is closest to the current position must first be found. The characteristic of this closest point is that the line joining the current point to it will be collinear with the normal of the ellipse at this closest point. The resistive force was then calculated using the distance between the current and closest point and the large stiffness used to penalise motion beyond the constraint boundary. Viscous damping was also introduced for motion along the normal direction of the constraint surface.

An extensive set of simulation trials had been carried out to determine the behaviour of the control strategies discussed above under a variety of operating conditions. The environment being considered in these simulation trials is shown in Figure 10.2. The potential function is plotted as a contour plot while the resistive force vectors associated the potential function is given in the form of a quiver plot. The state space model used in these simulations involved a point mass moving within this environment, assisted by a propulsion force vector applied to it by the control law. The reference trajectory for the simulation trials is also given as the dashed green line in Figure 10.2. It should be noted however that the initial position is located at the origin and an initial straight line reference path in the y-direction is used to guide the reference point from the origin to the top of the circular reference path at the start of the simulation. The trajectory has a period of 6s and travels in the clockwise direction on the x-y plane. The simulations were run for 15 cycles of the reference trajectory.

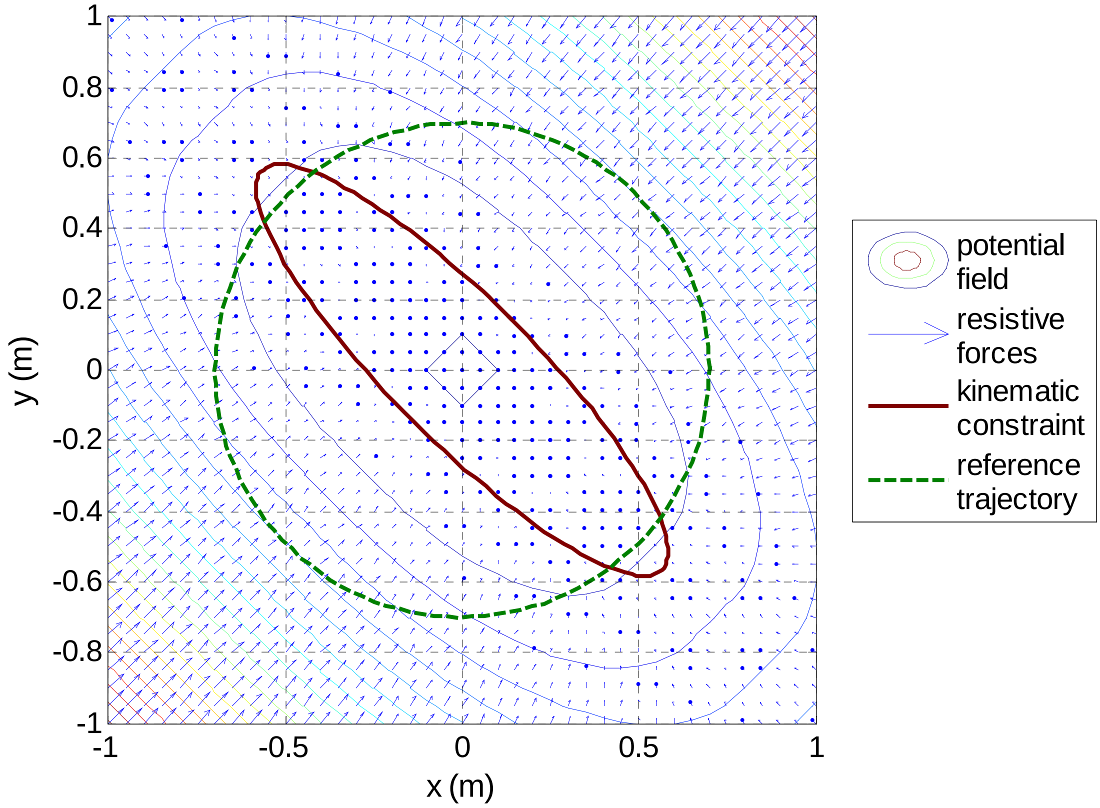

Figure 10.2: Graphical representation of the environment used in the simulation case study.

Four operating conditions were considered in this work. They are: a) passive and unconstrained; b) passive and constrained; c) active and unconstrained; and d) active and constrained. Under the passive operating condition, only the controller was applying a propulsion force to the point mass. The active condition on the other hand included application of an additional force vector to emulate active participation. This force vector had been obtained by applying a constant magnitude force along the direction of travel of the reference path. An elliptic constraint surface as depicted above was also applied when constrained motion was being simulated. This constraint is shown as the brown ellipse in Figure 10.2. A total of 12 different control schemes were tested in simulation for each operating condition. These schemes were formed by choice of different error dependency functions (EDF) in the adaptive law ($i = 1, 2, 3$), toggling of work based modification of controller stiffness and toggling of the reference trajectory modification scheme.

10.2.1 Results and Discussion

For completeness, simulation parameters and results for all simulation trials are summarised in Appendix D. The focus of this section however is placed on results which highlight the effects of different modules in the proposed control scheme.

Effects of error dependency functions in feed forward force adaptation

Two alternative EDFs in the feed forward force adaptation law were proposed in Section 10.1.2, and the influence of these different error dependency functions on the system's interactive behaviour can be investigated through analysis of the force and motion variables acquired from simulations conducted in this case study.

Figure 10.3a shows the trajectories traced by the point mass during the last cycle in simulations involving the passive and unconstrained operating condition. It should be noted that both the work based stiffness adjustment and trajectory modification modules are not active in these simulations. Three end point trajectories are presented, one for each type of EDF used in the adaptation law. More specifically, the blue line indicates the position recorded when the original approach based on a linear EDF ($i = 0$) is used in the adaptation law, while the red and green lines represent those of the saturated ($i = 1$) and parabolic ($i = 2$) approaches respectively. The reference trajectories for all these control schemes were identical and are shown as the dotted lines. Figure 10.3b-d on the other hand shows the reference trajectory (green dotted line), the point mass trajectory (blue line) and the control force vectors applied to the point mass at the corresponding locations (red lines).

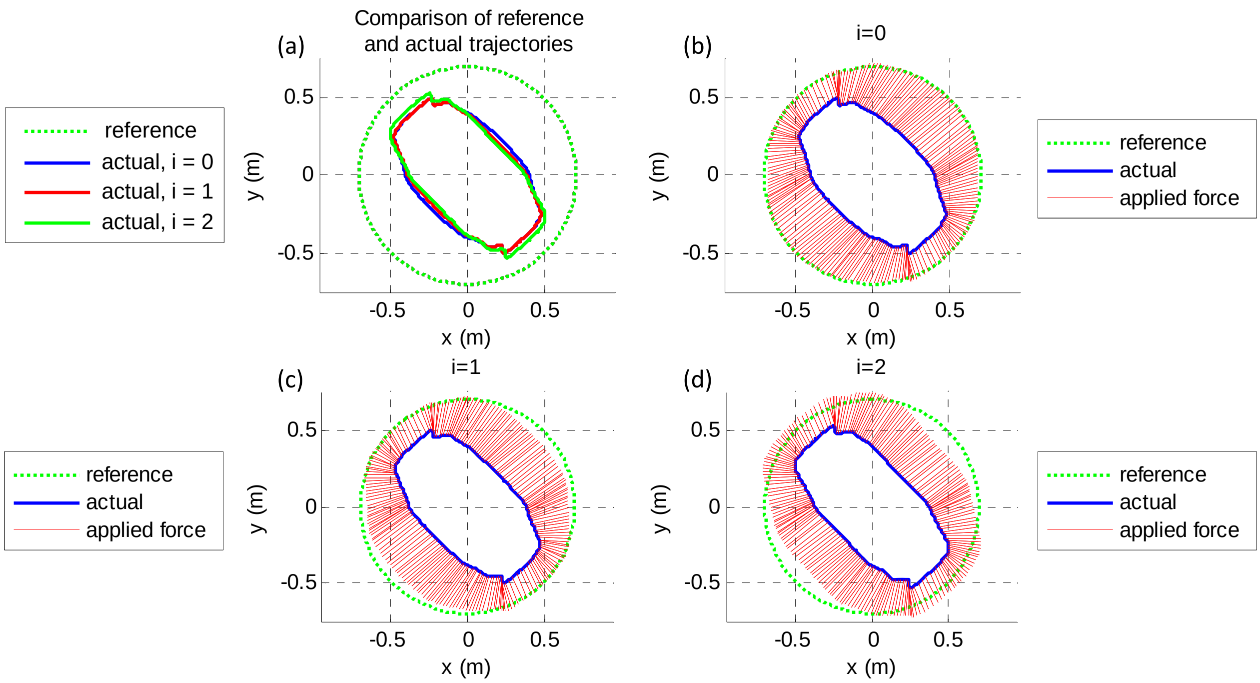

Figure 10.3: (a) Comparison of the reference and actual trajectories obtained from simulations on unconstrained motion using different error dependency functions. The force vectors applied at different points along the trajectories are shown for the linear, saturated and parabolic approaches in (b), (c) and (d) respectively.

It can be seen from Figure 10.3a that the extent of motion in the stiffer direction (refer to Figure 10.2) is greatest for the linear error dependency approach. This can be seen to be a consequence of larger forces being applied along this stiff direction (see Figure 10.3b). Figure 10.3c and Figure 10.3d on the other hand reveals that limiting the contribution of error to the feed forward force adaptation at large errors effectively reduces the forces being applied in the stiff direction, with a larger reduction in the parabolic EDF approach. As a result, the extent of motion for these two alternative approaches in the stiff direction is also smaller, although not by a large margin. Another interesting observation is that the parabolic EDF approach appears to provide the largest motion in the more compliant direction, while motion for the linear and saturated error dependency based methods are almost identical. This is also a result of the use of a parabolic EDF in the feed forward force adaptation law, where the feed forward force is allowed to grow at a faster rate when the errors are small.

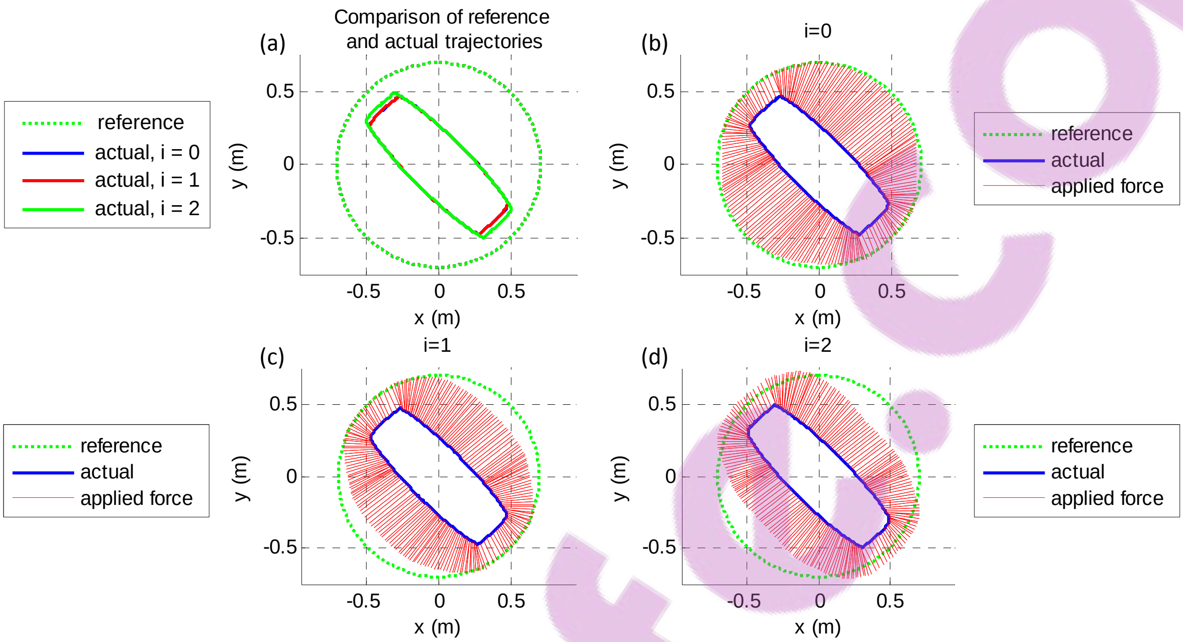

Figure 10.4: (a) Comparison of the reference and actual trajectories obtained from simulations on constrained motion using different error dependency functions. The force vectors applied at different points along the trajectories are shown for the linear, saturated and parabolic EDF approaches in (b), (c) and (d) respectively.

A similar set of plots are also shown in Figure 10.4 for simulations involving the passive and constrained operating condition. It can be seen from these plots that the trajectory made by both the linear and saturated EDF approaches are essentially identical, while the parabolic based adaptation approach produced larger motion in the more compliant direction. It can be seen from Figure 10.4b that rather large control forces were applied by the linear error dependency approach to the point mass, even as it was moving along the constrained surface. The magnitudes of the control forces for approaches based on the saturated (Figure 10.4c) and parabolic (Figure 10.4d) EDFs on the other hand are considerably smaller, with the parabolic EDF adaptation law having a more even distribution of force magnitudes along both the constrained and unconstrained direction. In scenarios where constraints are present in the environment, the forces applied on the constraint should be limited, even as position errors are large. The reason for this is to reduce the likelihood of environmental damage (or in the case of rehabilitation robots, user injury) due to excessive force application. From this perspective, an adaptation law that increases the assistance based solely on error magnitudes will not be adequate in realising this desired behaviour. As a result, these simulation results had put forward a strong case for the use of adaptation rules with saturated or parabolic EDFs.

Effects of incremental work based stiffness adjustment

Another controller module proposed in this research is the incremental work based adjustment of the robot stiffness. The aim of this adjustment rule is to provide the robot with a means in identifying whether it is applying a force to resist the current direction of motion, and subsequently allowing it to adjust its stiffness matrix so that actuator effort which acts to correct position errors along the direction of the reference velocity is minimised. This will therefore allow the point mass to move beyond its current reference position with smaller resistance. As discussed previously, the sign of the incremental work done by the robot can be used to identify whether resistance is being provided, with negative incremental work denoting that the robot forces are impeding motion. The goal is therefore to minimise the amount of negative work done by the robot. In order to study the effect of the work based stiffness adjustment control module, the simulation results obtained under the active and unconstrained as well as active and constrained operating conditions were considered. The feed forward force adaptation law with linear error dependency had been used to obtain these results, while the trajectory modification module was deactivated.

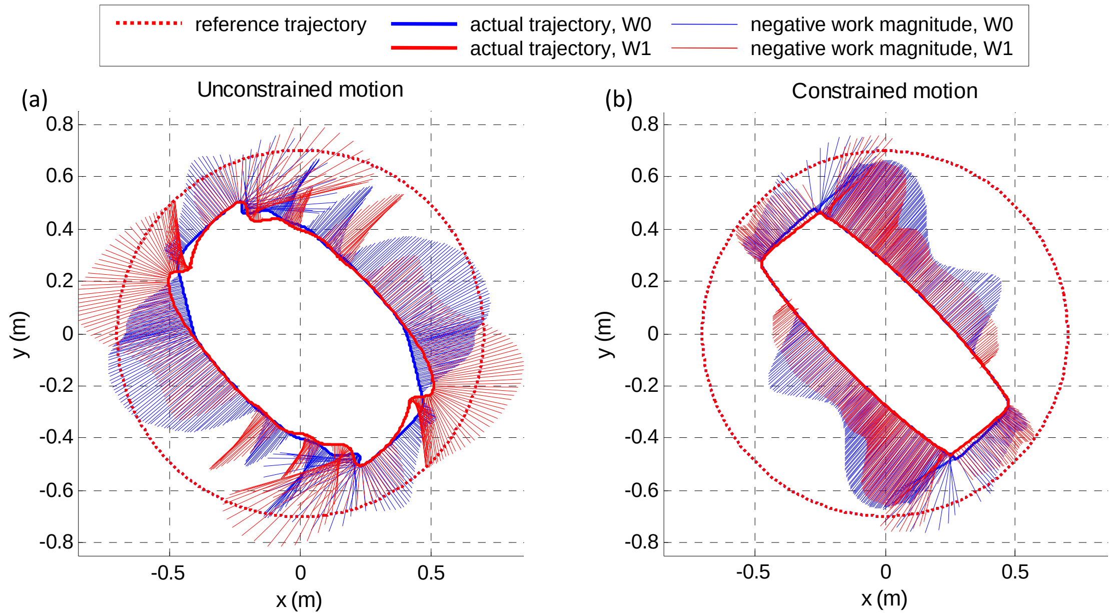

Figure 10.5: Comparison of the motion trajectories and the magnitudes of negative work done by the controller at different trajectory points for control schemes with (W1) and without (W0) work based adaptation for both unconstrained (a) and constrained (b) motions. Note that the lengths of the thin lines give an indication of the negative work magnitudes, with positive work having a length of zero.

Figure 10.5 shows plots containing information relating to both the end point trajectory and the negative work done by the robot at a particular location. Figure 10.5a is plotted for the results obtained without any kinematic constraints while Figure 10.5b is done for those obtained when constraints are present in the environment. The red and blue lines are respectively used to denote quantities relating to the control scheme with and without work based stiffness adjustment. In these plots, the negative work done by the robot at different locations are represented by lines along the normal of the end point trajectories, with the magnitude of this negative incremental work governing the lengths of these normal lines. It should also be noted that a length of zero is used where zero or positive work is recorded. Additionally, the motion of the end point was in the clockwise direction.

It can be seen from these plots that the stiffness adjustment module did not performed as well as expected as there are segments along the red trajectory where the negative incremental work done is much greater than that for the blue trajectory, particularly during unconstrained motion. This could be due to discrepancies in the directions of the actual and desired velocity. As a result of this, the stiffness adjustment module was not accurately removing the resistive efforts along the actual direction of motion. The plots show that the magnitude of negative work done at the turning points of the trajectory with the work based stiffness adjustment module active is considerably higher than that for the case without such stiffness adjustments. However, it is important to note that appreciable reduction in incremental work can be found at locations where the directions of the actual and desired motion are similar (i.e. when the end point is travelling diagonally downward from left to right and when it is travelling diagonally upward from right to left). This observation suggests that this control module can still be effective for such situations, which would most likely be encountered during reaching movements in a rehabilitation setting.

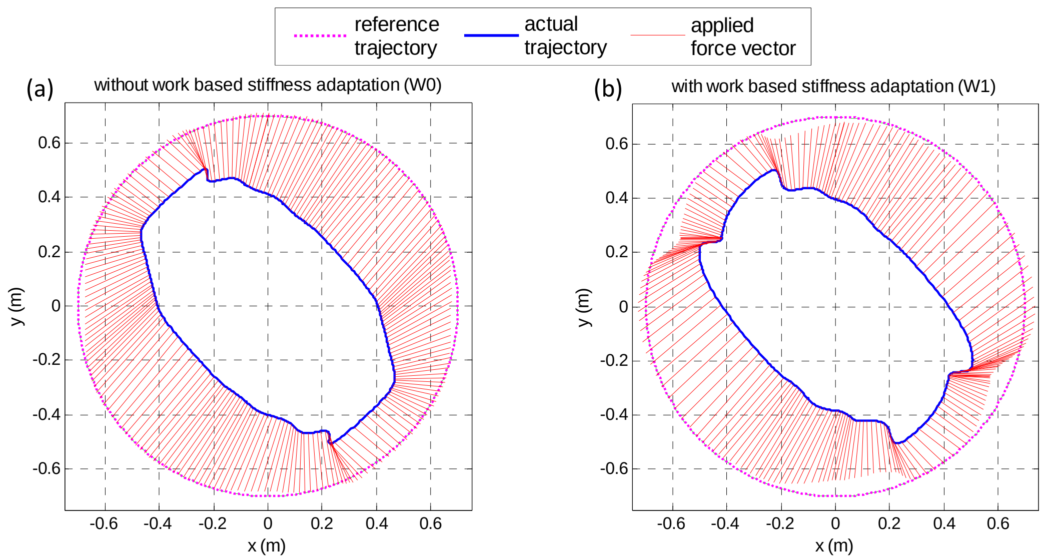

Figure 10.6: The forces applied along the actual trajectories during unconstrained motion for the controllers without (a) and with (b) work based stiffness adaptation. Note that force vectors are drawn at uniformly sampled time intervals.

The advantage offered by the stiffness adjustment approach can be seen by considering Figure 10.6, which shows the force vectors applied at various positions along the motion trajectory for the two control schemes considered under the unconstrained operating condition. One of the main points to be focused on in these plots is the spacing between these force vectors, which gives an indication of the velocity at which the end point is moving. It can be seen that this velocity towards the end of the "longer" sides of the actual motion trajectory is higher for the case when work based adjustment module is used (see Figure 10.6b). This means that controller's resistance towards the active effort applied by the object is reduced, thus allowing faster motion in the direction where the active force is applied. Some other points worth noting are the spacing and magnitude of the actuator force vectors at the corner segments of the motion trajectory (where significant negative work is observed) in Figure 10.6b. These magnitudes are not abnormally large, and the rather close spacing between the force vectors also indicates that the speed of movement in these regions is also relatively slow. As a result, the behaviour of the control scheme with work based stiffness adjustment can still be considered safe.

The effectiveness of the work based stiffness adjustment module is summarised for different operating conditions in the bar graph shown in Figure 10.7. It should be noted that the feed forward force adaptation law with linear error dependency is used to obtain the results shown. The heights of the bars indicate the average amounts of negative work done over the final movement cycle in simulations carried out for different operating conditions (P for passive, A for active, U for unconstrained and C for constrained). The effect of trajectory adjustment was also considered in these results. The shorthand TMx is used to denote the state of the trajectory modification module, with x = 0 indicating that the module is deactivated and x = 1 indicating that the module is active. A similar notation (Wx) is also used for the work based stiffness adjustment module.

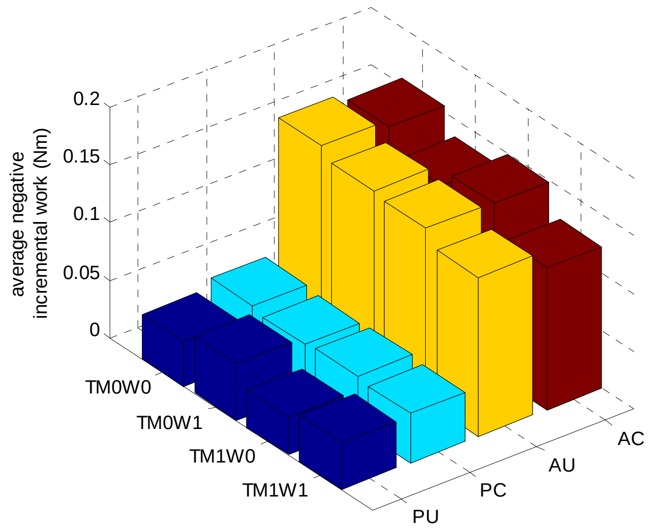

Figure 10.7: Summary of the average negative work done by different controllers with a linear error dependency function under various operating conditions.

It can be seen that the negative work done by the robot does indeed increase significantly from the passive to active scenarios. This suggests that the forces applied by the robot do provide resistance to the end point motion. It can be seen in fig x that apart from the passive unconstrained case, the use of a work based stiffness adjustment has resulted in a reduction in the average negative work under all other operating conditions. An interesting observation from considering the results obtained from simulations involving active forces is that the reduction in negative work is actually greater for control schemes with an active trajectory modification module. This trend holds for both constrained and unconstrained motion and is likely due to the fact that the modified trajectory bears greater similarity to the actual motion trajectory when compared with the nominal reference trajectory. This result suggests that in addition to being able to adapt the reference trajectory to reduce excessive actuator forces which arise due to stiff or constrained environments, the reference trajectory modification module can also contribute to greater effectiveness of the work based stiffness adaptation module by morphing the reference path to a shape which is more similar to the actual motion trajectory.

Effects of reference trajectory modification

The main aim of using the trajectory modification module is to allow adjustments on the nominal reference path in such a way that excessive position errors are reduced. Since the force applied to the environment is typically proportional to the position error, this module will prevent large forces from being applied to the environment. To study the efficacy of this trajectory modification module, simulation results carried out under both the passive unconstrained and passive constrained operating conditions were considered. Whilst the activation of the trajectory modification module was toggled for these trials, the error dependency in the feed forward force adaptation law was kept linear. The work based adjustment of controller stiffness was also deactivated. The main simulation results are summarised in Figure 10.8, with the first row of plots providing the reference (dotted lines) and actual (solid lines) trajectories obtained from the TM0W0 (blue lines) and TM1W0 (red lines) control schemes. The second and third rows then show plots of the force vectors produced by the TM0W0 and TM1W0 control schemes respectively. Additionally, all plots in the first column are obtained from simulations without any kinematic constraints in the environment while those in the second column are obtained from simulations with kinematic constraints. As with the notations used in Figure 10.8, TM1 indicates that the trajectory modification module is activated while TM0 denotes that it is deactivated. Also, W0 is used to represent that the work based stiffness adjustment module is deactivated.

From these results, it can be seen from the first row in Figure 10.8 that the proposed trajectory modification module does shrink the reference trajectories for both the constrained and unconstrained environments, with much greater reduction in the stiff or constrained directions. This had led to greater resemblance between the shape of the modified reference path and the actual motion trajectory. A consequence of this for the unconstrained case is lesser movement in the stiff directions. The constrained case on the other hand sees little difference between the actual trajectories obtained using either control schemes. In terms of the forces being applied, the levels of forces seen in the control scheme with trajectory modification were considerably smaller than those obtained using a control scheme with no trajectory adjustment. It should be kept in mind that the feed forward force adaptation law with linear error dependency was considered here. This shows that the trajectory modification scheme actually serves a similar function as the use of alternative EDFs in the feed forward force adaptation law. This, combined with the observation made in the previous section that trajectory modification also leads to improved effectiveness of the work based stiffness adjustment module, suggests that the this module can significantly improve the performance of interaction controllers during constrained and active motions.

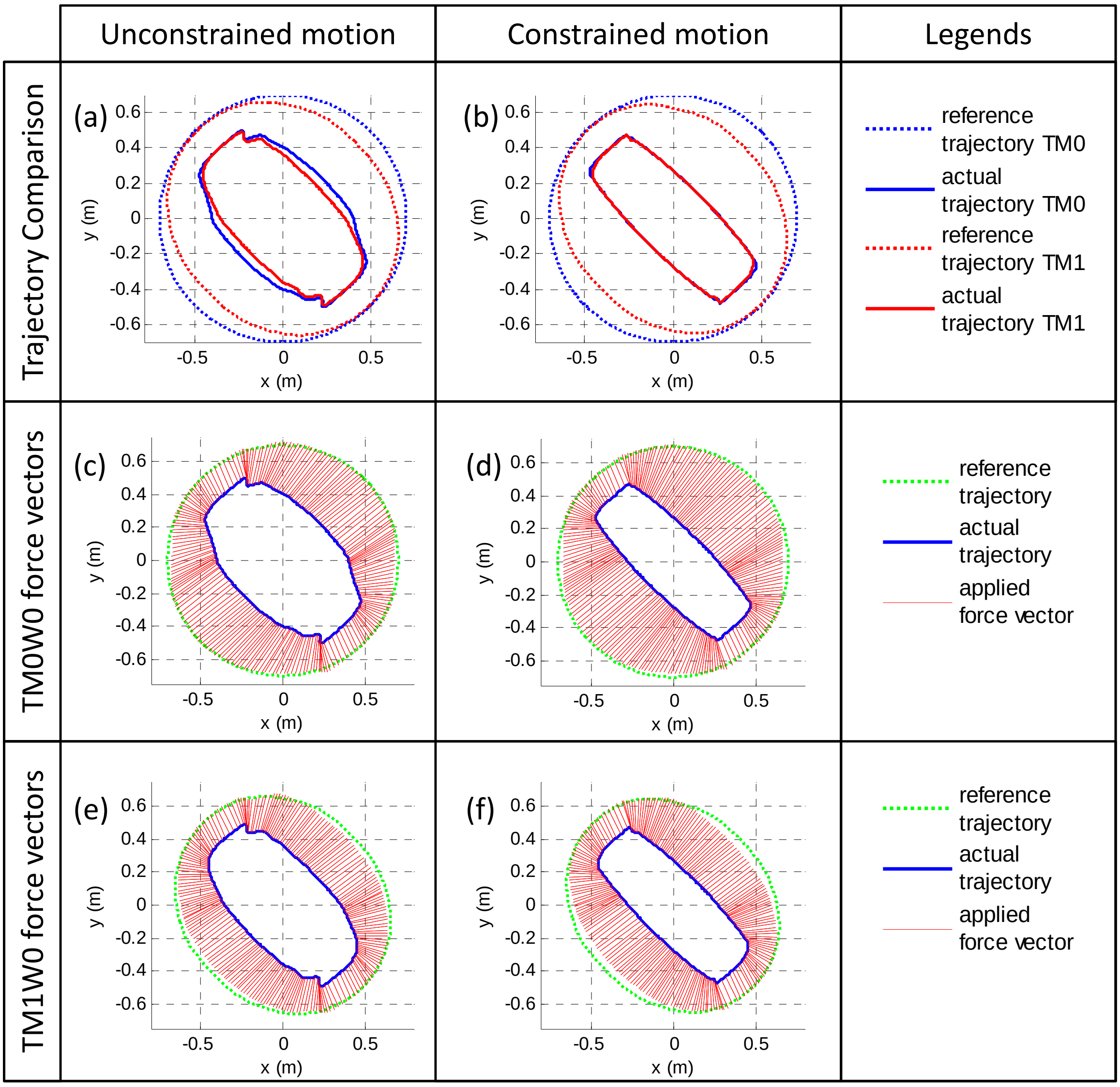

Figure 10.8: Simulation results for trajectory modification module: Comparison of the reference and actual trajectories for simulations involving both unconstrained (a) and constrained (b) motions; force vectors applied by the control scheme with no trajectory modification during unconstrained (c) and constrained (d) motions; and force vectors applied by the control scheme with trajectory modification during unconstrained (c) and constrained (d) motions.

Performance evaluation of control schemes

The significant amount of data produced by the simulation trials makes it difficult to gauge the relative merits of the control schemes considered. An attempt to solve this problem was made through the use of performance measures chosen to represent information which is releveant to physical interaction. In this work, four such measures were derived from the raw data obtained from the simulation runs, and they are ultimately combined to give a single performance index to facilitate the identification of the relative performance of each proposed control strategy. The four basic performance measures obtained from the raw simulation data are composed of the root mean square (RMS) of the applied control forces (10.47), the RMS of the position tracking error (10.48), the average of the negative work done by the control forces (10.49) and the RMS of the end point location (10.50). All these quantities were computed for the final cycle in the simulation runs to allow more time for parameters of the adaptation algorithms to approach their steady state values.

$$j_f = \sqrt{\frac{1}{N}\sum_{i=1}^{N}\left({F_{a,k}}^T F_{a,k}\right)} \tag{10.47}$$

$$j_e = \sqrt{\frac{1}{N}\sum_{i=1}^{N}\left({x_{e,k}}^T x_{e,k}\right)} \tag{10.48}$$

$$j_w = \frac{1}{N}\sum_{i=1}^{N}\max\left(0, -{F_{a,k}}^T \dot{x}_k\right) \tag{10.49}$$

$$j_x = \sqrt{\frac{1}{N}\sum_{i=1}^{N}\left({x_k}^T x_k\right)} \tag{10.50}$$

In the context of robot assisted rehabilitation, the reference trajectory should be followed as closely as possible as it is typically chosen to be representative of tasks executed during every day activities or to provide the desired rehabilitative effect. Forces on the other hand should be minimised to prevent it from reaching excessive levels that can compromise the safety of the user. In terms of the amount of negative work done, it should be kept as low as possible if the robot is to solely act as an assistive agent. Lastly, when the rehabilitation objective is to improve the range of motion and assuming that the limb/joint neutral position is located at the origin where resistance to motion increases with distance from the neutral position (note that this is the case in the simulated environment), a larger norm of the position vector will indicate that the user has negotiated higher levels of resistance and should therefore be considered favourably.

Once the above performance measures were identified, the combined performance cost index used in this work was computed for different assistance adaptation schemes, and subsequently compared within each operating condition. To achieve this, these performance measures were first normalised with respect to the largest values observed among all control schemes considered for the same operating condition. These normalised performance measures (denoted by subscript *norm*) are then used in the manner shown in (10.51) to obtain the final performance index. It can be seen that the measures to be minimised are all placed on the numerator of (10.51) while the measure to be maximised is used as the denominator. A better preformance is therefore given by a smaller value of J.

$$J = \frac{j_{f,norm} + j_{e,norm} + j_{w,norm}}{j_{x,norm}} \tag{10.51}$$

A summary of the performance indices obtained for each operating condition is given as bar graphs in Figure 10.9, while details of all the performance measures prior to and after normalisation is given in full in the Appendix D. In these graphs, the blue, green and red bars respectively correspond to control schemes utilising linear, saturated and parabolic EDFs in the feed forward force adaptation rule. It can be seen from Figure 10.9 that the alternative error dependency functions have outperformed the linear EDF approach in all but the passive unconstrained scenario. There is also a clear reduction in the performance index when trajectory modification is incorporated into the control scheme. This is particularly noticable when kinematic constraints exsit in the environment. Another point to note is that the performance indices for both the alternative error dependency functions are rather similar. Lastly, it can be said from these plots that work based stiffness adjustment only appears to contribute to improved overall performance when operating under the active and unconstrained condition.

The lower performance for the alternative feed forward force adaptatioin laws under the passive and unconstrained operating condition was rather unexpected. Further investigation in the the performance measures showed that the main reason the alternative approaches have lagged behind the linear error dependency approach under this operating condition is due to the larger negative work associated with them. As the magnitudes of negative work are relatively small in this scenario and negative work done by the robot/controller is not actually resisting user generated effort but rather the environmental forces, consideration of the negative work can be removed from the performance index. Using this modified performance index (Figure 10.10), it was found that the parabolic approach does outperform the linear approach, while the performance index of the saturated approach is roughly on par with that of the linear approach.

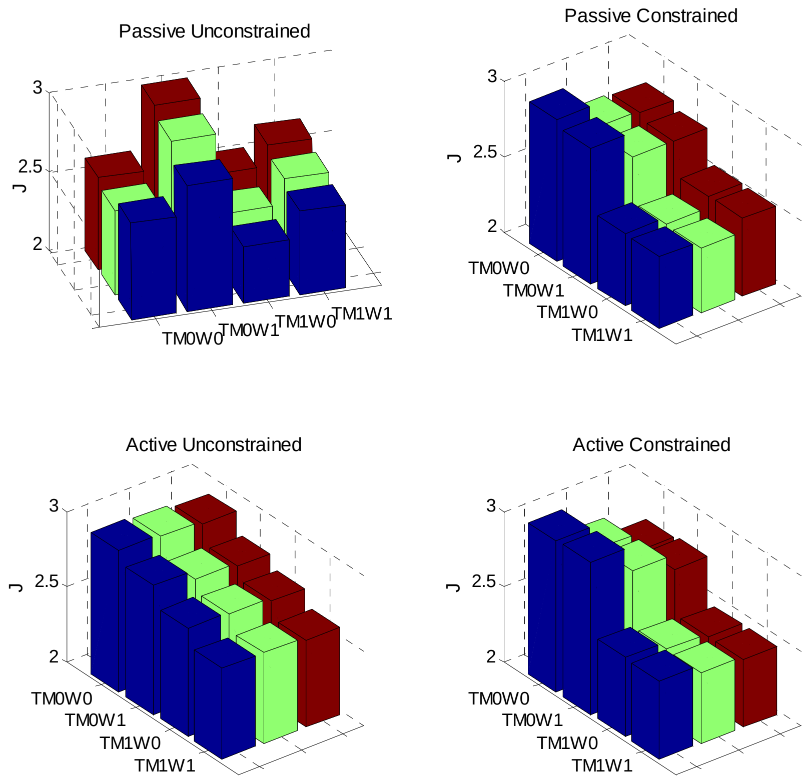

Figure 10.9: Summary of performance cost indices for controllers with different combinations of error dependency functions, work based stiffness adaptation activation and trajectory modification activation under various operation conditions considered in the simulation. Indices related to linear, saturated and parabolic error dependency functions are shown as blue, green and red bars respectively.

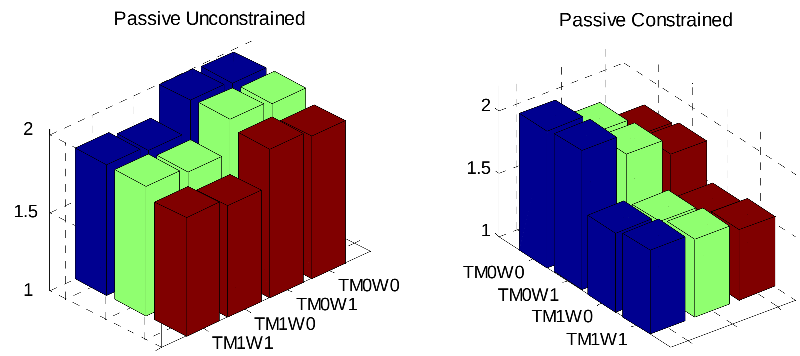

Figure 10.10: Modified performance cost indices (without negative work considerations) of the different controllers considered under the passive unconstrained and passive constrained simulation conditions. Indices related to linear, saturated and parabolic error dependency functions are shown as blue, green and red bars respectively.

10.2.2 Summary of Simulation Results

It can be seen from the simulation results that alternative EDFs in the adaptation of feed forward forces can considerably reduce actuator forces at the expense of a relatively small increase in position tracking error. The observations made thus far have also pointed to the conclusion that trajectory modification has a significant and positive impact on the physical interaction performance. From the simulations carried out, it was found that trajectory modification effectively reduces the actuator forces to levels similar to those obtained through utilisation of alternative EDFs in the feed forward force adaptation law. The proposed incremental work based controller stiffness adjustment module however only appears to have limited performance gains when used in the operating conditions considered in these simulations. In the author's opinion, this approach does have its merits (as suggested by the reduction in negative work along certain segments of the motion path) and further analysis using reaching movements may be able to better highlight the potential performance gains brought on by this approach. In all, simulations had shown that the proposed interaction controller is suitable for use in a rehabilitation setting. Consequently, it had been implemented and tested experimentally on the prototype ankle rehabilitation device developed in this research.

10.3 Experimental Results for Assistance Adaptation

Various experimental trials had been carried out on a single test subject (healthy adult male of 1.75m height, ethics approval reference 2009/480) to evaluate the performance of the different assistance adaptation schemes considered in this work. The experiments were used to test the different control schemes under three different scenarios. The first of these was the use of the robot to guide the subject's foot passively along the supination-pronation trajectory used in previous experiments. The second scenario on the other hand involved the use of the robot to move the subject's foot along the reference trajectory in a cooperative manner, where the subject is actively participating in the motion. Lastly, the third scenario involved the subject co-contracting the muscles around the ankle near the neutral foot configuration while the robot attempted to move the foot along the reference trajectory. The purpose of this test was to study the robot behaviour when interacting with an abnormally stiff or constrained environment. For the purpose of this section, experiments carried out under the first scenario will be referred to as passive motion trials, and those done under the second will be termed active motion trials. Finally, constrained motion trials are used to refer to tests completed under the third scenario. The data from these experiments are presented and discussed in this section to study the assistance adaptation schemes considered above. Constant robot impedance parameters were used in all experiments, with the controller gain matrices given as follows:

$$K_P = \begin{bmatrix} 10 & 0 & 0 \\ 0 & 10 & 0 \\ 0 & 0 & 5 \end{bmatrix} \qquad K_D = \begin{bmatrix} 2 & 0 & 0 \\ 0 & 2 & 0 \\ 0 & 0 & 1 \end{bmatrix}$$

Additionally, the parameters used for the feed forward adaptation law, incremental work based stiffness adjustment rule and the reference trajectory modification module are given in Table 10.2.

Table 10.2: Assistance adaptation scheme parameters used in the experimental trials.

Control Module	Feed forward moment adaptation			Incremental work based stiffness adjustment			Reference trajectory modification		
Parameter	τ	k	$x_{e,thres}$	γ_{max}	c	b	α	β	$x_{e,th}$
Value	5 s	6 N/rad	0.15 rad	0.9	5 s^{-1}	25 J^{-1}	0.1 s^{-1}	0.2 s^{-1}	0.15 rad

10.3.1 Basic Feed Forward Moment Adaptation

It is important to first compare the basic assistance adaptation scheme as proposed in [50] with a conventional impedance controller to identify the benefits and disadvantages of assistance adaptation. This was done by considering experimental results obtained from passive motion trials using a constant impedance controller and a constant impedance controller with assistance adaption. The assistance adaptation scheme used in this case was that with a linear EDF. The work based adaptation and trajectory modification modules of the assistance adaptation controller were also deactivated in this study. The foot position and the angular errors obtained from these passive motion trials are presented in Figure 10.11, while the assistive feed forward moment generated by the assistance adaptation scheme is shown in Figure 10.12. In addition to the passive motion trials, an active motion trial was also carried out using the basic assistance adaptation scheme to allow an investigation into the behaviour of this controller when the subject is actively participating in the rehabilitation exercise. The results of this trial are given in Figure 10.13. Lastly, constrained motion trials were also performed using both the conventional impedance controller and the basic assistance adaptation scheme and the results are presented in Figure 10.14.

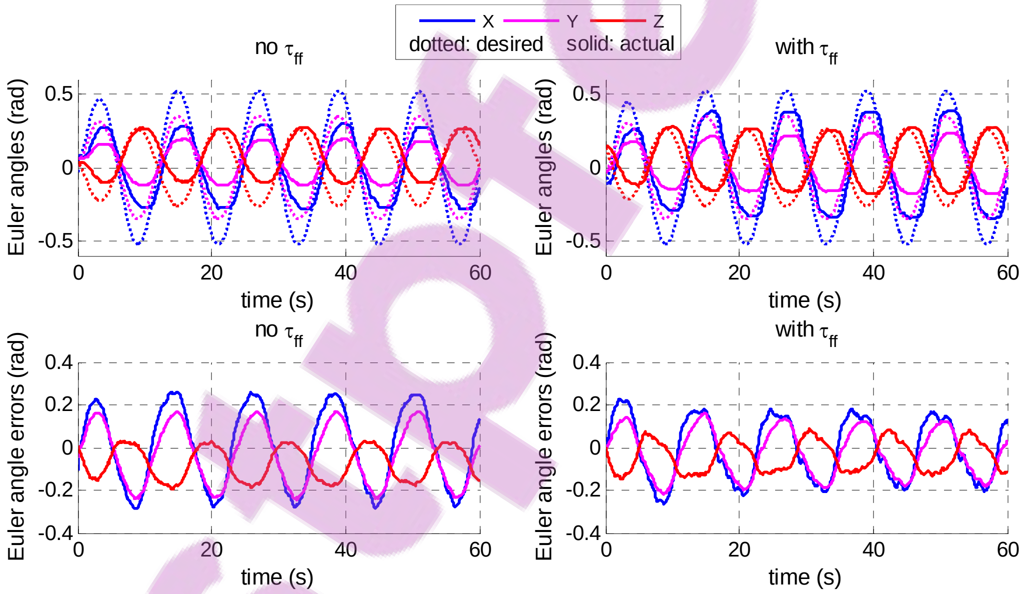

Figure 10.11: Desired and measured foot orientation, as well as tracking errors obtained from passive motion trials using the conventional impedance controller (without feed forward moments τ_{ff}) and the basic assistance adaptation scheme (with feed forward moments τ_{ff}).

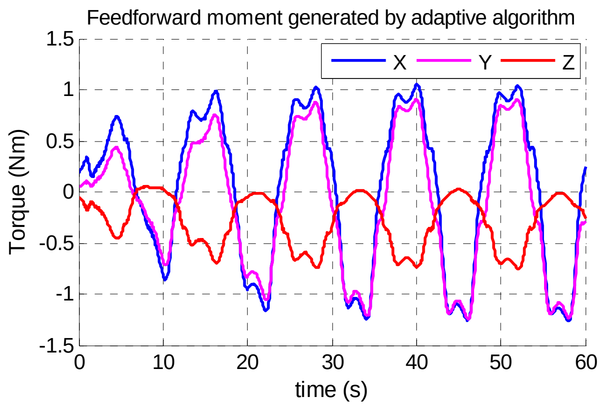

Figure 10.12: Feed forward moments generated by the basic assistance adaptation scheme.

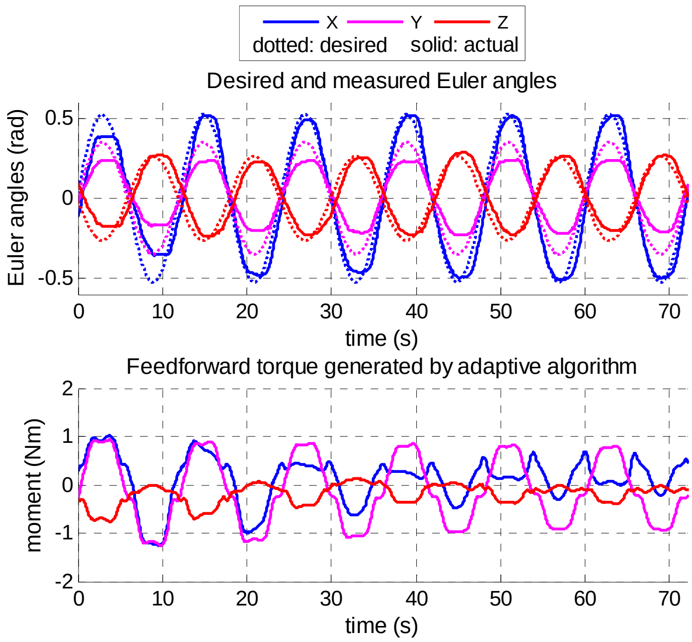

Figure 10.13: Desired and measured foot orientations, as well as the feed forward torque obtained from active motion trials using the basic assistance adaptation scheme.

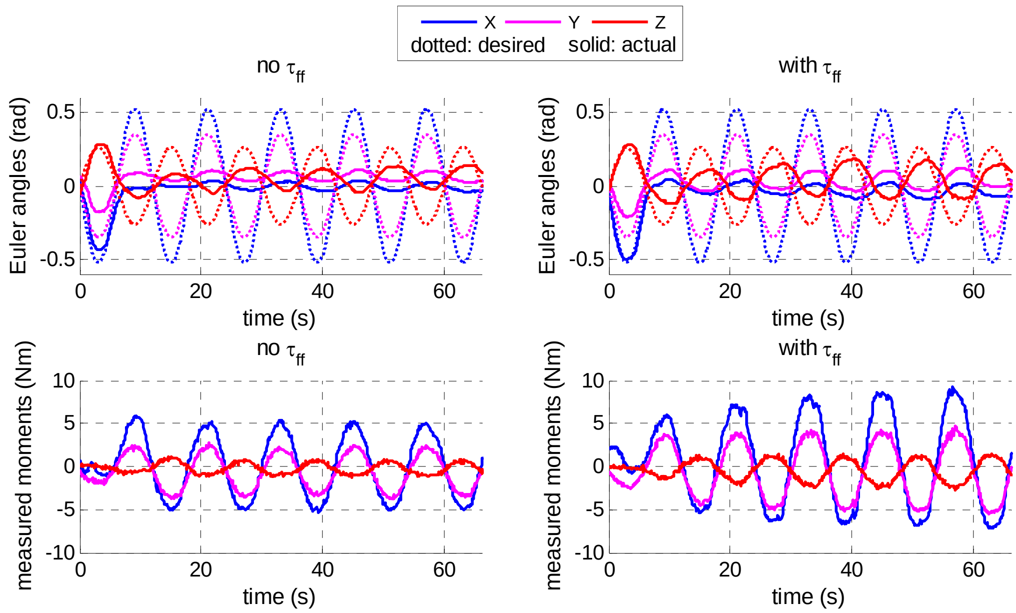

Figure 10.14: Desired and measured foot orientation, as well as measured moments obtained from constrained motion trials using the conventional impedance controller (without feed forward moments τ_{ff}) and the basic assistance adaptation scheme (with feed forward moments τ_{ff}).

Discussion

It is clear from the passive motion trial results (Figure 10.11) that the introduction of the adaptive feed forward moment has an effect of reducing the overall motion tracking error of the foot. This is of course due to the additional effort applied by the adaptive feed forward moments in the assistance adaptation scheme. The evolution of the assistive or feed forward moments shown in Figure 10.12 shows that the adaptation rule had converged rather quickly over a few cycles of the motion. It is important to note that due to the decaying term present in the adaptation law, the feed forward moment will not continue to increase until the position errors are eliminated. This ensures that a balance can be reached between acceptable levels of applied moments and reasonable trajectory following capability. Emphasis can be placed more heavily on each of these aspects by tuning the parameters in the adaptation law, with a larger gain k in (10.3) giving better positional accuracy and vice versa.

Results from the active motion trial shown in Figure 10.13 indicate that the reference trajectory can be followed much more closely when the subject is actively participating in the motion. It can also be seen that the feed forward moment used to provide additional assistance to the subject is reducing in directions with smaller position tracking errors as time progresses. This is a desired characteristic as the subject should be encouraged to produce the motion independently without relying on the rehabilitation robot.

In terms of performance in constrained motion trials, the results shown in Figure 10.14 suggest that the basic assistance adaptation scheme is applying significantly larger moments compared to the conventional impedance control scheme when the subject's foot is stiffened. This may not be desirable since stiff regions may turn out to be an actual kinematic constraint in the environment. This test therefore shows that when the reference trajectory is designed without knowledge of such constraints, large moments can be generated by the basic assistive adaptation scheme due to bigger position tracking errors. This indicates that while the basic assistive adaptation scheme can offer better position tracking capability to the rehabilitation robot, it can still be further improved to reduce the feed forward moments applied in situations where unknown constraints are encountered in the environment.

10.3.2 Effects of Different Error Dependency Functions

While the results presented previously focused on the differences between the conventional impedance controller and the basic assistance adaptation scheme, this subsection addresses how different error dependency functions in the feed forward moment adaptation law influences the overall behaviour of the rehabilitation robot. Both passive motion and constrained motion trials were considered for this purpose, and each of the linear, saturated and parabolic EDFs were tested (with the trajectory modification and work based adaptation modules disabled). The results for the passive motion trials are summarised in Figure 10.15, while those for the constrained motion trials are shown in Figure 10.16.

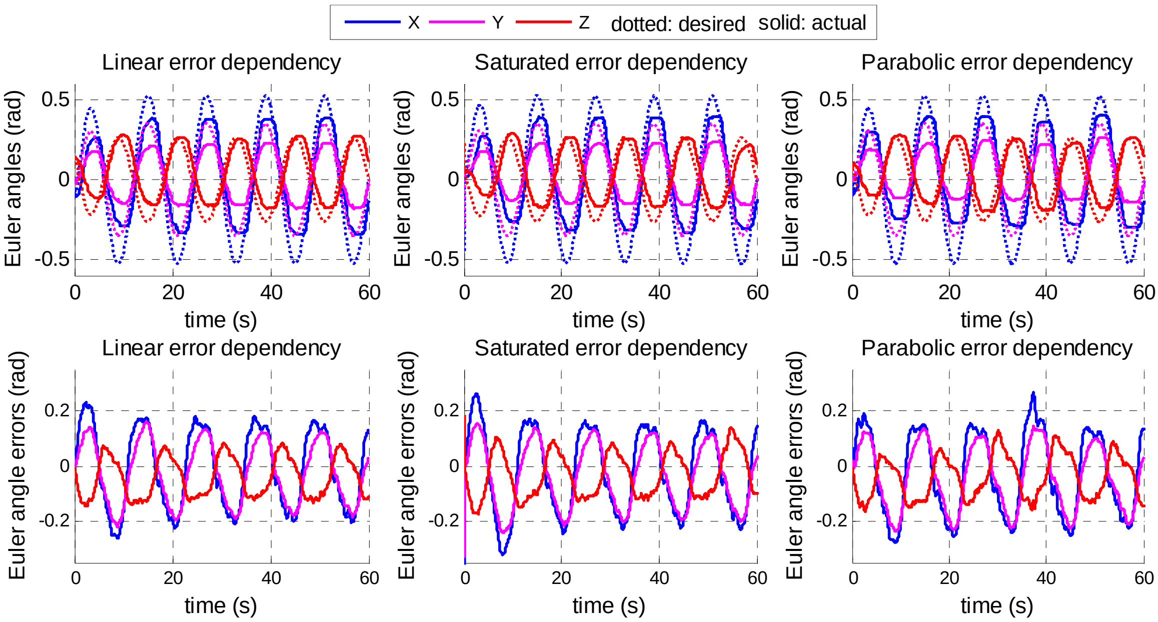

Figure 10.15: Desired and measured foot orientations, as well as tracking errors obtained from passive motion trials using assistance adaptation schemes with different error dependency functions in the feed forward moment adaptation law.

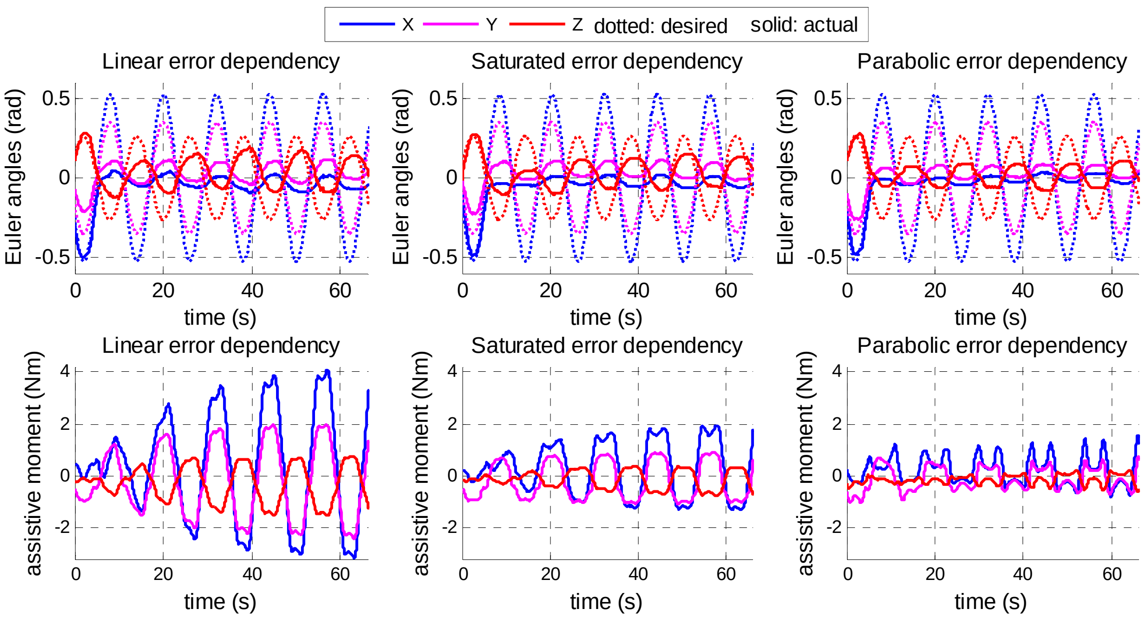

Figure 10.16: Desired and measured foot orientations, as well as assistive moments obtained from constrained motion trials using assistance adaptation schemes with different error dependency functions in the feed forward moment adaptation law.

Discussion

Results from the passive motion trials conducted have shown that all three error dependency functions appear to have very similar performances in terms of angular errors. Detailed Inspection of Figure 10.15 however reveals that use of the linear EDF resulted in marginally smaller position error in the pronation direction (negative x, negative y and positive z), while errors during this phase of motion appeared the largest for the controller utilising parabolic EDF in its adaptation law. When looking at the supination portion of the motion however, it appeared that the controller with parabolic EDF had a slight advantage in terms of smaller errors in the x and y directions. It should also be noted that apart from the initial cycle of the passive trial, the errors observed with the controller using saturated error dependency behaved very similarly to that of the linear error dependency case.

The above trends were expected since the linear error dependency function contributes to an "effort" to increase the feed forward moment in proportion to the magnitude of the error. The saturated error dependency function on the other hand behaves in an identical manner to the linear case up until the error threshold, above which it will hold the "effort" at a constant level, thus it is expected that the errors obtained using this approach will be equal or slightly larger than that for the linear case. The parabolic error dependency function however produces an effort which is larger than both the alternatives up until the error threshold, and beyond that, this effort will start to decrease until it reaches zero. This provides an explanation to the observation where errors in the parabolic dependency case is larger than that of the linear dependency case during pronation , but smaller when the foot is undergoing supination motion. This is because errors in supination are smaller or near the error threshold used while those in the pronation direction are larger than the threshold. The consequence of this is that the effort applied to increase the feed forward moment is larger in supination for the parabolic dependency case, but smaller when the foot is moving in pronation.

The choice of different error dependency functions also has significant influence on the performance of the constrained motion trials. By considering the assistive feed forward moments applied by the different control schemes, it can be seen that the controller with linear error dependency created the largest magnitude in the feed forward moments, followed by the control scheme with saturated error dependency and that with parabolic error dependency. This suggests that these latter two error dependency schemes can be used to improve the safety of the assistance adaptation scheme by limiting the increase of feed forward moment in stiff or constrained directions/regions.

10.3.3 Effects of Incremental Work Based Stiffness Adaptation

The effectiveness of the incremental work based stiffness adjustment module in the proposed assistance adaption scheme was also tested experimentally. Since the simulation case study as well as preliminary experimental testing showed that this module had little impact on passive motions, this subsection will focus on results of active motion trials. Two types of active motion trails had been carried out experimentally, the first involved the active participation of the subject in moving the foot along the pronation-supination reference trajectory (as used in all previous experiments), and the second required the subject to move the foot as much as possible in the direction of motion of the dorsiflexion-plantarflexion reference trajectory, but did not require precise tracking of the reference trajectory. The dorsiflexion-plantarflexion reference trajectory is given in (10.52) as it is an easier task for the subject to drive the foot in a single direction of rotaton rather than a combination of several rotational motions. Each of these active motion trials were completed for two different assistance adaptation schemes with a linear EDF and no trajectory modification. The only difference between these schemes was that one had the work based stiffness adaptation module activated while the other had it deactivated. The results for the first type of active motion trials are shown in Figure 10.17 while results for the second type of active motion trials are given in Figure 10.18.

$$\begin{aligned} \theta_x &= \frac{\pi}{9}\sin\left(\frac{\pi}{6}t\right) \\ \theta_y &= \theta_z = 0 \end{aligned} \tag{10.52}$$

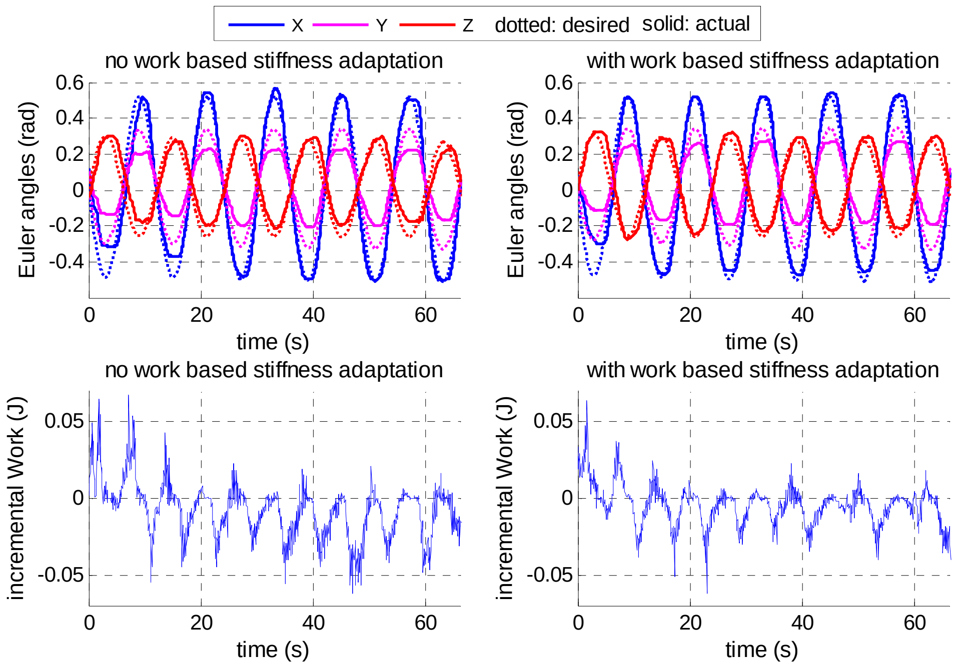

Figure 10.17: Desired and measured foot orientations, as well as incremental work done by the robot obtained from active motion trials requiring the subject to follow the reference trajectory as closely as possible. The incremental work based stiffness adaptation module was toggled between on and off for the two control schemes considered.

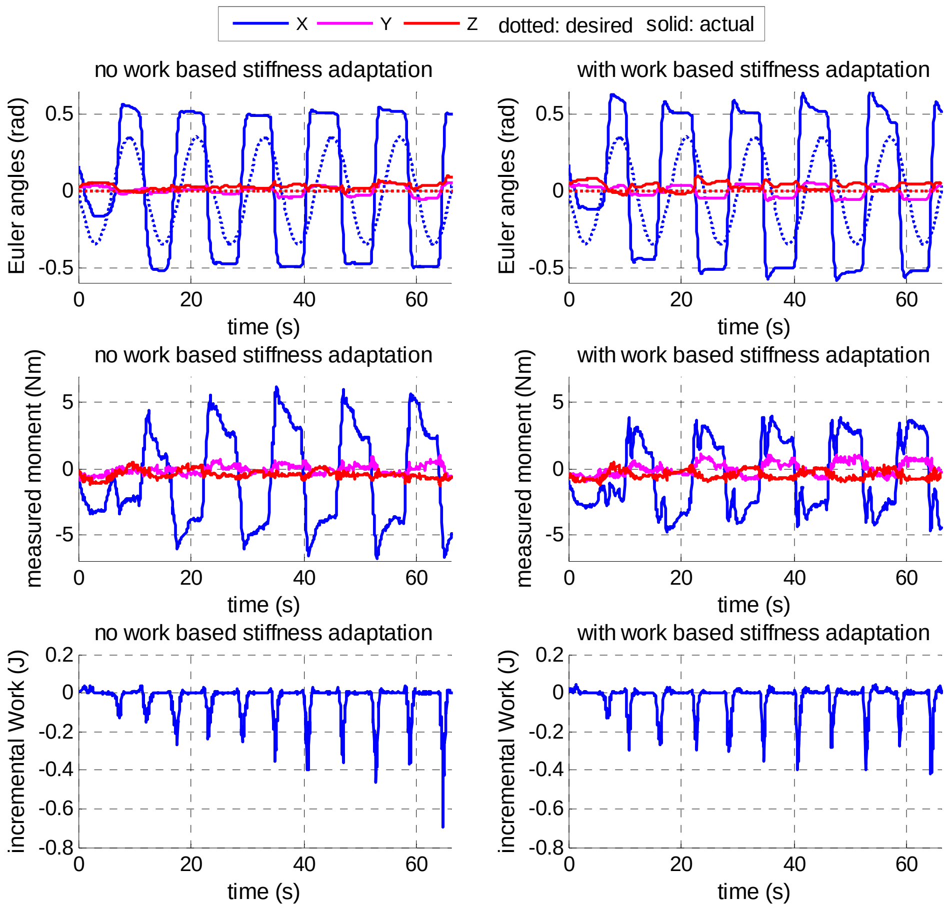

Figure 10.18: Desired/measured foot orientations, measured moments, as well as incremental work done by the robot obtained from active motion trials where subject attempts to move the foot as much as possible in the desired direction with no regard to trajectory tracking. The incremental work based stiffness adaptation module was toggled between on and off for the two control schemes considered.

Discussion

As previously discussed in the simulation case study, negative incremental work typically indicates that the robot is impeding the motion of the user. Negative work must therefore be minimised in robots used to provide assistance to the user's movement. Results from the first type of active motion trials (Figure 10.17) show that the negative incremental work done by the robot during the trials are rather similar between the two control schemes considered. Closer examination however suggests that the scheme with the incremental work based adaptation module active had slightly smaller levels of negative incremental work. Nevertheless, this observation is inconclusive since resistive moments applied by the robot are highly dependent on the position errors and this is not kept constant throughout both trials due to the active participation of the subject. This therefore makes direct comparison difficult, particularly when the difference between the two schemes is not very significant. The second type of active motion trial however can be used to better illustrate the contribution of the incremental work based stiffness adaptation module. It is clear from the results of these trials (Figure 10.18) that the controller with an active incremental work based stiffness adaptation module provided considerably smaller resistive moments to the subject. This had led to the larger movement amplitudes and lower levels of negative work. This therefore suggests that the incremental work based stiffness adaptation module is working as intended, and can be incorporated into the overall assistance adaptation controller to reduce the resistive moments applied when the user is capable of moving ahead of the reference trajectory.

10.3.4 Effects of Reference Trajectory Modification

The greatest motivation for the inclusion of the trajectory modification module into the overall assistance adaptation scheme is to allow the adaptation of the reference trajectory according to the position errors observed during the operation of the robot. By modifying the reference trajectory based on previously learnt position errors, the interaction force between the robot and the environment can be altered. For the purpose of this research, it is desired that excessive position errors be regarded as the presence of kinematic constraints. The trajectory modification scheme was therefore designed to reduce the interaction forces in these regions. The efficacy of the trajectory modification module was tested through constrained motion trials. Two different control schemes were considered, both having linear error dependency and no work based stiffness adaptation, while the only difference between the two is the activation/deactivation of the trajectory modification module. The results obtained from these experiments are shown in Figure 10.19.

Discussion

The results presented in Figure 10.19 shows that activation of the trajectory modification module does indeed cause a significant reduction in the estimated foot-robot interaction moment. It can be seen that this is a result of the “shrinking” reference trajectory which leads to reduction in position error and ultimately to a reduced feed forward moment from the adaptation law. This means that the trajectory modification module is actually acting in a similar capacity as the alternative error dependency functions in reducing the feed forward torque when the position errors are large. In fact, by modifying the reference trajectory itself, the reduction in applied force can even be greater due to reduced moment contribution from the basic impedance controller as well. One shortcoming of trajectory modification found from experimentation with this control module is the presence of high frequency oscillations in the actuator motors when the parameter β used in the parameter adaptation rule (10.44) is too large. This means that there is a limit on how quickly the trajectory can be adapted if stability of the system were to be maintained.

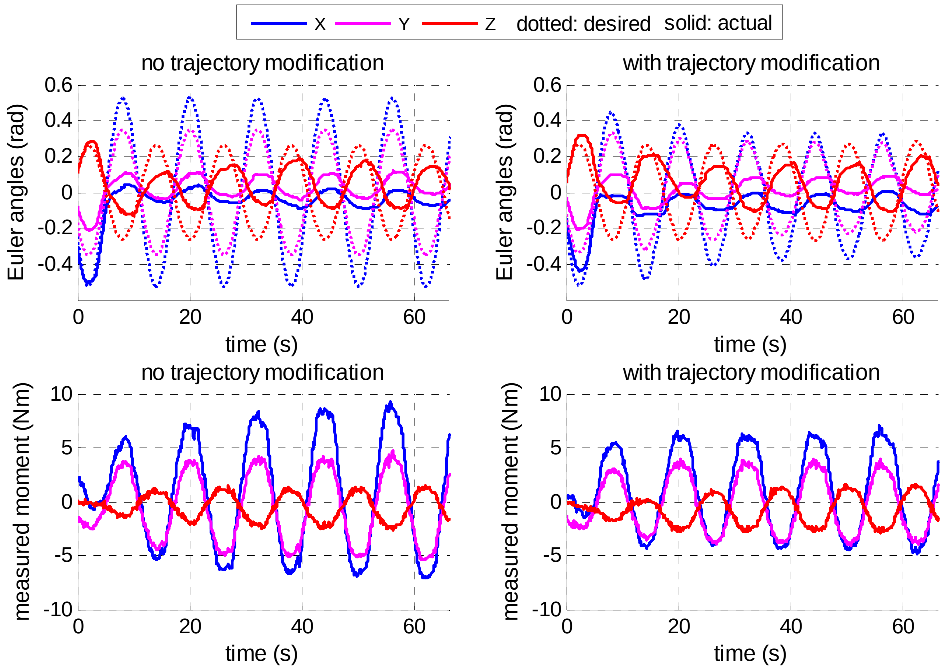

Figure 10.19: Desired and measured foot orientations, as well as estimated interaction moments obtained from constrained motion trials using assistance adaptation schemes without and with the reference trajectory modification module.

10.3.5 Summary of Experimental Results

Comparison of the basic impedance controller and the impedance controller with the existing assistance adaptation scheme [50] in place had shown that significant performance gains can be achieved through adoption of the assistance adaptation scheme, whereby the additional feed forward assistive moment can help improve the trajectory tracking capability of the robot. Additionally, the inclusion of adaptation also means that the robot's behaviour can better adjust to suit the needs of the user in terms of assistance. At the same time however, the experimental results had also highlighted the potential drawback of this adaptation scheme in the form of larger applied moments in stiff or constrained regions/directions. This therefore justifies the work in this research which attempts to modify the existing assistance adaptation scheme to address the above issue.

The experimental results on the effects of different EDFs have shown similar trends to those obtained from the simulation case studies, with the alternative EDFs performing better in terms of reducing the applied moments during constrained motion. The accuracy in trajectory tracking during passive motion trials was also not severely degraded by the use of alternative EDFs. This therefore supports the incorporation of the saturated or parabolic error dependency functions in the final assistance adaptation scheme.

Although not clearly shown in the simulations, the potential advantage of the work based stiffness adaptation scheme had been elucidated through the active motion trials which required the subject to generate the maximum possible movement in a similar direction of the reference trajectory. These trials clearly showed a reduction in resistive moment when the work based adaptation module is activated. Consequently, the integration of this module into the overall assistance adaptation scheme will provide more freedom to the user to control their movements, provided that this movement is in a direction similar to that of the reference trajectory.

The trajectory modification module also performed well in the experimental trials, whereby it contributed to a reduction in the foot-robot interaction moments during constrained motion trials. However, experimentation with this control module had suggested that it can cause high frequency oscillations in the actuator motors. As the stability proof of the trajectory modification module was not attempted in this work, it is unclear if this oscillation is inherent in the parameter adaptation law for the trajectory adjustment term or if it is caused by un-modelled dynamics and interaction between the inner and outer control loops of the robot. Further investigation is therefore necessary to better understand the cause for this oscillation. Nonetheless, the problem of actuator oscillation appeared to be negligible when lower gain values are used in the adaptation rule and given the benefits introduced by this module, a suitably tuned parameter adjustment rule can still be considered in an assistance adaptation scheme.

10.4 Overall Control Structure and Implementation of Rehabilitation Exercises

One of the main goals of this research is to develop a suitable adaptive interaction control framework to allow implementation of different ankle rehabilitation exercises on the developed ankle rehabilitation robot. The resulting interaction controller and its relation to the works presented earlier in this thesis can be summarised diagrammatically as Figure 10.20, where the lower level controller can be considered to be made up of the inner loop MIMO actuator force controller proposed in Chapter 7 and the elementary robot control scheme presented in Chapter 8. The higher level control on the other hand consists of the ankle kinematic parameter estimator, the robot impedance adaptation module and the assistance adaptation scheme. The ankle kinematic parameter estimation algorithm in Chapter 4 is used to provide estimates for the ankle and subtalar joint displacements which are in turn used to establish the ankle compliance at a particular configuration according to a lookup table generated using the computational ankle model discussed in Chapter 5. This ankle compliance is then processed by the impedance adaptation routine to select the appropriate robot stiffness. Although not used in the experimental trials, the rehabilitation trajectory optimisation routine proposed in Chapter 5 is also included in the diagram as it can potentially be used to generate suitable rehabilitation trajectories when desired characteristics of the rehabilitation motion such as limitations on ligament/muscle-tendon forces or ankle reaction moments are defined.

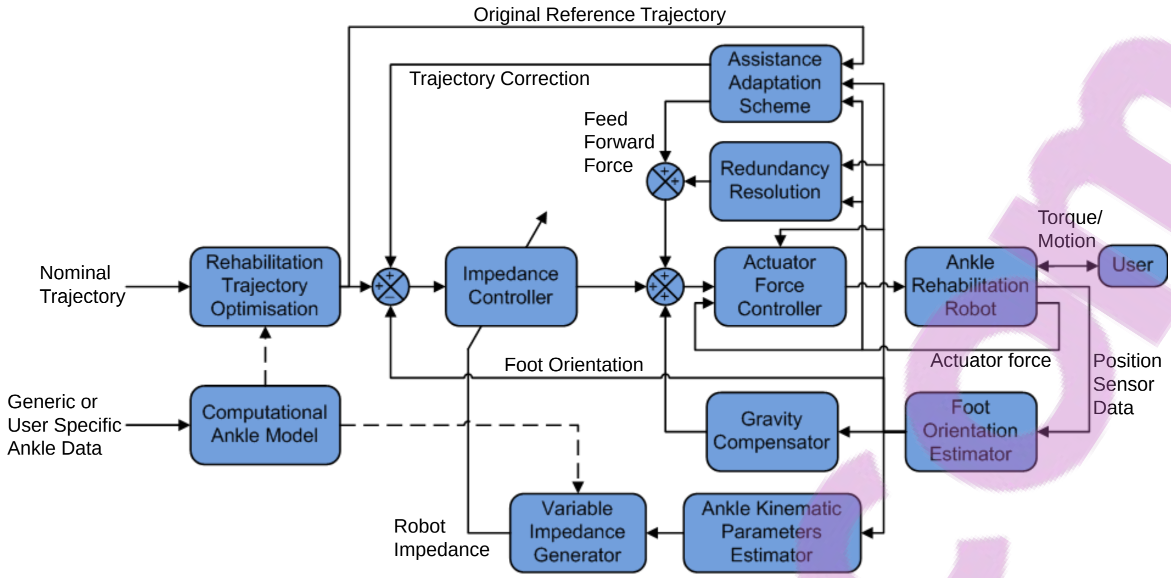

Figure 10.20: Overview of the interaction control scheme proposed in this research.

Different ankle rehabilitation exercises can be implemented using the proposed interaction controller. For instance, passive range of motion exercises can be easily implemented by using the basic impedance controller and the assistance adaptation scheme discussed in this chapter. The above control structure can also be applied directly to user-cooperative rehabilitation exercises which require active user participation in the exercises. The use of the assistance adaptation scheme means that the level of assistance provided by the robot will vary according to the capability of the user, thus allowing adaptive or assist-as-needed therapy which is widely believed to be beneficial in promoting recovery [2, 14, 49, 50].

The developed system also has the capability to administer muscle strengthening or resistive exercises and this can be achieved through the use of impedance control or explicit torque control. By defining a suitable robot impedance parameter and selecting a particular equilibrium position as the neutral position, the rehabilitation robot can be made to behave as a mechanical spring-damper unit which the user can work against. Using this setup, ankle resistive exercises such as those which involve the use of elastic bands can be recreated on the rehabilitation robot. However, due to the system's ability to alter the impedance parameters and the neutral position of the developed system, a larger range of resistive exercises can be achieved. Another mode of resistive exercise that can be realised on the robot is the application of a constant resistive load to the user. This operation would require the use of pure torque control about the ankle joint, which can be accomplished on the developed system by setting the robot impedance to zero. Results obtained from experimental trials involving the impedance based and constant torque resistive exercises are shown in Figure 10.21. The impedance based resistive exercise involved the subject applying a moment at the ankle to resist the foot motion in the plantarflexion direction (positive x-direction). The torque control based exercise on the other hand imposed a constant torque reference in the dorsiflexion direction, thus producing a resistive torque which opposed the user's plantarflexion movements.

From the moments recorded from the experimental trials, it is clear that the robot behaved in a similar manner as a torsional spring in the impedance based resistive exercise, where further deviation from the positional set point produced a larger resistive force. The trial involving the constant torque control showed that a relatively constant level of moment is maintained at the ankle joint, thus indicating that the user will be required to apply a steady effort to move the foot in the plantar direction. It should be noted however due to the imperfect rejection of frictional forces and moments, the observed moment is not exactly as desired. Nonetheless, the torque level can still be maintained within a relatively small band around the actual moment set point.

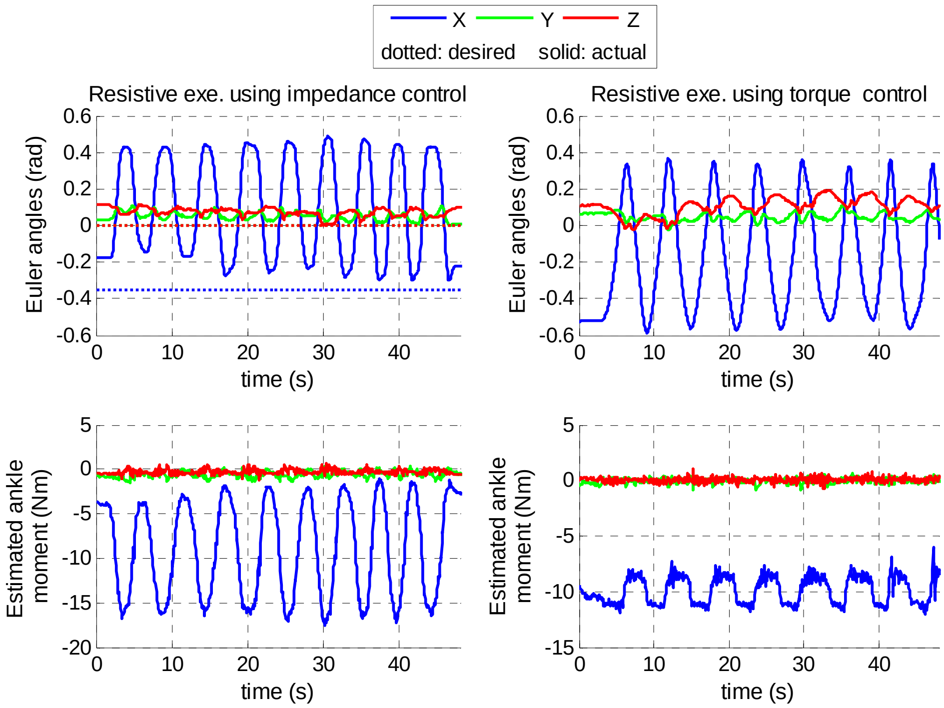

Figure 10.21: Experimental trials showing the implementation of resistive exercises on the developed ankle rehabilitation robot through the use of impedance control and torque control.

10.5 Chapter Summary

This chapter presented the assistance adaptation scheme developed in this research to achieve adaptive interaction control. The assistance adaptation scheme is primarily used to produce a feed forward moment which is fed into the interaction controller to provide additional assistance to the user. Additionally, this scheme also modifies the robot's stiffness and reference trajectory to improve interaction performances during constrained and active motions. This scheme is based on a similar scheme proposed in [50] but modifications had been incorporated into the original control scheme to achieve additional control objectives. The first of these objectives is to reduce the assistive force when the motion tracking error becomes too large, and it is based on the notion that large position errors are indicative of a kinematically constrained environment. The second objective on the other hand is to reduce the resistive forces exerted by the robot when the user is moving ahead of the defined reference trajectory. Testing in simulation and experiments had shown that the former objective can be achieved by using a different error dependency function in the feed forward force adaptation law and through the modification of the reference trajectory, while the latter objective can be accomplished by reducing the robot stiffness along the direction of reference motion when negative incremental work is registered.

The chapter ended with a summary of how the online ankle kinematic parameter estimation algorithm, the computational ankle model, the trajectory generation routine, the MIMO actuator force controller, the elementary robot control scheme and the two adaptive interaction control modules (variable impedance control and assistance adaptation) interacts to form the final control framework. Additionally, a discussion on how different ankle rehabilitation exercises can be implemented using the developed control schemes was also presented.

Chapter 11 Conclusions and Future Work

Various aspects including the design, modelling and control of the platform based ankle rehabilitation robot developed in this research had been discussed in previous chapters. This chapter seeks to summarise the main outcomes and conclusions of this research, as well as highlight the contributions made in this work. Lastly, this chapter also provides a discussion of future directions that can be explored to extend or advance the work presented in this thesis.

11.1 Outcomes, Conclusions and Contributions

A new platform based ankle rehabilitation robot was developed in this research with the aim of facilitating physical therapy of sprained ankles. The major works carried out in this research are identified as: development of a new platform based ankle rehabilitation robot; development of an online identification algorithm for the biaxial ankle kinematic model; derivation of a rigid body based computational ankle model to facilitate development of the robot interaction controller; development of a MIMO actuator force controller to realise force based impedance control; and development of an adaptive interaction control scheme which allows the robot to adapt its behaviour according to the foot configuration and user capability.

An overall adaptive interaction control framework was also devised in this research to achieve the central theme of this research which is to incorporate elements of adaptability into the resulting ankle rehabilitation robot. In such a framework, the kinematic parameter estimator and computational ankle model are used to facilitate environment based robot stiffness adaptation and limit interaction forces at stiff or constrained environments, while the MIMO actuator force control and the elementary robot control scheme are used to form the foundation of the interaction control scheme. The proposed assistance adaptation scheme on the other hand is included to provide assist-as-needed therapy and to improve the ability of the robotic system in dealing with constrained and active motion.

The outcomes, contributions and conclusions relating to the works conducted in this research are summarised in this section.

11.1.1 Development of a Novel Ankle Rehabilitation Robot

A new parallel robot had been proposed and developed in this research for the rehabilitation of ankle sprain injuries. While there are several designs of platform based robots used in ankle rehabilitation, the end effectors of these devices are typically constrained to rotate about a pivot which does not coincide with the human ankle's effective centre of rotation [10, 31, 32, 41, 42]. The design of this new robot therefore differs from most of these existing solutions in the sense that it is under-actuated when the user's lower limb is not attached to the robot. This means that when in use, the user's lower limb will form part of the robot's kinematic constraint, thus ensuring that the motion performed by the robot is in line with the natural ankle-foot movements. Additionally, since movement of the shank is kept to a minimal level during operation, the robot can also estimate the relative orientation of the foot with respect to the shank with greater precision, thus allowing it to provide more repeatable rehabilitation movements and serve as a better measurement tool for evaluation of the ankle's mechanical characteristics.

The design of the device was based on workspace, singularity and force analyses which were respectively carried out to ascertain the motion limits of the robot, the controllability of the robot within its motion limits and the actuator forces required by the robot to produce the desired robot-foot interaction moments. By treating the ankle as a spherical joint capable of three degrees of freedom rotational motion, it was found that singular regions will exist in the robot's reachable workspace if only three actuated links are used in the mechanism. More specifically, the reachable workspace will be bisected by a "surface" of orientations with ill conditioned manipulator Jacobians, thus making the robot more difficult to control. The remedy to this issue was found through the use of a redundantly actuated mechanism by including an additional actuating link to the mechanism, which successfully eliminated these regions of large condition number in the robot's reachable workspace. In addition to the elimination of singularity in the workspace, the redundant actuation degree of freedom is also exploited in this work to allow regulation of the total vertical load applied to the ankle. To the best of the author's knowledge, this feature is not yet available in existing ankle rehabilitation devices, but can be beneficial to the treatment of ankle sprains by allowing emulation of different levels of weight bearing to suit the needs of the user.

Further analyses were also conducted to investigate the impact of uncertain ankle joint centre locations on the robot's capability to satisfy the design requirements. It was found that despite the application of conservative approaches in the workspace and singularity analyses, the desired range of motion and moment requirements are still largely satisfied by the proposed design. Additionally, it was also confirmed that this can be achieved with a good level of manipulability within the reachable workspace.

The uncertainty in the ankle joint centre also presents a challenging problem for the control of the proposed ankle rehabilitation robot, particularly in the estimation of a correct foot configuration. A solution to this issue was proposed in this research through the use of redundant sensing which utilises additional pitch and roll measurements of the end effector to fully resolve the end effector configuration of the robot.

11.1.2 Kinematic Parameter Estimation of Human Ankle

It had been widely reported in literature that the kinematics of human ankle is complex and can vary significantly between individuals. However, since such kinematic information can be used in the adaptation of the robot's behaviour as auxiliary variables that can be processed to adjust the robot controller parameters, this research had proposed a new online estimation algorithm based on the recursive least squares filter to identify a subject specific description of the ankle kinematics. It should be noted that while studies had been carried out to identify the kinematic parameters of a biaxial ankle kinematic model [64, 79, 82], such works had mainly utilised offline nonlinear least squares methods. The proposed online estimation algorithm, driven by the need for it to be used in real time control scheme, is therefore a new development in ankle kinematic parameter identification.

Due to its relatively simple structure, the biaxial ankle model had been identified as an ankle kinematic model that is well suited for online parameter identification. Two different online identification techniques, the Extended Kalman Filter (EKF) and the Least Mean Square (LMS) method had been considered for parameter estimation of the biaxial ankle model. A simulation based comparison of the EKF and LMS approaches involving an ideal biaxial ankle model had shown that an EKF acting in the capacity of a Recursive Least Square (RLS) estimator have the ability to produce the best estimation results in terms of estimation accuracy and parameter convergence. This approach had therefore been used in subsequent investigations done in this research.

As numerous studies had found the orientations of the ankle and subtalar axes in the biaxial ankle model to vary with foot orientation [69, 71-73, 82], the conventional biaxial ankle model with constant axis tilt angles had been extended in this research. The extension essentially allows the axis tilt angles of the biaxial model to vary with the foot configuration and two variants of this extension had been proposed. The first version allows the axis tilt angles to vary linearly with respect to the ankle and subtalar joint displacements while the second version varies the tilt angles according to the X and Y Euler angles used to describe the foot orientation. The feasibility of using the conventional biaxial ankle model and both the extended biaxial ankle models (with different axis tilt angle dependencies) in the RLS algorithm was also tested in a simulation study that utilised the first extended biaxial ankle model to generate the training data. The results of this study indicated that while the RLS algorithm based on the conventional constant tilt axis biaxial model produced poor results by converging to incorrect parameters and producing large estimation errors in terms of the actual ankle and subtalar joint displacements, the second extended biaxial model performed in a more acceptable manner (though as expected the first extended model produced the best estimates). By considering the fact that the first extended biaxial model is significantly more computationally intensive (as it took approximately nine times longer to simulate in MATLAB), the approach based on the second extended model had been chosen for implementation on the actual ankle rehabilitation robot.

A limitation related to the use of the proposed RLS approach in online parameter estimation is that the inverse cross correlation used to initialise the RLS algorithm must be kept small to limit deviations of the axis tilt angles from their nominal values (which in turn prevents discontinuities in the ankle and subtalar displacement estimates). Consequently, the use of different initial guesses in the RLS algorithms will result in convergence to different parameters (even though the final estimation errors remain similar). Preliminary testing using the alternative extended biaxial model in the estimation of axis tilt angles based on data collected from the actual ankle rehabilitation robot had also suggested that the algorithm produced unrealistic parameter estimates.

To address the above issue, a new modified RLS algorithm which imposes penalty on deviation of parameters from their nominal/expected values was proposed in this research. Testing of this algorithm had shown that the parameter and ankle/subtalar displacements estimates obtained were more in line with expected values without excessive increase in estimation errors. Larger inverse cross correlation matrices can also be used to initialise the algorithm to produce more consistent parameter estimates. The modified RLS algorithm had also been applied to the conventional biaxial model and it was found that it had a similar effect of producing more reasonable estimates. However, examination of the overall cost function still showed that the alternative extended biaxial model performed better in terms of estimation accuracy. It was therefore concluded that of the approaches considered, the modified RLS algorithm can be used with the second extended biaxial ankle model to provide the most suitable algorithm for online identification of subject specific ankle kinematics.

11.1.3 Computational Ankle Model for Controller Development

A computational ankle model in the form of a state space model had been derived in this research to facilitate the development and simulation of the robot control scheme. A three segmented rigid body model had been proposed together with the biaxial ankle kinematic constraint to reduce the computational complexity of the model, thus making it more suitable for controller simulations. Ligaments and muscle-tendon units had also been included in the model as force elements to allow monitoring of the tensions along these elements.

The developed model was validated through simulation studies involving both passive and active motion of the foot. It was found that the moment-displacement characteristic of the simulated foot along the flexion direction is largely in agreement with what is reported in literature, where larger ankle stiffness is found in the dorsiflexion direction. Simulations involving active muscular contractions also showed that activation of different muscle groups produced motion in the expected direction of motion, while also achieving movements within the typical motion limits of the human ankle. Data from an experimental trial had also been used to evaluate the validity of the developed computational model by feeding the moments computed from load cell measurements of the robot into the developed ankle model. Comparison of the simulated and actual ankle motion showed both motion trajectories to be similar in a qualitative sense for the pitch and roll directions, thus suggesting that a non subject specific ankle model can still be used to obtain a reasonable description of the ankle behaviour.

A sensitivity analysis was also carried out on the developed model and it was found that changes in the relaxed lengths of tendons and ligaments appear to have the greatest bearing on the changes in resistive forces and moments encountered at the simulated ankle joint, with the reduction in such parameters causing a greater change in these resistive forces/moments due to the nonlinear tension-length relationships of these elements.

The computational ankle model developed in this research had been utilised in various ways to facilitate the design and implementation of the ankle rehabilitation robot. One such application is in the generation of rehabilitation trajectories. Such a problem had been studied in this research and an optimisation based rehabilitation trajectory generation routine which aims to minimise forces on ligaments/tendons as well as joint reaction moments had been proposed. In this context, the computational ankle model is used as a means for estimating the force and moment quantities considered in the objective function for a particular foot motion trajectory. It was found through simulation that the optimisation approach is capable of generating a trajectory with lower objective function value than the path of minimal distance between the desired start and end points. This suggests that the optimisation based approach can potentially be used to tailor the rehabilitation trajectory according to a patient’s specific condition.

In addition to trajectory generation, the developed ankle model had also been used to facilitate the development of the interaction control scheme used in this research. Apart from its obvious use in controller simulation, it had also been used to provide the ankle stiffness properties for stability analysis of the actuator force controller. Additionally, the ankle stiffness matrices derived from the model were also used to generate a lookup table for the robot impedance adaptation scheme.

11.1.4 MIMO Actuator Force Control

A prerequisite for the implementation of force based impedance control is the availability of force/torque controlled actuators. This, together with the need to regulate the robot vertical force in the redundancy resolution scheme, makes the development of an actuator force controller an essential aspect of this research. Due to the presence of higher order dynamics introduced by compliances in the actuator and force sensor, large force feedback gains will lead to system instability. The disturbance rejection capability of the force controller is therefore also capped by these gain limits, which are generally not uniform for coupled systems. A MIMO actuator force control had been proposed in this research to provide performance gains over independent force control along individual actuators. The proposed controller is capable of partial decoupling of the interactions between actuator forces and currents and was developed based on consideration of the stable gain limits imposed by higher order dynamics along different decoupled directions of the system.

Analyses carried out in this research had shown that motor current applied to one actuator does not exclusively affect the force output of that particular actuator due to the coupling imposed by the parallel mechanism's kinematic constraint and inertia. It was also found that allowable force feedback gain values are dependent on this coupling. More specifically, it was found that when the manipulator inertia matrix is proportional to its damping and stiffness matrices, the interaction between the currents and forces of different actuators can be decoupled and different gain margins are available along different decoupled directions. These gain margins were determined to be dependent on the effective manipulator inertia along that particular decoupled direction. Based on this finding, a MIMO actuator force controller was proposed to allow improved force control performance by applying different force control gains along these decoupled directions. The major advantage that the proposed approach has over independent control of actuator forces (which uses uniform gains) is the application of larger gains along more stable decoupled directions. This can therefore improve force control performance along these decoupled directions and enhance the overall performance of the force controlled system.

As simplified assumptions had been used to establish the gain margins along the different principal directions, a robust stability analysis using structured singular values was carried out by considering the existence of uncertainties in the manipulator inertia, damping and stiffness matrices. This analysis utilised the ankle stiffness obtained from the computational ankle model as the environmental stiffness and it was found that the proposed force controller (with gains determined using gain margins obtained from the simplified analysis) would remain stable throughout a range of end effector orientations provided the actual stiffness/damping matrices are within 10% of their nominal values (in terms of multiplicative uncertainties) and the principal components of the robot inertia tensor is within approximately 5% of their nominal values.

Simulation results had shown that the proposed MIMO force controller does outperform the uniform gain approach in terms of disturbance rejection. Additionally, it had also shown the proposed method to be more capable in improving the backdriveability of the mechanism by producing a more uniform (smaller condition number) effective robot inertia. Experimental results have also shown the MIMO approach to be more stable than the uniform gain approach, even when the highest gain used in the MIMO controller is larger than that of the uniform gain controller.

Performance of the MIMO actuator force controller was also determined to be superior in experiments with significant reduction in force errors (approximately 50%). However, due to the large actuator transmission ratios, a considerable level of friction still exists within the force controlled mechanism, ultimately leading to task space moment errors in the vicinity of 1.5Nm. This error however had been shown to remain relatively constant regardless of the level of desired moment. While the presence of this residual friction moment degrades the accuracy and backdriveability of the robot, it will not lead to serious safety concerns as this level of friction can be easily overcome by the user.

11.1.5 Adaptive Interaction Control

Interaction control is crucial for any rehabilitation robots as it takes into account both force and motion of the robot to facilitate human-robot interaction. While most of the existing ankle rehabilitation devices are capable of some basic form of interaction control, these control schemes are typically non-adaptive. This research therefore aims to enhance the safety and functionality of existing ankle rehabilitation robots through the incorporation of adaptive interaction control schemes. Adaptability was incorporated in this work through two channels, first by adjusting the robot stiffness parameters according to the environmental compliance and second by implementation of an assistance adaptation scheme to vary the assistance provided by the robot according to the user's capability.

A gain scheduled scheme for robot stiffness adjustment had been proposed in this research. This scheme is based on the result obtained in [29] which states that the weighted sum of position error and actuating effort can be minimised by selecting the robot impedance to be proportional to the environmental admittance. Following this rule, the proposed scheme adjusts the robot stiffness by first identifying the ankle compliance with the aid of a lookup table, and then scaling the compliance by a proportionality constant to yield the final robot stiffness. This lookup table is constructed using the computational ankle model and the auxiliary variables used for the gain scheduling are those of the ankle and subtalar joint displacements estimated from the ankle kinematic model parameters provided by the online identification of the biaxial ankle model. By applying this adjustment rule, the robot was able to trade off positional accuracy for lower interaction moments, thus preventing application of large forces/moments at stiff foot configurations.

Simulation results had shown the proposed adjustment scheme to be effective, with large reductions in the cost index for the controller with stiffness adaptation. The efficacy of the stiffness adaptation had also been evaluated through experimental trials. However, although use of the adaptive controller still resulted in a lower cost index than the constant impedance controller, the relative difference was considerably smaller. This is most likely due to discrepancies between the model and actual foot stiffness, as well as to the presence of friction within the mechanism. Even so, the behaviour of the robot with stiffness adjustment showed that larger movements were allowed when the foot is moving in the more compliant supination direction while actuator efforts were reduced in the stiffer pronation direction. This shows that the proposed stiffness adjustment scheme can still be used to produce the general desired behaviour even with mismatched model and actual foot stiffness. Additionally, the results also suggest that the proposed scheme should be used with a feed forward moment to allow greater movements in stiff direction without resorting to increment of the robot stiffness.

An assistance adaptation scheme was also proposed in this research. This control scheme is based on the feed forward force adaptation strategy given in [50] but includes additional modifications designed to improve the robot's performance during constrained and active motion. The central idea of the proposed assistance adaptation scheme is to increase the assistive moments applied to the foot according to the position tracking error in a positively correlated manner up until a certain error threshold, while also reducing the assistance over time. Additionally, the incremental work done by the robot is also monitored and the robot stiffness is adjusted in such a way that it will not act along the reference direction of motion when a negative incremental work with large magnitude is observed. The stability analysis used in [50] was also extended in this work to accommodate the changes made to the error dependency function and the inclusion of the work based stiffness adaptation module. Lastly, the final module of the assistance adaptation scheme operates in a similar way as the feed forward moment adaptation rule, but is instead applied to modify the reference trajectory.

A simulation case study had been carried out on a two degree of freedom point mass moving in a two dimensional potential field. Different scenarios were simulated involving the combination of passive/active and constrained/unconstrained motions. Three error dependency functions (linear, saturated and parabolic) were tested in the adaptation of the feed forward moment in the simulations and it was found that while the alternative approaches (saturated and parabolic) produced slightly poorer tracking accuracy in unconstrained motion, the feed forward forces observed from these alternative approaches during constrained motion were considerably smaller than the rule with linear error dependency. This indicates that these alternative approaches are valuable in preventing large forces from being applied in kinematically constrained directions. The work based stiffness adjustment scheme was also tested in simulation and was found to be particularly useful in reducing the resistance applied by the robot when the user's active effort is driving the robot to locations beyond its reference position. Lastly, simulations involving the trajectory modification module have shown that it is capable of maintaining a low level of feed forward forces during constrained motion, even when a linear error dependency function is used in the feed forward force adaptation law. Results of the simulation study therefore suggests that each of the proposed modification to the basic assistance adaptation scheme can contribute to either improved safety (by reducing forces when large position errors are observed) or to reduce the resistance to constructive active motion.

Similar findings were also obtained from the consideration of experimental data involving the use of the developed ankle rehabilitation robot. In particular, the original assistance adaptation scheme used in [50] was shown to be effective in providing assistance as required to improve the tracking accuracy of the robot. However, it was also found that its use can lead to large moments in stiffer environments, and that utilisation of the alternative error dependency functions in the adaptation rule can help alleviate this issue. Additionally, evaluation of the work based stiffness adjustment module in experimental reaching movements had shown that activation of this control module did indeed reduce the level of resistance provided by the robot, both in terms of smaller negative incremental work and lower resistive moments, when the subject was moving ahead of the reference trajectory. The experimental results therefore confirmed the applicability of the proposed assistance adaptation scheme in rehabilitation.

11.2 Future Work

11.2.1 Design Optimisation and Improvement

One of the main issues compromising the performance of the developed ankle rehabilitation robot is the relatively large actuator friction. Consequently, further development of the ankle rehabilitation robot should involve a re-evaluation of the suitability of existing linear actuators, with an emphasis on decreasing the transmission ratio to reduce the effective frictional forces. However, this must be done in conjunction with the stability analysis of the force controller to ensure that reduction in effective actuator mass does not compromise system stability. An alternative solution is to modify the design of the robot in terms of the robot kinematic parameters, this will lead to changes in singular values of the manipulator Jacobian, which will then propagate to changes in the singular values of the effective robot inertia matrix and hence will ultimately lead to modifications in gain limits of the MIMO actuator force controller. Ideally, a design optimisation problem which takes into account the workspace, singularity, force requirements, force control stability and spatial constraints can be formulated and solved to synthesise the most suitable robot kinematic parameters.

Additionally, since one of the error sources for the kinematic estimation algorithm is believed to be the unmeasured motion between the foot and shank with the ankle rehabilitation robot, improvements can also be made on the foot and shank braces to minimise unwanted motion to allow more accurate measurements of the relative orientation between the user’s foot and shank, and thus allow the applicability of the extended biaxial ankle model to be evaluated in greater detail.

11.2.2 Further Investigation of Kinematic Estimation Algorithm

As discussed previously, results of the kinematic estimation algorithm are influenced by the rather large experimental errors which arise from unmeasured movements of the foot and shank during operation of the ankle rehabilitation robot. While these errors can be reduced through design improvements of the ankle rehabilitation robot, a more complete evaluation of the capability of the algorithm and the suitability of the underlying biaxial ankle kinematic model can only be done in a more controlled environment. Future work can therefore involve the use of cadaveric studies and/or optical tracking based methods to identify the precise six dof motion of the foot bones. Comparison of offline nonlinear system identification techniques and the proposed online algorithm on the more accurate measurements can then be used to establish the true efficacy of the proposed algorithm. Additionally, an online estimation algorithm which takes into account both foot orientation and translation can also be implemented and included in the future study to identify any tradeoffs between simpler model structure and estimation accuracy.

11.2.3 Customisation of Computational Ankle Model

The computational model used in this research was developed based on generic information of muscles, tendons and ligaments. Although the surface geometry of the foot bones used in this research was obtained from CT scans, it is a publicly available data set and was not specific to the subject who participated in the experimental trials. The points of origin and insertion for different ligaments and tendons were also determined in accordance to anatomical resources through visual identification of bony landmarks on the available foot bone surface model. Due to the non-subject specific nature of the computational ankle model, it cannot be expected to be able to accurately replicate the actual foot behaviour. While the “generic” computational model appeared to provide the behaviour required in the adjustment of the robot stiffness parameters in a qualitative sense, a more accurate model will be able to afford a better approximation of the ankle stiffness and thus improve the robot performance. Additionally, a subject specific model will also be important in the generation of rehabilitation trajectory as it will be able to offer a more precise prediction of tensions along the force elements.

Further development of the ankle model presented in this research should therefore include the design of a streamlined process for incorporating patient specific data into the computational model. While it is difficult to ascertain the parameters of muscles, tendons and ligaments in an in vivo manner, information on bone surface geometry and force element attachment points should be more readily accessible through the use of medical imaging techniques. The graphical user interface developed in this research can therefore be extended to facilitate the translation of the medical imaging data into the required origin/insertion point coordinates. The axes of rotations of the biaxial ankle model can also be obtained through either inspection of foot bone geometry or through parameter identification of the subject's ankle. Furthermore, the biaxial ankle model with variable axis tilt angles can also be incorporated into the computational ankle model if it were found to be applicable in the more detailed kinematic investigations.

A more meaningful evaluation of rehabilitation trajectories can also be done once a more subject specific ankle model is established. Even though the tensions along the force elements and joint reaction moments are not directly measurable, the interaction forces between the robot and foot can be used to partially evaluate the effectiveness of the trajectory generation algorithm in an experimental study.

11.2.4 MIMO Actuator Force Control Design

The MIMO actuator force controller developed in this research is based on analysis of a simplified actuator-robot-environment system. As a result, the gains selected from this approach can still be unstable for the actual system if the uncertainties assumed in the robustness analysis are in fact less than what is observed in the real system. This has been observed during simulation of the basic impedance control scheme in Chapter 8. A more complete approach must therefore be used in the design of the MIMO force controller. This can involve the use of constrained optimisation techniques which seek to maximise the controller gains while at the same time ensuring that robust stability is achieved when the full manipulator model is considered. The simplified approach can still be used to obtain a good starting point for the optimisation and the controller can follow a similar structure as that proposed (i.e. parameterised by four gains acting along the principal directions of the coupling matrix) to reduce the dimensionality of the optimisation problem.

In addition to an investigation into the controller optimisation problem, different control structure along each principal direction can also be explored. In other words, alternative filters such as lead-lag controller can be used in place of the PD filter to increase the gain margin along the considered principal direction. This can be done by taking into account the frequency response along different principal directions. Last but not least, application of feed forward friction compensators can also be explored to further improve the actuator force control performance.

11.2.5 Further Investigation of Adaptive Interaction Controller

Further work can also be done on the adaptive interaction control scheme proposed in this research to improve its performance. As the current environment based stiffness adaptation scheme used in this research is reliant on the accuracy of a lookup table which is generated from consideration of the computational ankle model, its performance is dependent on the model accuracy. An alternative method which can be used to bypass the need of the ankle model is the online identification of foot stiffness. This approach can however be challenging due to the real time requirements and the fact that ankle stiffness varies with respect to muscle activation. Consequently, online estimation of passive ankle stiffness will only be feasible if information on both the ankle active stiffness and the leg muscle activation levels are available. Implementation of such an estimation scheme will therefore require the robot to be capable of measuring and processing the electromyography signals of the leg muscles. Additionally, investigations into the relationship between muscle activation and ankle stiffness must also be carried out.

While Lyapunov stability of the feed forward force adaptation rule with work based stiffness adjustment had been established in Chapter 10, the resulting stability conditions are overly conservative due to the consideration of worst case scenarios. Further investigation into the stability of this proposed scheme is therefore required in order to obtain a necessary and sufficient stability condition which can be used as a better guideline to select the parameters in the adaptation rules. Additionally, as stability of the trajectory modification module has yet to be proven, efforts should also be mode into identifying the associated stability criterion so that the reason behind the high frequency oscillations observed in the experiments involving the use of this trajectory modification algorithm can be studied in more detail. Further development can also be made on the work based stiffness adaptation scheme to obtain a smoother transition between the negative work phase (when robot stiffness is reduced along the direction of reference motion) and its complementary phase (when stiffness of the robot is returned to its nominal value) to reduce abrupt changes in the forces being applied to the foot.

Last but not least, further effort should also be placed into identifying the most suitable controller parameters for different rehabilitation exercises, and in the development of a higher level supervisory controller which automatically determines the gains required according to a given type of rehabilitation exercise and information regarding the maximum permissible moments/forces. This is important to enhance the usability of the system for healthcare professionals, who may not be familiar with the significance of different controller parameters.

Appendix A Supplementary Material on Robot Design Analysis

This appendix contains additional information on the design analysis of the ankle rehabilitation robot. This includes the test conditions used to establish the maximum actuator force requirements. Additionally, it also provides a summary of additional results on workspace, singularity and force analysis for three linked designs with different parameters.

A.1 Test Conditions for Force Analysis

As discussed in Chapter 3, the actuator force requirement was computed for different designs based on application of different moments in different end effector configurations. Table A.1 provides a summary of the configuration-moment pairing considered in the force analysis.

Table A.1: Configuration-moment pairings used in force analysis.

End effector orientation in XYZ Euler angles (deg)			Applied moments along the Euler angle axes (Nm)		
θ_x	θ_y	θ_z	τ_x	τ_y	τ_z
0	0	0	±100	±40	∓40
0	0	0	±100	0	0
0	0	0	0	±40	0
0	0	0	0	0	±40
40	20	-30	±100	±40	∓40
-40	-20	30	±100	±40	∓40
40	0	0	±100	0	0
0	20	0	0	±40	0
0	0	30	0	0	±40
-40	0	0	±100	0	0
0	-20	0	0	±40	0
0	0	-30	0	0	±40

Appendix B Supplementary Mathematical Proofs

This appendix provides supporting proofs for some of the mathematical relationships used in the main section of this thesis. The first section of this appendix presents the simplification of the effective inertia matrix found in Chapter 7 while the second section provides the workings required to obtain the relationships used in Chapter 10.

B.1 Simplification of the Effective Inertia Matrix

The coupling between currents and forces of different actuators is presented in Section 7.2. An actuator force control law was therefore proposed to completely decouple this system to improve force control performance. This section presents the working required to arrive at the effective manipulator inertia matrix given in (6.12).

The inverse of the coupling matrix which describes the inter-connection between currents and forces of different actuators can be written as (B.1). By noting that the singular decompositions of the manipulator Jacobian and the manipulator inertia matrix can be respectively represented by (B.2) and (B.3), the inverse of the coupling matrix can be expanded to give (B.4)

$$D^{-1} = I + {K_a}^2 J_{eff} J M^{-1} J^T \tag{B.1}$$

$$J = U_J \begin{bmatrix} \Sigma_J \\ 0_{1\times 3} \end{bmatrix} {V_J}^T \tag{B.2}$$

$$M = U_M \Sigma_M {U_M}^T \tag{B.3}$$

$$D^{-1} = I + m_a U_J \begin{bmatrix} \Sigma_J \\ 0_{1\times 3} \end{bmatrix} {V_J}^T U_M {\Sigma_M}^{-1} {U_M}^T V_J [\Sigma_J \quad 0_{1\times 3}] {U_J}^T \tag{B.4}$$

The decoupling force feedback gain is given in (B.5), with K_f being the feedback gain in the disturbance observer structure and h being the effective scaling applied to the D^{-1} matrix. Substitution of the feedback gain into the effective inertia expression in (6.11) with $m_a = {K_a}^2 J_{eff}$ will then result in (B.6).

$$H = \frac{K_f}{(1 - K_f)} D^{-1} = h D^{-1} \tag{B.5}$$

$$
\begin{aligned}
&M + m_a J^T (I + H)^{-1} J \\
&= M + m_a V_J [\Sigma_J \quad \mathbf{0}] \left[(1+h)I + h m_a \begin{bmatrix} \Sigma_J \\ \mathbf{0} \end{bmatrix} {V_J}^T M^{-1} V_J [\Sigma_J \quad \mathbf{0}] \right]^{-1} \begin{bmatrix} \Sigma_J \\ \mathbf{0} \end{bmatrix} {V_J}^T \\
&= M + m_a V_J [\Sigma_J \quad \mathbf{0}] \begin{bmatrix} (1+h)I + h m_a \Sigma_J {V_J}^T M^{-1} V_J \Sigma_J & \mathbf{0} \\ \mathbf{0} & (1+h) \end{bmatrix}^{-1} \begin{bmatrix} \Sigma_J \\ \mathbf{0} \end{bmatrix} {V_J}^T \\
&= M + m_a V_J \Sigma_J \left[(1+h)I + h m_a \Sigma_J {V_J}^T M^{-1} V_J \Sigma_J \right]^{-1} \Sigma_J {V_J}^T \\
&= M + \left[\tfrac{(1+h)}{m_a} V_J {\Sigma_J}^{-2} {V_J}^T + h M^{-1} \right]^{-1}
\end{aligned} \tag{B.6}
$$

B.2 Supplementary Material for Stability Analysis of the Assistance Adaptation Scheme

B.2.1 Simplification of the $B^T C^+ B$ Matrix

Stability analysis of the assistance adaptation scheme in Section 10.1.4 suggests that the $Q - \frac{1}{4} B^T C^+ B$ matrix should be positive definite to give a bounded Lyapunov candidate function. Greater understanding of the behaviour of the $B^T C^+ B$ term is therefore required to allow establishment of a stability criterion.

The full expressions of the B and C matrices are respectively restated in (B.7) and (B.8), where the regressor matrix Y can be expressed as (B.9) after application of the singular value decomposition operation. Note that $\Sigma_Y = [\Sigma_{Y1} \;\; 0]$, Σ_{Y1} is a diagonal and square matrix.

$$
B = Y^T [\Lambda(I - A_i) \;\; (1 - \varsigma_i) I] \tag{B.7}
$$

$$
C = \frac{1}{\tau k} Y^T (Y Y^T)^{-1} Y \tag{B.8}
$$

$$
Y = U_Y \Sigma_Y {V_Y}^T \tag{B.9}
$$

The regressor matrix in the form shown in (B.9) can then be used to obtain a simplified expression for $Y^T (Y Y^T)^{-1} Y$ as shown in (B.10). This indicates that the matrix C is actually rank deficient. By ignoring the zero singular values in C and only inverting the non zero singular values, the pseudo-inverse of C can be expressed as (B.11).

$$
\begin{aligned}
Y^T (Y Y^T)^{-1} Y &= V_Y {\Sigma_Y}^T {U_Y}^T \left(U_Y {\Sigma_{Y1}}^2 {U_Y}^T \right)^{-1} U_Y \Sigma_Y {V_Y}^T \\
&= V_Y {\Sigma_Y}^T {\Sigma_{Y1}}^{-2} \Sigma_Y {V_Y}^T \\
&= V_Y \begin{bmatrix} I & 0 \\ 0 & 0 \end{bmatrix} {V_Y}^T
\end{aligned} \tag{B.10}
$$

$$C^{+} = \tau k V_Y \begin{bmatrix} I & 0 \\ 0 & 0 \end{bmatrix} {V_Y}^T \tag{B.11}$$

With (B.11) established, the matrix $B^T C^+ B$ can be expanded to give the result shown in (B.12).

$$\begin{aligned} B^T C^+ B &= \begin{bmatrix} \Lambda(I - A_i) \\ (1 - \varsigma_i)I \end{bmatrix} Y C^+ Y^T [\Lambda(I - A_i) \ \ (1 - \varsigma_i)I] \\ &= \tau k \begin{bmatrix} (I - A_i)\Lambda \\ (1 - \varsigma_i)I \end{bmatrix} U_Y \Sigma_Y \begin{bmatrix} I & 0 \\ 0 & 0 \end{bmatrix} \Sigma_Y {U_Y}^T [\Lambda(I - A_i) \ \ (1 - \varsigma_i)I] \\ &= \tau k \begin{bmatrix} (I - A_i)\Lambda \\ (1 - \varsigma_i)I \end{bmatrix} U_Y {\Sigma_{Y1}}^2 {U_Y}^T [\Lambda(I - A_i) \ \ (1 - \varsigma_i)I] \\ &= \tau k \begin{bmatrix} (I - A_i)\Lambda U_Y {\Sigma_{Y1}}^2 {U_Y}^T \Lambda(I - A_i) & (1 - \varsigma_i)(I - A_i)\Lambda U_Y {\Sigma_{Y1}}^2 {U_Y}^T \\ (1 - \varsigma_i) U_Y {\Sigma_{Y1}}^2 {U_Y}^T \Lambda(I - A_i) & (1 - \varsigma_i)^2 U_Y {\Sigma_{Y1}}^2 {U_Y}^T \end{bmatrix} \end{aligned} \tag{B.12}$$

B.2.2 Establishment of Bounds on $\dot{\gamma}$

The incremental work based stiffness adjustment scheme utilises a state variable γ to control the extent to which the robot stiffness along the reference direction of motion is reduced when negative incremental work is being done by the robot. The differential equation governing this state variable is given in (B.13).

$$\dot{\gamma} = c\left[-\frac{\gamma}{\gamma_{max}} + f(w)\right] \tag{B.13}$$

The dynamic behaviour of this state variable can be better understood when considering the quadratic function given in (B.14) and its derivative (B.15). It is clear from (B.15) that (B.16) must hold if the quadratic function V were to remain stationary or decrease over time (i.e. $\dot{V} \leq 0$).

$$V = \frac{1}{2} r \gamma^2 \tag{B.14}$$

$$\begin{aligned} \dot{V} &= r\gamma\dot{\gamma} \\ &= r\gamma c\left[-\frac{\gamma}{\gamma_{max}} + f(w)\right] \end{aligned} \tag{B.15}$$

$$\gamma[\gamma - \gamma_{max} f(w)] \geq 0 \tag{B.16}$$

The condition given in (B.16) states that γ will decrease when $\gamma > \gamma_{max} f(w)$ and increase otherwise. However, by noting that $f(w)$ is by definition lower bounded by zero and upper bounded by unity, the magnitude of γ will remain constant when $f(w)$ is equal to its upper bound and $\gamma = \gamma_{max}$ simultaneously. This means that it is not possible for γ to exceed the value of γ_{max}. Consequently, once γ enters the region between 0 and γ_{max}, it will remain within this region. The inequality shown in (B.17) must therefore be true when $0 < \gamma < \gamma_{max}$.

$$-1 \leq -\frac{\gamma}{\gamma_{max}} + f(w) \leq 1 \tag{B.17}$$

Appendix C Simulation Parameters for MIMO Actuator Force Control

Table C.1 provides a summary of the parameters used in the analysis and simulation of the MIMO actuator force controller.

Table C.1: Parameters used in simulation and analysis of the MIMO Actuator Force Controller.

<table>
<tr><th>Description</th><th>Symbol</th><th>Value/Expression</th><th>Remarks</th></tr>
<tr><td>Motor rotational inertia</td><td>J_m</td><td>4.2×10^{-6} kg m^2</td><td rowspan="15">Parameters used to describe the hardware characteristics throughout the entire Chapter 7</td></tr>
<tr><td>Motor viscous damping</td><td>b_m</td><td>2.6×10^{-6} Nm s/rad</td></tr>
<tr><td>Motor torque constant</td><td>K_t</td><td>0.0365 Nm/A</td></tr>
<tr><td>Belt stiffness</td><td>k_b</td><td>1×10^{6} N/m</td></tr>
<tr><td>Belt viscous damping</td><td>b_b</td><td>5 N s/m</td></tr>
<tr><td>Motor pulley radius</td><td>r_m</td><td>0.004 m</td></tr>
<tr><td>Ball screw rotational inertia</td><td>J_s</td><td>1.15×10^{-6} kg m^2</td></tr>
<tr><td>Ball screw viscous damping</td><td>b_s</td><td>1×10^{-6} Nm s/rad</td></tr>
<tr><td>Ball screw pulley radius</td><td>r_s</td><td>0.02 m</td></tr>
<tr><td>Ball screw transmission ratio</td><td>G_s</td><td>$\frac{2\pi}{0.003175}$ rad/m</td></tr>
<tr><td>Actuator rod mass</td><td>m_r</td><td>0.2 kg</td></tr>
<tr><td>Actuator rod viscous damping</td><td>b_r</td><td>0.05 N s/m</td></tr>
<tr><td>Force sensor mass</td><td>m_f</td><td>0.2 kg</td></tr>
<tr><td>Force sensor stiffness</td><td>k_f</td><td>15×10^{6} N/m</td></tr>
<tr><td>Force sensor damping</td><td>b_f</td><td>2500 N s/m</td></tr>
<tr><td>Derivative gain</td><td>K_d</td><td>0.002 s</td><td rowspan="2">Parameters used in the discretised PD controller</td></tr>
<tr><td>Sampling time</td><td>T</td><td>0.00075 s</td></tr>
<tr><td>Environmental inertia matrix at neutral position</td><td>M_{e0}</td><td>$\begin{bmatrix} 0.047 & 0 & 0 \\ 0 & 0.045 & 0 \\ 0 & 0 & 0.04 \end{bmatrix}$ kg m^2</td><td>-</td></tr>
<tr><td rowspan="2">Environmental damping matrix</td><td rowspan="2">B_e</td><td>$0.1I_{3\times3}$ Nm s/rad</td><td>For analysis in Section 7.4.2</td></tr>
<tr><td>$0.1I_{3\times3} + 0.005K_{ankle}$ Nm s/rad</td><td>For analysis in Section 7.5</td></tr>
<tr><td rowspan="2">Environmental stiffness matrix</td><td rowspan="2">K_e</td><td>$10I_{3\times3}$ Nm/rad</td><td>For analysis in Section 7.4.2</td></tr>
<tr><td>K_{ankle} Nm/rad</td><td>For analysis in Section 7.5</td></tr>
<tr><td rowspan="2">Gain matrix in simulation</td><td rowspan="2">K</td><td>$[U_m{}' \;\; v_0]diag(5 \;\; 5 \;\; 5 \;\; 5)[U_m{}' \;\; v_0]^T$</td><td>For simulation of uniform gain controller</td></tr>
<tr><td>$[U_m{}' \;\; v_0]diag(5 \;\; 15 \;\; 45 \;\; 7)[U_m{}' \;\; v_0]^T$</td><td>For simulation of the proposed MIMO actuator force controller</td></tr>
</table>

Appendix D Simulation Parameters and Results for Assistance Adaptation Scheme

This appendix provides the parameters used in the simulated case study conducted in Chapter 10 to evaluate the efficacy of the different assistance adaptation scheme. Additionally, the simulation results and performance measures obtained from the passive-unconstrained, passive-constrained, active-unconstrained and active-constrained motion trials are also presented.

D.1 Simulation Parameters

Table D.1: Parameters used in the simulation case study for the proposed assistance adaptation scheme.

Description	Symbol	Value
Rotational offset of environmental coordinates from robot/global coordinates	Φ	$\frac{\pi}{4}$ rad
Stiffness along negative x-axis of environment coordinates	k_1	110 N/m
Stiffness along positive x-axis of environment coordinates	k_2	110 N/m
Stiffness along negative y-axis of environment coordinates	k_3	25 N/m
Stiffness along positive y-axis of environment coordinates	k_4	25 N/m
Zero potential boundary in negative x-direction of the environment coordinates	u_{01}	-0.1 m
Zero potential boundary in positive x-direction of the environment coordinates	u_{02}	0.1 m
Zero potential boundary in negative y-direction of the environment coordinates	u_{03}	-0.1 m
Zero potential boundary in positive y-direction of the environment coordinates	u_{04}	0.1 m
End effector mass	m	1 kg
Environmental viscous damping	b_{env}	5 N s/m
Radius of circular reference trajectory	r_{ref}	0.7 m
Minor radius of elliptic kinematic constraint	l_a	0.2 m
Major radius of elliptic kinematic constraint	l_b	0.8 m
Rotational offset of semi-minor axis from positive x-axis of global frame	φ	$\frac{\pi}{4}$ rad
Stiffness of constraint boundary	k_{con}	1×10^6 N/m
Damping of constraint boundary	b_{con}	1000 N s/m

D.2 Simulation Results for Passive Unconstrained Motion

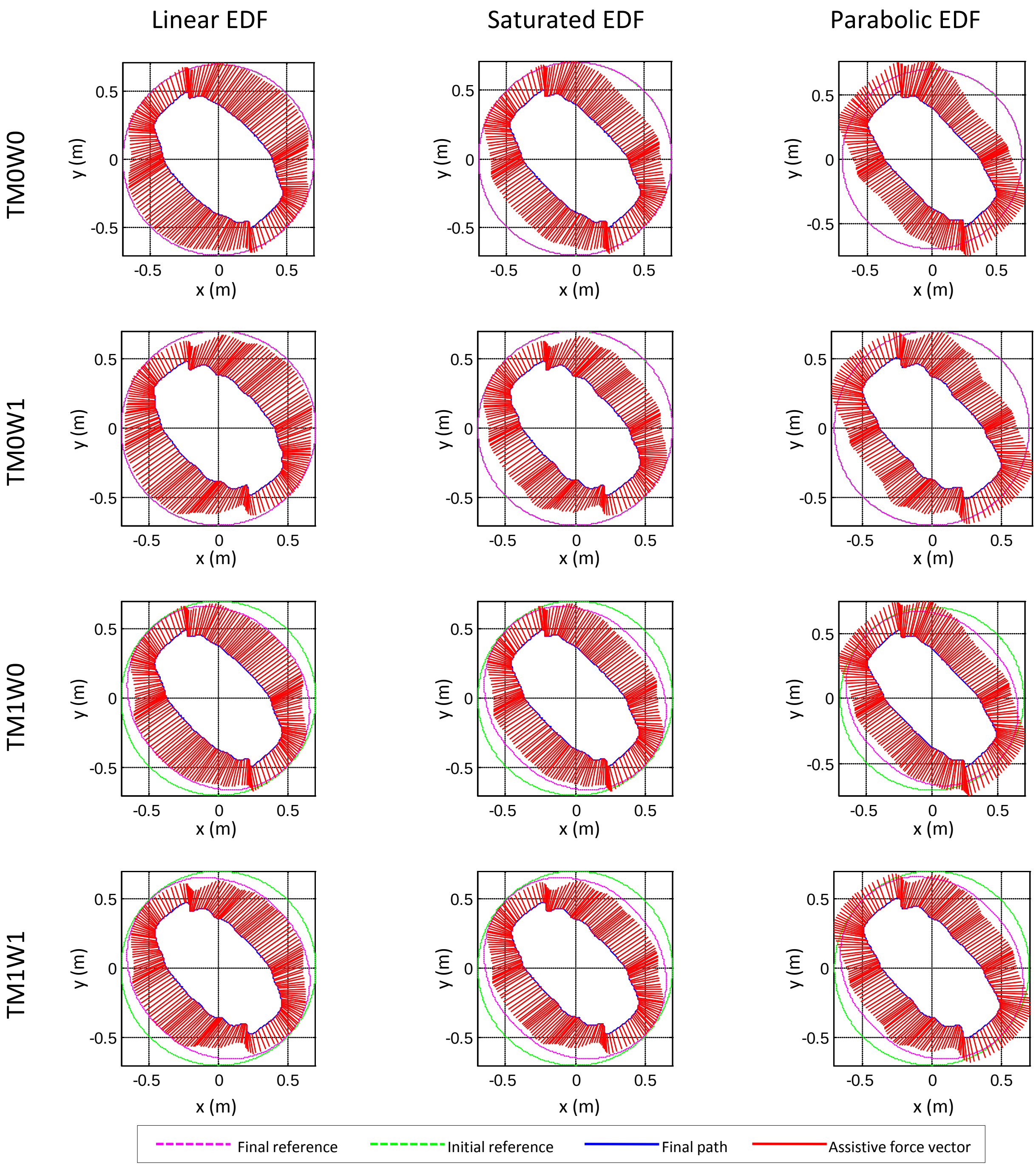

Figure D.11.1: Feed forward forces in the final motion cycle (red vectors), original reference trajectory (green dashed lines), final reference trajectory (magenta dashed lines) and final actual path (blue lines) for passive unconstrained motion trials. TM is the flag used to denote activation of the trajectory modification module and W is the flag used to indicate activation of the work based stiffness adjustment module.

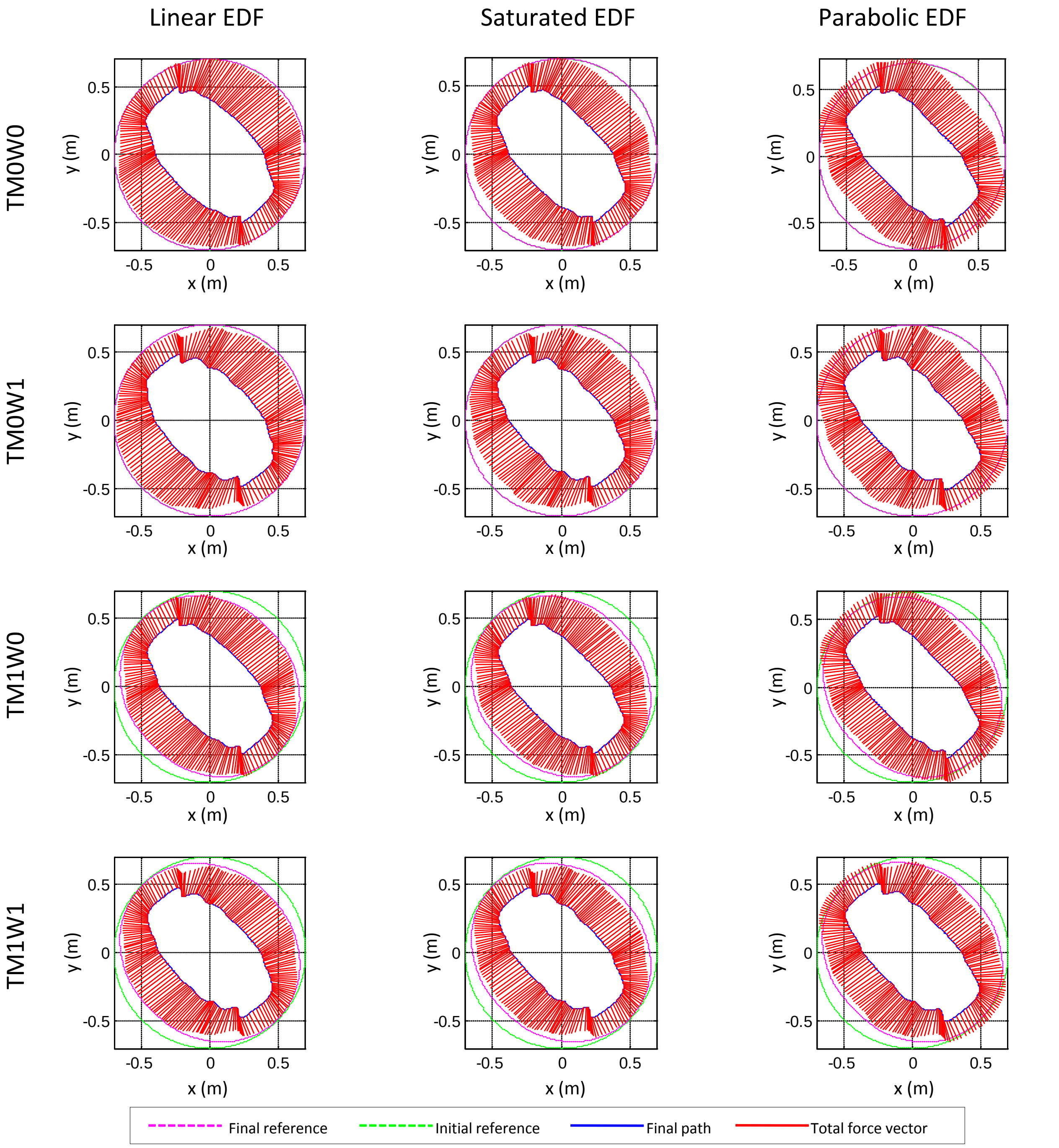

Figure D.11.2: Total driving forces in the final motion cycle (red vectors), original reference trajectory (green dashed lines), final reference trajectory (magenta dashed lines) and final actual path (blue lines) for passive unconstrained motion trials. TM is the flag used to denote activation of the trajectory modification module and W is the flag used to indicate activation of the work based stiffness adjustment module.

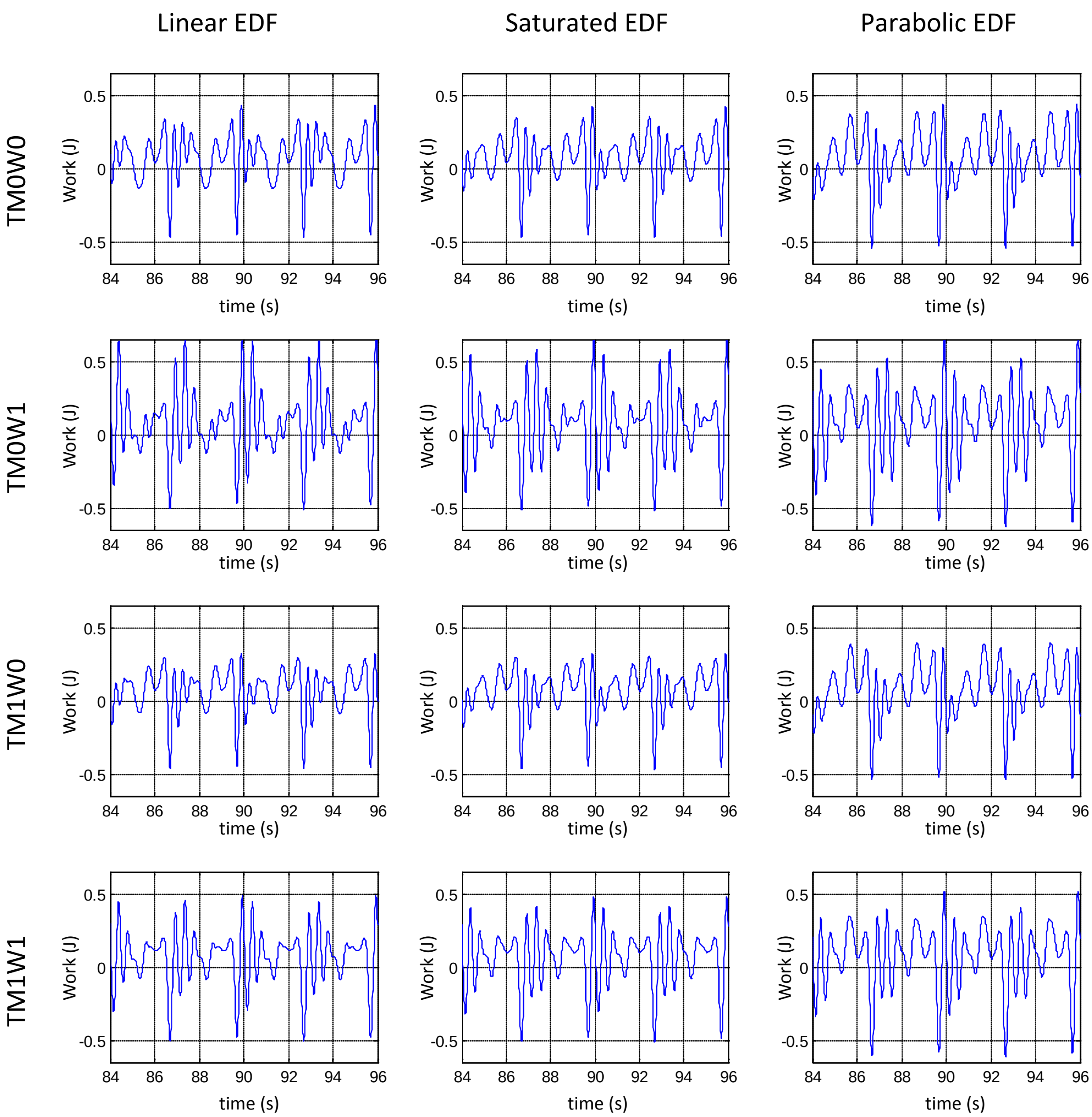

Figure D.11.3: Incremental work done by the robot in the final cycle of passive unconstrained motion trials. TM is the flag used to denote activation of the trajectory modification module and W is the flag used to indicate activation of the work based stiffness adjustment module.

D.3 Simulation Results for Passive Constrained Motion

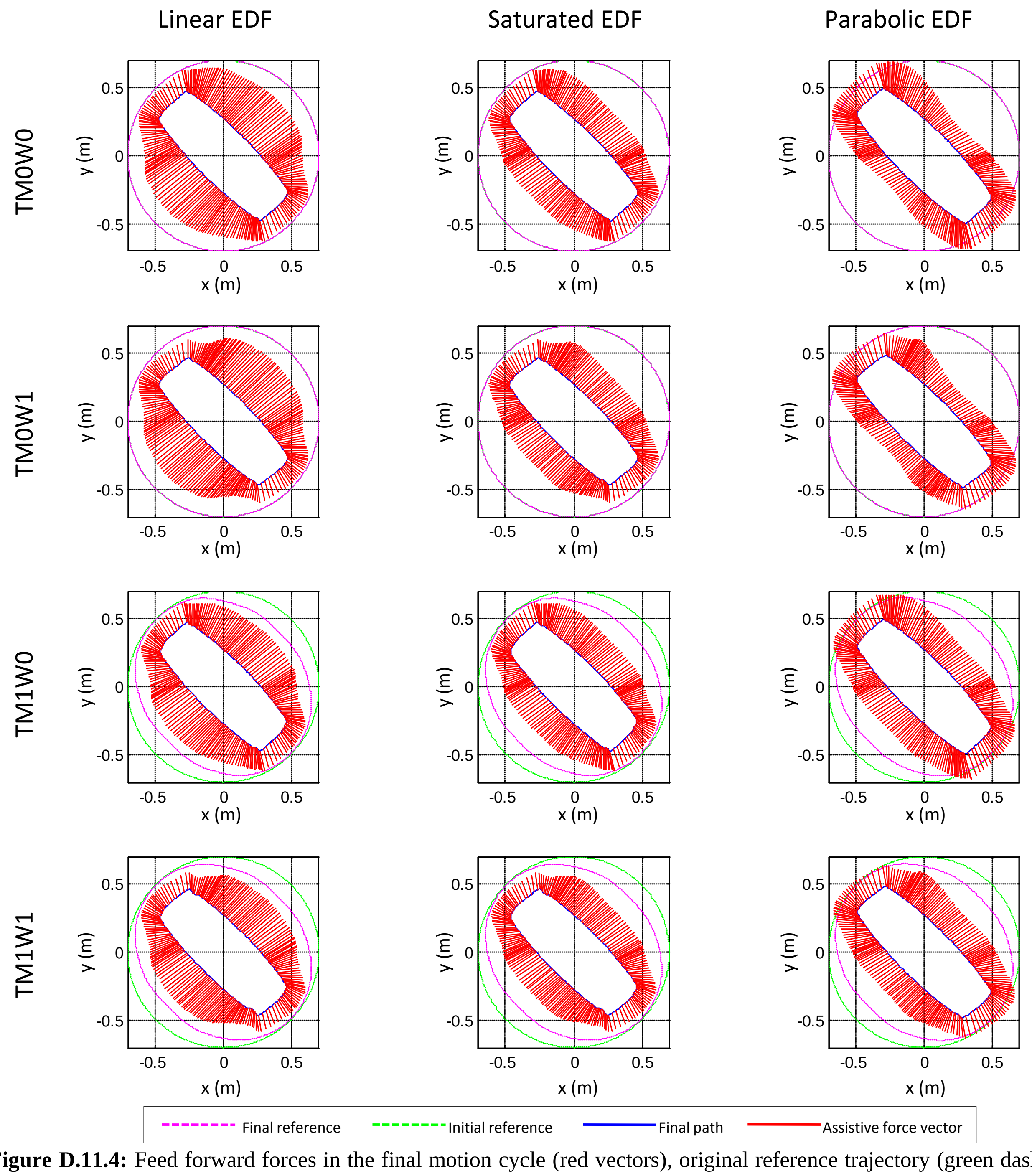

Figure D.11.4: Feed forward forces in the final motion cycle (red vectors), original reference trajectory (green dashed lines), final reference trajectory (magenta dashed lines) and final actual path (blue lines) for passive constrained motion trials. TM is the flag used to denote activation of the trajectory modification module and W is the flag used to indicate activation of the work based stiffness adjustment module.

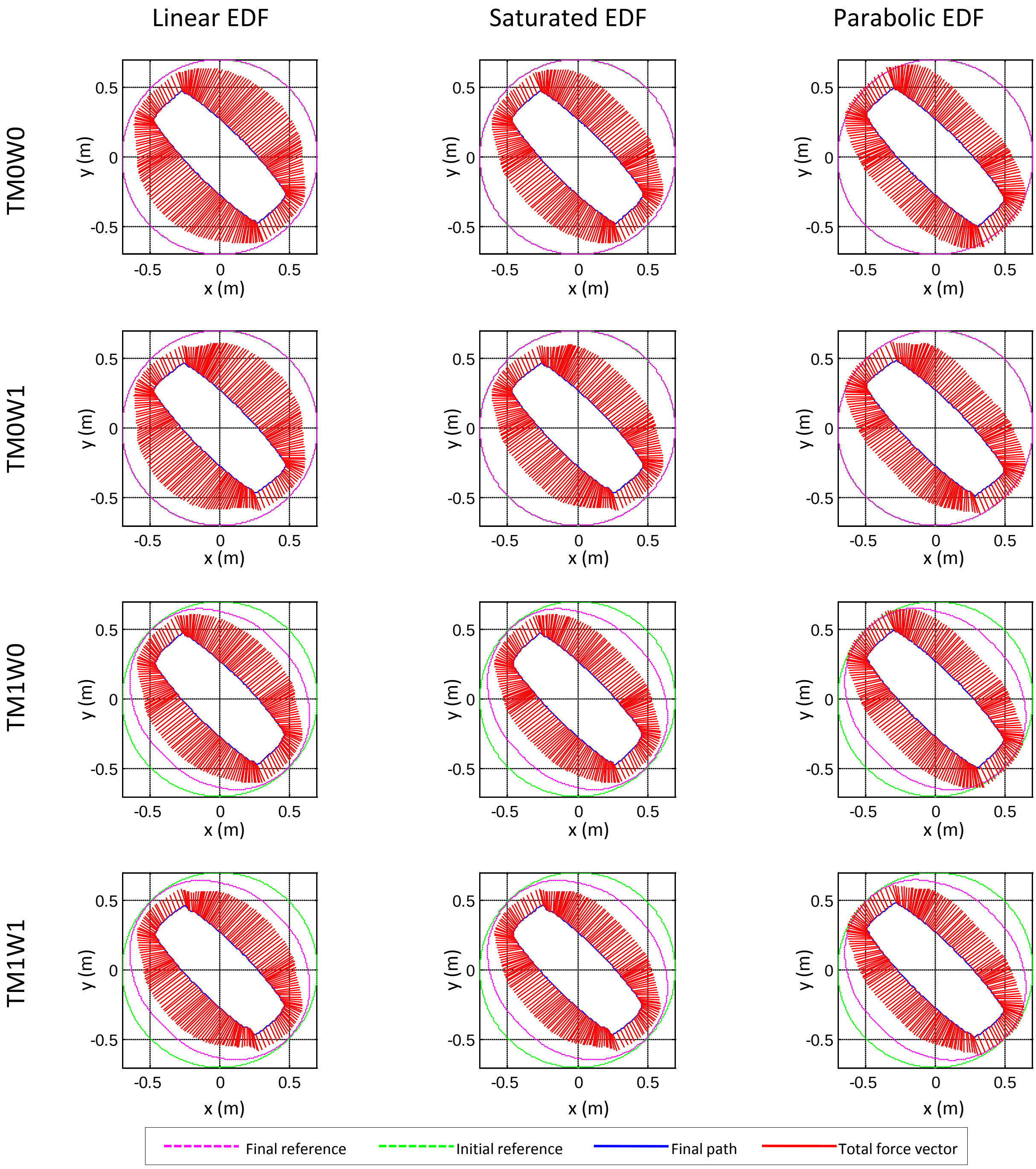

Figure D.11.5: Total driving forces in the final motion cycle (red vectors), original reference trajectory (green dashed lines), final reference trajectory (magenta dashed lines) and final actual path (blue lines) for passive constrained motion trials. TM is the flag used to denote activation of the trajectory modification module and W is the flag used to indicate activation of the work based stiffness adjustment module.

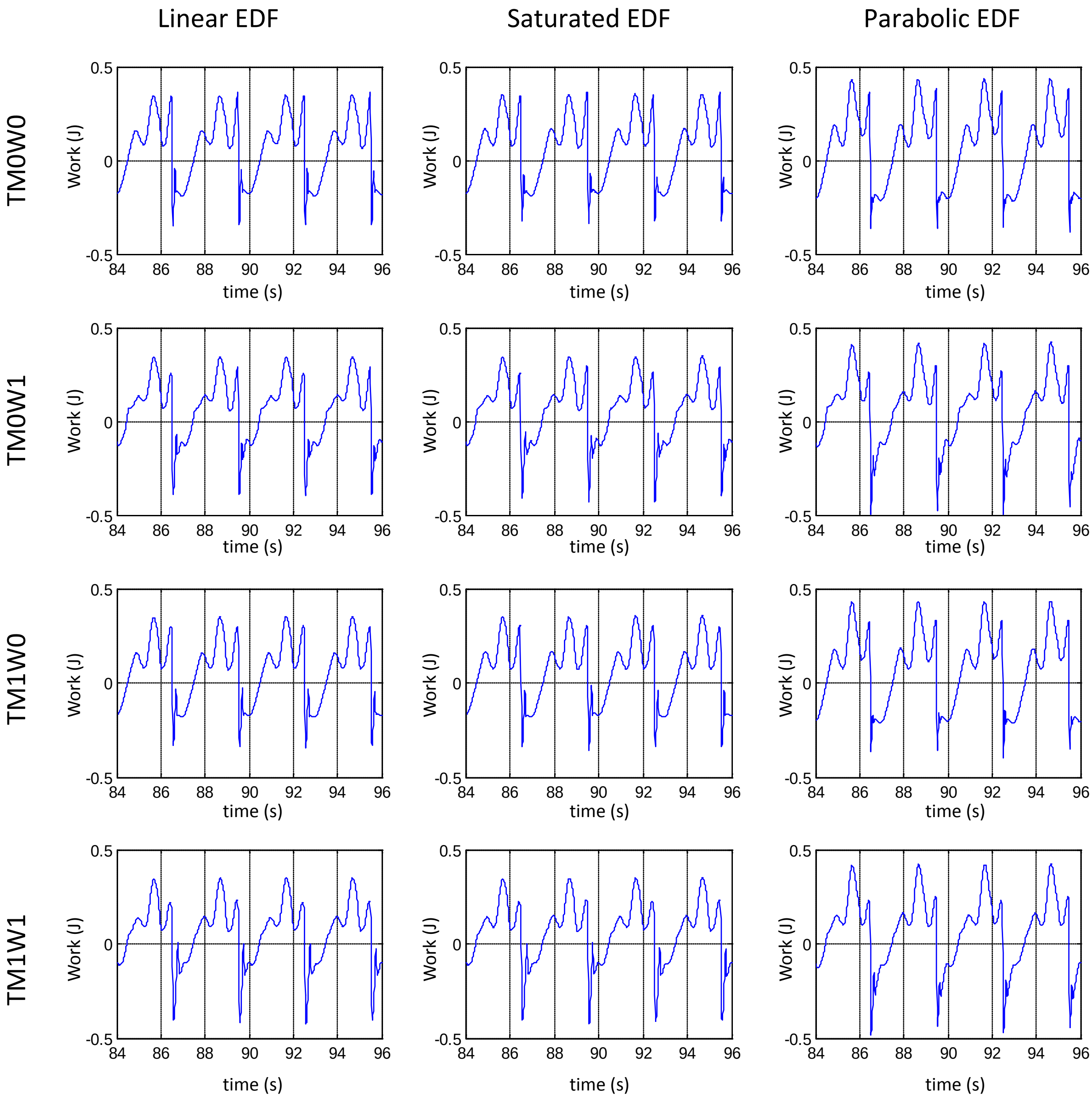

Figure D.11.6: Incremental work done by the robot in the final cycle of passive constrained motion trials. TM is the flag used to denote activation of the trajectory modification module and W is the flag used to indicate activation of the work based stiffness adjustment module.

D.4 Simulation Results for Active Unconstrained Motion

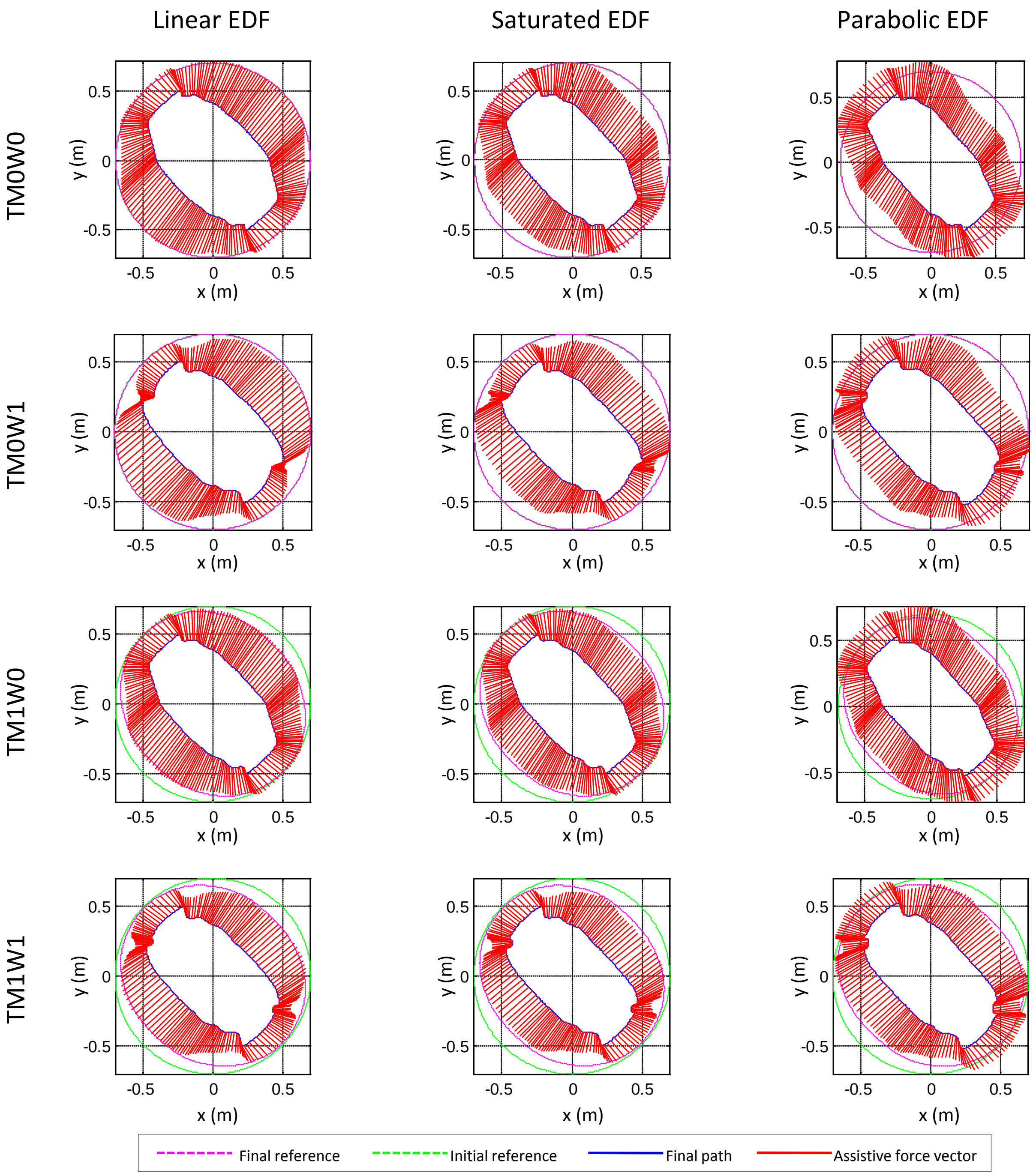

Figure D.11.7: Feed forward forces in the final motion cycle (red vectors), original reference trajectory (green dashed lines), final reference trajectory (magenta dashed lines) and final actual path (blue lines) for active unconstrained motion trials. TM is the flag used to denote activation of the trajectory modification module and W is the flag used to indicate activation of the work based stiffness adjustment module.

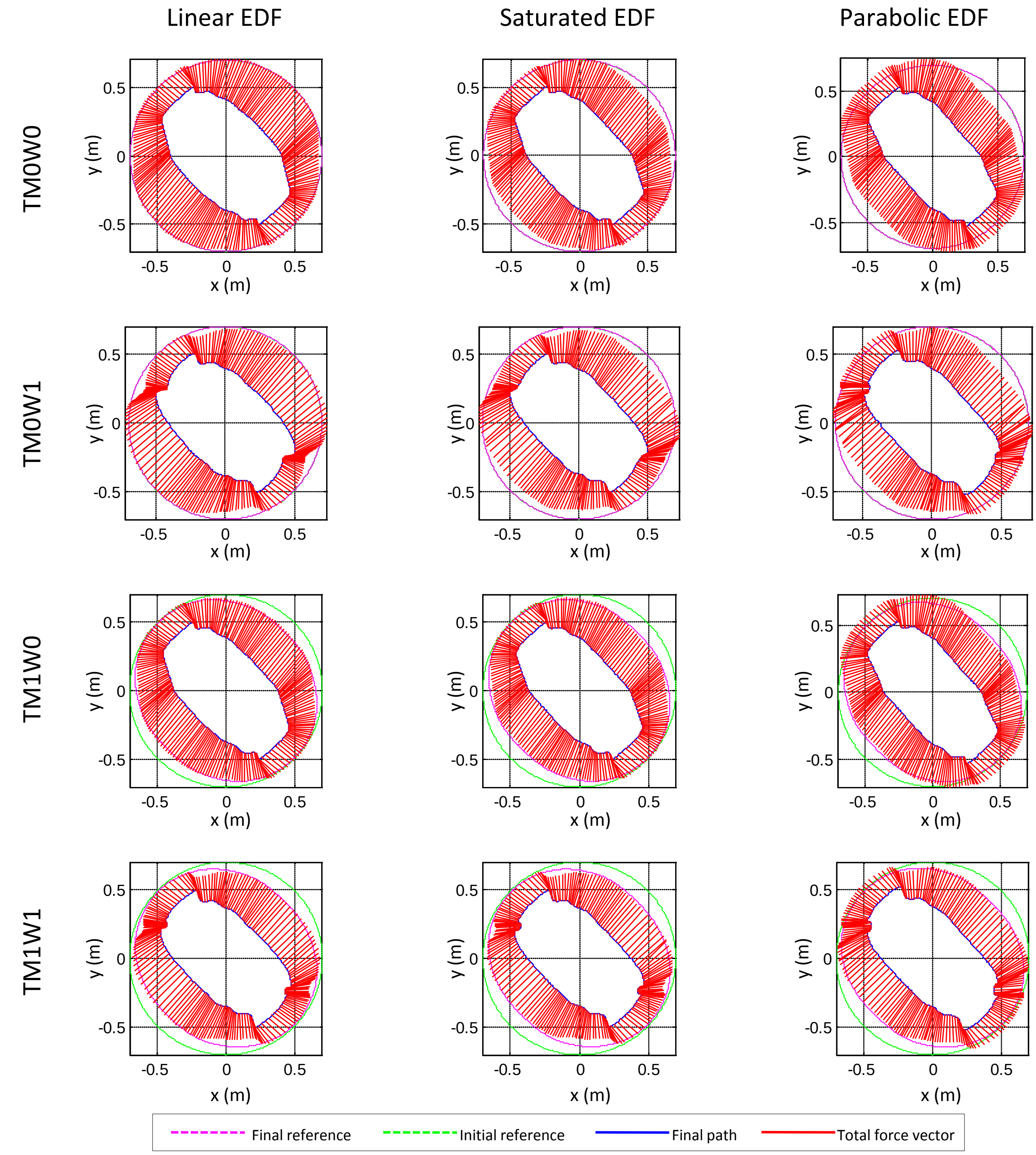

Figure D.11.8: Total driving forces in the final motion cycle (red vectors), original reference trajectory (green dashed lines), final reference trajectory (magenta dashed lines) and final actual path (blue lines) for active unconstrained motion trials. TM is the flag used to denote activation of the trajectory modification module and W is the flag used to indicate activation of the work based stiffness adjustment module.

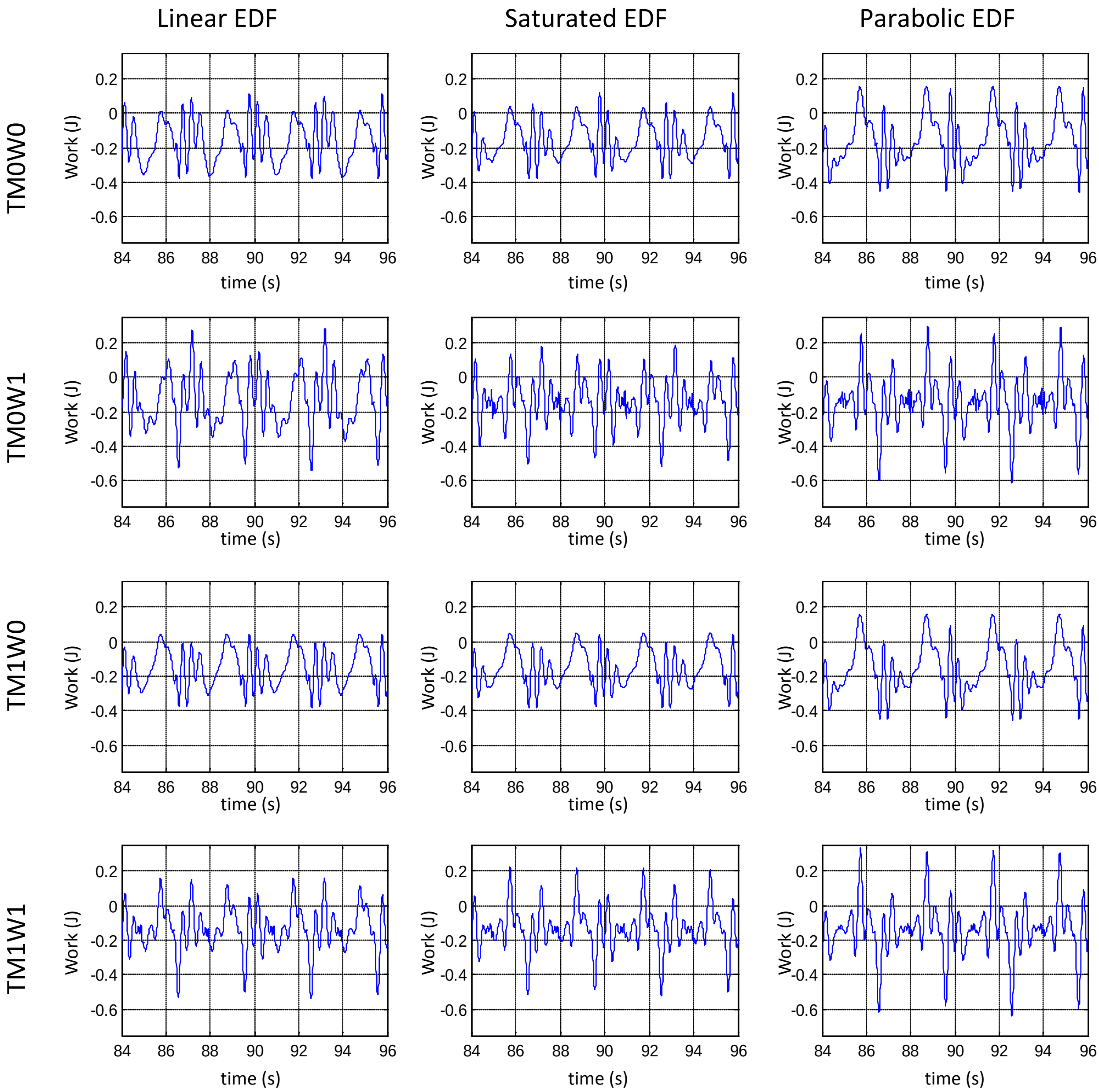

Figure D.11.9: Incremental work done by the robot in the final cycle of active unconstrained motion trials. TM is the flag used to denote activation of the trajectory modification module and W is the flag used to indicate activation of the work based stiffness adjustment module.

D.5 Simulation Results for Active Constrained Motion

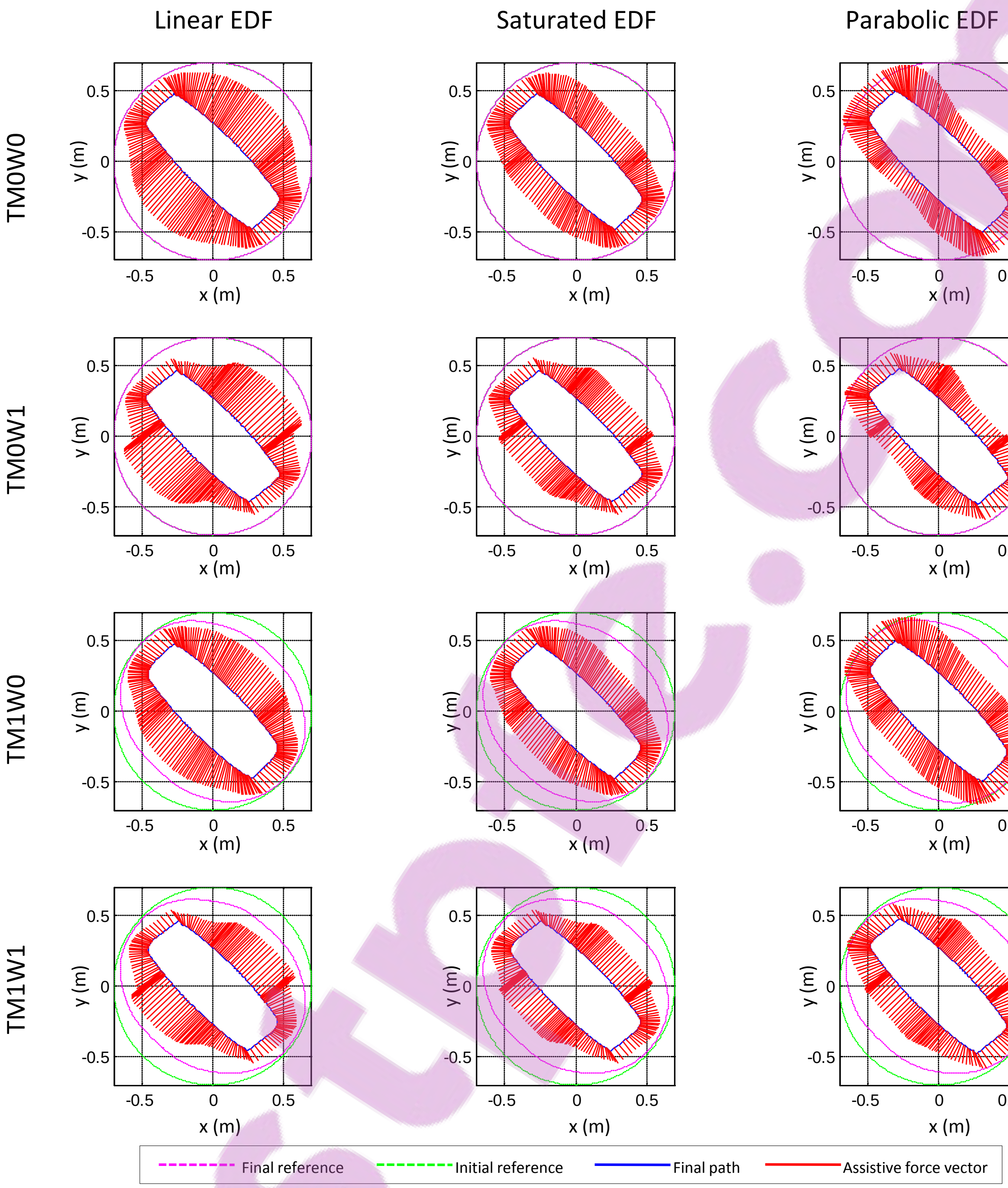

Figure D.11.10: Feed forward forces in the final motion cycle (red vectors), original reference trajectory (green dashed lines), final reference trajectory (magenta dashed lines) and actual path (blue lines) for active constrained motion trials. TM is the flag used to denote activation of the trajectory modification module and W is the flag used to indicate activation of the work based stiffness adjustment module.

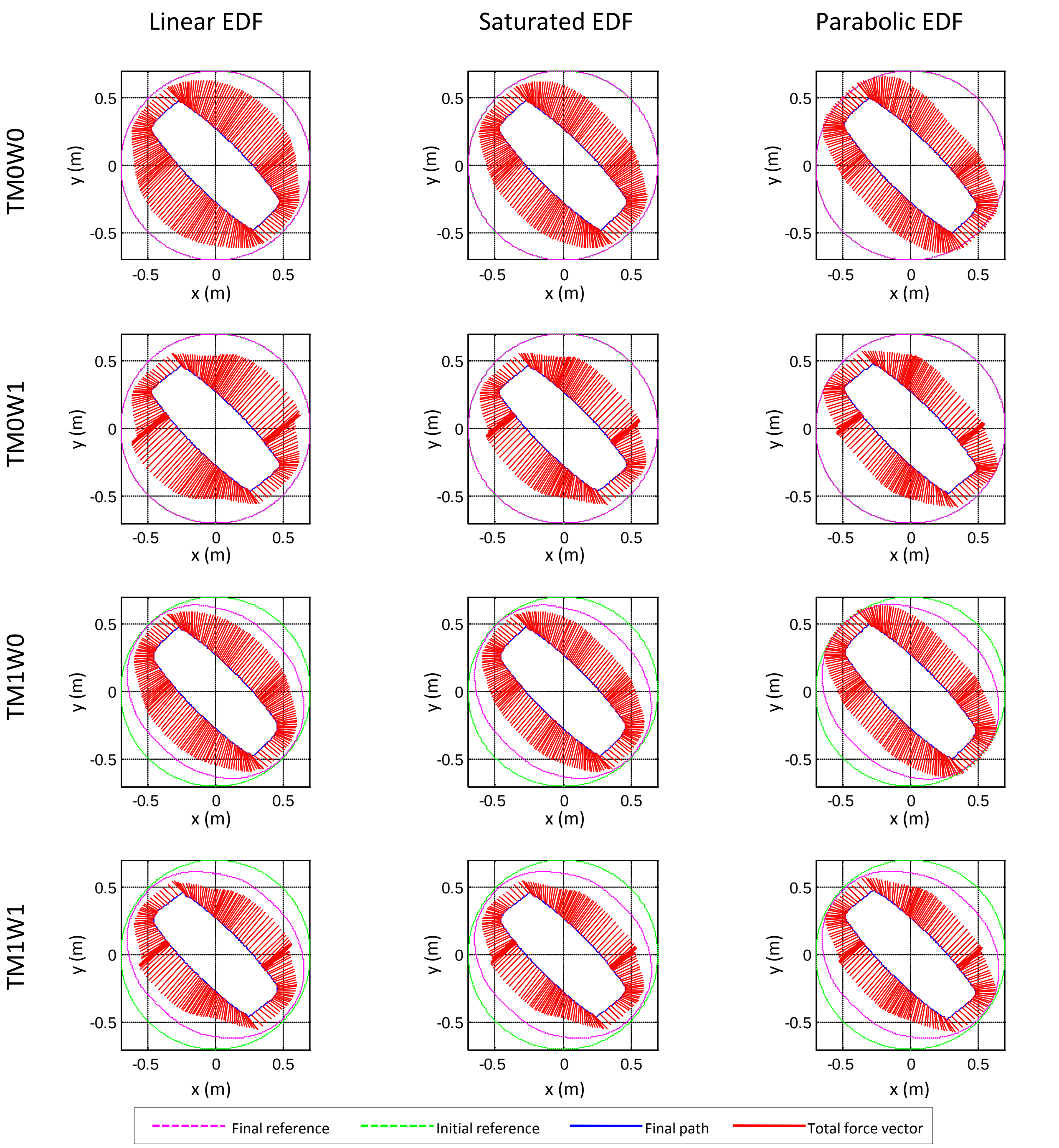

Figure D.11.11: Total driving forces in the final motion cycle (red vectors), original reference trajectory (green dashed lines), final reference trajectory (magenta dashed lines) and final actual path (blue lines) for active constrained motion trials. TM is the flag used to denote activation of the trajectory modification module and W is the flag used to indicate activation of the work based stiffness adjustment module.

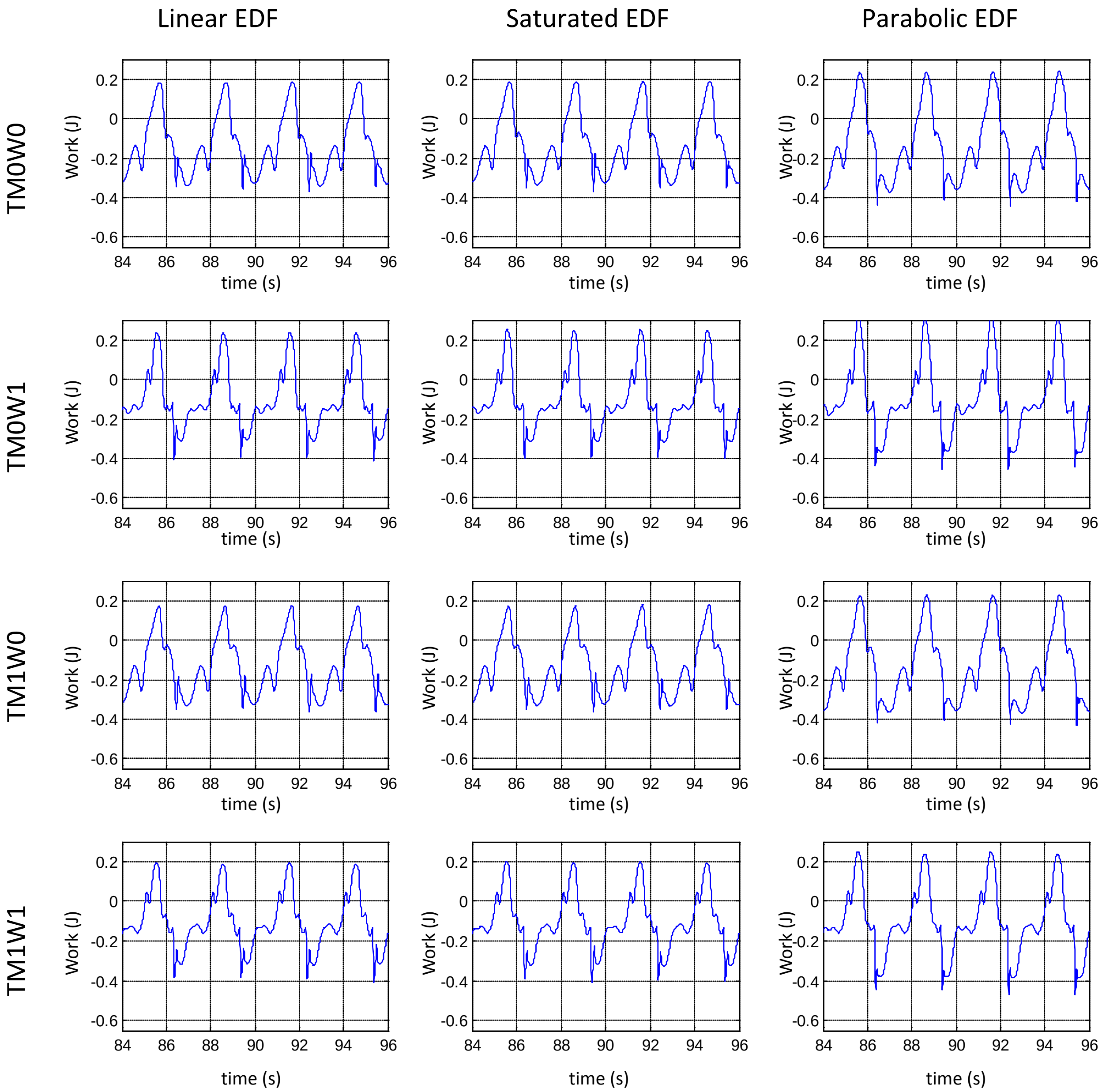

Figure D.11.12: Incremental work done by the robot in the final cycle of active constrained motion trials. TM is the flag used to denote activation of the trajectory modification module and W is the flag used to indicate activation of the work based stiffness adjustment module.

D.6 Summary of Performance Cost Index

Table D.2: Performance cost indices of motion trials in the simulation case study prior to normalisation.

Performance measure	Mode	Passive Unconstrained			Passive Constrained			Active Unconstrained			Active Constrained		
		M1	M2	M3	M1	M2	M3	M1	M2	M3	M1	M2	M3
j_x	TM0W0	0.4534	0.4470	0.4623	0.4140	0.4143	0.4340	0.4562	0.4503	0.4629	0.4159	0.4162	0.4337
	TM0W1	0.4489	0.4414	0.4522	0.4081	0.4084	0.4229	0.4631	0.4643	0.4742	0.4009	0.4013	0.4110
	TM1W0	0.4313	0.4289	0.4509	0.4072	0.4073	0.4291	0.4364	0.4343	0.4521	0.4110	0.4110	0.4293
	TM1W1	0.4228	0.4201	0.4378	0.3976	0.3977	0.414	0.4434	0.4417	0.4550	0.3910	0.3913	0.4029
j_f	TM0W0	35.566	33.284	33.134	43.066	36.623	34.435	35.63	33.584	33.604	43.23	36.833	34.641
	TM0W1	34.79	32.77	32.742	42.328	35.822	33.425	31.878	30.798	31.026	41.942	35.51	33.054
	TM1W0	29.737	28.78	29.898	32.101	30.176	31.192	29.794	29.004	30.172	32.222	30.339	31.331
	TM1W1	29.135	28.243	29.252	31.636	29.699	30.583	26.85	26.418	27.771	30.935	29.164	30.038
j_e	TM0W0	0.2835	0.2944	0.2913	0.3541	0.3541	0.3485	0.2843	0.2939	0.2898	0.3553	0.3553	0.3493
	TM0W1	0.2880	0.2980	0.2952	0.3563	0.3562	0.3517	0.3224	0.3264	0.3224	0.3764	0.3760	0.3722
	TM1W0	0.2538	0.2561	0.2465	0.2804	0.2803	0.2737	0.2545	0.2564	0.2465	0.2815	0.2815	0.2746
	TM1W1	0.2573	0.2596	0.2511	0.2833	0.2833	0.2781	0.2831	0.2849	0.2759	0.3057	0.3054	0.3008
j_w	TM0W0	0.0385	0.0334	0.0429	0.0465	0.0468	0.0570	0.1622	0.1583	0.1692	0.1555	0.1550	0.1656
	TM0W1	0.0489	0.0549	0.0643	0.0425	0.0426	0.0514	0.1531	0.1466	0.1541	0.1346	0.1346	0.1410
	TM1W0	0.0326	0.0360	0.0489	0.0454	0.0457	0.0570	0.1501	0.1487	0.1624	0.1489	0.1483	0.1606
	TM1W1	0.0399	0.0429	0.0525	0.0421	0.0422	0.0520	0.1371	0.1362	0.1434	0.1227	0.1224	0.1296

Table D.3: Performance cost indices of motion trials in the simulation case study after normalisation.

Performance measure	Mode	Passive Unconstrained			Passive Constrained			Active Unconstrained			Active Constrained		
		M1	M2	M3	M1	M2	M3	M1	M2	M3	M1	M2	M3
j_x	TM0W0	0.9807	0.9669	1.0000	0.9539	0.9546	1.0000	0.9621	0.9496	0.9760	0.9590	0.9596	1.0000
	TM0W1	0.9711	0.9549	0.9781	0.9402	0.9410	0.9743	0.9766	0.9790	1.0000	0.9243	0.9254	0.9477
	TM1W0	0.9330	0.9276	0.9753	0.9381	0.9385	0.9886	0.9203	0.9159	0.9534	0.9477	0.9476	0.9899
	TM1W1	0.9146	0.9087	0.9469	0.9161	0.9163	0.9537	0.9349	0.9314	0.9596	0.9017	0.9023	0.9289
j_f	TM0W0	1.0000	0.9358	0.9316	1.0000	0.8504	0.7996	1.0000	0.9426	0.9432	1.0000	0.8520	0.8013
	TM0W1	0.9782	0.9214	0.9206	0.9829	0.8318	0.7761	0.8947	0.8644	0.8708	0.9702	0.8214	0.7646
	TM1W0	0.8361	0.8092	0.8406	0.7454	0.7007	0.7243	0.8362	0.8140	0.8468	0.7454	0.7018	0.7248
	TM1W1	0.8192	0.7941	0.8225	0.7346	0.6896	0.7101	0.7536	0.7415	0.7794	0.7156	0.6746	0.6948
j_e	TM0W0	0.9512	0.9878	0.9774	0.9941	0.9940	0.9783	0.8710	0.9006	0.8879	0.9440	0.9440	0.9281
	TM0W1	0.9663	1.0000	0.9905	1.0000	0.9999	0.9873	0.9878	1.0000	0.9879	1.0000	0.9991	0.9889
	TM1W0	0.8516	0.8595	0.8271	0.7871	0.7869	0.7684	0.7800	0.7856	0.7553	0.7480	0.7480	0.7297
	TM1W1	0.8635	0.8710	0.8424	0.7953	0.7952	0.7807	0.8676	0.8731	0.8455	0.8123	0.8114	0.7992
j_w	TM0W0	0.5992	0.5190	0.6667	0.8158	0.8213	1.0000	0.9586	0.9358	1.0000	0.9390	0.9358	1.0000
	TM0W1	0.7598	0.8541	1.0000	0.7468	0.7479	0.9026	0.9049	0.8667	0.9110	0.8128	0.8128	0.8513
	TM1W0	0.5069	0.5604	0.7611	0.7973	0.8024	0.9995	0.8871	0.8792	0.9600	0.8994	0.8956	0.9698
	TM1W1	0.6214	0.6670	0.8171	0.7390	0.7406	0.9122	0.8107	0.8049	0.8477	0.7412	0.7394	0.7828

References

[1] N. Tejima, "Rehabilitation robotics: a review," *Advanced Robotics*, vol. 14, pp. 551-564, 2000.

[2] H. I. Krebs, J. J. Palazzolo, L. Dipietro, M. Ferraro, J. Krol, K. Rannekleiv, B. T. Volpe, and N. Hogan, "Rehabilitation robotics: Performance-based progressive robot-assisted therapy," *Autonomous Robots*, vol. 15, pp. 7-20, 2003.

[3] S. Hesse, H. Schmidt, C. Werner, and A. Bardeleben, "Upper and lower extremity robotic devices for rehabilitation and for studying motor control," *Current Opinion in Neurology*, vol. 16, pp. 705-710, 2003.

[4] J. Hertel, "Functional anatomy, pathomechanics, and pathophysiology of lateral ankle instability," *Journal of Athletic Training*, vol. 37, pp. 364-375, 2002.

[5] W. S. Harwin, T. Rahman, and R. A. Foulds, "A review of design issues in rehabilitation robotics with reference to North American research," *IEEE Transactions on Rehabilitation Engineering*, vol. 3, pp. 3-13, 1995.

[6] H. I. Krebs, B. T. Volpe, M. L. Aisen, W. Hening, A. Adamovich, H. Poizner, K. Subrahmanyan, and N. Hogan, "Robotic applications in neuromotor rehabilitation," *Robotica*, vol. 21, pp. 3-11, 2003.

[7] H. I. Krebs, B. T. Volpe, M. L. Aisen, and N. Hogan, "Increasing productivity and quality of care: Robot-aided neuro-rehabilitation," *Journal of Rehabilitation Research and Development*, vol. 37, pp. 639-652, 2000.

[8] R. Riener, M. Frey, M. Bernhardt, T. Nef, and G. Colombo, "Human-centered rehabilitation robotics," in *IEEE International Conference on Rehabilitation Robotics*, 2005, pp. 319-322.

[9] M. Girone, G. Burdea, M. Bouzit, V. Popescu, and J. E. Deutsch, "Stewart platform-based system for ankle telerehabilitation," *Autonomous Robots*, vol. 10, pp. 203-212, 2001.

[10] J. A. Saglia, N. G. Tsagarakis, J. S. Dai, and D. G. Caldwell, "Control strategies for ankle rehabilitation using a high performance ankle exerciser," in *IEEE International Conference on Robotics and Automation*, 2010, pp. 2221-2227.

[11] A. Duschau-Wicke, J. Von Zitzewitz, A. Caprez, L. Lunenburger, and R. Riener, "Path control: A method for patient-cooperative robot-aided gait rehabilitation," *IEEE Transactions on Neural Systems and Rehabilitation Engineering*, vol. 18, pp. 38-48, 2010.

[12] A. Roy, H. I. Krebs, S. L. Patterson, T. N. Judkins, I. K. Larry, R. M. Macko, and N. Hogan, "Measurement of human ankle stiffness using the anklebot," in *International Conference on Rehabilitation Robotics*, 2007, pp. 356-363.

[13] H. Vallery, A. Duschau-Wicke, and R. Riener, "Generalized elasticities improve patient-cooperative control of rehabilitation robots," in *2009 IEEE International Conference on Rehabilitation Robotics, ICORR 2009,* 2009, pp. 535-541.

[14] L. Marchal-Crespo and D. J. Reinkensmeyer, "Review of control strategies for robotic movement training after neurologic injury," *Journal of NeuroEngineering and Rehabilitation,* vol. 6, 2009.

[15] T. Nef, M. Mihelj, and R. Riener, "ARMin: a robot for patient-cooperative arm therapy," *Medical and Biological Engineering and Computing,* vol. 45, pp. 887-900, 2007.

[16] J. E. Deutsch, J. Latonio, G. Burdea, and R. Boian, "Post-stroke rehabilitation with the Rutgers Ankle System: A case study," *Presence,* vol. 10, pp. 416-430, 2001.

[17] D. J. Reinkensmeyer, J. L. Emken, and S. C. Cramer, "Robotics, motor learning, and neurologic recovery," *Annual Review of Biomedical Engineering,* vol. 6, pp. 497-525, 2004.

[18] H. I. Krebs, D. Williams, J. Celestino, S. K. Charles, D. Lynch, and N. Hogan, "Robot-aided neurorehabilitation: A robot for wrist rehabilitation," *IEEE Transactions on Neural Systems and Rehabilitation Engineering,* vol. 15, pp. 327-335, 2007.

[19] Hocoma. http://www.hocoma.com/en/products/lokomat/

[20] R. Riener, L. Lunenburger, S. Jezernik, M. Anderschitz, G. Colombo, and V. Dietz, "Patient-cooperative strategies for robot aided treadmill training: First experimental results," *IEEE Transactions on Neural Systems and Rehabilitation Engineering,* vol. 13, pp. 380-394, 2005.

[21] S. Jezernik, G. Colombo, and M. Morari, "Automatic gait-pattern adaptation for rehabilitation with 4-dof robotic orthosis," *IEEE Transactions on Robotics and Automation,* vol. 20, pp. 574-582, 2004.

[22] J. A. Blaya and H. Herr, "Adaptive control of a variable-impedance ankle-foot orthosis to assist drop-foot gait," *IEEE Transactions on Neural Systems and Rehabilitation Engineering,* vol. 12, pp. 24-31, 2004.

[23] N. Hogan, "Stable execution of contact tasks using impedance control," in *IEEE International Conference on Robotics and Automation*, 1987, pp. 1047-1054.

[24] N. Hogan and S. P. Buerger, "Impedance and interaction control," in *Robotics and Automation Handbook,* T. Kurfess, Ed., ed New York: CRC Press, 2005.

[25] B. Siciliano and L. Villani, *Robot force control*. Boston: Kluwer Academic Publishers, 1999.

[26] T. Lefebvre, J. Xiao, H. Bruyninckx, and G. Gersem, "active compliant motion: a survey," *Advanced Robotics*, vol. 19, pp. 479-499, 2005.

[27] G. Zeng and A. Hemami, "An overview of robot force control," *Robotica*, vol. 15, pp. 473-482, 1997.

[28] M. H. Raibert and J. J. Craig, "Hybrid position/force control of manipulators," *Journal of Dynamic Systems, Measurement and Control, Transactions of the ASME,* vol. 103, pp. 126-133, 1981.

[29] N. Hogan, "Impedance control: An approach to manipulation: Parts I,II and III," *Journal of Dynamic Systems, Measurement, and Control,* vol. 107, pp. 17-24, 1985.

[30] A. Roy, H. I. Krebs, D. Williams, C. T. Bever, L. W. Forrester, R. M. Macko, and N. Hogan, "Robot-aided neurorehabilitation: A novel robot for ankle rehabilitation," *IEEE Transactions on Robotics,* vol. 25, pp. 569-582, 2009.

[31] J. Yoon, J. Ryu, and K.-B. Lim, "Reconfigurable ankle rehabilitation robot for various exercises," *Journal of Robotic Systems*, vol. 22, pp. S15-S33, 2006.

[32] J. A. Saglia, N. G. Tsagarakis, J. S. Dai, and D. G. Caldwell, "A high-performance redundantly actuated mechanism for ankle rehabilitation," *The International Journal of Robotics Research,* vol. 28, pp. 1216-1227, 2009.

[33] M. Bernhardt, M. Frey, G. Colombo, and T. Rahman, "Hybrid force-position control yields cooperative behaviour of the rehabilitation robot LOKOMAT," in *IEEE International Conference on Rehabilitation Robotics*, 2005, pp. 536-539.

[34] R. Colbaugh, H. Seraji, and K. CGlass, "Direct adaptive impedance control of robot manipulators," *Journal of Robotic Systems,* vol. 10, pp. 217-248, 1993.

[35] C.-C. Cheah and D. Wang, "Learning impedance control for robotic manipulators," *IEEE Transactions on Robotics and Automation*, vol. 14, pp. 452-465, 1998.

[36] S. K. Singh and D. O. Popa, "Analysis of some fundamental problems in adaptive control of force and impedance behavior: theory and experiments," *IEEE Transactions on Robotics and Automation,* vol. 11, pp. 912-921, 1995.

[37] M. Dettwyler, A. Stacoff, I. A. Kramers-de Quervain, and E. Stussi, "Modelling of the ankle joint complex. Reflections with regards to ankle prostheses," *Foot and Ankle Surgery,* vol. 10, pp. 109-119, 2004.

[38] Accident Compensation Corporation, New Zealand. http://www.acc.co.nz/for-providers/resources/WCMZ002647?ssSourceNodeId=4249&ssSourceSiteId=1494

[39] M. R. Safran, J. E. Zachazewski, R. S. Benedetti, A. R. I. Bartolozzi, and R. Mandelbaum, "Lateral ankle sprains: a comprehensive review Part 2: Treatment and rehabilitation with an emphasis on the athlete," *Medicine & Science in Sports & Exercise,* vol. 31, pp. S438-S447, 1999.

[40] C. G. Mattacola and M. K. Dwyer, "Rehabilitation of the ankle after acute sprain or chronic instability," *Journal of Athletic Training*, vol. 37, pp. 413-429, 2002.

[41] J. Yoon and J. Ryu, "A novel reconfigurable ankle/foot rehabilitation robot," in *IEEE International Conference on Robotics and Automation*, Barcelona, Spain, 2005, pp. 2290-2295.

[42] G. Liu, J. Gao, H. Yue, X. Zhang, and G. Lu, "Design and kinematics simulation of parallel robots for ankle rehabilitation," in *IEEE International Conference on Mechatronics and Automation*, Luoyang, China, 2006, pp. 1109-1113.

[43] I. C. Wright, R. R. Neptune, A. J. Van den Bogert, and B. M. Nigg, "The influence of foot positioning on ankle sprains," *Journal of Biomechanics*, vol. 33, pp. 513-519, 2000.

[44] I. C. Wright, R. R. Neptune, A. J. Van den Bogert, and B. M. Nigg, "The effects of ankle compliance and flexibility on ankle sprains," *Medicine & Science in Sports & Exercise*, vol. 32, pp. 260-265, 2000.

[45] P. C. Liacouras and J. S. Wayne, "Computational modeling to predict mechanical function of joints: Application to the lower leg with simulation of two cadaver studies," *Journal of Biomechanical Engineering*, vol. 129, pp. 811-817, 2007.

[46] J. T.-M. Cheung and B. M. Nigg, "Clinical applications of computational simulation of foot and ankle," *Sports Orthopaedics and Traumatology*, vol. 23, pp. 264-271, 2008.

[47] J. T.-M. Cheung, M. Zhang, and K.-N. An, "Effects of plantar fascia stiffness on the biomechanical responses of the ankle-foot complex," *Clinical Biomechanics*, vol. 19, pp. 839-846, 2004.

[48] J. T.-M. Cheung, M. Zhang, A. K.-L. Leung, and Y.-B. Fan, "Three dimensional finite element analysis of the foot during standing - a material sensitivity study," *Journal of Biomechanics*, vol. 38, pp. 1045-1054, 2005.

[49] M. Mihelj, T. Nef, and R. Riener, "A novel paradigm for patient-cooperative control of upper-limb rehabilitation robots," *Advanced Robotics*, vol. 21, pp. 843-867, 2007.

[50] E. T. Wolbrecht, V. Chan, D. J. Reinkensmeyer, and J. E. Bobrow, "Optimizing compliant, model-based robotic assistance to promote neurorehabilitation," *IEEE Transactions on Neural Systems and Rehabilitation Engineering*, vol. 16, pp. 286-297, 2008.

[51] Y. H. Tsoi and S. Q. Xie, "Design and control of a parallel robot for ankle rehabilitation," *International Journal of Intelligent Systems Technologies and Applications*, vol. 8, pp. 100-113, 2010.

[52] Y. H. Tsoi and S. Q. Xie, "Impedance control of ankle rehabilitation robot," in *International Conference on Robotics and Biomimetics*, 2008, pp. 840-845.

[53] Y. H. Tsoi, S. Q. Xie, and A. E. Graham, "Design, modeling and control of an ankle rehabilitation robot," in *Design and Control of Intelligent Robotic Systems*, D. Liu*, et al.*, Eds., ed Berlin: Springer, 2009.

[54] Y. H. Tsoi, S. Q. Xie, and G. D. Mallinson, "Joint force control of parallel robot for ankle rehabilitation," in *IEEE International Conference on Control and Automation*, 2009, pp. 1856-1861.

[55] Y. H. Tsoi and S. Q. Xie, "Trajectory generation for ankle rehabilitation: A biomechanical model based approach," in *UKACC International Conference on Control*, 2010 (Accepted for presentation).

[56] K. Bharadwaj, T. G. Sugar, J. B. Koeneman, and E. J. Koeneman, "Design of a robotic gait trainer using spring over muscle actuators for ankle stroke rehabilitation," *Journal of Biomechanical Engineering,* vol. 127, pp. 1009-1013, 2005.

[57] D. P. Ferris, J. M. Czerniecki, and B. Hannaford, "An ankle-foot orthosis powered by artificial pneumatic muscles," *Journal of Applied Biomechanics,* vol. 21, pp. 189-197, 2005.

[58] Human-Machine Interface Laboratory, Rutgers University. http://www.caip.rutgers.edu/vrlab/projects/ankle/ankle.html

[59] G. S. Sawicki and D. P. Ferris, "A pneumatically powered knee-ankle-foot orthosis (KAFO) with myoelectric activation and inhibition," *Journal of NeuroEngineering and Rehabilitation,* vol. 6, art. no. 23, 2009.

[60] G. S. Sawicki, K. E. Gordon, and D. P. Ferris, "Powered lower limb orthoses: Applications in motor adaptation and rehabilitation," in *2005 IEEE International Conference on Rehabilitation Robotics*, 2005, pp. 206-211.

[61] A. W. Boehler, K. W. Hollander, T. G. Sugar, and D. Shin, "Design, implementation and test results of a robust control method for a powered ankle foot orthosis (AFO)," in *IEEE International Conference on Robotics and Automation*, 2008, pp. 2025-2030.

[62] A. Agrawal, S. K. Banala, S. K. Agrawal, and S. A. Binder-Macleod, "Design of a two degree-of-freedom ankle-foot orthosis for robotic rehabilitation," in *IEEE International Conference on Rehabilitation Robotics*, 2005, pp. 41-44.

[63] J. W. Wheeler, H. I. Krebs, and N. Hogan, "An ankle robot for a modular gait rehabilitation system," in *IEEE/RSJ International Conference on Intelligent Robots and Systems*, Sendai, Japan, 2004, pp. 1681-1684.

[64] A. C. Satici, A. Erdogan, and V. Patoglu, "Design of a reconfigurable ankle rehabilitation robot and its use for the estimation of the ankle impedance," in *International Conference on Rehabilitation Robotics*, 2009, pp. 257-264.

[65] C. E. Syrseloudis and I. Z. Emiris, "A parallel robot for ankle rehabilitation-evaluation and its design specifications," in *IEEE International Conference on BioInformatics and BioEngineering*, 2008.

[66] J. S. Dai and T. Zhao, "Sprained ankle physiotherapy based mechanism synthesis and stiffness analysis of a robotic rehabilitation device," *Autonomous Robots,* vol. 16, pp. 207-218, 2004.

[67] C.-C. K. Lin, M.-S. Ju, S.-M. Chen, and B.-W. Pan, "A specialized robot for ankle rehabilitation and evaluation," *Journal of Medical and Biological Engineering,* vol. 28, pp. 79-86, 2008.

[68] J. G. Sun, J. Y. Gao, J. H. Zhang, and R. H. Tan, "Teaching and playback control system for parallel robot for ankle joint rehabilitation," in *IEEE International Conference on Industrial Engineering and Engineering Management*, 2007, pp. 871-875.

[69] C. H. Barnett and J. R. Napier, "The axis of rotation at the ankle joint in man; its influence upon the form of the talus and the mobility of the fibula," *Journal of Anatomy,* vol. 86, pp. 1-9, 1952.

[70] A. Lundberg, O. K. Svensson, G. Nemeth, and G. Selvik, "The axis of rotation of the ankle joint," *Journal of Bone and Joint Surgery - Series B,* vol. 71, pp. 94-99, 1989.

[71] J. R. Engsberg, "A biomechanical analysis of the talocalcaneal joint - in vitro," *Journal of Biomechanics*, vol. 20, pp. 429-442, 1987.

[72] D. M. Demarais, R. A. Bachschmidt, and G. F. Harris, "The instantaneous axis of rotation (IAOR) of the foot and ankle: A self-determining system with implications for rehabilitation medicine application," *IEEE Transactions on Neural Systems and Rehabilitation Engineering*, vol. 10, pp. 232-238, 2002.

[73] N. Ying and W. Kim, "Determining dual Euler angles of the ankle complex in vivo using "flock of birds" electromagnetic tracking device," *Journal of Biomechanical Engineering,* vol. 127, pp. 98-107, 2005.

[74] A. Leardini, J. J. O'Connor, F. Catani, and S. Giannini, "A geometric model of the human ankle joint," *Journal of Biomechanics,* vol. 32, pp. 585-591, 1999.

[75] J. Apkarian, S. Naumann, and B. Cairns, "A three-dimensional kinematic and dynamic model of the lower limb," *Journal of Biomechanics,* vol. 22, pp. 143-155, 1989.

[76] J. Dul and G. E. Johnson, "A kinematic model of the human ankle," *Journal of Biomedical Engineering,* vol. 7, pp. 137-143, 1985.

[77] S. H. Scott and D. A. Winter, "Biomechanical model of the human foot: kinematics and kinetics during the stance phase of walking," *Journal of Biomechanics,* vol. 26, pp. 1091-1104, 1993.

[78] S. L. Delp, F. C. Anderson, A. S. Arnold, P. Loan, A. Habib, C. T. John, E. Guendelman, and D. G. Thelen, "OpenSim: Open-source software to create and analyze dynamic simulations of movement," *IEEE Transactions on Biomedical Engineering,* vol. 54, pp. 1940-1950, 2007.

[79] A. J. van den Bogert, G. D. Smith, and B. M. Nigg, "In vivo determination of the anatomical axes of the ankle joint complex: an optimization approach," *Journal of Biomechanics,* vol. 27, pp. 1477-1488, 1994.

[80] V. T. Inman, *The joints of the ankle*. Baltimore: Williams and Wilkins, 1976.

[81] R. D. Gregorio, V. Parenti-Castelli, J. J. O'Connor, and A. Leardini, "Mathematical models of passive motion at the human ankle joint by equivalent spatial parallel mechanisms," *Medical and Biological Engineering and Computing,* vol. 45, pp. 305-313, 2007.

[82] G. S. Lewis, H. J. Sommer, and S. J. Piazza, "In vitro assessment of a motion-based optimization method for locating the talocrural and subtalar joint axes," *Journal of Biomechanical Engineering,* vol. 128, pp. 596-603, 2006.

[83] R. J. de Asla, L. Wan, H. E. Rubash, and G. Li, "Six dof in vivo kinematics of the ankle joint complex: Application of a combined dual-orthogonal fluoroscopic and magnetic resonance imaging technique," *Journal of Orthopaedic Research,* vol. 24, pp. 1019-1027, 2006.

[84] R. E. Kearney, P. L. Weiss, and R. Morier, "System identification of human ankle dynamics: intersubject variability and intrasubject reliability," *Clinical Biomechanics,* vol. 5, pp. 205-217, 1990.

[85] R. Riener and T. Edrich, "Identification of passive elastic joint moments in the lower extremities," *Journal of Biomechanics,* vol. 32, pp. 539-544, 1999.

[86] I. W. Hunter and R. E. Kearney, "Dynamics of human ankle stiffness: Variation with mean ankle torque," *Journal of Biomechanics,* vol. 15, pp. 747-752, 1982.

[87] R. E. Kearney and I. W. Hunter, "Dynamics of human ankle stiffness: Variation with displacement amplitude," *Journal of Biomechanics,* vol. 15, pp. 753-756, 1982.

[88] C. S. Parenteau, D. C. Viano, and P. Y. Petit, "Biomechanical properties of human cadaveric ankle-subtalar joints in quasi-static loading," *Journal of Biomechanical Engineering,* vol. 120, pp. 105-111, 1998.

[89] J. Chen, S. Siegler, and C. D. Schneck, "The three-dimensional kinematics and flexibility characteristics of the human ankle and subtalar joint- Part II: Flexibility characteristics," *Journal of Biomechanical Engineering,* vol. 110, pp. 374-385, 1988.

[90] S. J. Piazza and G. S. Lewis, "Computational models of the foot and ankle," *Current Opinion in Orthopaedics,* vol. 14, pp. 79-83, 2003.

[91] V. L. Giddings, G. S. Beaupre, R. T. Whalen, and D. R. Carter, "Calcaneal loading during walking and running," *Medicine & Science in Sports & Exercise,* vol. 32, pp. 627-634, 2000.

[92] A. Leardini and D. Moshcella, "Dynamic simulation of the natural and replaced human ankle joint," *Medical and Biological Engineering and Computing,* vol. 40, pp. 193-199, 2002.

[93] N. Haraguchi, R. S. Armiger, M. S. Myerson, J. T. Campbell, and E. Y. S. Chao, "Prediction of three-dimensional contact stress and ligament tension in the ankle during stance determined from computational modeling," *Foot & Ankle International*, vol. 30, pp. 177-185, 2009.

[94] F. L. Lewis, D. M. Dawson, and C. T. Abdallah, *Robot manipulator control*, Second ed. New York: Marcel Dekker, 2004.

[95] A. Deneve, S. Moughamir, L. Afilal, and J. Zaytoon, "Control system design of a 3-DOF upper limbs rehabilitation robot," *Computer Methods and Programs in Biomedicine,* vol. 89, pp. 202-214, 2008.

[96] D. Erol and N. Sarkar, "Design and implementation of an assistive controller for rehabilitation robotic systems," *International Journal of Advanced Robotic Systems,* vol. 4, pp. 271-278, 2007.

[97] C. J. Kempf and S. Kobayashi, "Disturbance observer and feedforward design for a high-speed direct-drive positioning table," *IEEE Transactions on Control Systems Technology,* vol. 7, pp. 513-526, 1999.

[98] Y. Wang, Z. Xiong, H. Ding, and X. Zhu, "Nonlinear friction compensation and disturbance observer for a high-speed motion platform," in *International Conference on Robotics & Automation*, New Ordleans, LA, 2004, pp. 4515-4520.

[99] C. H. An and J. M. Hollerbach, "Dynamic stability issues in force control of manipulators," in *IEEE International Conference on Robotics and Automation*, 1987, pp. 890-896.

[100] J. E. Colgate and N. Hogan, "Robust control of dynamically interacting systems," *International Journal of Control,* vol. 48, pp. 65-88, 1988.

[101] J. E. Colgate and N. Hogan, "An analysis of contact instability in terms of passive physical equivalents," in *IEEE International Conference on Robotics and Automation*, 1989, pp. 404-409.

[102] S. P. Buerger and N. Hogan, "Relaxing passivity for human-robot interaction," in *IEEE/RSJ International Conference on Intelligent Robots and Systems*, 2006, pp. 4570-4575.

[103] S. P. Buerger and N. Hogan, "Complementary stability and loop shaping for improved human–robot interaction," *IEEE Transactions on Robotics,* vol. 23, pp. 232-244, 2007.

[104] T. Murakami, F. Yu, and K. Ohnishi, "Torque sensorless control in multidegree-of-freedom manipulator," *IEEE Transactions on Industrial Electronics,* vol. 40, pp. 259-265, 1993.

[105] S. Katsura, Y. Matsumoto, and K. Ohnishi, "Analysis and experimental validation of force bandwidth for force control," *IEEE Transactions on Industrial Electronics,* vol. 53, pp. 922-928, 2006.

[106] K. Kong, M. Tomizuka, H. Moon, B. Hwang, and D. Jeon, "Mechanical design and impedance compensation of SUBAR (Sogang University's Biomedical Assist Robot)," in *IEEE/ASME International Conference on Advanced Intelligent Mechatronics,* Xi'an, China, 2008, pp. 377-382.

[107] W. S. Newman, "Stability and performance limits of interaction controllers," *Journal of Dynamic Systems, Measurement, and Control,* vol. 114, pp. 563-570, 1992.

[108] S. Siegler, J. Chen, and C. D. Schneck, "The three-dimensional kinematics and flexibility characteristics of the human ankle and subtalar joints-Part I: Kinematics," *Journal of Biomechanical Engineering,* vol. 110, pp. 364-373, 1988.

[109] Mrabet, Y. http://commons.wikimedia.org/wiki/File:Human_anatomy_planes.svg

[110] J.-P. Merlet, *Parallel robots,* Second ed. Netherlands: Springer, 2006.

[111] L.-W. Tsai, *Robot analysis: the mechanics of serial and parallel manipulators*. New York: John Wiley & Sons, 1999.

[112] R. E. Isman and V. T. Inman, "Anthropometric studies of the human foot and ankle," Biomechanics Laboratory, University of California, San Francisco and Berkeley, Technical Report 58, San Francisco, The Laboratory, May 1968.

[113] J. R. Raol, G. Girija, and J. Singh, *Modelling and parameter estimation of dynamic systems*. London: Institution of Electrical Engineers, 2004.

[114] K. Madsen, H. B. Nielsen, and O. Tingleff. (2004). *Methods for non-linear least squares problems*. Available: http://www2.imm.dtu.dk/pubdb/views/edoc_download.php/3215/pdf /imm3215.pdf

[115] J. R. Funk, G. W. Hall, J. R. Crandall, and W. D. Pilkey, "Linear and quasi-linear viscoelastic characterization of ankle ligaments," *Journal of Biomechanical Engineering,* vol. 122, pp. 15-22, 2000.

[116] J. M. Winters, "Hill-based muscle models: A system engineering perspective," in *Multiple Muscle Systems: Biomechanics and Movement Organization*, J. M. Winters and S. L.-Y. Woo, Eds., ed New York: Springer-Verlag, 1990, pp. 69-91.

[117] H. Yamada and J. Kajzer, "A mathematical model of skeletal muscle and numerical simulations of its response under stretching," *JSME International Journal, Series C: Mechanical Systems, Machine Elements and Manufacturing,* vol. 42, pp. 508-513, 1999.

[118] F. E. Zajac, "Muscle and Tendon: Properties, Models, Scaling and Application to Biomechanics and Motor Control," *Critical Reviews in Biomedical Engineering,* vol. 17, pp. 359-411, 1989.

[119] Primal Pictures Ltd. www.anatomy.tv

[120] Department of Radiology, University of Washington. http://www.rad.washington.edu/academics/academic-sections/msk/muscle-atlas/lower-body/

[121] G. T. Yamaguchi, A. G. U. Sawa, D. W. Moran, M. J. Fessler, and J. M. Winters, "A survey of human musculotendon actuator parameters," in *Multiple Muscle Systems: Biomechanics and Movement Organization*, J. M. Winters and S. L.-Y. Woo, Eds., ed New York: Springer-Verlag, 1990.

[122] VAKHUM public dataset. http://www.ulb.ac.be/project/vakhum/public_dataset/public-data.htm

[123] P. Martin and M. R. Emami, "Real-time fuzzy trajectory generation for robotic rehabilitation therapy," in *IEEE International Conference on Rehabilitation Robotics*, 2009, pp. 354-359.

[124] H. Vallery, E. H. F. van Asseldonk, M. Buss, and H. van der Kooij, "Reference trajectory generation for rehabilitation robots: Complementary limb motion estimation," *IEEE Transactions on Neural Systems and Rehabilitation Engineering,* vol. 17, pp. 23-30, 2009.

[125] S. Babaci, Y. Amirat, J. Pontnau, and C. Francois, "Fuzzy adaptation impedance of a 6 d.o.f parallel robot. Application to peg in hole insertion," 1996, pp. 1770-1776.

[126] M. Callegari, M. C. Palpacelli, and M. Principi, "Dynamics modelling and control of the 3-RCC translational platform," *Mechatronics,* vol. 16, pp. 589-605, 2006.

[127] L. F. Baptista, J. M. Sousa, and J. M. G. Sa da Costa, "Fuzzy predictive algorithms applied to real-time force control," *Control Engineering Practice,* vol. 9, pp. 411-423, 2001.

[128] L. E. Bruzzone, R. M. Molfino, and M. Zoppi, "An impedance-controlled parallel robot for high-speed assembly of white goods," *Industrial Robot,* vol. 32, pp. 226-233, 2005.

[129] J. A. Saglia, C. J. Tsaprounis, J. S. Dai, and D. G. Caldwell, "Inverse-kinematics-based control of a redundantly actuated platform for rehabilitation," *Proceedings of the Institution of Mechanical Engineers, Part I: Journal of Systems and Control Engineering,* vol. 223, pp. 53-70, 2009.

[130] S. Katsura, K. Irie, and K. Ohishi, "Wideband force control by position-acceleration integrated disturbance observer," *IEEE Transactions on Industrial Electronics,* vol. 55, pp. 1699-1706, 2008.

[131] R. Dorf and R. H. Bishop, *Modern control systems*. Upper Saddle River, NJ: Pearson Education, 2005.

[132] D. G. Bates and I. Postlethwaite, "The structured singular value and mu-analysis," in *Advanced techniques for clearance of flight control laws*, C. Fielding*, et al.*, Eds., ed Berlin: Springer, 2002, pp. 37-55.

[133] S. P. Buerger, "Stable, high-force, low impedance robotic actuators for human-interactive machines," PhD dissertation, Dept. Mech. Eng., MIT, Cambridge, MA, 2005.

[134] NASA. http://msis.jsc.nasa.gov/sections/section03.htm

[135] H. Cheng, Y.-K. Yin, and Z. Li, "Dynamics and control of redundantly actuated parallel manipulators," *IEEE/ASME Transactions on Mechatronics,* vol. 8, pp. 483-491, 2003.

[136] A. Bjorck, *Numerical methods for least squares problems*. Philadelphia: SIAM, 1996.

[137] L. J. Love and W. J. Book, "Force reflecting teleoperation with adaptive impedance control," *IEEE Transactions on Systems, Man, and Cybernetics,* vol. 34, pp. 159-165, 2004.

[138] T. Tsumugiwa, R. Yokogawa, and K. Hara, "Variable impedance control based on estimation of human arm stiffness for human-robot cooperative calligraphic task," in *International Conference on Robotics & Automation*, Washington DC, 2002, pp. 644-650.

[139] S. Miyaguchi, K. Nojiri, N. Matsunaga, and S. Kawaji, "Impedance control of pro-/supination based on the skeleton model of upper limbs," in *International Conference on Control, Automation and Systems*, 2007, pp. 968-973.